PARAMETERIZATION OF MUDFLAT PROFILE CHANGES CAUSED BY SEASONAL TIDE LEVEL VARIATIONS

by

FUMIHIKO YAMADA AND NOBUHISA KOBAYASHI

RESEARCH REPORT NO. CACR-03-02

MARCH, 2003

CENTER FOR APPLIED COASTAL RESEARCH

OCEAN ENGINEERING LABORATORY

UNIVERSITY OF DELAWARE

NEWARK, DE 19716

ABSTRACT

Global warming is expected to raise sea level up to 1 m over the next 100 years. Mudflats with very gentle slopes are very sensitive to changes in sea level. Concern has been raised about the impact of considerable land loss and flooding risk along the mudflat coastal area. Environmental protection and management in the coastal area also require the understanding of mudflat response to time-varying driving forces including sea level rise. However, the morphology of mudflats is poorly understood in comparison to that of sandy beaches and no quantitative model exists to predict the temporal variation of the mudflats profile under time-varying driving forces.

A parameterized mudflat profile with no nearshore bar is proposed using a quadratic polynomial equation fitted to the measured cross-shore profiles on meso-tidal mudflats in the vicinity of a river mouth. This parameterization allows the separation of the temporal and spatial variations of mudflat profiles under time-varying driving forces. The three parameters consisting of the quadratic convexity, mean slope, and vertical displacement of the fitted quadratic profile are used to examine the correlations between the profile

temporal variations and time-varying physical processes. The vertical displacement and mean slope parameters are shown to be highly correlated with the seasonal tide level variation of approximately 40 cm. The quadratic convexity parameter varied semiannually and might be correlated in unknown manners with the average tide level, averaged spring-neap tidal range, and rainfall.

In order to estimate the relative importance of tides and waves in causing the sediment transport on the meso-tidal mudflats, the depth-averaged tidal currents and wave orbital velocities are computed numerically using simple models. Assuming the alongshore uniformity of the cross-shore tide level and mudflat profile, the depth-averaged tidal currents are estimated using only the conservation of water volume. The wave orbital velocities are calculated assuming normally incident linear monochromatic waves. These computed results indicate that wind waves may play an important role in mud suspension and transport and that the combined effects of tides and wind waves will need to be accounted for to predict the sediment transport on the mudflats.

The findings of this study will be useful in developing a meso-tidal mudflat morphological model based the three profile parameters varying with time.

ACKNOWLEDGEMENTS

This study was supported by a grant from the Foundation of Kyushu Industrial Technology Center in Japan and performed at the Center for Applied Coastal Research, University of Delaware as a joint research.

We would like to thank the Kumamoto Port Construction Bureau of Ministry of Land, Infrastructure, and Transport in Japan and the Kumamoto Local Meteorological Observatory of Japan Meteorological Agency for supplying the oceanographic and meteorological data.

We would also like to thank Professor K. Takikawa, Dr. K. Tanaka, and Dr. T. Kakinoki for their valuable discussions. Messrs. S. Maruyama, T. Hokamura, M. Taniguchi, K. Nishimoto, and E. Kinoshita participated in the field surveys and made significant contributions to this study.

TABLE OF CONTENTS

Chapter 1

INTRODUCTION

Long-term sea level rise is likely to occur due to global warming. Eustatic (global) sea level rise has been estimated at approximately 17 cm in the last century (ASCE Task Committee 1992). The future rate of global sea level rise will be larger than the past rate due to the greenhouse effect. Intergovernmental Panel on Climate Change (2001) projects that global mean sea level may rise up to 88 cm between the years 1990 and 2100. Mudflats with very gentle slopes are very sensitive to changes in sea level. Sea level rise may cause considerable land loss and risk of flooding. Environmental protection and management in estuaries require the understanding of mudflat response to changing sea level, oceanography, climate, and anthropogenic pressure (e.g., Dyer 1998).

Mudflats are composed of mixture of sand with its particle diameter d in the range d = 0.075 – 2 mm and mud with $d < 0.075$ mm (Japanese Standard Association 2000a). As the mud content in the sediment increases, the sediment becomes more cohesive. The morphology of mudflats in estuaries depends on a number of physical processes such as tidal range, sea level (average tide level), tidal currents, wind waves, river discharge, and infrequent storm action.

Hayes (1975) emphasized the importance of tidal range for the morphology of sand deposit and classified estuaries using mean spring tidal range as follows: micro-tidal estuaries for tidal range of 0 – 2 m; meso-tidal estuaries for tidal range of 2 – 4 m; and macro-tidal estuaries for tidal range exceeding 4 m. However, the morphology of mud deposit is poorly understood in comparison to that of sand deposit. This arises partly from the greater complexity of the behavior of cohesive sediment, being influenced by chemical and biological as well as physical processes (Kirby 2000). For instance, due to the interparticle forces, cohesive sediments form loose aggregates or flocs in a saline environment, and diatom growth on the mud surface can restrict erosion [e.g., Teisson *et al.* (1993)]. Dyer (1998) discussed a number of processes that might control the erodability of the mud and the development of the profile shape. On the other hand, using a canonical correlation analysis (CCA) for the data of the sandy beach profile and waves at Duck, N.C., Larson *et al.* (2000) presented a high correlation between the beach profiles and nearshore wave conditions. Very little work is currently available on the relationships between mudflat profiles and physical processes in the estuaries (e.g., Bassoullet *et al.* 2000)

Many mudflats appear to be accreting at the same rate as sea level rise, thereby suggesting that an equilibrium condition exists between the dynamic forcing and the sedimentary response (Dyer 1998; Christie *et al.* 2001). A concept of equilibrium beach profiles, which is proposed for sandy beach cross-shore profiles [e.g., Bruun (1962, 1983); Dean (1991)], might hence be applicable in evaluating the mudflat profiles. Assuming wave action as the most predominant

factor for mudflat profile changes, Mehta *et al.* (1996), Lee and Mehta (1997), and Kirby (2000) extended the concept of equilibrium beach profiles to the mudshore profiles. On the other hand, Pattullo *et al.* (1955) examined seasonal oscillations of mean sea level with the maximum value over 1 m in the ocean and coasts facing open sea in the world. Lisitzin and Pattullo (1961) discussed the principal causes of sea level fluctuations and emphasized the contributions of steric (thermal and haline) and atmospheric pressure variations. Unoki (1983) presented the annual variation of the mean sea level in bays in Japan and pointed out the importance of steric, atmospheric pressure, and wind variations. In addition, considerable evidence has been accumulated to show that the temporal variations of mudflats have a number of time scales including tide-cycle (Christie *et al.* 1999), semi-lunar (O'Brien *et al.* 2000), monthly (Anderson *et al.* 1981), and seasonal variation (Bale *et al.*, 1985; Frostick and McCave 1979; Kirby *et al.* 1993). Therefore, the applicability of the concept of equilibrium beach profiles to the mudshore profiles is not clear in the presence of various time scales.

The mudflat profile is characterized conventionally using both its curvature and mean bed slope [e.g., Dieckmann *et al.* (1987); Kirby (1992, 2000); Dyer *et al.* (2000)]. Kirby (1992, 2000) proposed that the curvature of the mudflat profile could be used to classify the relative contributions caused by wind waves and tidal motions to the total sediment transport. Convex-upward profiles were correlated with large tide ranges, long-term accretion and/or low wave activity. Concave-upward profiles were correlated with small tide ranges, long-term

erosion and/or high wave activity. Dyer (1998) and Dyer *et al.* (2000) proposed a statistical scheme for typology and classification of intertidal mudflats using tidal range, wave action, and mean bed slope as the most important variables. However, no quantitative model exists to predict the temporal variation of the mudflat profile under the time-varying driving forces.

Empirical orthogonal eigenfunction (EOF) methods, which do not assume a specific profile form, have been used widely for the analysis of the temporal and spatial patterns of sandy beach morphology [e.g., Winant et al. (1975); Aubrey (1979); Dick and Dalrymple (1984); Wijnberg and Terwindt (1995); Larson *et al.* (1999); Dean and Dalrymple (2002)]. The primary advantage of the EOF analysis is its ability to compress the complicated variability of the observed data set into the fewest possible modes. However, eigenfunctions for the cross-shore profile are not universal among various beaches. Furthermore, it is difficult to interpret the physical meanings of both eigenfunctions and coefficients when this method is applied to mudflat profiles as will be shown later. It is desirable to develop a simple model specifically for tidal flat profiles.

In this study, a parameterized mudflat profile with no nearshore bar is proposed using the measured bed levels on meso-tidal mudflats in the vicinity of a river mouth. This parameterization allows the separation of the temporal and spatial variations of mudflat profiles under time-varying driving forces. A quadratic polynomial equation is adopted to describe the measured mudflat profiles. The three parameters for the quadratic convexity, mean slope, and

vertical displacement of the fitted profile are used to examine the time scales and lags between the profile temporal variations and the time-varying physical processes. The findings of this study will be useful in developing a morphological model for predicting the three profile parameters as a function of time.

In the following, field observations of meso-tidal mudflat profiles in the vicinity of the Shirakawa River mouth in Japan are described first. Temporal variations of the measured cross-shore profiles are presented together with the corresponding oceanographic conditions. The validity of an equilibrium mudflat profile is assessed to show the need of a new approach. Second, the measured mudflat profile is shown to be expressible using a quadratic polynomial equation involving the three parameters: (a) quadratic convexity; (b) mean slope; and (c) vertical displacement. The three parameters representing the measured mudflat profiles express the temporal profile changes. Third, the temporal variations of the three parameters are correlated with the temporal variations of tide level, wind waves, and river discharge to identify the dominant oceanographic factors, which cause the temporal variations of these three parameters. Fourth, depth-averaged tidal currents and wave orbital velocities are computed numerically to estimate the relative importance of tides and waves in causing the sediment transport on the meso-tidal mudflats. Finally, the findings of this study are summarized.

Chapter 2

FIELD MEASUREMENTS

In this chapter, field observations of meso-tidal mudflat profiles in the vicinity of the Shirakawa River mouth in Kyushu Island, Japan are described. In Section 2.1, the location and morphological feature of the field site, the sediment characteristics, and the survey instrument and method for bed level monitoring are described. In Section 2.2, the spatial and temporal variations of the measured cross-shore mudflat profiles are presented. In Section 2.3, the characteristic time scales and features of the measured tides, wind waves, winds, and river discharge are analyzed using the available oceanographic and meteorological data.

2.1 Bed Level Monitoring

2.1.1 Field site

Ariake Bay is located in Kyushu Island, Japan as shown in Fig. 1. Ariake Bay is a closed inner bay and connected to the East China Sea through a narrow strait in the southwest corner. The length of the bay along the central axis is 97 km, the average width is 20 km, and the total bay area is about 1,700 km^2. The average water depth in the bay is approximately 20 m, and tidal

and tidal flats are common along the bay shoreline. The total tidal flat area is about 12 % of the total bay area. This bay is famous for the highest tidal range in Japan and its maximum spring tidal range becomes almost 6 m in the northern corner on the basis of the oceanographic data described by Isozaki and Kitahara (1977).

An open rectangle in Fig. 1 indicates the field site of this study located at the mouth of the Shirakawa River. The Shirakawa River is situated on the center of the eastern coast of Ariake Bay. The Shirakawa River originates in Mt. Aso, an active volcano and carries a large amount of fine sediment from the mountain area to the mouth of the Shirakawa River.

Fig. 2 shows the map of the field site area. The intertidal flat at the mouth of the Shirakawa River is approximately 2.0 km wide with the average bottom slope of 1/800. This field site has been selected partly because of the available oceanographic data such as the tide level, significant wave height and period, and wind velocity measured at an observation tower of Kumamoto Port located 4.0 km south-west of the Shirakawa River. The simultaneous measurements of tides and wind waves in Ariake Bay are limited to this observation tower. The observation tower was built in 4 m depth below the mean monthly-lowest water level, which is 2.45 m below Tokyo Peil (T.P.). The T.P. datum is the standard ground elevation in Japan based on the Tokyo Bay mean sea level. The water and land levels used in this study are defined relative to this standard datum in Japan. The measuring equipments at the tower and the surrounding oceanographic conditions were described in detail by Tsuruya *et al.* (1990).

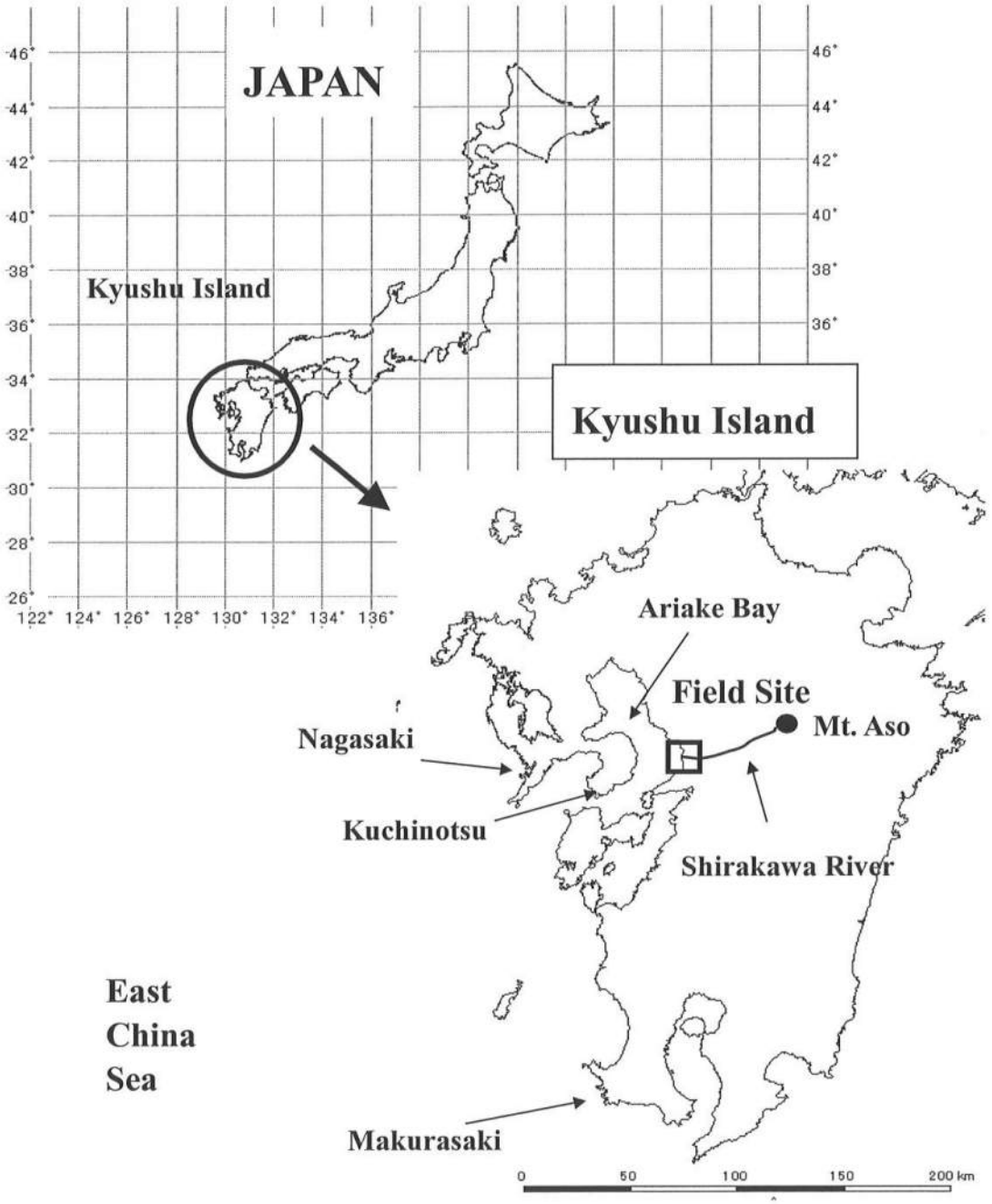

FIG. 1. Field Site in Ariake Bay at Mouth of Shirakawa River in Kyushu, Japan

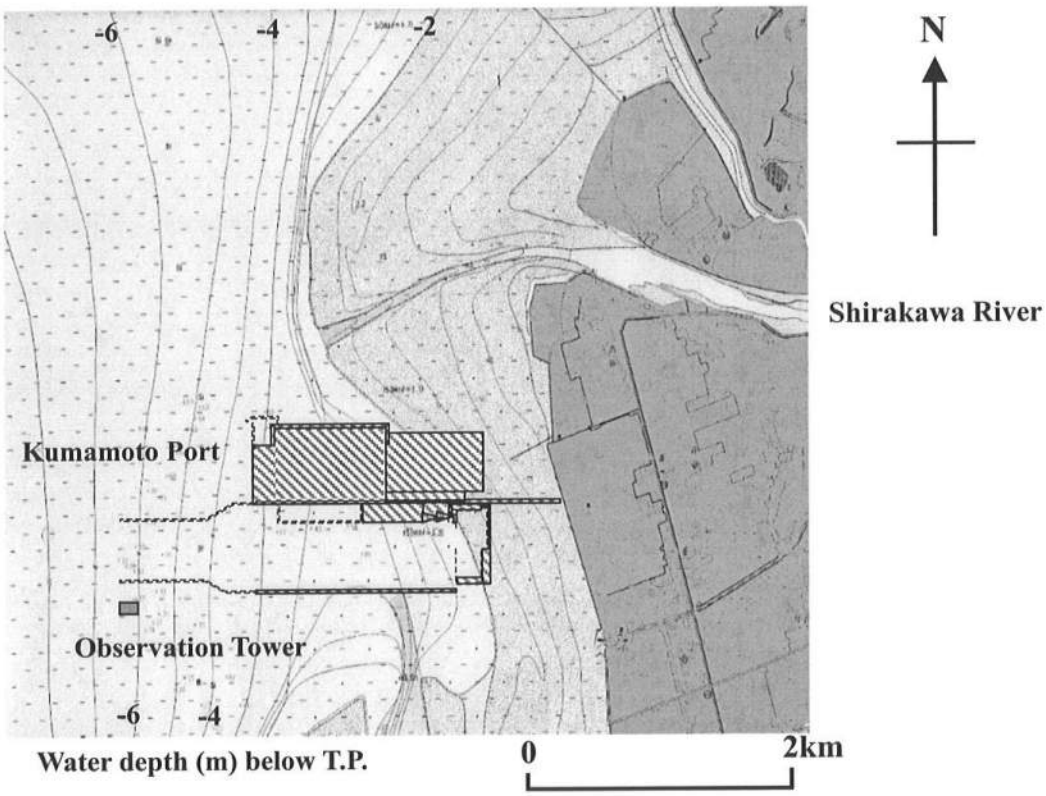

FIG. 2. Map of Field Site Area

Fig. 3 shows the schematic cross-shore profile at the survey site together with the mean monthly-highest and lowest water level based on the measurement from 1975 to 1994 at Kumamoto Port by Kumamoto Port Construction Bureau of Ministry of Land, Infrastructure, and Transport, Japan. The tide is semidiurnal at this site. The offshore distance is measured from the seawall whose crest elevation is 6.0 m above T.P. The mean sea level was specified at 0.00 m T.P by Tsuruya *et al.* (1990) but the average tide level observed from 2000 to 2002 was 0.14 m above T.P. The bottom slope is approximately 1/800 above the mean monthly-lowest water level and increases to approximately 1/350 offshore. Tsuruya *et al.* (1990) pointed out the mean spring tidal range at Kumamoto port to be 3.86 m. Then, the survey site is meso-tidal (Hayes 1975). The survey was not conducted under water but extended close to the mean monthly-lowest water level. The survey method employed in this study is described in detail in Section 2.1.3.

Fig. 4 indicates the two cross-shore profile lines installed on the left and right banks at the mouth of the Shirakawa River. In order to establish fixed survey points, a 2 m-long and 5 cm-square wood stake was driven vertically 1.7 m below the mudflat surface at each point. Each line consisted of 30 fixed survey points spaced at an interval of 50 m and the total length was 1,500 m. The survey number 0 in Table 1 indicates this installation date in October 2000. The installation of 60 stakes may have disturbed the survey lines. As a result, the bed level survey was started in December 2000. The profile measurements were carried out almost every

month during low waters on days of spring tides as listed in Table 1. The survey number 17 for the left profile and 15 for the right profile were not made due to prolonged bad weather. So far, we have measured 20 profiles along the two cross-shore lines over two years.

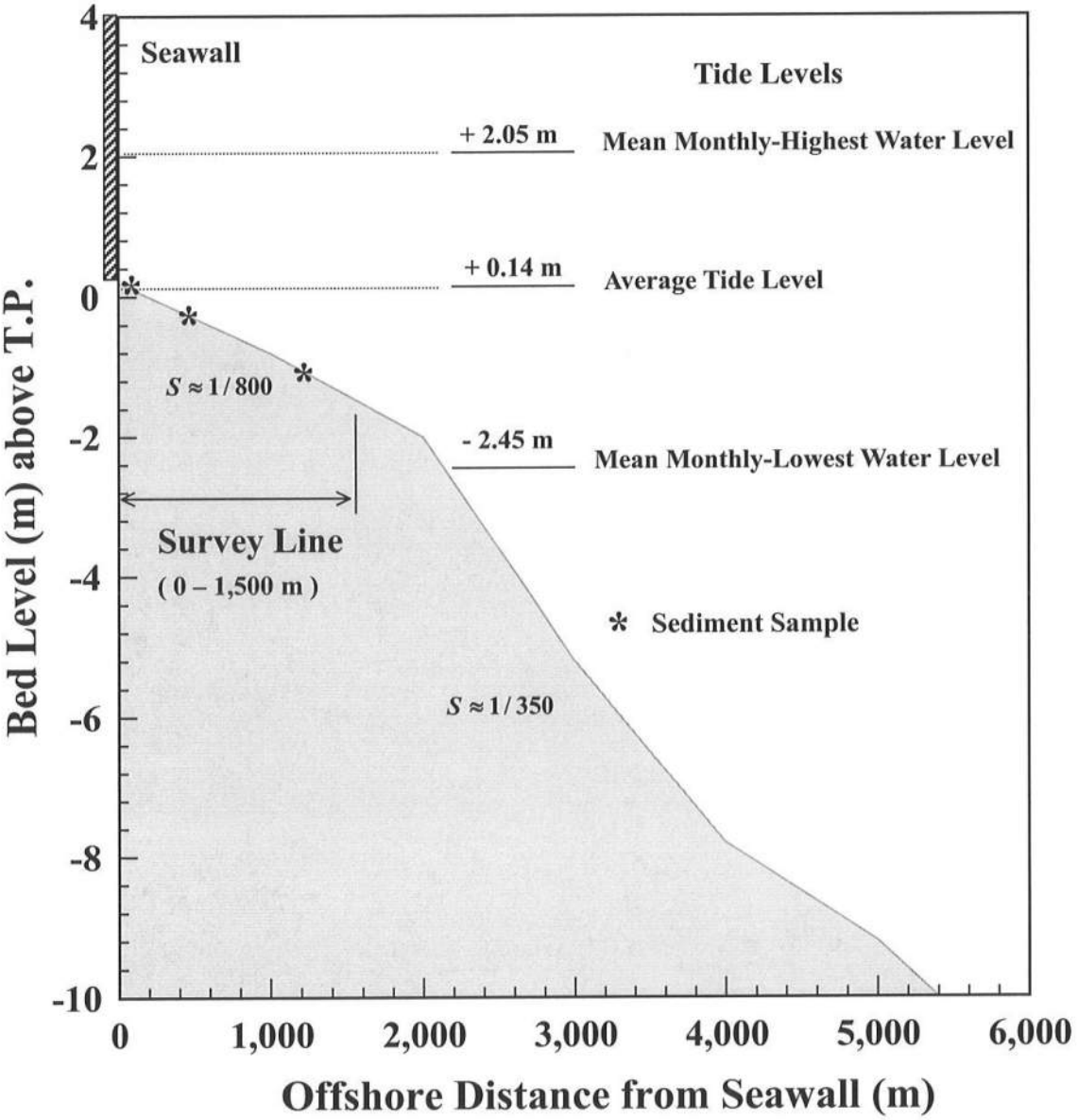

FIG. 3. Schematic Cross-shore Profile and Tide Levels along Survey Line and Offshore

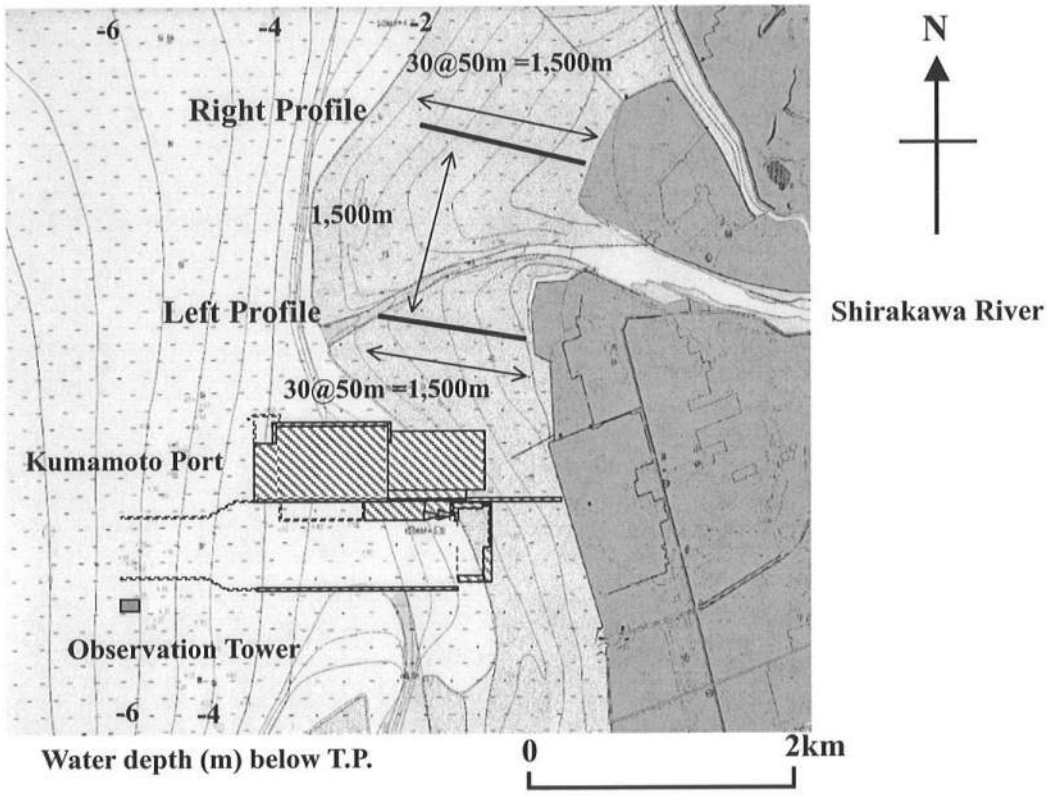

FIG. 4. Location of Two Cross-shore Profile Lines

Table 1: Date of Profile Survey

Survey	Left Profile	Right Profile
0	10/ 4/2000	10/ 5/2000
1	12/11/2000	12/12/2000
2	2/22/2001	2/23/2001
3	4/23/2001	4/25/2001
4	6/01/2001	6/04/2001
5	7/02/2001	7/03/2001
6	9/04/2001	9/05/2001
7	10/18/2001	10/20/2001
8	10/31/2001	11/02/2001
9	11/28/2001	11/30/2001
10	12/26/2001	12/27/2001
11	1/24/2002	1/25/2002
12	2/25/2002	2/26/2002
13	3/29/2002	3/27/2002
14	4/26/2002	4/25/2002
15	6/13/2002	----------
16	7/08/2002	7/11/2002
17	----------	8/08/2002
18	9/24/2002	9/20/2002
19	10/21/2002	10/22/2002
20	11/19/2002	11/18/2002
21	12/18/2002	12/17/2002

2.1.2 Sediment characteristics

Six core samples were collected using a thin-wall sampler (YMB Yoshida Co. ltd) that is 42.5 cm long and 7.5 cm in diameter as shown in Photo 1 at the offshore distances of 100 m, 500 m, and 1,200 m, as marked in Fig. 3, along the left and right cross-shore profile lines in September 2001. The measured parameters for each 10-cm thick layer from the bed surface included the sediment water content, specific gravity, and grain size distribution. The sediment sizes are classified here using the test method recommended by Japanese Standard Association (2000a) whose classification is listed in Table 2 because it is slightly different from the classification used in the US (e.g., Dean & Dalrymple 2002).

Figs. 5 and 6 plot the cumulative size distribution curves for the three layers of each core sample using the sieving test recommended by Japanese Standard Association (2000a). The median diameter (d_{50}) was obtained directly from each distribution and listed in Tables 3 and 4 for the left and right profiles, respectively, where the phi (ϕ) size defined as $\phi = -log_2 d$ with d in millimeters is also presented. The median diameter along the left profile increased slightly downward but was in the narrow range of 0.10 to 0.15 mm. For the surface layer, the median diameter increased slightly and then decreased in the offshore direction. The median diameter for the right profile was in the range 0.14 to 0.18 mm and slightly larger than d_{50} for the left profile. The vertical and cross-shore variations of d_{50} were similar for the two profiles.

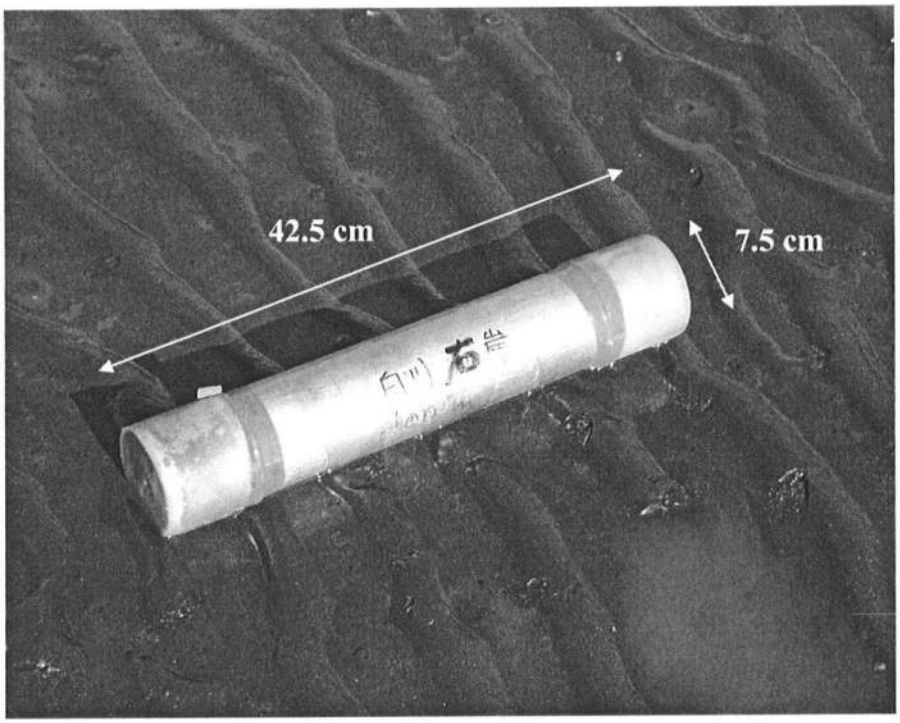

Photo 1: Sediment Core (YMB Yoshida Co. Ltd.)

Table 2: Sediment Size Classification

Size Description (Diameter ≤ 2.00 mm)		Grain Diameter d (mm)	Phi Size ($\phi = -\log_2 d$)
Sand	Very coarse	$2.00 \geq d > 0.85$	$-1.00 \leq \phi < 0.23$
	Coarse	$0.85 \geq d > 0.425$	$0.23 \leq \phi < 1.23$
	Medium	$0.425 \geq d > 0.25$	$1.23 \leq \phi < 2.00$
	Fine	$0.25 \geq d > 0.106$	$2.00 \leq \phi < 3.24$
	Very fine	$0.106 \geq d > 0.075$	$3.24 \leq \phi < 3.74$
Mud	Silt	$0.075 \geq d > 0.005$	$3.74 \leq \phi < 7.64$
	Clay	$0.005 \geq d$	$7.64 \leq \phi$

Japanese Standard Association (2000a) "JIS A 1204: Test method for particle size distribution of soils"

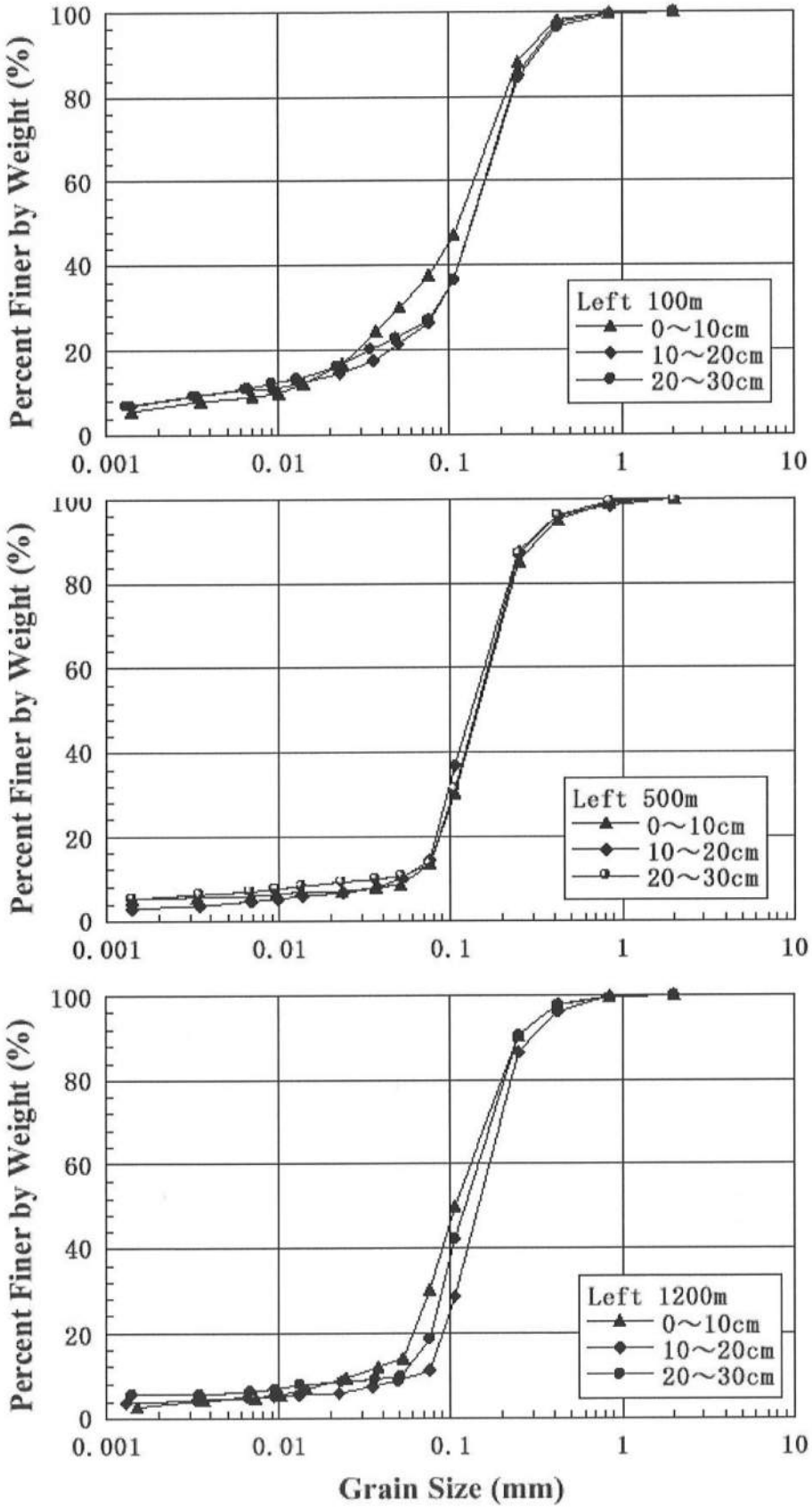

Fig. 5 Cumulative Grain Size Distribution for Left Profile

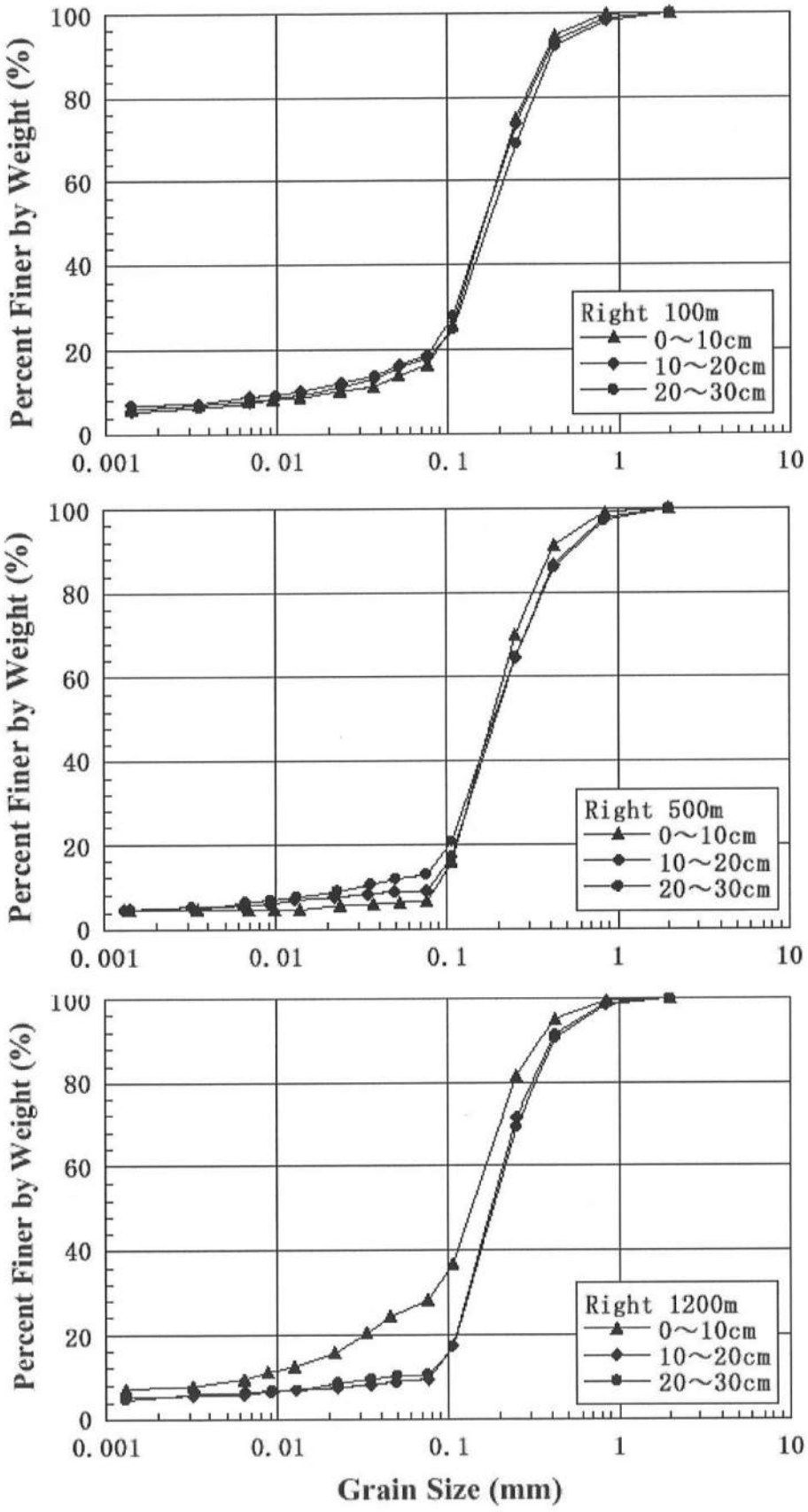

Fig. 6 Cumulative Grain Size Distribution for Right Profile

Tables 3 and 4 also list the mean diameter $M_{d\phi}$ and standard deviation σ_ϕ of the phi size ϕ calculated as follows (e.g., Dean and Darlymple 2002):

$$M_{d\phi} = \frac{(\phi_{84} + \phi_{50} + \phi_{16})}{3} \tag{1}$$

$$\sigma_\phi = \frac{(\phi_{16} - \phi_{84})}{2} \tag{2}$$

where $\phi_p = -\log_2(d_p)$ for given p = percent finer by weight. If ϕ is given by the normal distribution, $\phi_{50} = M_{d\phi}$. The difference $(M_{d\phi} - \phi_{50})$ listed in Tables 3 and 4 indicates that the point of 100 m along the left profile has a more asymmetrical size distribution than the other points. This difference tends to correspond to the increase of the percent finer by weight in the grain size less than about 0.1 mm.

The standard deviation σ_ϕ indicates the sorting of the sediment sample. Perfectly sorted sediment would consist of particles with the same diameter, whereas poorly sorted sediment contains a wide range of sizes. For beach sand, the range $\sigma_\phi \leq 0.5$ is considerd well sorted, whereas sediment with $\sigma_\phi \geq 1.0$ is considered poorly sorted (Dean and Dalrymple 2002). In Tables 3 and 4, $\sigma_\phi \geq 0.8$ and these sediments are not well sorted as can also be inferred from Figs. 5 and 6.

Table 3: Sediment Size Parameters along Left Profile

Offshore Distance (m)	Sediment Size Parameters						
	Distance below Bed	d_{16} (mm)	d_{50} (mm)	d_{84} (mm)	$M_{d\phi}$	$M_{d\phi} - \phi_{50}$	σ_ϕ
		ϕ_{16}	ϕ_{50}	ϕ_{84}			
100	0-10 (cm)	0.02	0.12	0.22	3.63	0.57	1.73
		5.64	3.06	2.18			
	10-20 (cm)	0.03	0.15	0.25	3.27	0.52	1.53
		5.06	2.74	2.00			
	20-30 (cm)	0.02	0.15	0.25	3.46	0.72	1.82
		5.64	2.74	2.00			
500	0-10 (cm)	0.08	0.13	0.25	2.86	-0.08	0.82
		3.64	2.94	2.00			
	10-20 (cm)	0.08	0.15	0.25	2.79	0.05	0.82
		3.64	2.74	2.00			
	20-30 (cm)	0.08	0.15	0.25	2.79	0.05	0.82
		3.64	2.74	2.00			
1200	0-10 (cm)	0.05	0.10	0.22	3.28	-0.04	1.07
		4.32	3.32	2.18			
	10-20 (cm)	0.08	0.15	0.25	2.79	0.05	0.82
		3.64	2.74	2.00			
	20-30 (cm)	0.07	0.12	0.22	3.03	-0.03	0.83
		3.84	3.06	2.18			

Table 4: Sediment Size Parameters along Right Profile

Offshore Distance (m)	Sediment Size Parameters						
	Distance below Bed	d_{16} (mm)	d_{50} (mm)	d_{84} (mm)	$M_{d\phi}$	$M_{d\phi} - \phi_{50}$	σ_ϕ
		ϕ_{16}	ϕ_{50}	ϕ_{84}			
100	0-10 (cm)	0.08	0.16	0.30	2.68	0.04	0.95
		3.64	2.64	1.74			
	10-20 (cm)	0.05	0.16	0.30	2.90	0.26	1.29
		4.32	2.64	1.74			
	20-30 (cm)	0.05	0.17	0.32	2.84	0.28	1.34
		4.32	2.56	1.64			
500	0-10 (cm)	0.11	0.18	0.35	2.39	-0.08	0.84
		3.18	2.47	1.51			
	10-20 (cm)	0.10	0.19	0.40	2.35	-0.05	1.00
		3.32	2.40	1.32			
	20-30 (cm)	0.09	0.19	0.40	2.40	0.00	1.08
		3.47	2.40	1.32			
1200	0-10 (cm)	0.02	0.14	0.28	3.44	0.60	1.90
		5.64	2.84	1.84			
	10-20 (cm)	0.11	0.18	0.38	2.35	-0.12	0.89
		3.18	2.47	1.40			
	20-30 (cm)	0.11	0.18	0.40	2.33	-0.14	0.93
		3.18	2.47	1.32			

The mud content, water content, and specific gravity of the sediment are listed in Tables 5 and 6 for the left and right profiles. Mud is defined here as the sediments whose size is smaller than 0.075 mm and is sum of silt and clay. The mud content is the percent by weight of mud obtained from the cumulative size distribution shown in Figs. 5 and 6 where water is excluded. The water content is the percent by weight between the original sediment sample including water and the corresponding dried sediment sample. The specific gravity is the ratio by weight between the dry sediment and the distilled water ($15^{\circ}C$) with the same volume of this sediment. The ratio between the silt and clay contents is about two along the left profile but about one along the right profile. The mud content averaged vertically is in the range 13.8 to 30.1 % for the left profile but in the range 9.4 to 17.7 % for the right profile. Somehow, more mud is present along the left profile. For both profiles, the mud content becomes smaller in the middle slightly below the average tide level as shown in Fig. 3. On the other hand, the water content and specific gravity are fairly constant except that the water content tends to be larger near the bed.

The samples for the soil organic matter were collected at 500, 1000, and 1500 m along the left and right profile on August 14, 2001 and analyzed using the test method for ignition loss of soils by Japanese Standard Association (2000b). The loss-on-ignition (LOI) is defined as the mass in percentage of soil components lost when a soil sample is ignited for one hour at $750^{\circ}C$ to cause the complete oxidation of organic materials and expressed as

$$LOI\ (\%) = (W_3 - W_2)/(W_2 - W_1) \tag{3}$$

where W_1 = weight of empty crucible and lid, W_2 = weight of empty crucible with lid and oven-dried soil, and W_3 = weight of empty crucible with lid and ignited soil.

Table 7 lists the LOI for the left and right profiles. The LOI remains constant until 1000 m offshore and increases by a factor of two at 1500 m offshore. Paterson (1997) observed that the amount of the chlorophyll *a* and diatom biomass in the mudflat was correlated positively with the microbiology stabilizing the mudflat surface and that the critical shear stress for the erosion was higher for the larger chlorophyll *a* and diatom biomass. The critical shear stress in August 2001 may have increased with the increase of the offshore distance because the LOI is considered to be proportional to the amount of the chlorophyll *a* and diatom biomass.

Table 5: Mud Content, Water Content, and Specific Gravity along Left Profile

Offshore Distance (m)	Distance below Bed	Silt Content (%)	Clay Content (%)	Mud Content (%)	Average Mud Content	Water Content (%)	Specific Gravity
100	0-10 (cm)	29.0	8.0	37.0	30.1 %	58.8	2.72
	10-20 (cm)	16.4	10.0	26.4		40.1	2.77
	20-30 (cm)	16.9	10.0	26.9		43.9	2.76
500	0-10 (cm)	9.4	4.0	13.4	13.8 %	38.4	2.77
	10-20 (cm)	10.5	4.0	14.5		38.6	2.76
	20-30 (cm)	7.1	6.5	13.6		38.6	2.74
1200	0-10 (cm)	25.9	4.5	30.4	20.0 %	55.8	2.72
	10-20 (cm)	6.5	4.5	11.0		40.9	2.81
	20-30 (cm)	12.6	6.0	18.6		39.7	2.78

Table 6: Mud Content, Water Content, and Specific Gravity Along Right Profile

Offshore Distance (m)	Distance below Bed	Silt Content (%)	Clay Content (%)	Mud Content (%)	Average Mud Content	Water Content (%)	Specific Gravity
100	0-10 (cm)	8.3	8.0	16.3	17.7 %	58.4	2.78
	10-20 (cm)	10.8	8.0	18.8		33.0	2.78
	20-30 (cm)	11.0	7.0	18.0		34.9	2.78
500	0-10 (cm)	1.7	4.7	6.4	9.4 %	30.8	2.80
	10-20	3.9	5.0	8.9		32.3	2.87
	20-30	6.8	6.0	12.8		33.6	2.79
1200	0-10 (cm)	19.3	9.0	28.3	16.1 %	58.4	2.76
	10-20 (cm)	3.6	6.0	9.6		33.0	2.79
	20-30 (cm)	4.3	6.1	10.4		34.9	2.78

Table 7: Loss-On-Ignition for the Left and Right Profiles

Offshore Distance (m)	LOI	
	Left (%)	Right (%)
500	1.7	1.8
1000	1.9	1.8
1500	3.6	3.7

2.1.3 Survey instrument and method

The mudflat bed level along the 1.5 km cross-shore line must be measured very accurately because the mudflat profile may not change much. At the same time, the survey must be completed during low water. Therefore, use was made of an electric total station (SOKIA SET3A) to measure the elevation and distance of a survey point simultaneously. The measured bed elevation using this total station was found to agree with that of conventional leveling within an error of 2 cm along the 1.5 km survey line on a hard ground. The horizontal distance of each wood stake relative to its initial position was checked in each survey to ensure the stationarity of the wood stake.

Fig. 7 shows the schematic diagram of the bed level measuring procedure. In order to survey the entire cross-shore line, the total station was set first on a fixed point on the crest of the seawall. The elevation of the total station was obtained from the nearby benchmark. Second, a reflected prism on the top of a reflector pole was placed in front of the fixed wood stake as shown in Photo 2. A large wood plate whose thickness was 13 mm was placed on the mud surface and the reflector pole was set on the plate as shown in Photo 3 to measure the representative bed level. Third, the slanting length, SL, and the angle, θ, below the instrument elevation were read by the total station. The vertical distance, $dh = SL \times sin\theta$, between the instrument elevation and the reflected prism was calculated automatically by the total station. The bed level elevation was obtained by subtracting the vertical distance dh, the reflector pole length of 1.7 m, and the wood

plate thickness of 13 mm from the known instrument elevation as illustration in Fig. 7. The horizontal distance between the seawall and fixed point was calculated as $SL \times cos\theta$. This procedure was repeated from one point to the next point along the entire survey line for a duration of low water during day time. The measurement along the second survey line was carried out on the next day of good weather as listed in Table 1, where the survey number 17 for the left profile and the survey number 15 for the right profile were not carried out due to prolonged bad weather.

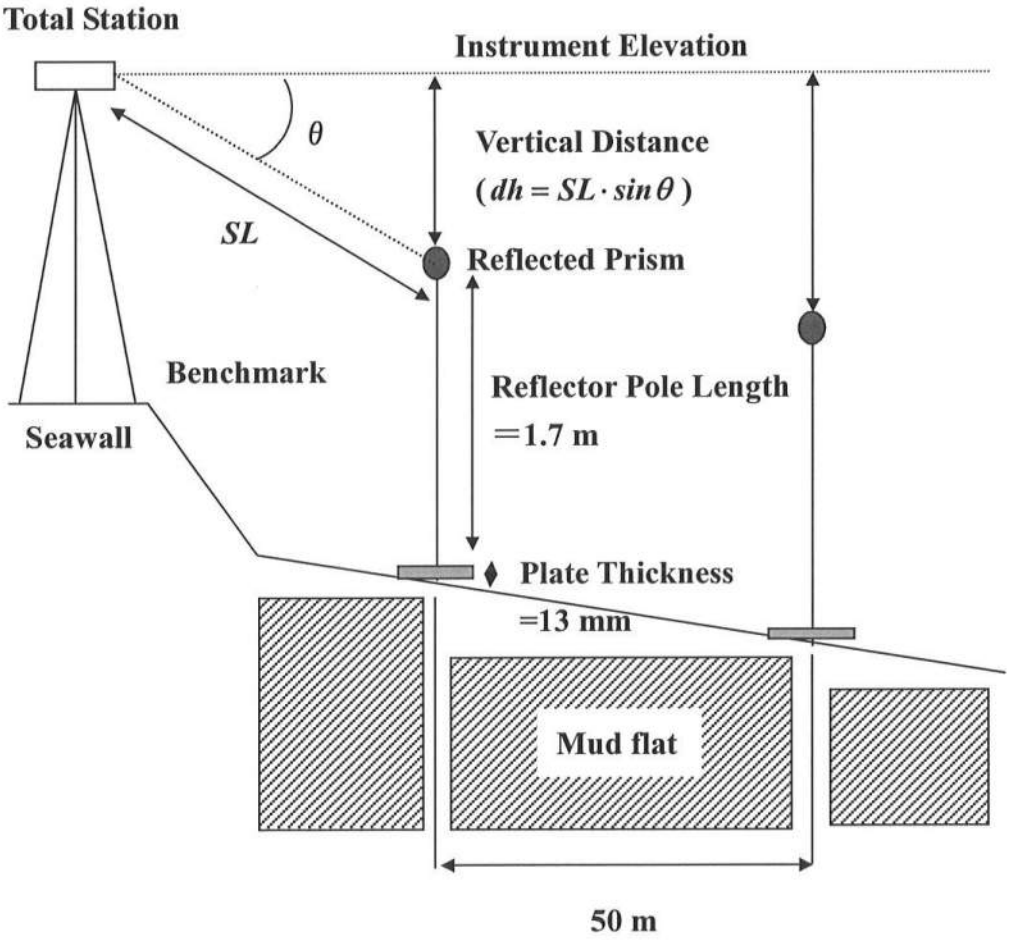

FIG. 7. Schematic Diagram of Bed Level Measurement

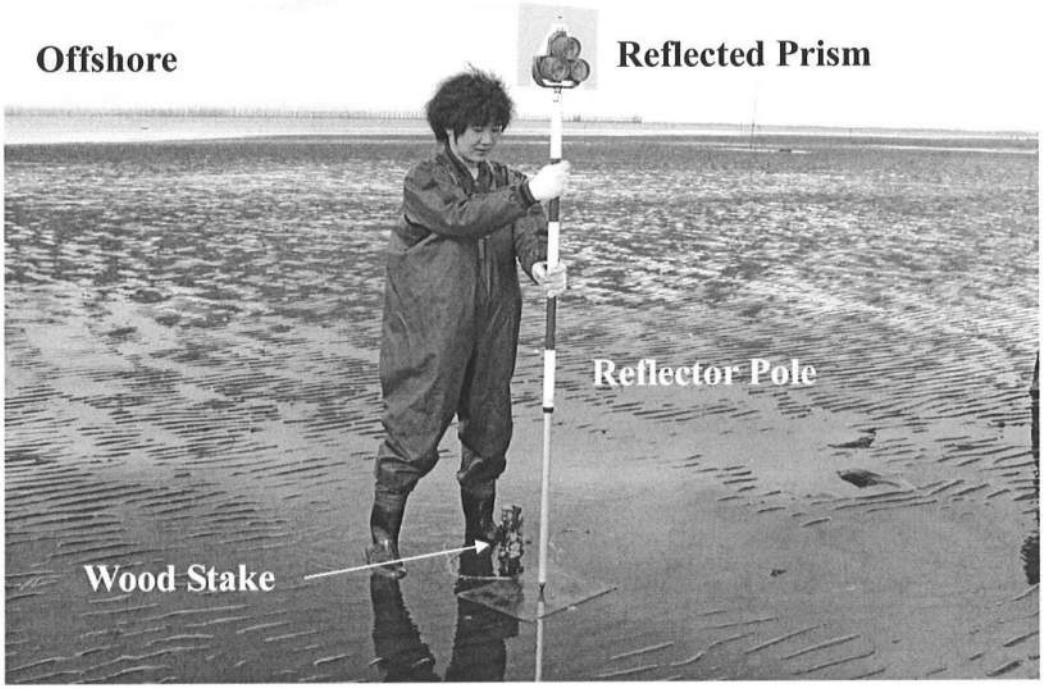

Photo 2: Reflected Prism on Top of Reflector Pole

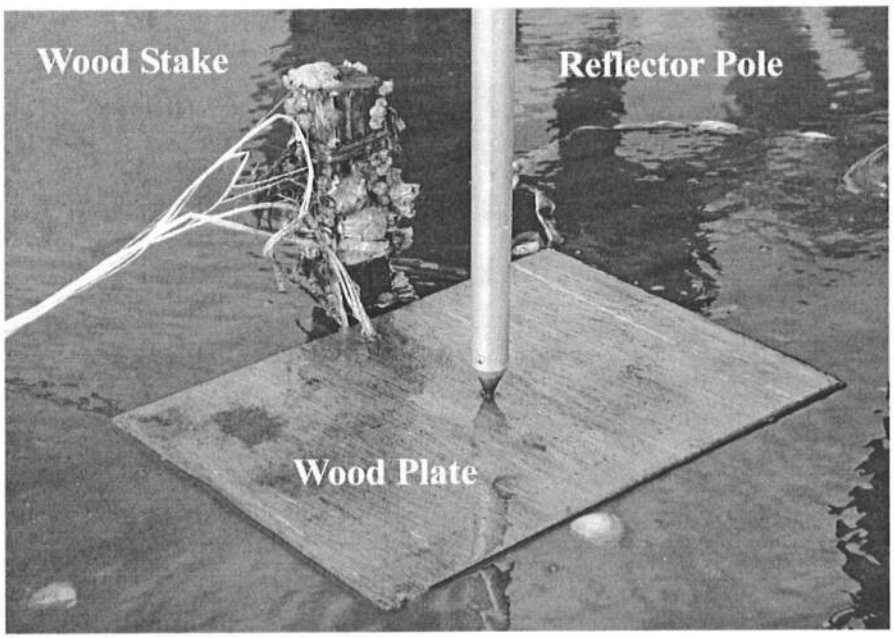

Photo 3: Reflector Pole Set on Wood Plate

2.2 Mudflat Profile Variations

2.2.1 Spatial variations

The measured 19 mudflat profiles along the left profile from February 2001 to December 2002 are plotted in the top panel of Fig. 8. The measured profile for the survey number 1 in December 2000 was excluded because the profile data was less reliable. The fluctuations of the measured bed level increased gradually with the offshore distance and then more quickly after the offshore distance exceeded about 800 m. The average profile and standard deviation of the 19 profiles are shown in the middle and bottom panels of Fig. 8.

Only the bed level survey points located between 100 to 1,050 m from the seawall could be measured always because the bed surface within 100 m from the seawall and farther offshore was too soft sometimes. The reflected prism on the top of the reflector pole could not be placed in front of the fixed survey stake when the mud was too soft. The average cross-shore profile is hence shown for the distance between 100 to 1,050 m. The average bottom slope was almost 1/900 and very gentle. The shape of the average profile is convex-upward, unlike that of sandy beaches, which usually show concave-upward. The mudflats with convex-upward profile were correlated with large tidal range and/or long-term accretion (e.g., Kirby 2000). The relationships between the mudflat profile change and driving forces are investigated in detail in Chapter 5.

The standard deviations of the bed level between 100 to 1,050 m along the left profile plotted in the bottom panel of Fig. 8 increased gradually offshore, and then more abruptly in the

region of the offshore distance exceeding 800 m. The standard deviation was in the range of 2.0 to 8.0 cm.

The measured 19 mudflat profiles along the right profile from February 2001 to December 2002 are shown in the top panel of Fig. 9. The survey number 1 is not included in this figure as was the case for the left profile. The fluctuations of the measured bed level increased gradually offshore and more abruptly in the region of about 700 m. The trends of the bed level fluctuations are similar for the left and right profiles. Like the left profile, only the bed level survey points located between 100 to 1,050 m from the seawall could be measured always.

The middle panel of Fig. 9 illustrates the corresponding average cross-shore profile between 100 to 1,050 m from the seawall for the right profile. The average bottom slope of almost 1/700 was 20 % steeper than that of the left profile. The average cross-shore profile was less convex upward than the left profile.

The standard deviation of the bed level between 100 to 1,050 m along the right profile is plotted in the bottom panel of Fig. 9. The standard deviation increased gradually offshore and then more abruptly around 700 m. The standard deviation was in the range of 2.0 to 8.0 cm. In short, the left and right profiles are slightly different but their larger variations offshore are almost the same.

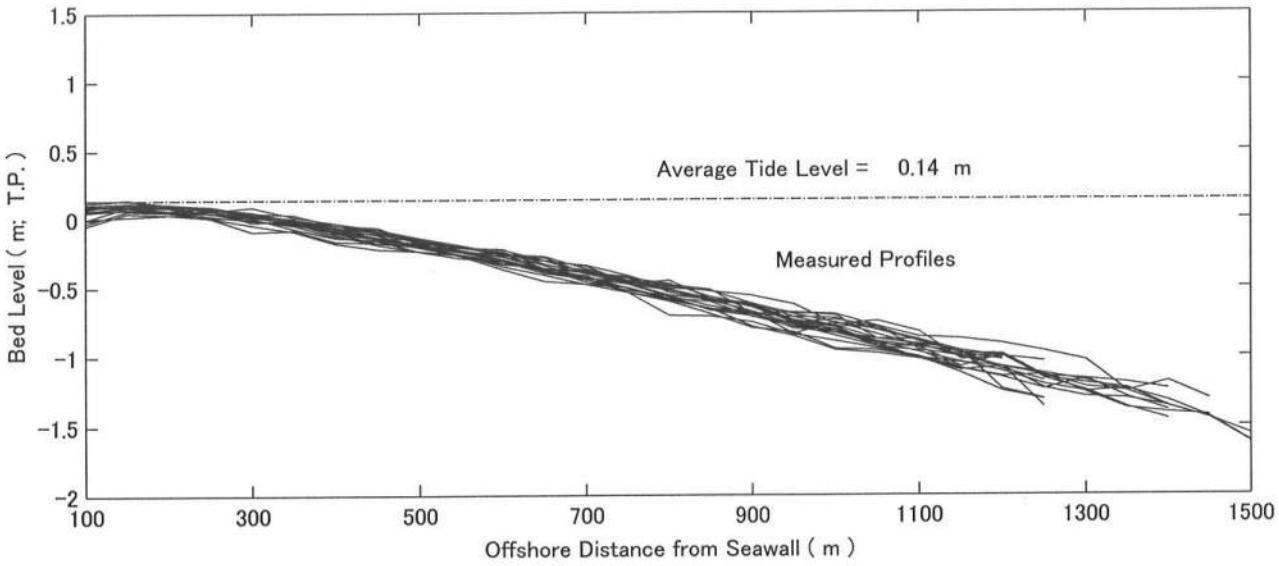

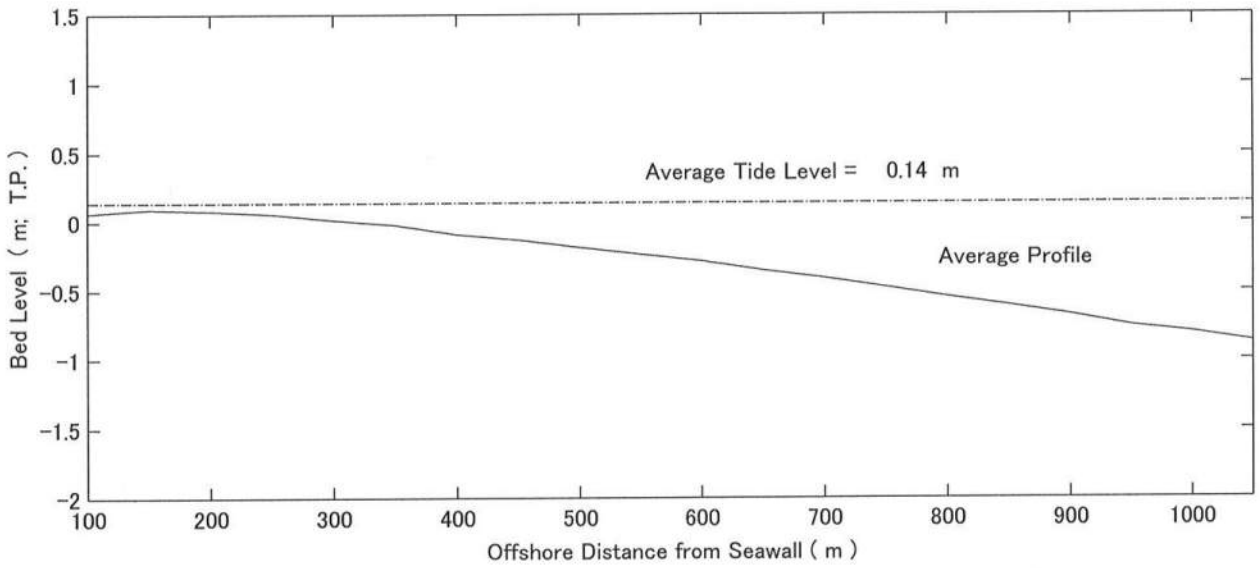

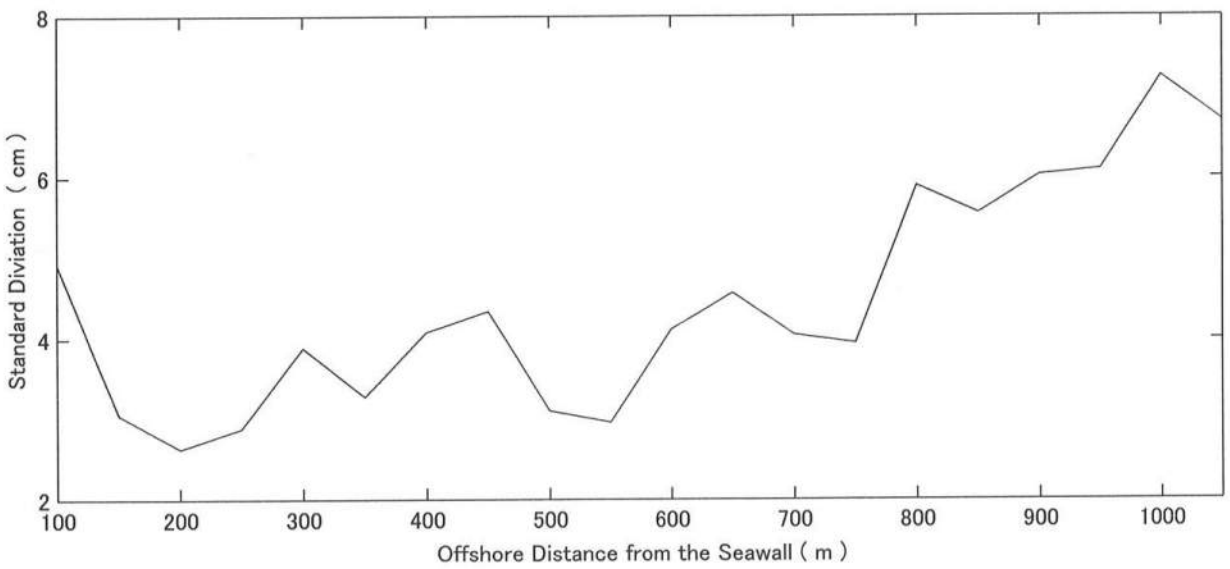

FIG. 8. Observed Cross-shore Profiles, Average Profile, and Standard Deviation for Left Profile

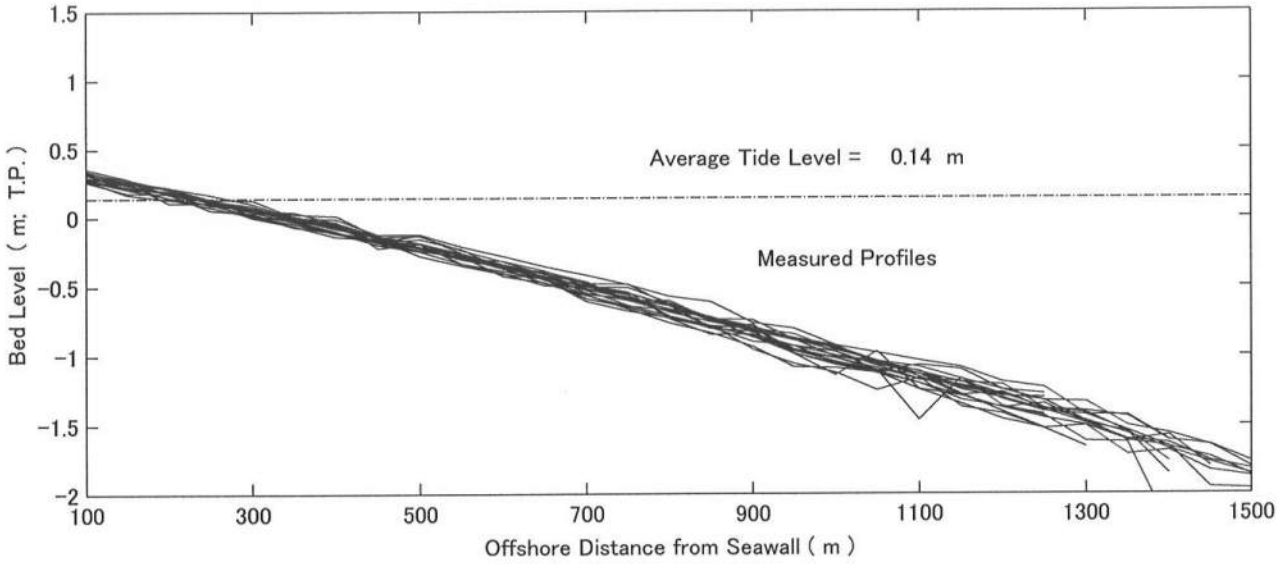

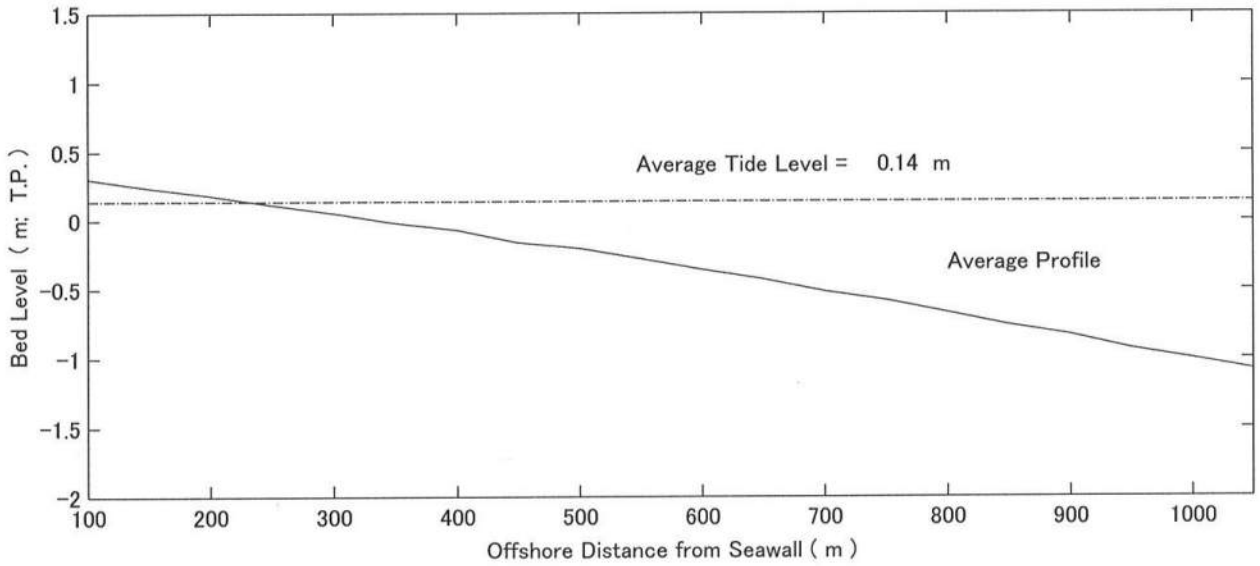

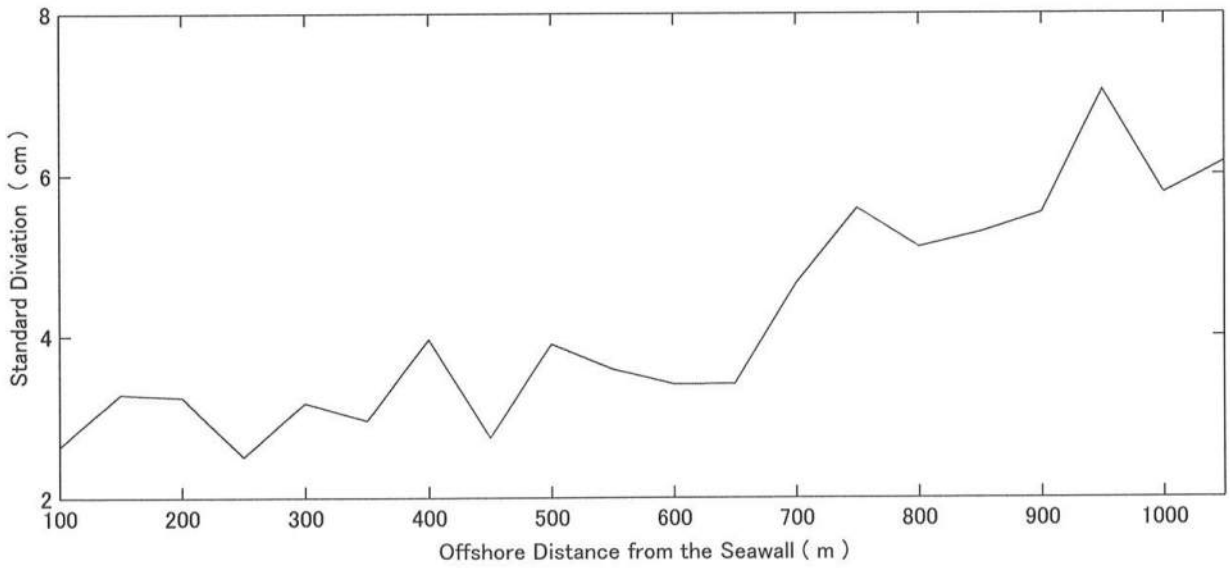

FIG. 9. Observed Cross-shore Profiles, Average Profile, and Standard Deviation for Right Profile

2.2.2 Temporal variations

Fig. 10 shows the bed level deviation from the average profile plotted along the left profile for each profile survey. A positive value of the bed level deviation means accretion from the average profile and a negative value implies erosion from the average profile. The maximum accretion of 0.13 m occurred at 950 m in September 2002 and the maximum erosion of –0.15 m occurred at 1,000 m in January 2002. Both accretion and erosion along the left profile were normally larger offshore than nearshore. The deviation was not uniform along the left profile but generally positive or negative along the entire profile at each survey data. This sign change shows seasonal variations.

Fig. 11 shows the temporal variation of the cross-shore averaged bed level along the left profile. The mean cross-shore averaged bed level was 0.305 m below T.P. and its standard deviation was 0.038 m. The bed level varied annually. The cross-shore averaged bed level was the highest during September and October but the lowest during January and February. Correspondingly, the average mudflat volume along the left profile varied annually.

Fig. 12 shows the bed level deviation from the average profile varying along the right profile for each profile survey. The maximum accretion of 0.15 m occurred at 850 m in August 2002 and the maximum erosion of –0.17 m occurred at 1,050 m in December 2001. Both accretion and erosion along the right profile were normally larger offshore than nearshore. The bed level deviation varied annually in the same way as the left profile.

Fig. 13 shows the temporal variation of the cross-shore averaged bed level along the right profile. The mean cross-shore averaged bed level was 0.349 m below T.P. and its standard deviation was 0.032 m. The cross-shore averaged bed level was the highest during September and October and the lowest during January and February like the left profile.

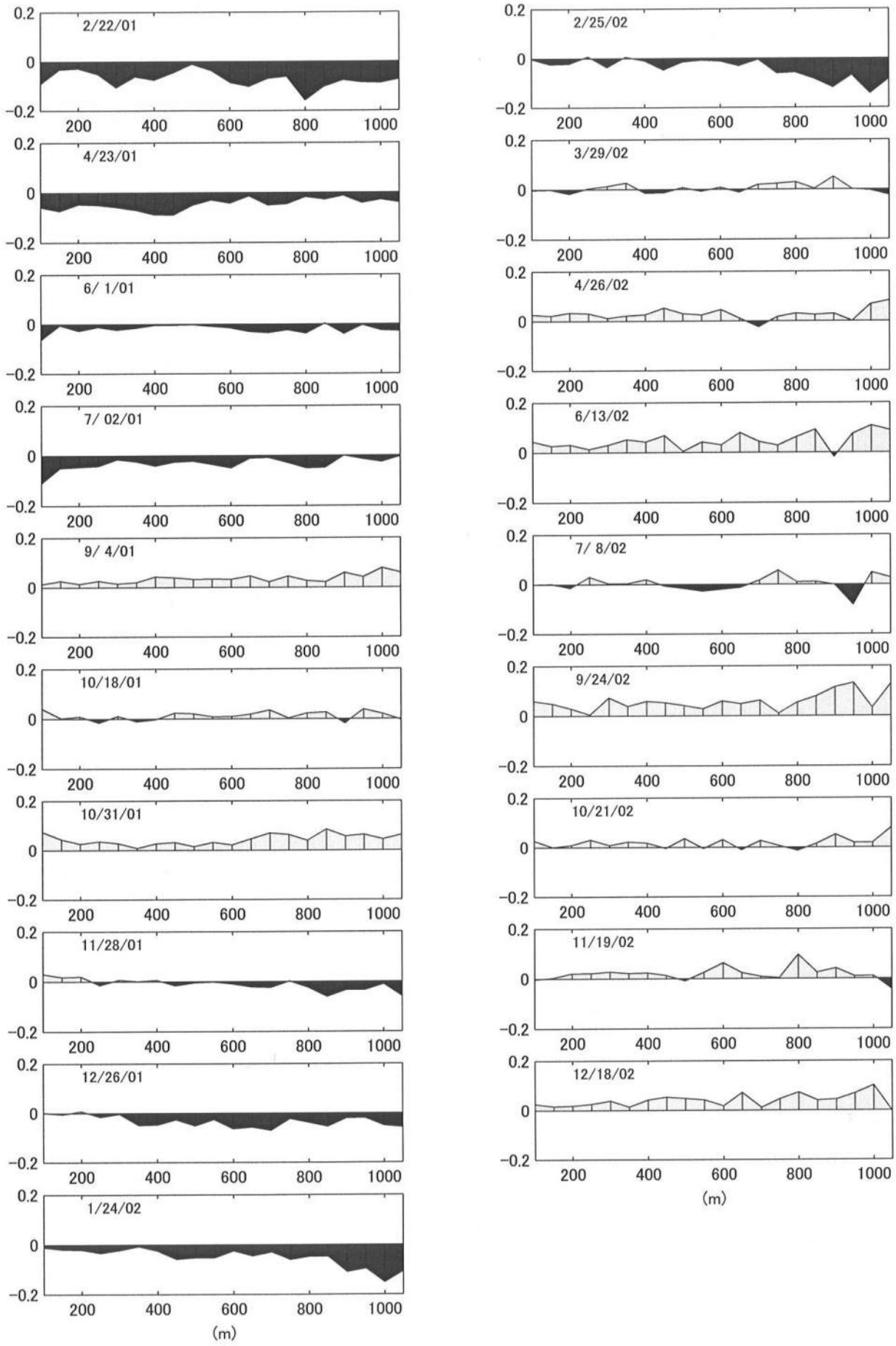

FIG. 10. Temporal and Spatial Variations of Bed Level Deviation for Left Profile

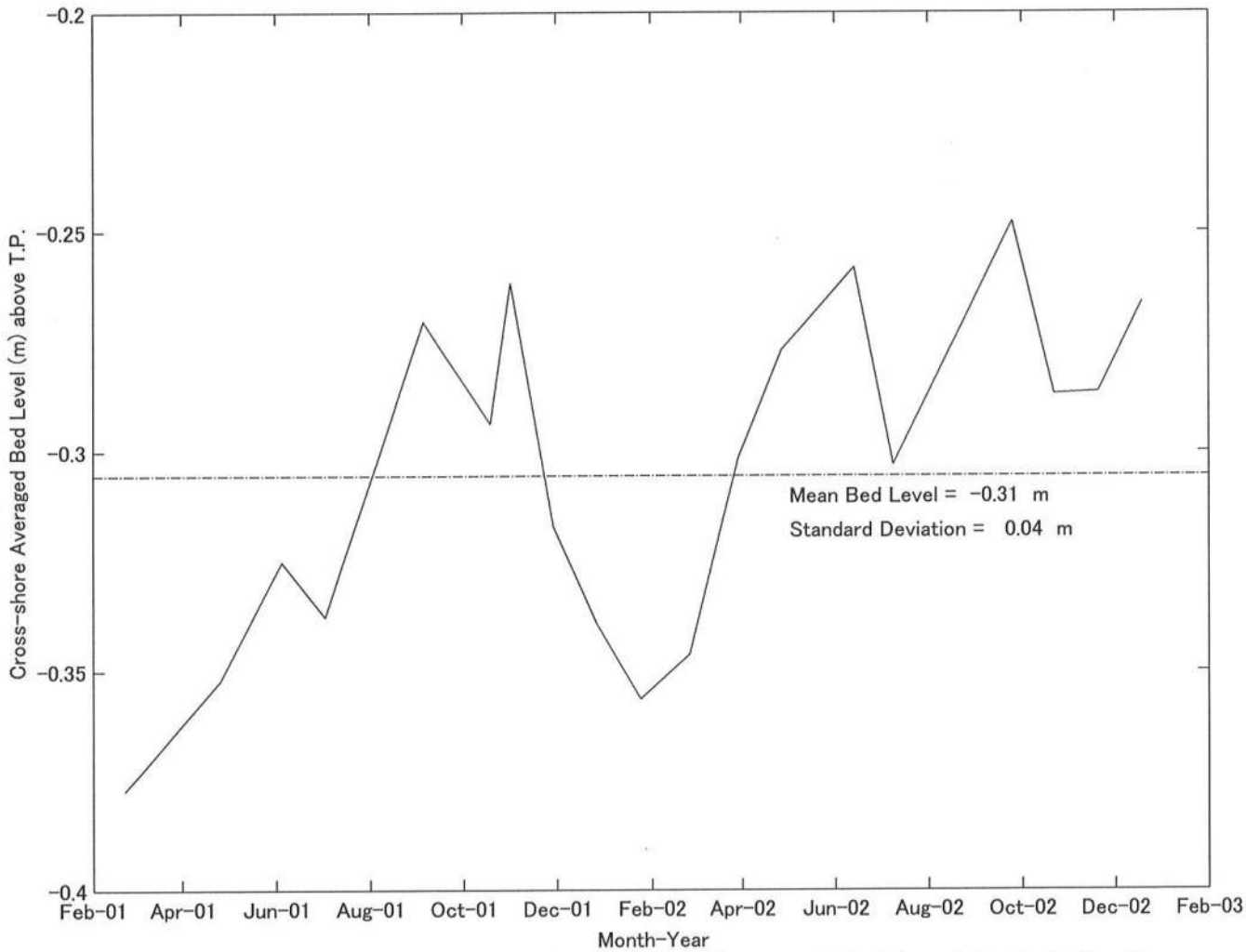

FIG. 11. Temporal Variation of Cross-shore Averaged Bed Level for Left Profile

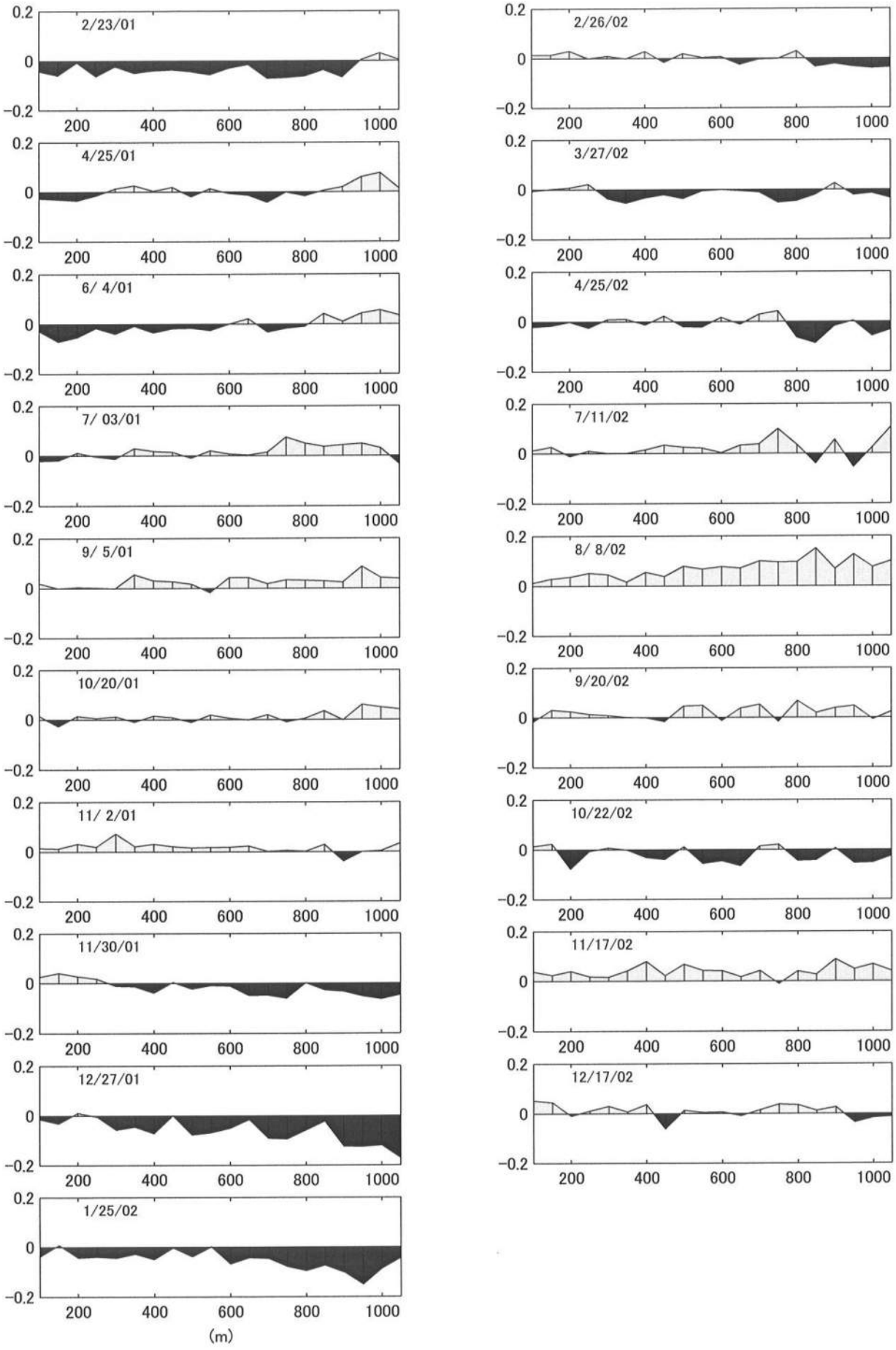

FIG. 12. Temporal and Spatial Variations of Bed Level Deviation for Right Profile

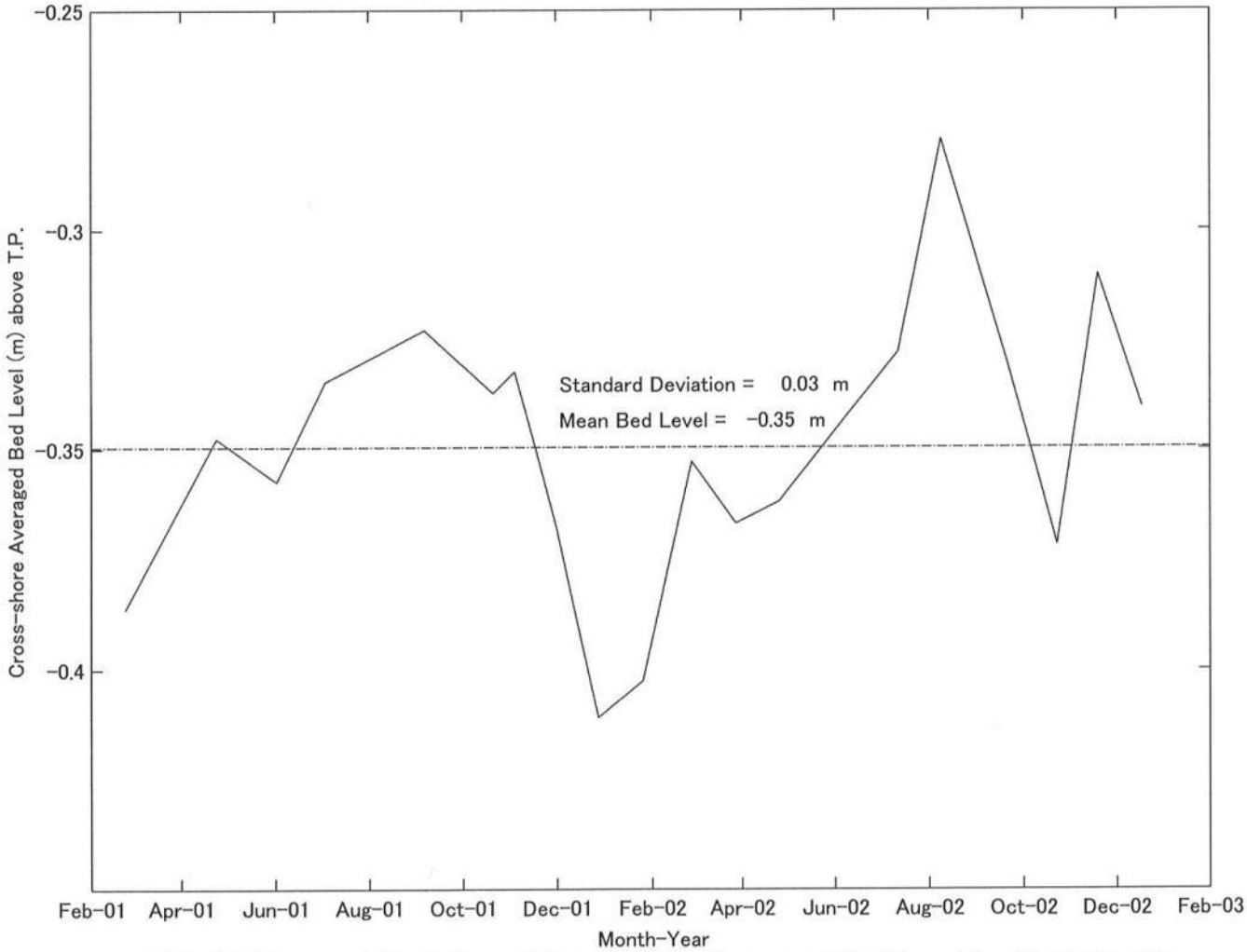

FIG. 13. Temporal Variation of Cross-shore Averaged Bed Level for Right Profile

2.3 Available Oceanographic and Meteorological Data

2.3.1 Tides

The tide level has been measured continuously using a tide gage at the observation tower of Kumamoto Port by Kumamoto Port Construction Bureau of Ministry of Land, Infrastructure, and Transport in Japan. The time series of the measured hourly tide level is available. Fig. 14 plots the time series data from February 2000 to December 2002. The average tide level and its standard deviation were 0.14 m above T.P. and 1.10 m, respectively. The tide levels varied periodically within –3.0 m below T.P. and 3.0 m above T.P. The tidal range and components estimated from the hourly time series are described in the following.

The top panel of Fig. 15 shows the time variation of the tidal range for one tide cycle where each tide cycle was obtained using a zero-upcrossing method about the average tide level shown in Fig. 14 with 2,052 tides cycles. The tidal cycle is defined as the time span between the two successive upcrossing points. The tidal range is defined here as the distance between the maximum and minimum tide levels in each tide cycle. The average tidal range and its standard deviation for the 2,052 tide cycles were 2.88 m and 0.91 m, respectively. The average tidal day was 1.03 days assuming one tidal cycle to be 12 hours and 25 minutes because the tide is semidiurnal at this field site. The spring and neap tides occurred alternatively at an interval of approximately 14 days. The time scale for the tidal range variation will need to be selected for

the purpose of establishing the relationships between the measured monthly bed levels and the time-varying tide levels.

In the top panel of Fig. 15, the spring and neap tidal range may vary with different oscillation patterns and the envelopes of the spring and neap tidal range are illustrated in the middle panel. The envelope of the spring tidal range exhibits regular oscillations of approximately 1 m. On the other hand, the envelope of the neap tidal range shows irregular oscillations of approximately 2 m.

The bottom panel of Fig. 15 shows the time series of the spring-neap tidal range, which is calculated as the difference between the spring and neap tidal range. This time series varied periodically with a half-year period and the half-year period was choose as the representative time scale for the tidal range variation at this field site.

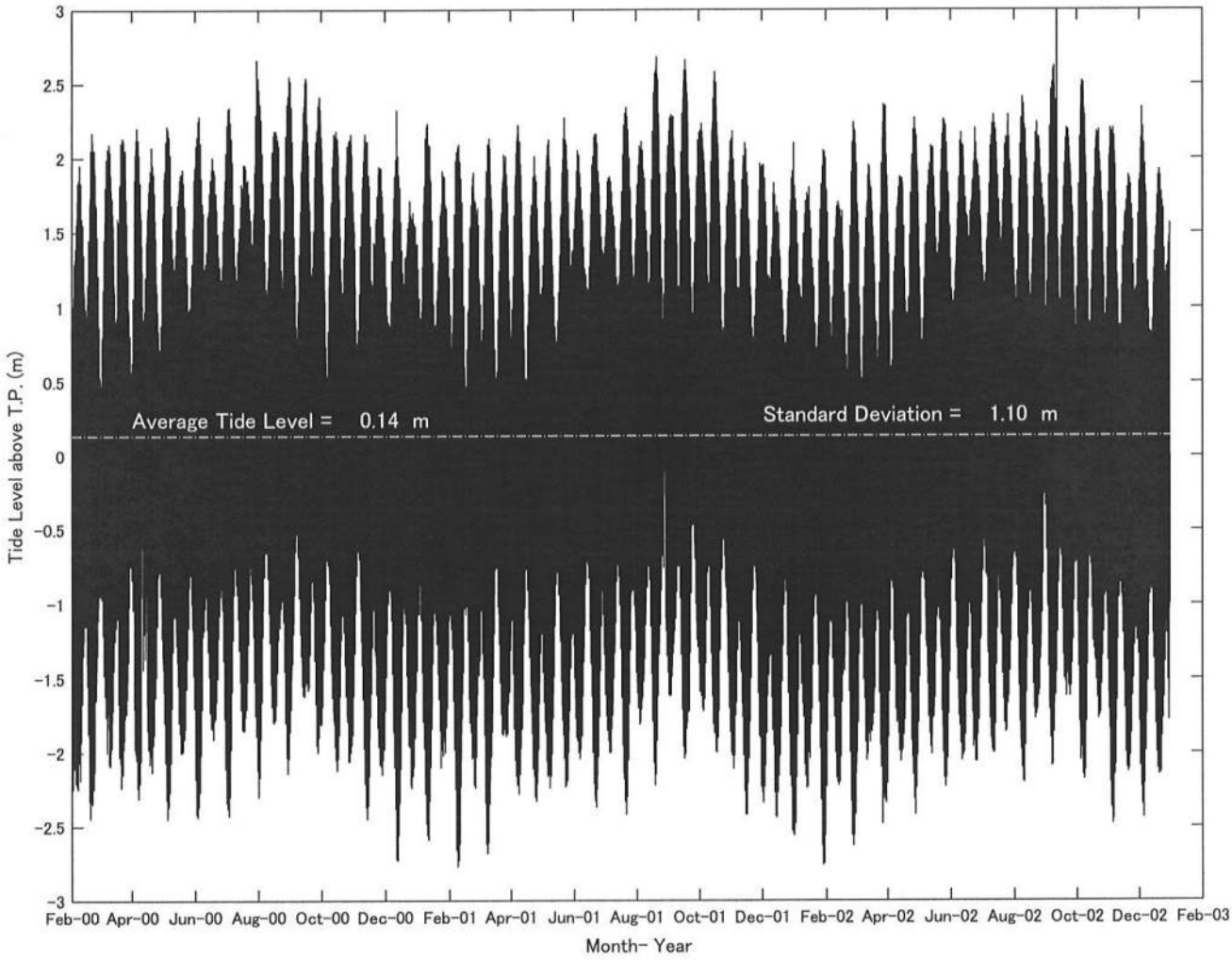

FIG.14. Time Series of Tide Level at Kumamoto Port

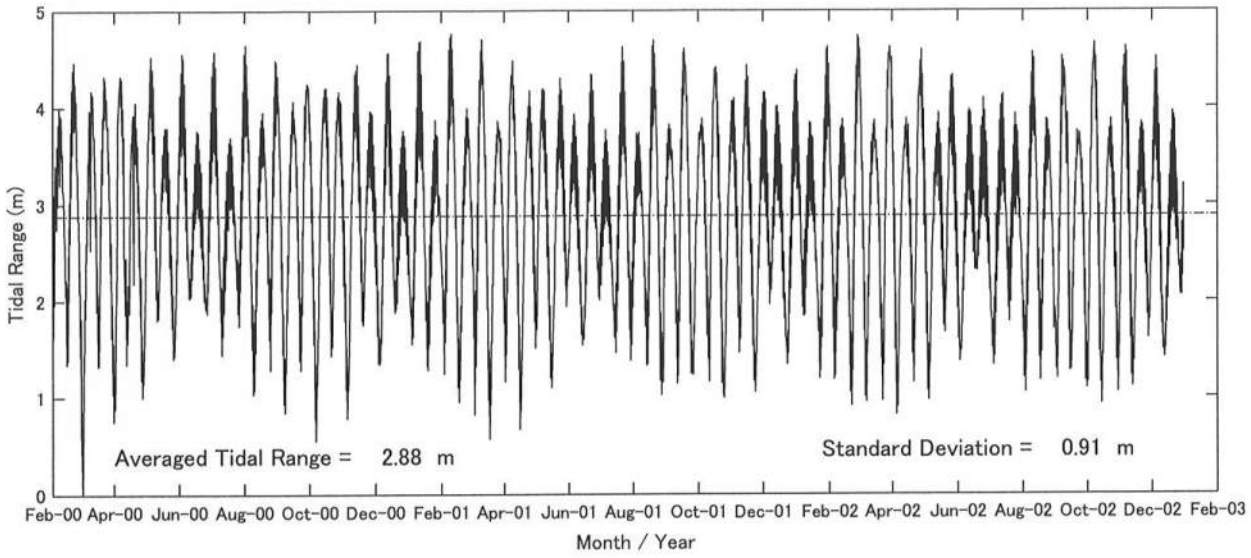

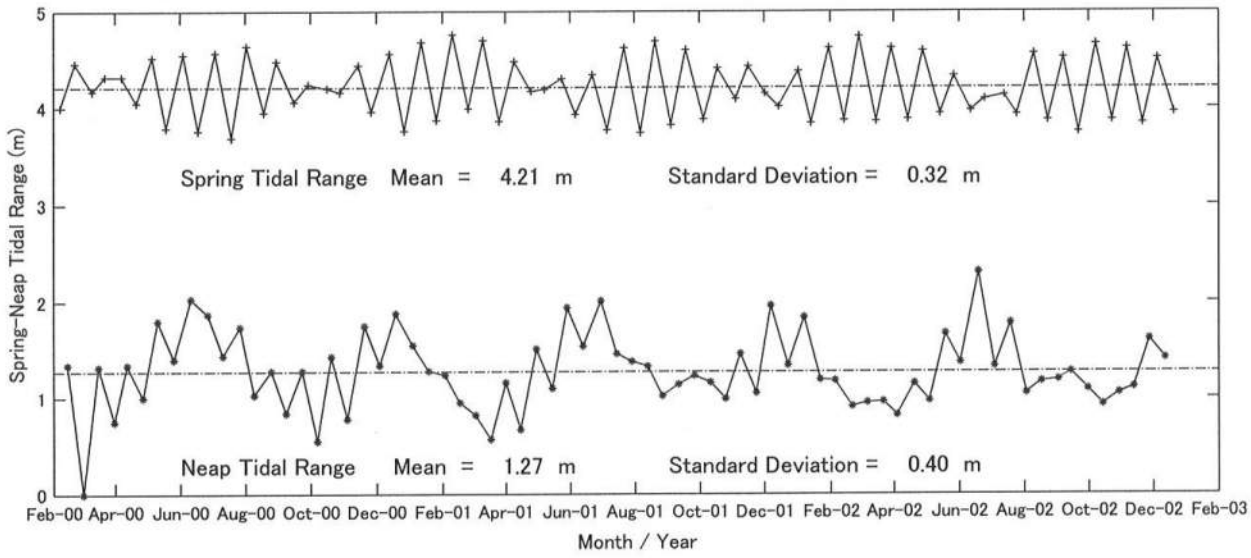

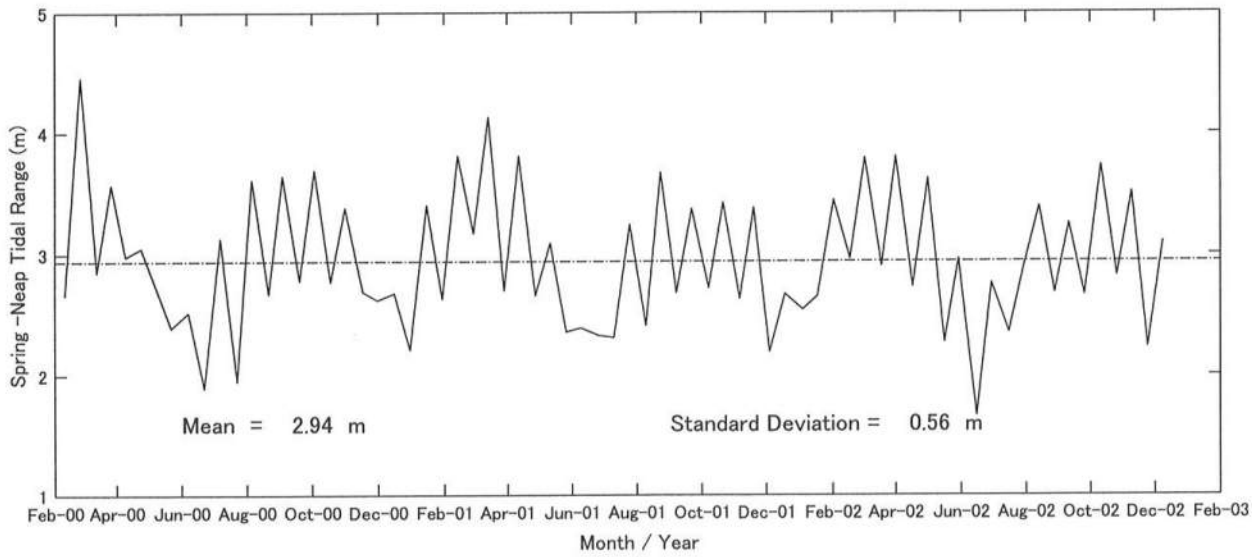

FIG.15. Time Series of Tidal Range at Kumamoto Port

The top panel of Fig. 16 shows the time variation of the moving averaged tide level using the averaging duration of 56 days together with the measured hourly tide level where the daily tide level was obtained by averaging the hourly tide levels in each day. The 56-day moving averaged tide level η_{56}, which corresponds to the middle of 56 days except at the beginning and end of the measured tide level, was calculated as follows:

$$(\eta_{56})^i = \frac{(\eta^{i-r} + \cdots + \eta^{i-1} + \eta^i + \eta^{i+1} + \cdots + \eta^{i+r})}{2r+1} \tag{4}$$

where η_q = moving averaged tide level using the averaging duration of days involving $(q+1)$ points with $q = 2r$. For this computation, $q = 56$ and $r = 28$. The superscript in Eq. (4) indicates the time level of the daily tide level. This moving averaged tide level is regarded here as the averaged tide level during the 56-day interval starting from February 1, 2000. Its mean value and standard deviation during the last three years were 0.14 m above the T.P. and 0.15 m, respectively. The temporal variation of this 56-day averaged tide level varied annually with its peak during August to October.

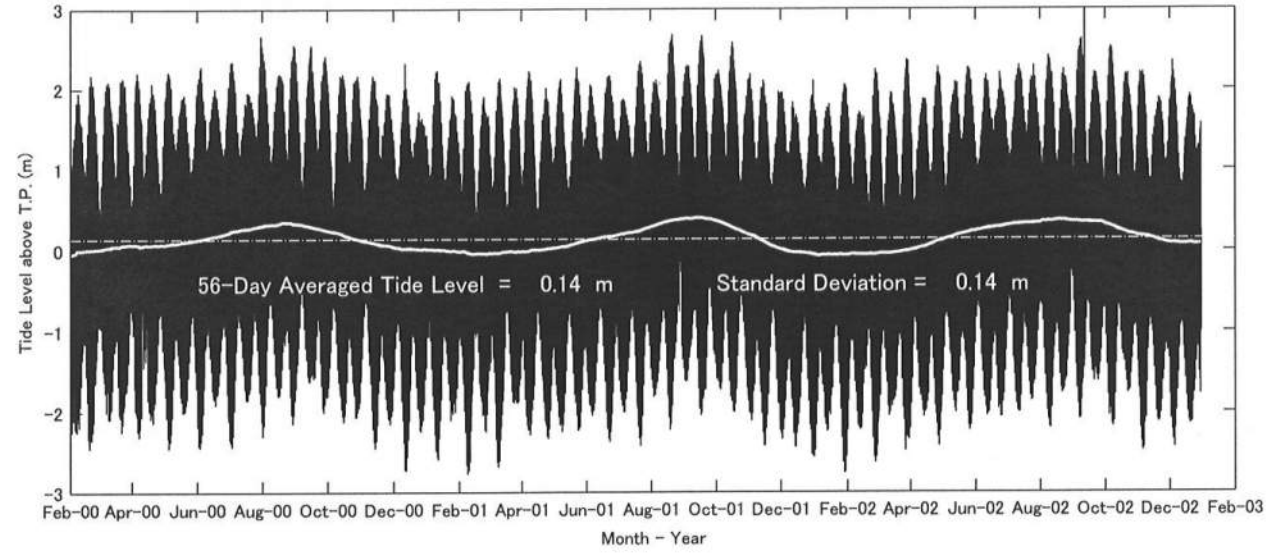

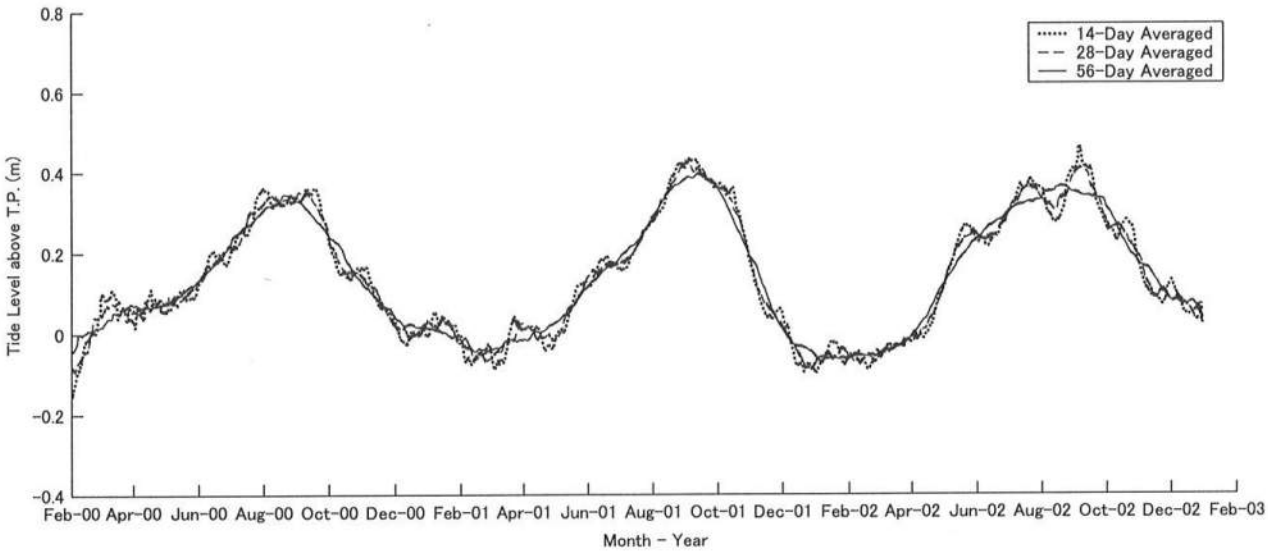

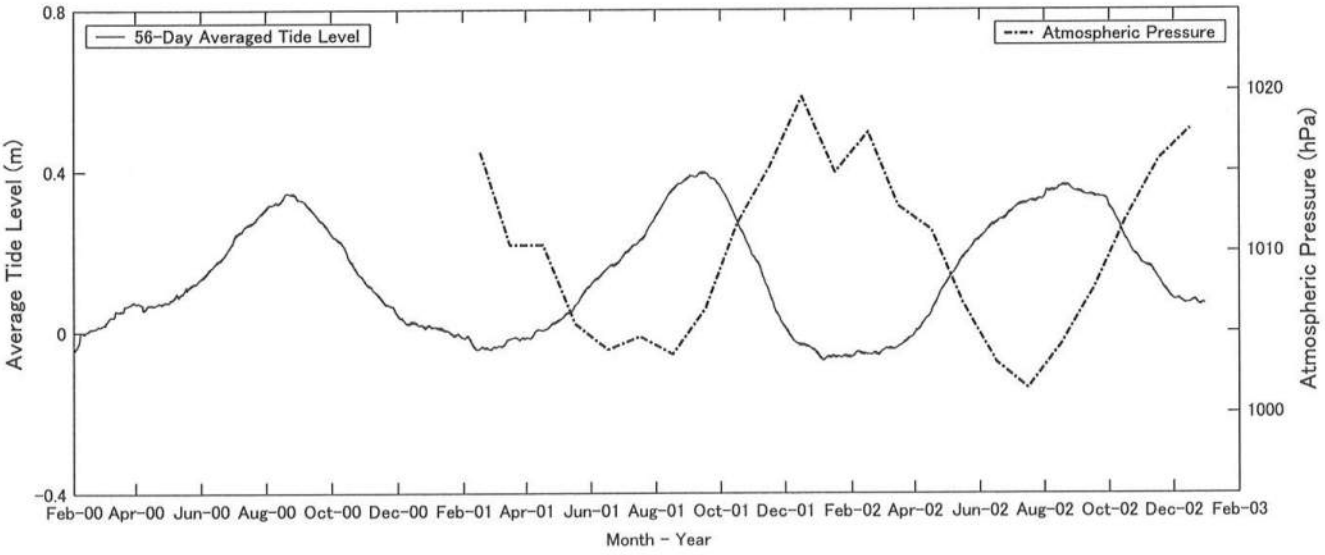

FIG. 16. Time Series of Moving Averaged Tide levels

The middle panel of Fig. 16 shows the comparison of the time variations of the 14-day, 28-day, and 56-day moving averaged tide level. The moving averaged tide level is insensitive to the averaging duration of 14-56 days and the 56-day moving averaged tide level is used as the seasonal tide level variation at this field site. The difference between the maximum and minimum values of the 56-day averaged tide level was approximately 40 cm. The seasonal variations of the averaged tide level were also observed during the same period at Kuchinotsu at the mouth of Ariake Bay, Nagasaki, and Makurasaki whose locations are shown in Fig. 1.

Lisitzin and Pattullo (1961) discussed the principal causes of sea level fluctuations and emphasized the contributions of steric (thermal and haline) and atmospheric pressure variations. The bottom panel of Fig.16 shows the temporal variation of the 56-day moving averaged tide level relative to that of the atmospheric pressure in Kumamoto City. The atmospheric pressure has been observed 10 km upstream from the river mouth at a one-hour interval by the local meteorological observatory of Japan Meteorological Agency. The one-day averaged atmospheric pressure is used in this figure. The atmospheric pressure varied annually. The average tide level varied inversely with the atmospheric pressure as expected from the static force balance at the mean tide level. The atmospheric pressure peaked in December before the lowest temperature in January.

In the static conditions, average tide level rises or falls 1.0 cm when the atmospheric pressure decreases or increases 1.0 hPa (e.g., Dean & Darlymple 2002). The difference between the low and high atmospheric pressures during July 2002 to December 2002 was approximately 15 hPa and the corresponding tide level change was 15.0 cm due to the atmospheric pressure. Therefore, approximately 40 % of the annual tide level variation of 40 cm was caused due to the atmospheric pressure variation. Unoki (1983) presented the annual variation of the mean sea level in bays in Japan and pointed out the importance of steric, atmospheric pressure, and wind variations. However, the causes of the tide level seasonal variation in shallow water under dynamic conditions are still uncertain.

The vertical distributions of the tidal currents were measured using an electromagnetic current and direction meter (ACM210-D, Alexs Electronics) at two points 2.5 km west and 5.0 km south from this field site, where the water depths at these two points were 4.0 m and 3.0 m below T.P., in June 18 to 19, 2000 by Yamada *et al.* (2001). The velocity distributions were measured from the water surface to the bottom at a 50-cm interval every 30-min interval. The measured current was landward during flood tides and seaward during ebb tides as may be expected from the large intertidal zone at the field site. The maximum surface tidal current velocity was in the range of 40 to 60 cm/s and the surface velocity was about 20 cm/s larger than the bottom velocity. Thus, the maximum depth-averaged tidal current velocity was in the range 30 to 40 cm/s.

2.3.2 Wind Waves

Wind waves have been measured every three hours using an ultra-sonic wave gage at the observation tower of Kumamoto Port by Kumamoto Port Construction Bureau. The daily significant wave height and period are available. The top panel of Fig. 17 plots the time series of the significant wave period during February 2001 to December 2002. The average wave period was 3.03 sec and almost constant during the last two years.

The middle panel of Fig. 17 shows the temporal variation of the significant wave height. During February and April 2001, the wave height was over 1.0 m frequently but decreased abruptly after August 2001. The average wave height during the last two years was 0.2 m. The temporal variation of the squared significant wave height, which is proportional to the wave energy, is shown in the bottom panel of Fig. 17. Several peaks occurred between February and April 2001 but the wave energy was relatively low.

The wave heights in Ariake Bay are small partly because the fetch lengths are limited in this closed shallow bay. Table 8 lists the fetch lengths from the observation tower to the opposite coast of Ariake Bay. The north-west (NW), west-northweat (WNW), and south-west (WS) fetch lengths are relatively large but no more than 60 km.

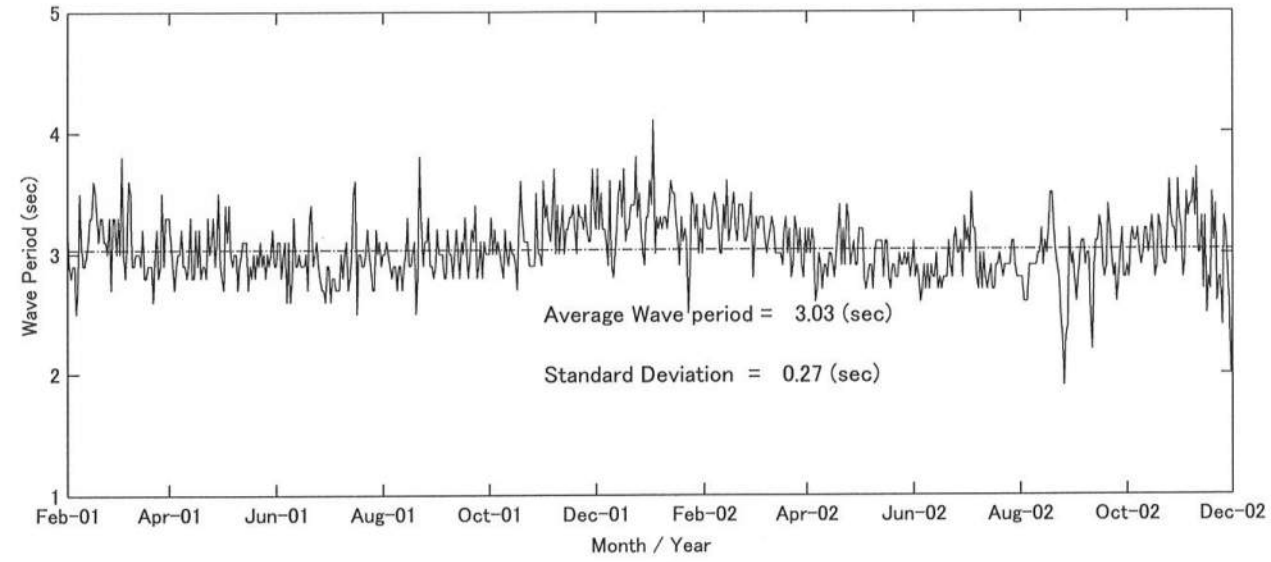

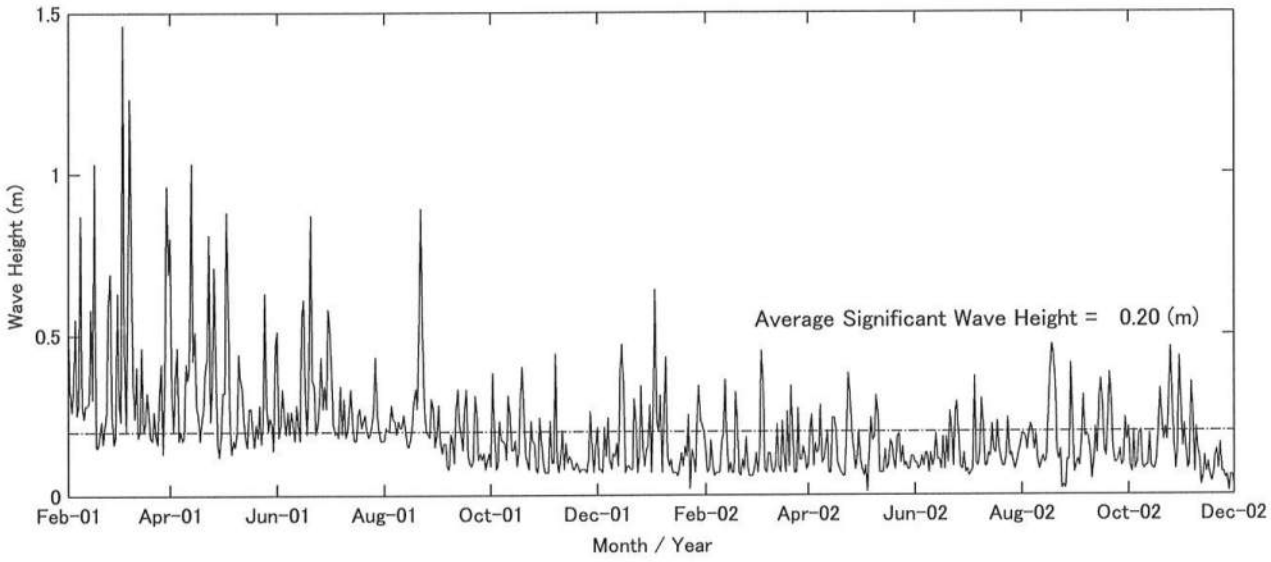

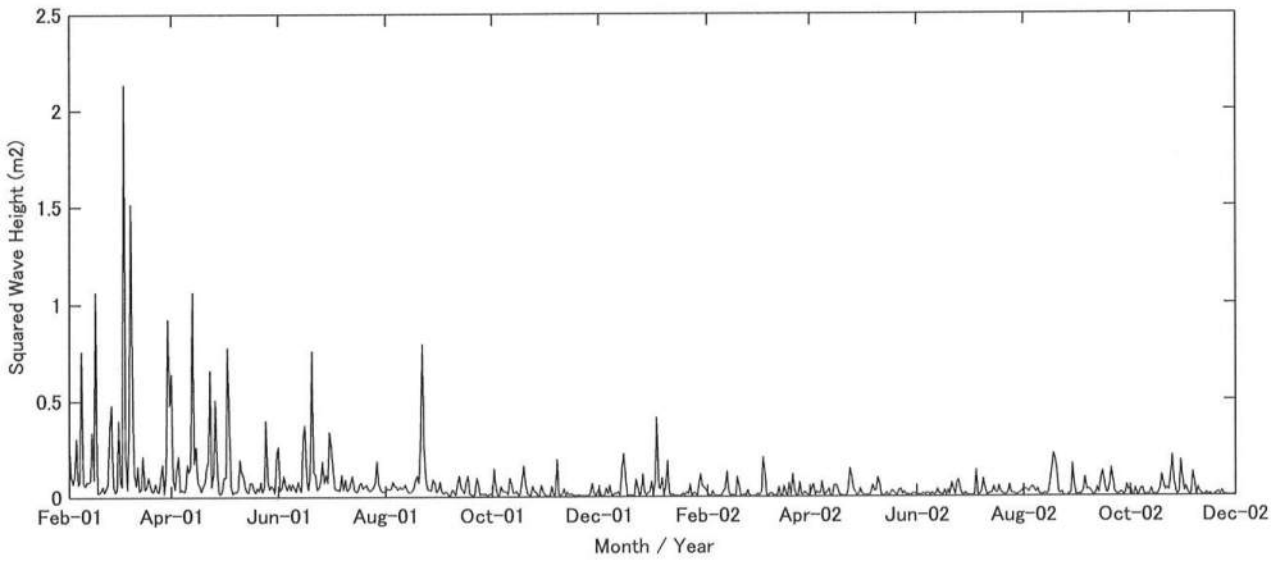

FIG. 17. Time Series of Significant Wave Height and Period

Table 8: Fetch Lengths from Observation Tower at Kumamoto Port

Direction	Fetch Length (km)
N	11.0
NNW	15.0
NW	56.0
WNW	40.0
W	15.0
WSW	23.0
SW	45.0
SSW	10.0
S	5.0

2.3.3 Winds

The wind velocity near the field site has been measured every one hour using an anemometer at the observation tower of Kumamoto Port by Kumamoto Port Construction Bureau. The hourly wind speed and direction are available. The top panel of Fig. 18 plots the time series of the wind speed during February 2001 to December 2002. There were no distinct differences before and after August 2001 unlike the wave height shown in Fig. 17.

The bottom panel of Fig. 18 plots the time series of the measured wind direction. To facilitate the interpretation of this time series, the frequency distributions of the wind direction during three intervals of 3 months are shown in Fig. 19. The top panel of Fig. 19 shows the frequency distribution of the wind direction during February to April 2001 and the wind direction was mostly from the WNW direction. 60 % of the strong (over 10 m/s) wind direction was the WNW direction.

On the other hand, as shown in the middle panel of Fig.19, the frequency distribution of the wind direction during August to October 2001 was wide but only 10 % of the wind blew from the dominant NWN direction.

The bottom panel of Fig. 19 plots the frequency distribution of the wind direction during February to April 2002. The distribution of the wind direction was wider than that of the top panel for the same months in the previous year.

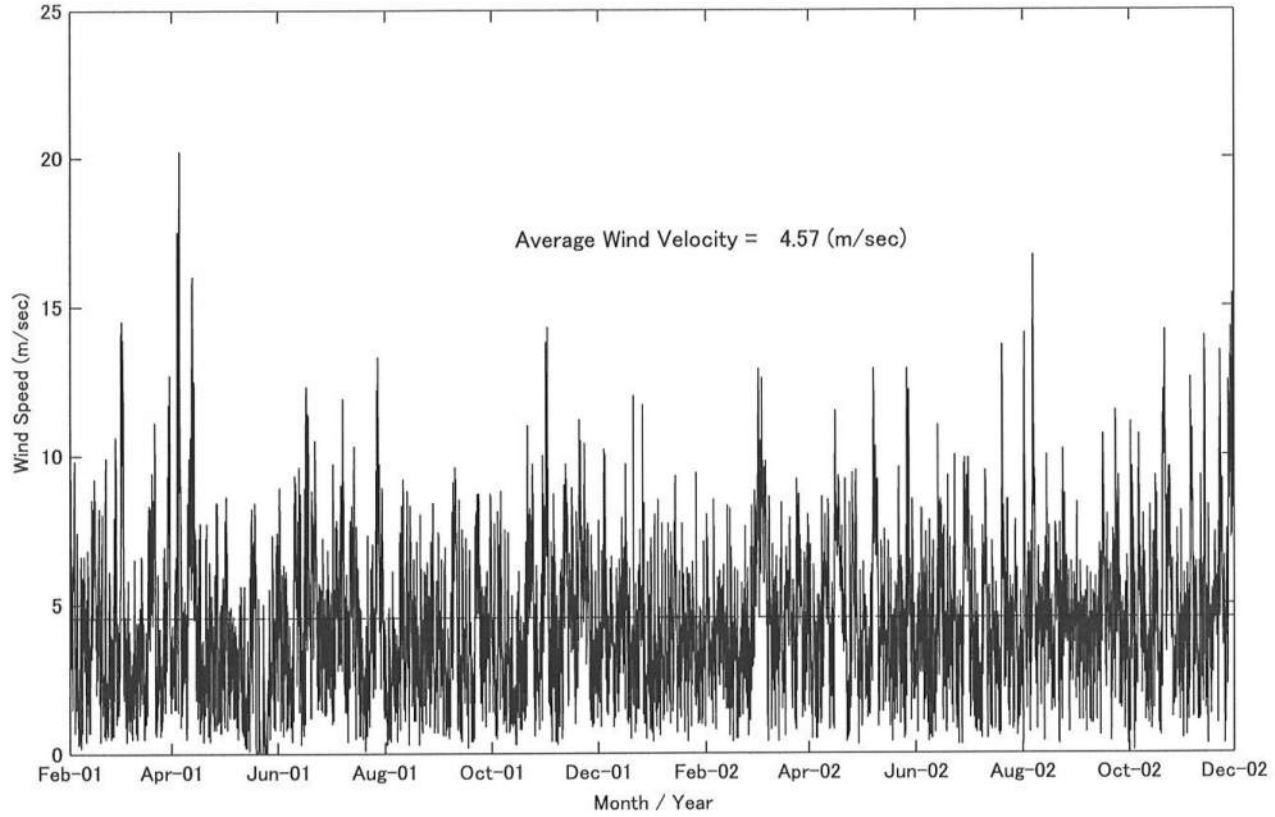

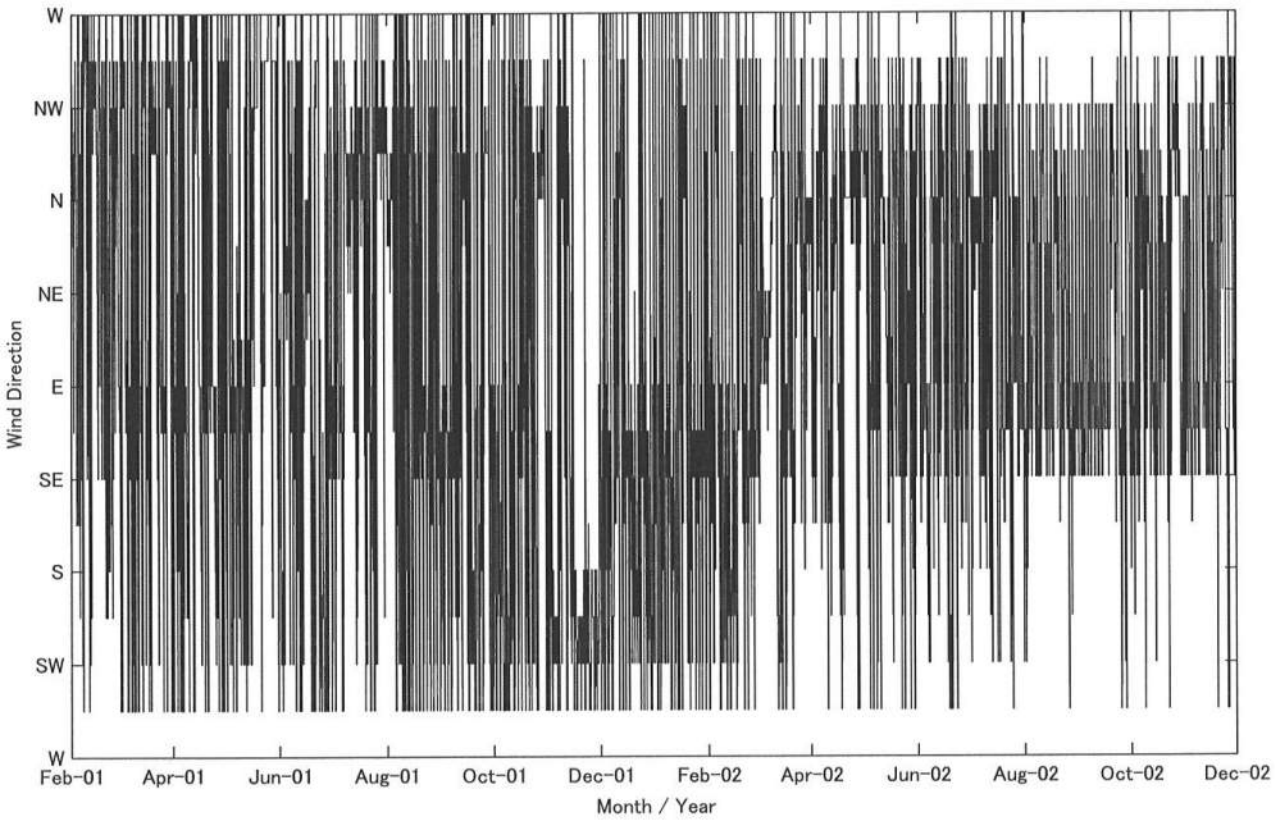

FIG.18. Time Series of Measured Wind Velocity and Direction

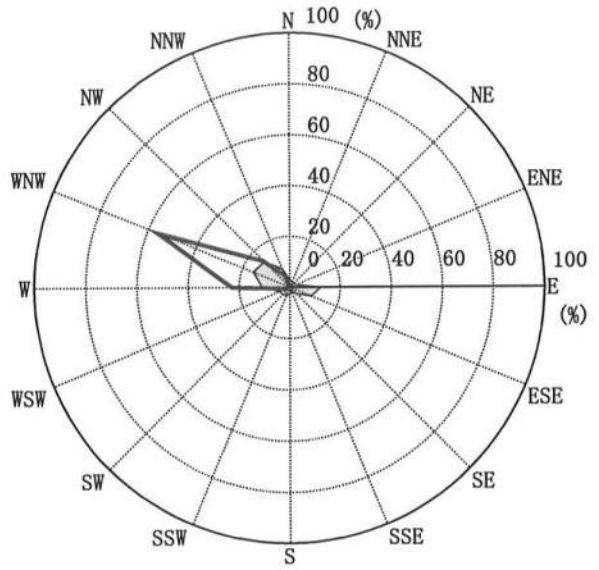

February 2001

to

April 2001

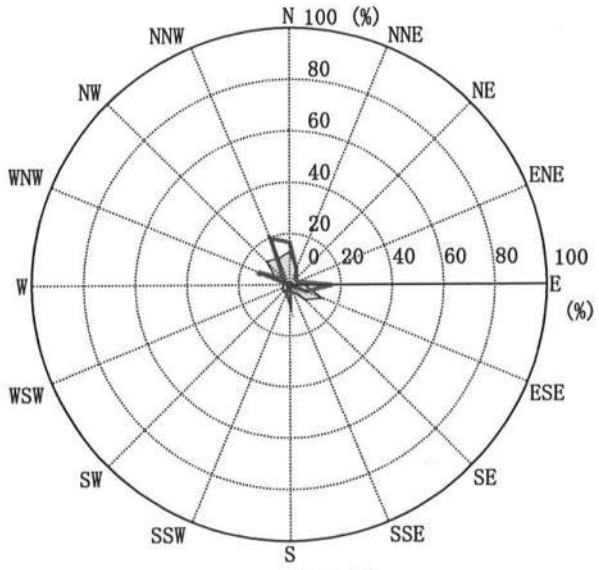

August 2001

to

October 2001

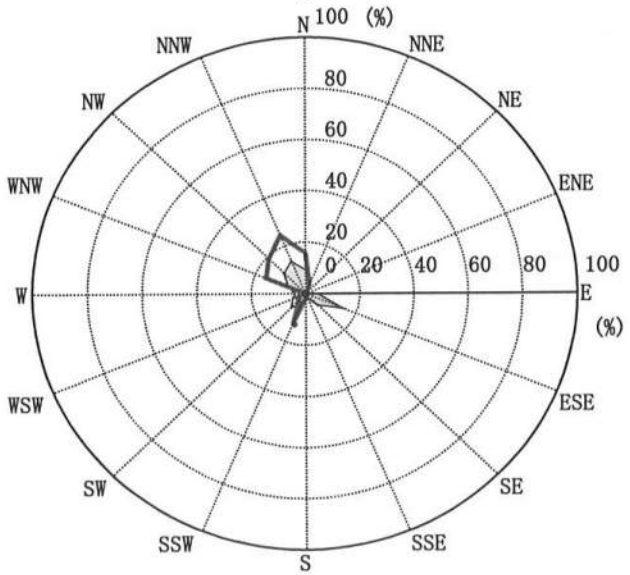

February 2002

to

April 2002

FIG. 19. Frequency Distribution of Wind Direction

2.3.4 River discharge and rainfall

The water level in the Shirawaka River was monitored every hour using an ultra-sonic water level meter 5 km upstream from the river mouth, and the river discharge was calculated using an empirical relationship between the water level and river discharge by Ministry of Land, Infrastructure, and Transport in Japan. The daily river discharge is available but the measured river discharge in a particular year is published one year later after the data for the entire year is collected and analyzed. Therefore, a relationship between the river discharge and rainfall in Kumamoto City is examined as shown in the top panel of Fig. 20. The rainfall in Kumamoto City has been observed every hour by Kumamoto local meteorological observatory. The daily rainfall was available. The peak of the river discharge occurs during June to July due to the rainy season in Japan. The time series of the rainfall is correlated with that of the river discharge. As a result, the measured rainfall in Kumamoto City was used instead of the discharge of the Shirakawa River.

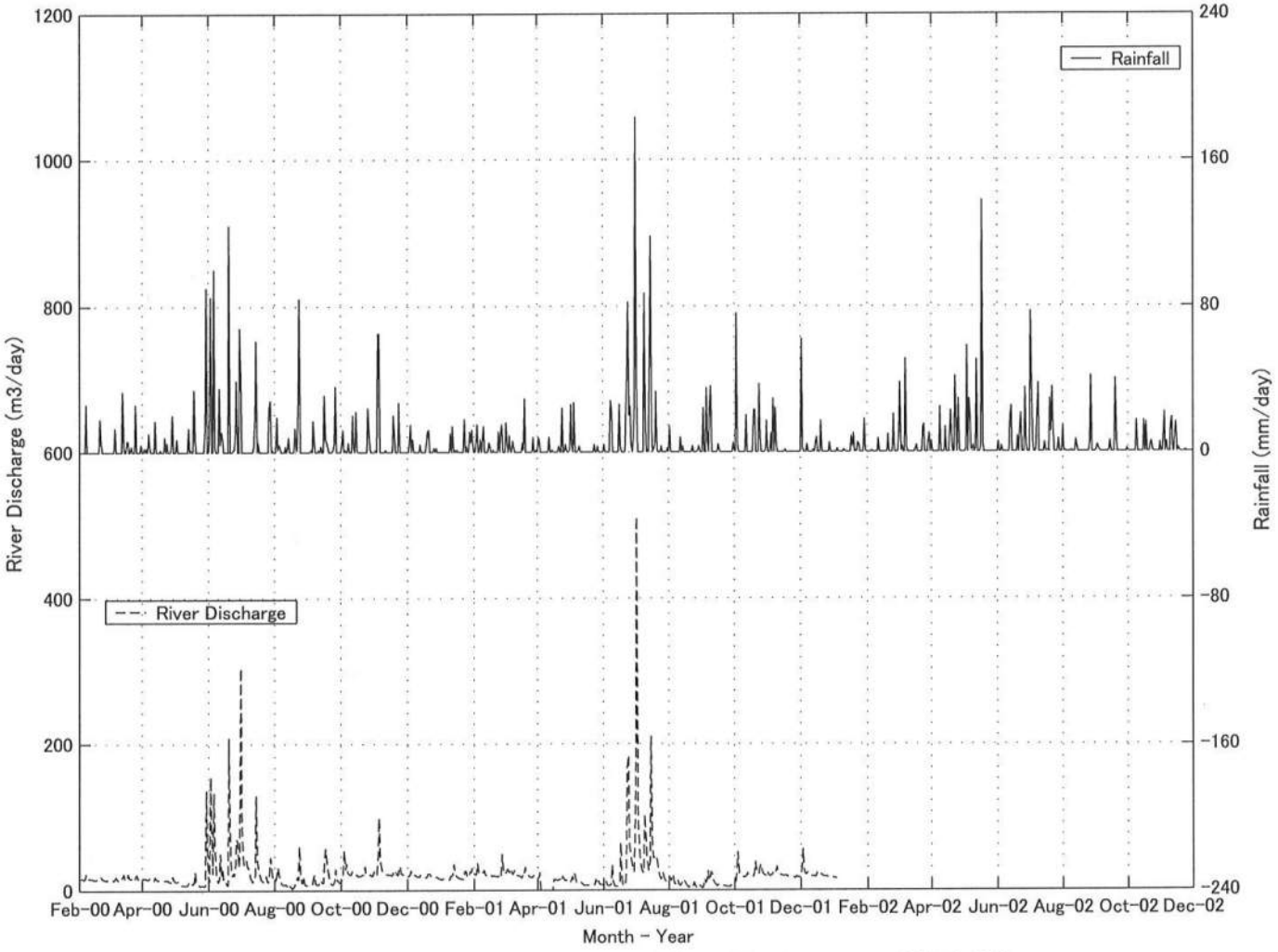

FIG. 20 Relationship between River Discharge and Rainfall

Chapter 3

EXISTING APPROACHES

This chapter investigates the temporal variations of mudflat profile changes in the vicinity of the Shirakwa River using the existing approaches such as the equilibrium profile concept and empirical orthogonal eigenfunction (EOF) methods. The equilibrium profile concept is shown to be not applicable directly to the present seasonal profile change data. The EOF method is found to require additional eigenfuncions in comparison to sandy beaches. The existing approaches are assessed here first to show the need of a simpler model in the subsequent chapter.

3.1 Equilibrium Mudflat Profile

Many mudflats appear to be accreting at the same rate as sea (tide) level rise, thereby suggesting that an equilibrium condition exists between the dynamic forcing and the sedimentary response (Dyer 1998; Christie *et al.* 2001). A concept of equilibrium beach profiles, which is proposed for sandy beach cross-shore profiles [e.g., Bruun (1962, 1983); Dean (1991)], might hence be applicable in evaluating the mudflat profiles. Assuming wave action as the most predominant factor for mudflat profile changes, Mehta *et al.* (1996), Lee and Mehta (1997), and

Kirby (2000) extended the concept of equilibrium beach profiles to the mudflat profiles but they did not take account of the seasonal profile changes.

On the other hand, mean tide level, which is one of the driving forces for bed level changes, tends to vary. The seasonal variation of mean tide level at this field site was approximately 40 cm as described in Section 2.3.1. In addition, the temporal variations of mudflats have been shown to have a number of time scales including tide-cycle (Christie *et al.* 1999), semi-lunar (O'Brien *et al.* 2000), monthly (Anderson *et al.* 1981), and seasonal variations (Bale *et al.*, 1985; Frostick and McCave 1979; Kirby *et al.* 1993). Therefore, the applicability of the concept of equilibrium beach profiles to the mudshore profiles is not clear in the presence of various time scales.

Fig. 21 shows the time series of the cross-shore averaged bed level deviation presented in Section 2.2.2 for the left and right profiles together with the 56-day averaged tide level discussed in Section 2.3.1. These time series are closely related to that of the averaged tide level. Both time series varied periodically with a one-year period and no noticeable time lag. The tidal flat accreted with the tide level rise during August to October, and eroded with the tide level fall during January to March. Very little work is currently available on the effects of the seasonal sea level variation to the beach profile and LaFond (1938) demonstrated the correspondence between the monthly sea level and sandy beach bed level.

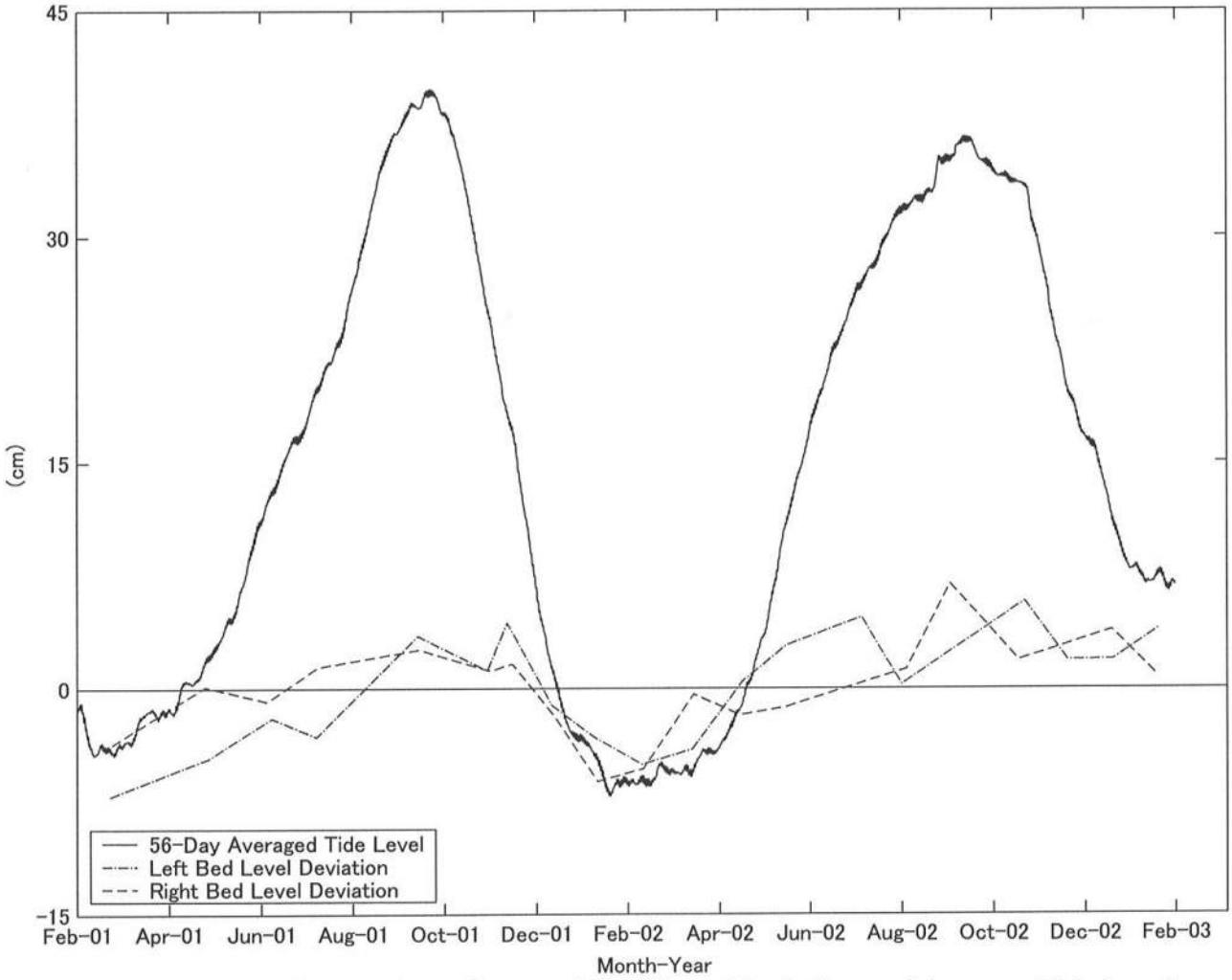

FIG. 21. Cross-shore Averaged Bed Level Deviation and Average Tide Level

Fig. 22 shows the linear regression analysis of the time series between the cross-shore averaged bed level deviation z(*t*) for the left profile and the 56-day averaged tide level $\eta_{56}(t)$. The correlation coefficient is 0.749 and reasonably high. The linear relationship is expressed as

$$z(t) = A\left[\eta_{56}(t) - \eta_0\right] = 0.195\left[\eta_{56}(t) - 14.0\right] \quad \text{in centimeters} \qquad (5)$$

where A is the dimensionless gradient of the regression line and η_0 is the shift of $\eta_{56}(t)$ which turns out to be almost the same as the average level 14.0 cm of the 56-day averaged tide level. Likewise, the time series between the cross-shore averaged bed level deviation for the right profile is also correlated with the 56-day averaged tide level as listed in Table 9.

The equilibrium profile concept assumes that the profile adjusts itself to the tide level by the same vertical increment, which requires $A = 1.0$ in Eq. (5). As listed in Table 9, however, the value of A is approximately 0.2 for the left and right profiles. The measured profiles changed much less vertically as tide level fluctuated, possibly because the rise of the tide level lasted only for several months. The equilibrium profile concept assumes that the sand material eroded from the upper beach will be deposited offshore as the sea level rise. In the present field data, however, the seasonal tide level rise caused the mudflat bed level rise along the entire survey lines unlike the equilibrium profile concept. Consequently, the equilibrium profile concept is not applicable directly for the present seasonal profile change data.

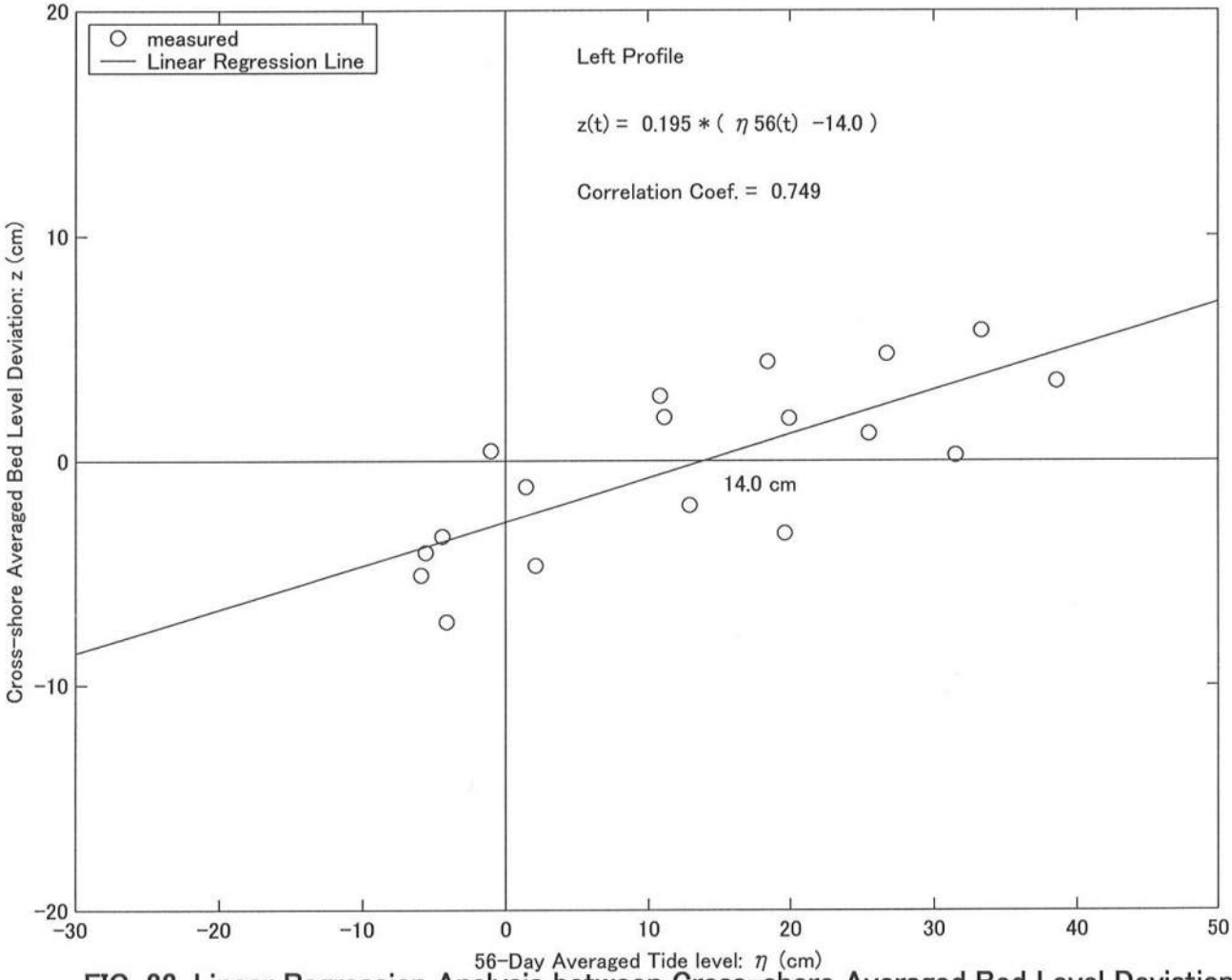

FIG. 22. Linear Regression Analysis between Cross-shore Averaged Bed Level Deviation and Average Tide Level for Left Profile

Table 9: Linear Regression Analysis of Time Series between Cross-shore Averaged Bed Level Deviation $z(t)$ for Left and Right Profiles and 56-Day Averaged Tide Level, $\eta_{56}(t)$, Base on $z(t) = A\left[\eta_{56}(t) - \eta_0\right]$ where average value of $\eta_{56}(t)$ is 14.0 cm.

Regression Coefficients	Left Profile	Right Profile
A	0.195	0.164
η_0 (cm)	14.0	13.0
Correlation Coefficient	0.749	0.782

3.2 Empirical Orthogonal Eigenfunction (EOF) Method

Empirical orthogonal eigenfunction (EOF) methods, which do not assume a specific profile form, have been used widely for the analysis of the temporal and spatial patterns of sandy beach morphology [e.g., Winant et al. (1975); Aubrey (1979); Dick and Dalrymple (1984); Wijnberg and Terwindt (1995); Larson *et al.* (1999); Dean and Dalrymple (2002)]. The EOF method assumes that the observed bed level is expressed as

$$h_{ik} = \sum_{n=1}^{N} C_{nk} \cdot e_{ni} \tag{6}$$

where h_{ik} = measured bed level with k = survey number and i = location along the profile, n = eigenfunction mode, N = number of eigenfunctions, e_{ni} = n-th spatial dimensionless eigenfunction evaluated at the i-th location, and C_{nk} = k-th temporal dimensional coefficient evaluated for the n-th eigen mode, which varies with time. In short, Eq. (6) allows us to separate the spatial and temporal variations of the measured bed level.

The primary advantage of the EOF analysis is its ability to compress the complicated variability of the observed data set into the fewest possible modes where the first three eigenfunctions with $N=3$ are normally used for the sandy beach profile. The physical interpretations of these three modes were given by Winant *et al.* (1975). The top panel of Fig. 23 shows the first spatial eigenfunctions for the left and right profiles. The first eigenfunction is called a mean beach function, analogous to the arithmetic mean profile. The first spatial eigenfunction for the mudflat shown in Fig. 23 corresponds to the arithmetic mean profile.

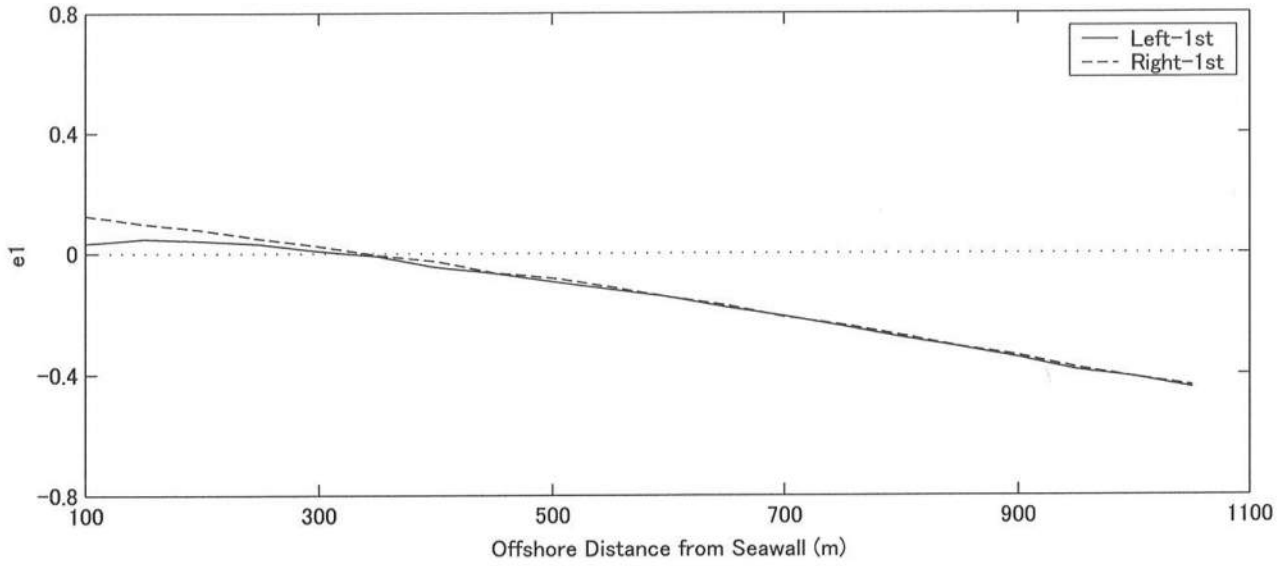

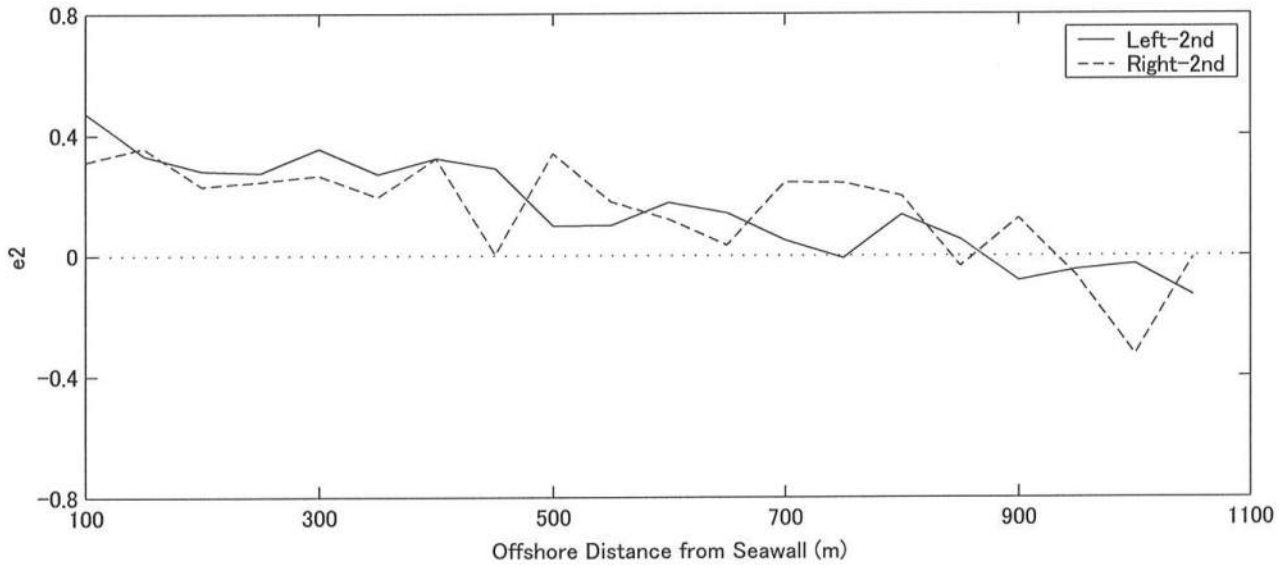

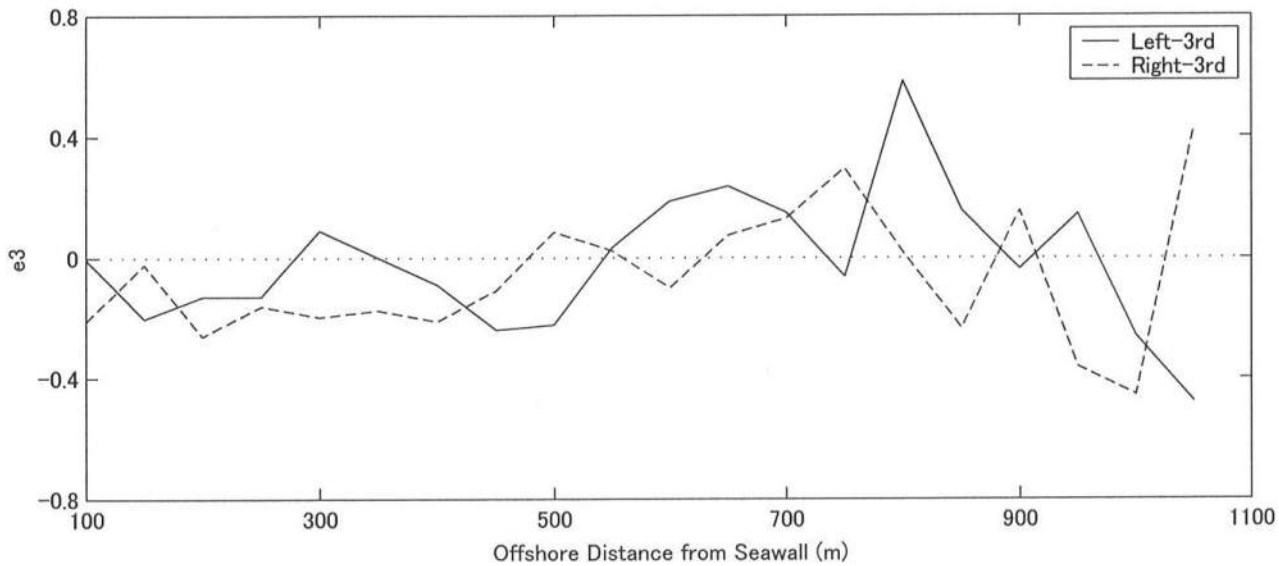

FIG. 23. Spatial Eigenfunctions for Left and Right Profiles

Table 10: Summary of Empirical Orthogonal Eigenfunction (EOF) Analysis

Eigenfunctions	Left Profile (%)	Right Profile (%)	Sandy Beach (Winant et al. 1975)
1st	99.52	99.67	99.70
2nd	0.25 (53.2)	0.14 (43.4)	0.16 (56.5)
3rd	0.05 (10.0)	0.06 (18.2)	0.08 (28.8)
Sub Total	99.82 (63.2)	99.87 (61.6)	99.84 (85.3)

The second spatial eigenfunction for the sandy beach is named a bar-berm function associated with a strong seasonal variation with some peaks in the nearshore and offshore. However, there are no distinct peaks along the entire survey lines as shown in the middle panel in Fig. 23 because no bar and berm existed for the present profiles unlike the sandy beaches. The physical interpretation of the second eigenfunction is difficult due to the similarity of the first and second eigenfunctions.

The bottom panel of Fig. 23 shows the third spatial eigenfunctions of both profiles. The spatial variations become large in the region offshore of 800 m in a manner similar to the third eigenfunction called a terrace function for the sandy beach, which has a broad maximum near the low-tide terrace.

Table 10 lists the percentage of the mean square value of the measured bed level of the left and right profiles explained by the three largest eigenfunctions where the percentage in parentheses indicates the residual mean square value explained after removing the first eigenvalue. The EOF results for the sandy beach obtained by Winant *et al.* (1975) are also listed for comparison. Like the sandy beach, the first eigenfunctions for the left and right profiles explain the most of the mean square value and the second eigenfunction describes approximately 50 % of the residual mean square value. However, the residual mean square value of the third

eigenfunction and the subtotal of the mudflat profile were less by about 20 % relative to the sandy beach. As a result, additional eigenfuncions, which are more difficult to interpret physically, will be needed to explain the mudflat profile change using the EOF method. A simpler model specifically for the mudflat profile change is developed in the following.

Chapter 4

QUADRATIC PROFILE APPROACH

In this chapter, a parameterized mudflat profile with no nearshore bar is proposed using the measured bed levels on meso-tidal mudflats in the vicinity of the Shirawaka River mouth. This parameterization allows the separation of the temporal and spatial variations of mudflat profiles under time-varying driving forces. A quadratic polynomial equation is adopted to describe the measured mudflat profiles. The measured mudflat profile is shown to be expressible using a quadratic polynomial equation involving the three parameters: (a) quadratic convexity; (b) mean slope; and (c) vertical displacement. The three parameters representing the measured mudflat profiles express the temporal profile changes.

4.1 Quadratic Polynomial Equation

The measured cross-shore profiles with no nearshore bar on the meso-tidal mudflat in the vicinity of Shirakawa River mouth are parameterized using a quadratic polynomial equation to interpret the spatial and temporal variations of the measured profile changes. Fig. 24 shows the definition of the parameterized mudflat profile. The quadratic polynomial equation fitted to the measured profiles is as follows:

$$z(t,x) = -a(t)x^2 - b(t)x + c(t) \tag{7}$$

where z = measured bed level above T.P. defined to be positive upward, t = time in months, x = offshore distance, and a = convexity parameter which is positive for a convex upward profile, b = local slope at $x = 0$ which is positive downward, and c = uniform vertical displacement which is positive upward with $z = c$ at $x = 0$. The parameters a, b and c are assumed to depend on t only. The temporal variation of the bed level z can be interpreted using the temporal variations of a, b and c if the measured cross-shore profiles can be fitted by Eq. (7) accurately.

The local slope, s_l, which is positive downward, and the profile curvature A which is positive for a concave upward profile, are given by

$$\frac{\partial z}{\partial x} = -(2ax + b) = -s_l \tag{8}$$

$$\frac{\partial^2 z}{\partial x^2} = -2a = A \tag{9}$$

The parameter a (m^{-1}) is one half of the profile curvature A where the sign depends whether the curvature is positive for an upward convex or concave profile. The dimensionless parameter b is the local bed slope at $x = 0$. The parameter c (m) is the bed level at $x = 0$ which is located at the seawall as shown in Fig. 3. The parameters a, b and c do not depend on x for the measured profile in the range $x_1 \le x \le x_2$ as shown in Fig. 24, whereas the local slope parameters s_l depend on x.

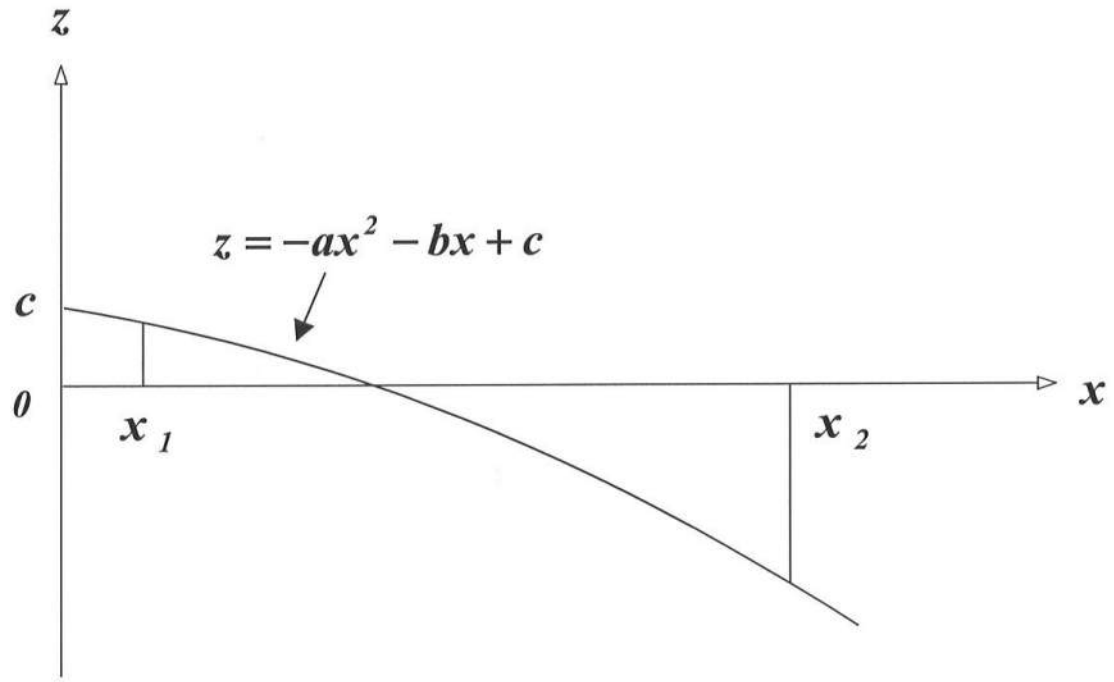

FIG. 24 Parameterization of Measured Mudflat Profile at Given Time

4.1.1 Comparison with measured profile data

Typical examples of the measured and fitted cross-shore profiles together with the average profile are shown in Figs. 25 to 28. Figs. 25 and 26 show the accreted left and right profiles, respectively, where accretion was normally larger offshore. Figs. 27 and 28 are the eroded left and right profiles, respectively, where the erosion was normally larger offshore. These figures indicate that that the measured profiles can be fitted by Eq. (7) using the method of least squares. The other measured and fitted profiles are presented in Appendix.

In order to evaluate the degree of agreement quantitatively, use is made of the average deviation ε between the measured and fitted profiles defined as

$$\varepsilon = \frac{1}{L}\sum_{l=1}^{L}\left|z_l - (-ax_l^2 - bx_l + c)\right| \qquad (10)$$

where L is the total number of data points along the survey line and $L = 20$ in the region $x_1 = 100$ m and $x_2 = 1050$ m.

Tables 11 and 12 list the fitted values of a, b and c and the average deviation ε for each of the measured left and right profiles, respectively. The fitted profile agrees with the measured profile within an error of 3 cm where this error is slightly larger than the survey error of 2 cm. The average cross-shore profile of all the measured profiles is also expressed as

$$z_m = -a_m x^2 - b_m x + c_m \tag{11}$$

where z_m = time averaged bed level during the entire survey period, and a_m, b_m and c_m = quadratic polynomial coefficients for this time averaged profile. The average profile is obtained separately for the left and right profiles. The average fitted left profile is gentler and more convex upward than the average fitted right profile as shown in Fig. 29. In Tables 11 and 12, the arithmetic mean values of a, b and c for all the measured profiles are identical to a_m, b_m and c_m for the average profile. This equivalence of each parameter is expected because the time averaging of Eq. (7) yields Eq. (11).

The quadratic convexity Q, the mean slope S, and the vertical displacement D are introduced here in order to interpret the temporal variations of a, b and c because the parameters b and c characterize the quadratic profile at $x = 0$ outside the present survey domain from $x_1 = 100$ m to $x_2 = 1050$ m. The new parameters are intended to represent the overall mudflat profile in the region $x_1 \le x \le x_2$ and are described in detail in the following.

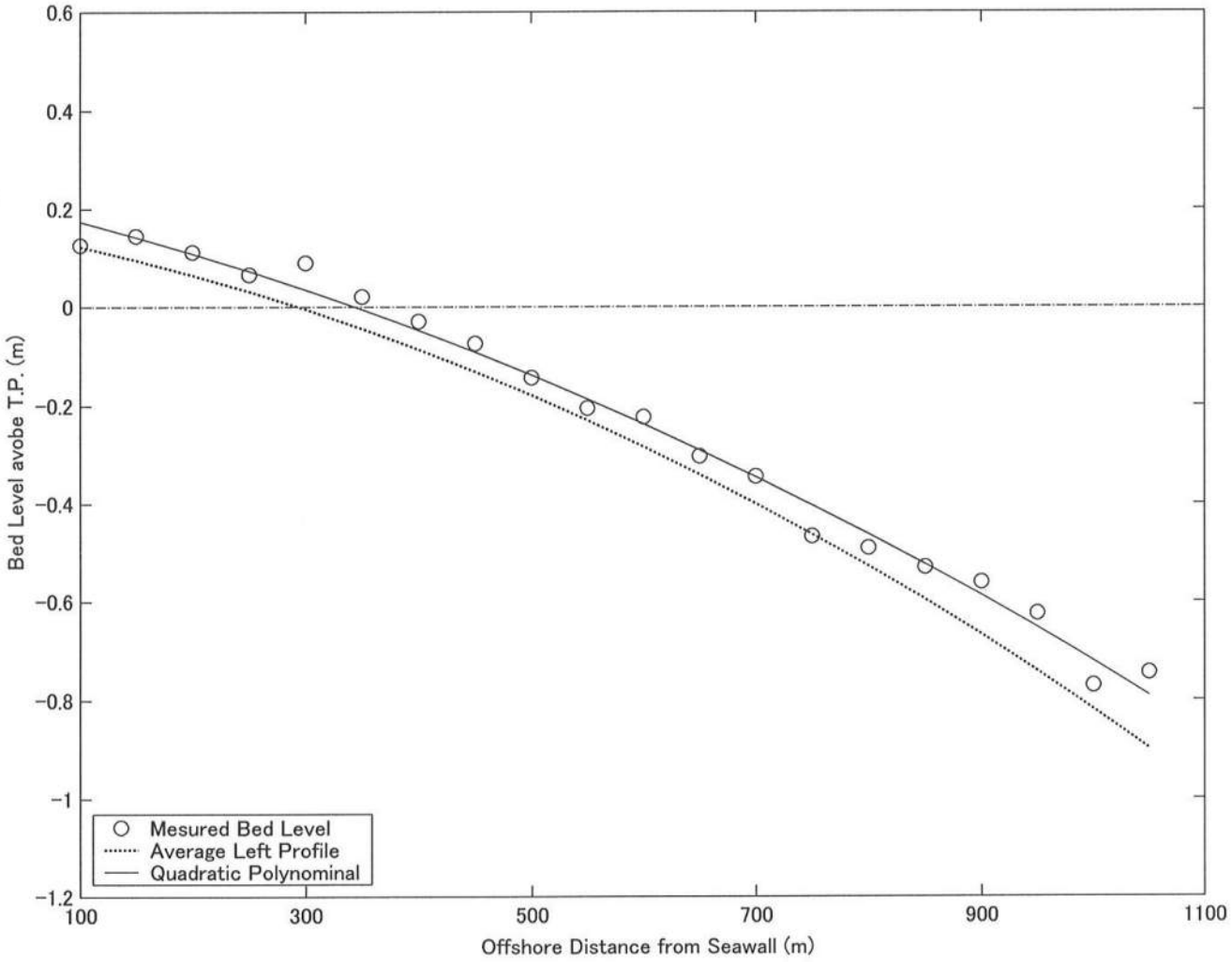

FIG. 25. Quadratic Equation Fitted to Accreted Left Profile on September 24, 2002

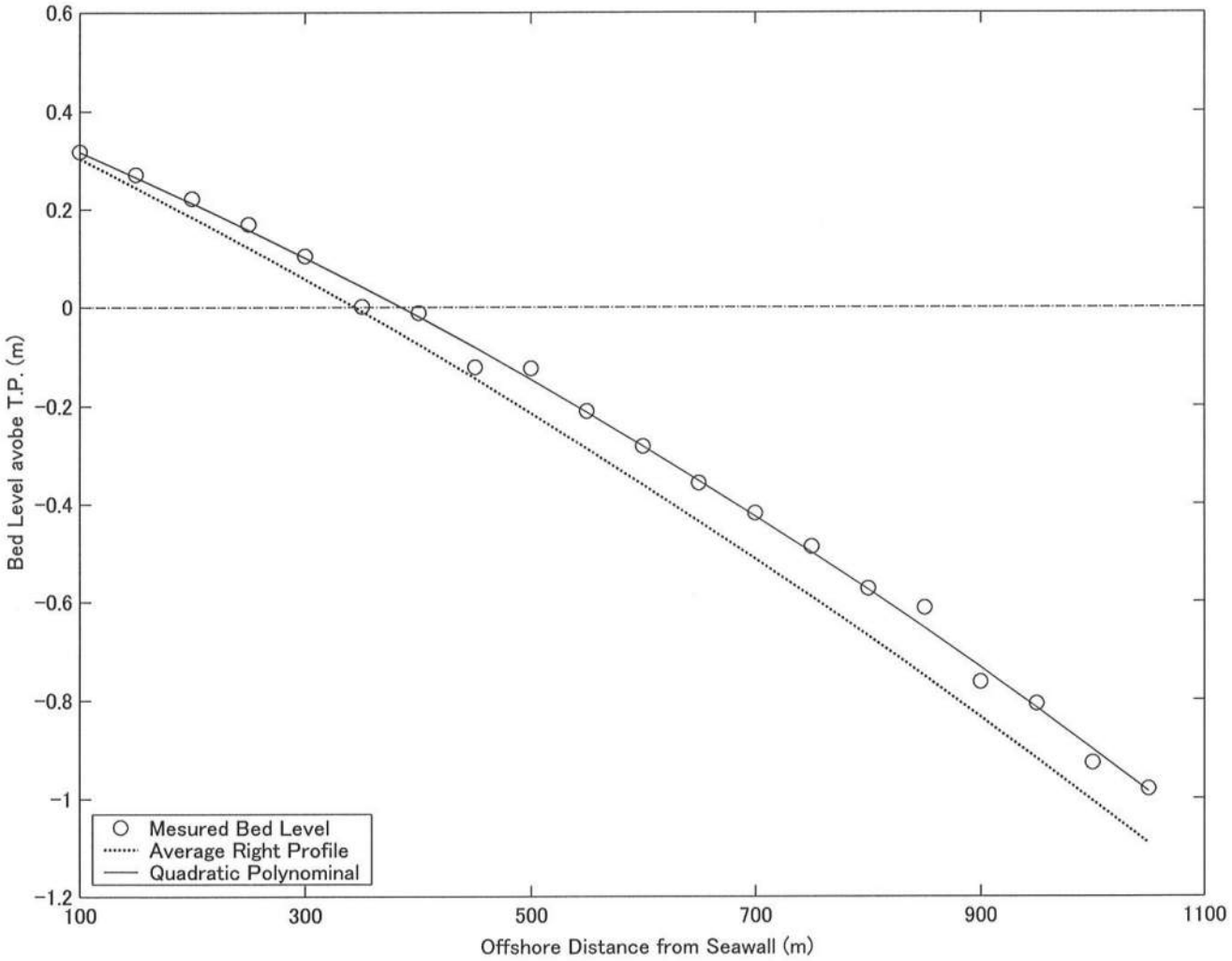

FIG. 26. Quadratic Equation Fitted to Accreted Right Profile on August 8, 2002

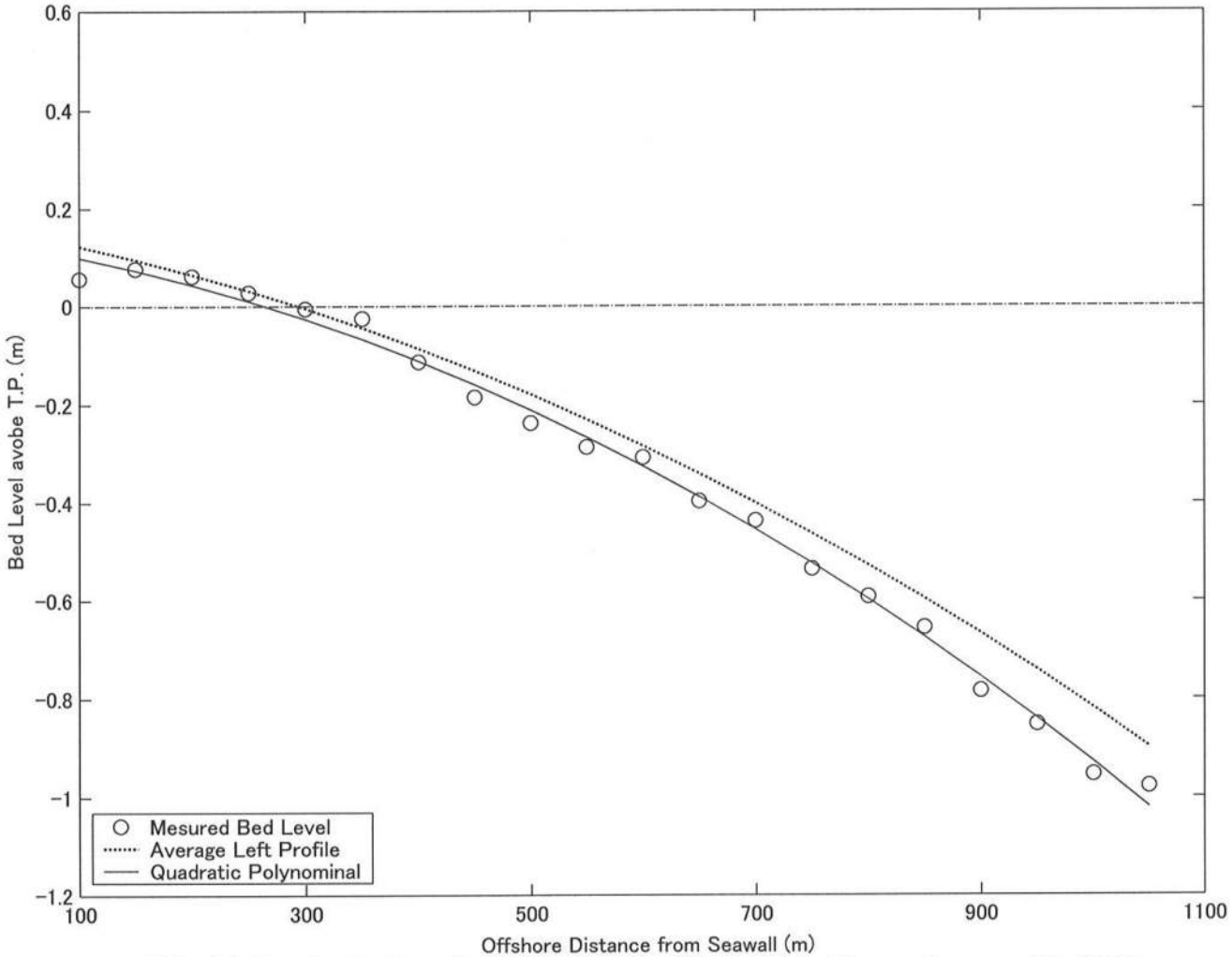

FIG. 27. Quadratic Equation Fitted to Eroded Left Profile on January 24, 2002

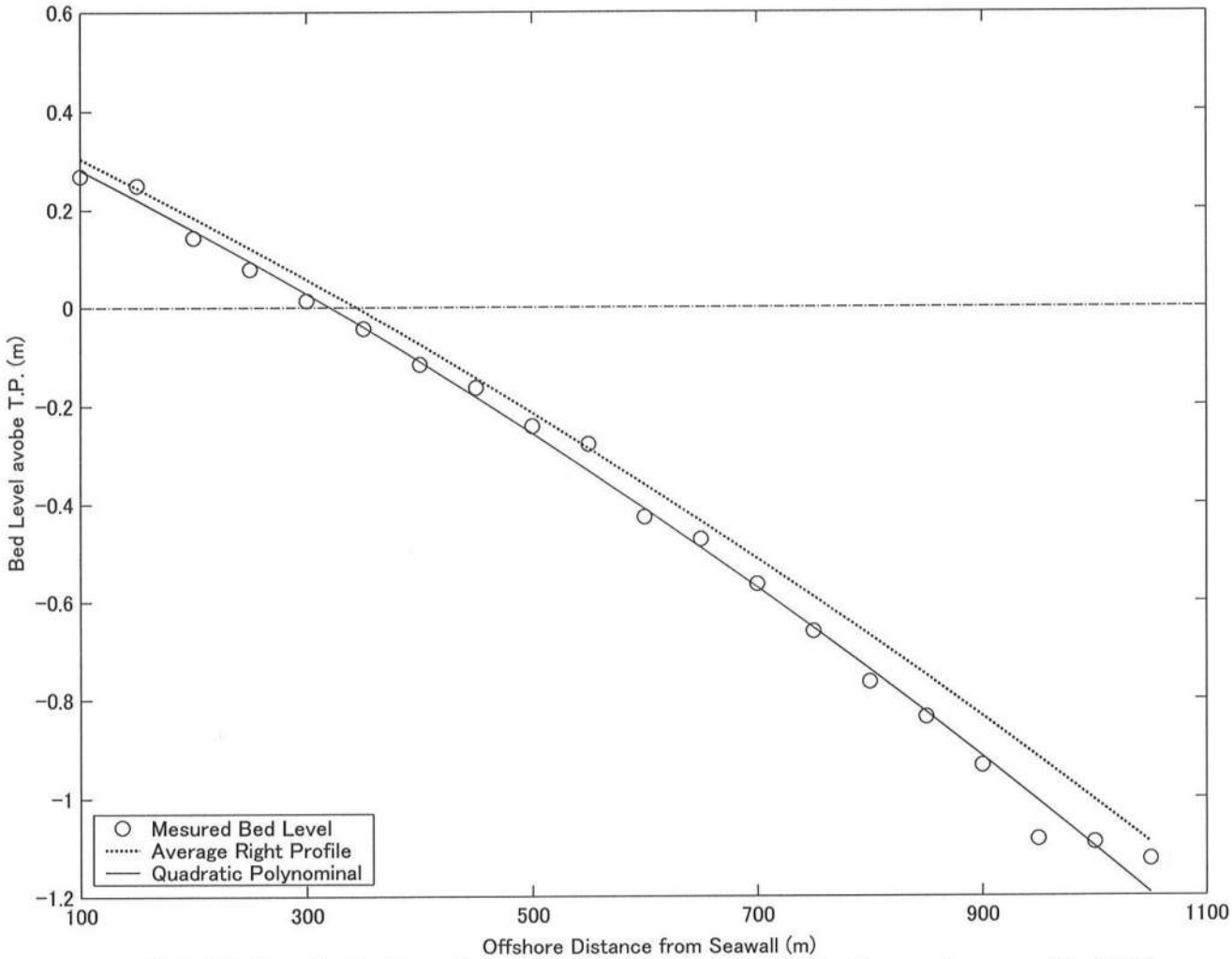

FIG. 28. Quadratic Equation Fitted to Eroded Right Profile on January 25, 2002

Table 11: Fitted Parameters and Estimated Error for Left Profile

No.	Date	$a \times 10^7$ (1/m)	$b \times 10^3$ (Dimensionless)	$c \times 10$ (m)	$\varepsilon \times 10^2$ (m)
1	2/22/01	6.26	0.39	1.09	2.76
2	4/23/01	5.75	0.37	0.98	1.93
3	6/ 1/01	6.58	0.32	1.31	2.24
4	7/ 2/01	6.69	0.26	0.89	2.58
5	9/ 4/01	5.50	0.40	1.89	1.88
6	10/18/01	5.78	0.41	1.79	1.27
7	10/31/01	4.69	0.51	2.23	1.25
8	11/28/01	5.70	0.49	1.98	1.59
9	12/26/01	4.48	0.60	1.93	1.87
10	1/24/02	7.33	0.34	1.40	2.04
11	2/25/02	7.76	0.29	1.42	2.27
12	3/29/02	6.39	0.33	1.53	1.80
13	4/26/02	4.69	0.52	2.16	2.72
14	6/13/02	4.92	0.46	2.10	2.58
15	7/ 8/02	5.38	0.45	1.79	2.85
16	9/24/02	4.28	0.52	2.31	2.39
17	10/21/02	4.63	0.52	2.05	2.54
18	11/19/02	7.40	0.22	1.48	2.46
19	12/18/02	6.31	0.32	1.77	1.97
Mean Value		5.82	0.40	1.69	2.16
Average Profile		$a_m \times 10^7$ (1/m)	$b_m \times 10^3$ (Dimensionless)	$c_m \times 10$ (m)	$\varepsilon_m \times 10^2$ (m)
		5.82	0.40	1.69	1.51

Table 12: Fitted Parameters and Estimated Error for Right Profile

No.	Date	$a \times 10^7$ (1/m)	$b \times 10^3$ (Dimensionless)	$c \times 10$ (m)	$\varepsilon \times 10^2$ (m)
1	2/23/01	1.58	1.26	4.02	2.13
2	4/25/01	2.51	1.13	4.03	1.83
3	6/ 4/01	2.50	1.09	3.72	1.47
4	7/ 3/01	4.37	0.92	3.77	1.69
5	9/ 5/01	2.97	1.09	4.24	1.49
6	10/20/01	2.15	1.18	4.31	1.18
7	11/ 2/01	3.25	1.12	4.49	1.56
8	11/30/01	2.30	1.29	4.68	1.43
9	12/27/01	4.50	1.08	3.93	2.35
10	1/25/02	3.80	1.12	3.96	2.20
11	2/26/02	3.83	1.08	4.28	1.59
12	3/27/02	2.48	1.20	4.25	1.80
13	4/25/02	4.55	0.98	3.87	2.01
14	7/11/02	3.05	1.09	4.23	2.71
15	8/ 8/02	3.86	0.93	4.14	1.41
16	9/20/02	3.61	1.03	4.10	2.27
17	10/22/02	2.73	1.19	4.23	2.72
18	11/18/02	2.86	1.12	4.53	1.92
19	12/17/02	2.85	1.17	4.52	2.18
Mean Value		3.14	1.11	4.17	1.89
Average Profile		$a_m \times 10^7$ (1/m)	$b_m \times 10^3$ (Dimensionless)	$c_m \times 10$ (m)	$\varepsilon_m \times 10^2$ (m)
		3.14	1.11	4.17	0.65

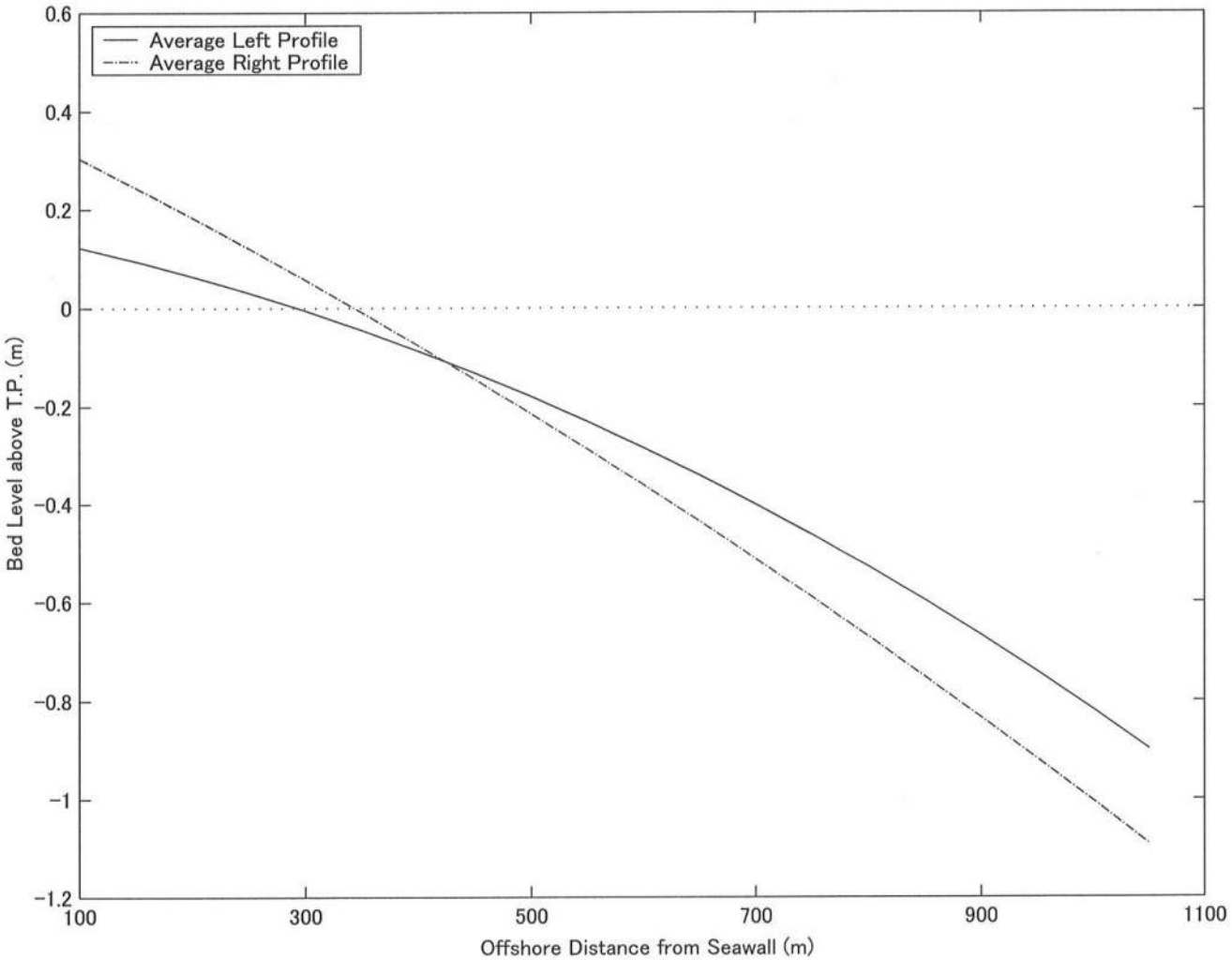

FIG. 29 Average Fitted Left and Right Profiles

4.1.2 Quadratic convexity parameter

Kirby (1992, 2000) proposed that the profile curvature of the mudflat profile could be used to classify the relative contributions caused by wind waves and tidal motions to the total sediment transport. Convex-upward profiles were correlated with large tide ranges, long-term accretion and/or low wave activity. Concave-upward profiles were correlated with small tide ranges, long-term erosion and/or high wave activity. All the measured profiles at this field site were convex-upward and $a > 0$ and $A < 0$ in Eq. (9).

In order to relate the profile curvature to the seasonal tide level and bed level variations quantitatively, it is more convenient to characterize the profile curvature using a representative vertical length. For that purpose, the quadratic convexity parameter Q is introduced here as shown in Fig. 30. The two points (x_1, z_1) and (x_2, z_2) on the fitted mud profile are the landward and seaward ends of the survey line, respectively. The straight line connecting these two points is expressed as

$$z_q = \frac{z_1 - z_2}{x_1 - x_2} x + \frac{x_1 z_2 - x_2 z_1}{x_1 - x_2}$$

$$= -\left[a(x_1 + x_2) + b\right] x + (a x_1 x_2 + c) \qquad (12)$$

where use is made of $z_1 = -a x_1^2 - b x_1 + c$ and $z_2 = -a x_2^2 - b x_2 + c$.

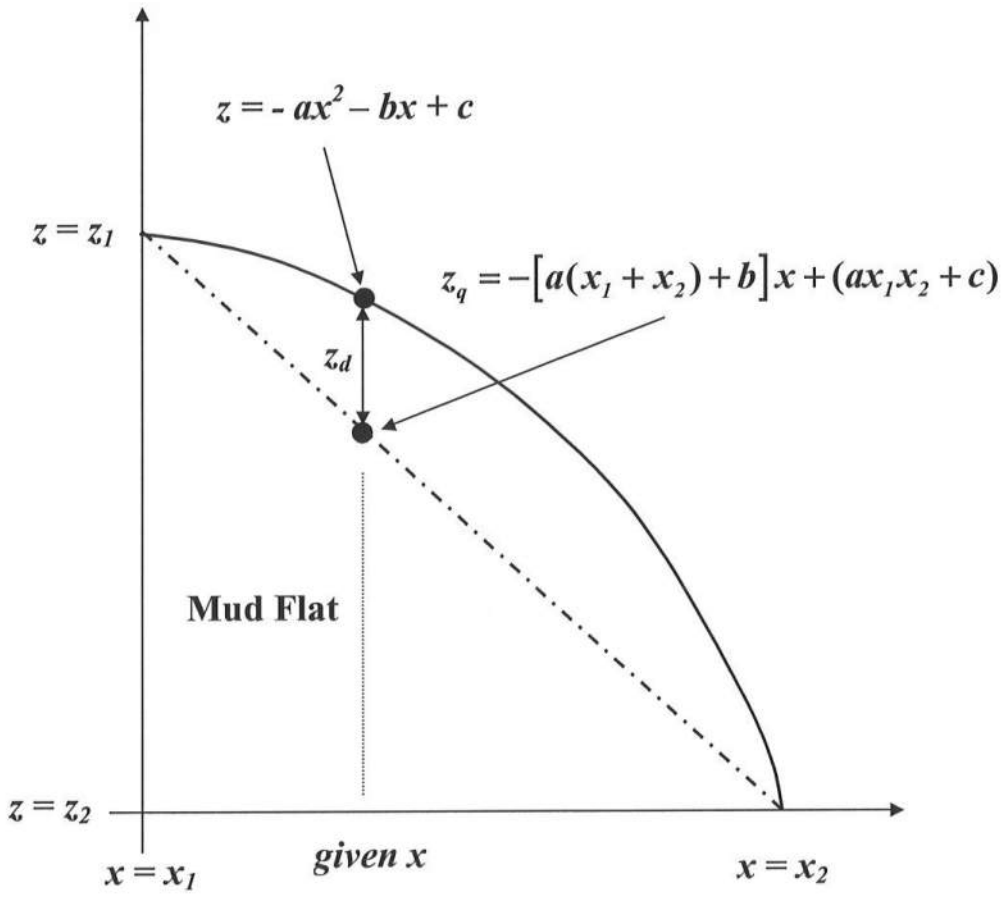

FIG. 30 Definition of Quadratic Convexity Parameter

The vertical distance z_d of the quadratic profile above the straight line is given by

$$z_d(t,x) = z(t,x) - z_q(t,x)$$

$$= -a(x - x_1)(x - x_2) \tag{13}$$

where $z_d = 0$ at $x = x_1$ and $x = x_2$. Differentiation of Eq. (13) with respect to x yields

$$\frac{\partial z_d}{\partial x} = -2ax + a(x_1 + x_2) \tag{14}$$

Thus, the local maximum of z_d occurs at the middle point located at

$$x = \frac{x_1 + x_2}{2} \tag{15}$$

The maximum value of z_d is called here as the quadratic convexity parameter Q and given by

$$\left[z_d(t,x)\right]_{\max} \equiv Q = a \cdot \left(\frac{x_2 - x_1}{2}\right)^2 \tag{16}$$

The parameter Q (m) depends on the parameter a and the survey line length $(x_2 - x_1)$. If the fitted profile is a straight line, $Q = 0$ and no convexity exists. Considering the average value of the vertical distance z_d in the region from $x = x_1$ to $x = x_2$, the average value Q_a is given by

$$Q_a \equiv \frac{1}{x_2 - x_1} \int_{x_1}^{x_2} z_d(t,x)dx$$

$$= \frac{a}{6}(x_2 - x_1)^2 \tag{17}$$

Comparing Eqs. (16) and (17), $Q/Q_a = 3/2$. As a result, the quadratic convexity parameter Q is sufficient to express the deviation of the quadratic profile from the straight line.

4.1.3 Mean slope parameter

Dyer (1998) and Dyer *et al.* (2000) proposed a statistical scheme for typology and classification of intertidal mudflats using tidal range, wave action, and mean bed slope as the most important variables. The mean slope, *S*, for the fitted quadratic profile is defined here as the average value of the local slope $s_l = (2ax + b)$ in the region from $x = x_1$ to $x = x_2$ as follows:

$$S \equiv \frac{1}{x_2 - x_1} \int_{x_1}^{x_2} (2ax + b)dx$$
$$= a(x_1 + x_2) + b \tag{18}$$

The parameter *S* (dimensionless) depends on the parameter *a*, *b*, x_1, and x_2. The mean slope *S* is the sum of the local slope *b* at *x* = 0 and the additional slope $a(x_1 + x_2)$ due to the profile curvature *a* in the region $x_1 \le x \le x_2$. The mean slope also equals to the local slope s_l at *x* $= \frac{x_1 + x_2}{2}$ and its magnitude equals to the gradient of z_q using the first term of the right hand side of Eq. (12)

$$S = s_l\left(\frac{x_1 + x_2}{2}\right) = -\left(\frac{z_1 - z_2}{x_1 - x_2}\right) \tag{19}$$

which implies that *S* is the downward slope connecting the two end points in Fig. 30.

Figs. 31 and 32 show the temporal variations of the mean slope *S* and its two components, $a(x_1 + x_2)$ and *b* in Eq. (18) for the left and right profiles, respectively. The mean

slope is dominated by the additional slope $a(x_1 + x_2)$ for the left profile but by the local slope b at $x = 0$ for the right profile because the right profile is more straight as shown in Fig. 29. The two components vary with time more than the mean slope, resulting in the opposite trend of the temporal variations of the two components.

Tables 13 and 14 list the calculated values of the mean slope and two components for the left and right profiles together with their ratios. The additional slope term for the left profile is approximately twice larger than that for the right profile. However, the local slope b for the left profile is approximately one-third of that for the right profile. The ratio between the additional slope term and the mean slope for the left profile is approximately 60 % but the ratio between the local slope b and the mean slope for the right profile is approximately 75 %. Consequently, the two components, $a(x_1 + x_2)$ and b of the mean slope parameter S are different for the left and right profiles. This difference between the left and right profiles could be seen in the values of a and b listed in Tables 11 and 12 but it is much clearer in Tables 13 and 14.

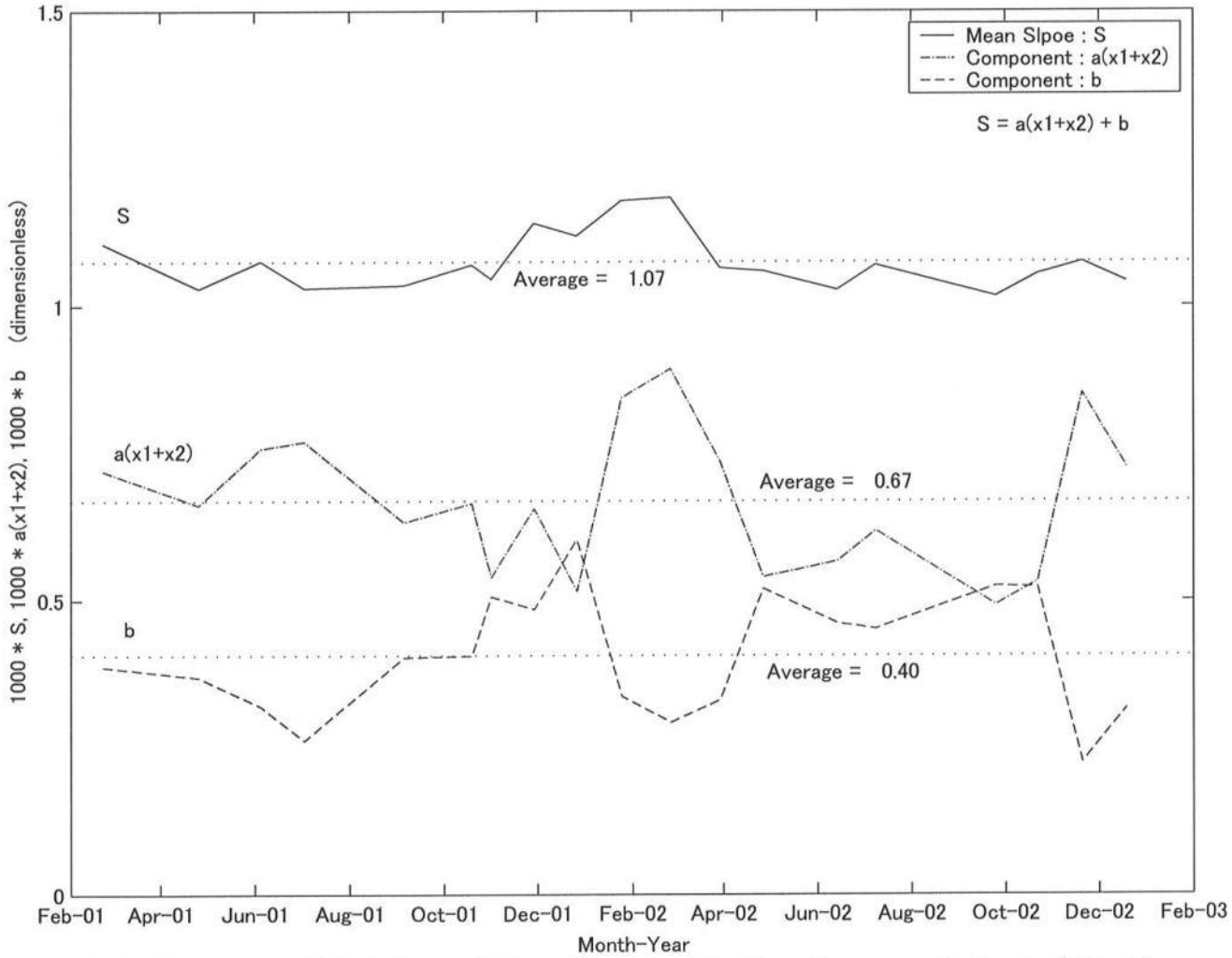

FIG. 31. Temporal Variations of Mean Slope and Its Two Components for Left Profile

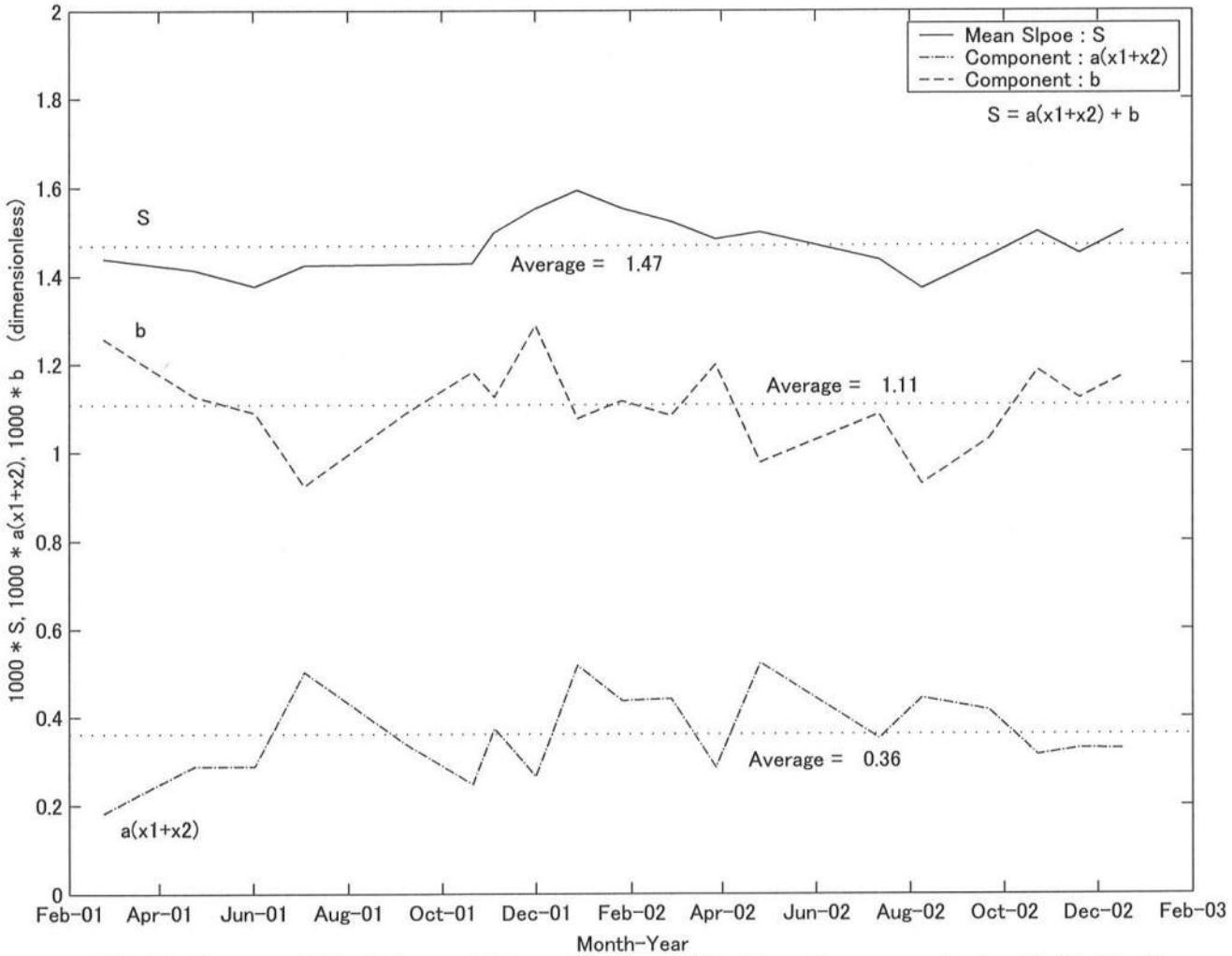

FIG. 32. Temporal Variations of Mean Slope and Its Two Components for Right Profile

Table 13: Mean Slope, Two Components and Ratio for Left Profile

No.	Data	$S \times 10^3$ (Dimensionless)	$a(x_1 + x_2) \times 10^3$ (Dimensionless)	$b \times 10^3$ (Dimensionless)	$a(x_1 + x_2)/S$ (%)	b/S (%)
1	2/22/01	1.11	0.72	0.39	65.1	34.9
2	4/23/01	1.03	0.66	0.37	64.3	35.7
3	6/ 1/01	1.08	0.76	0.32	70.3	29.7
4	7/ 2/01	1.03	0.77	0.26	74.7	25.3
5	9/ 4/01	1.03	0.63	0.40	61.1	38.9
6	10/18/01	1.07	0.67	0.41	62.1	37.9
7	10/31/01	1.05	0.54	0.51	51.6	48.4
8	11/28/01	1.14	0.66	0.49	57.5	42.5
9	12/26/01	1.12	0.52	0.60	46.0	54.0
10	1/24/02	1.18	0.84	0.34	71.5	28.5
11	2/25/02	1.18	0.89	0.29	75.4	24.6
12	3/29/02	1.06	0.74	0.33	69.1	30.9
13	4/26/02	1.06	0.54	0.52	50.9	49.1
14	6/13/02	1.03	0.57	0.46	55.1	44.9
15	7/ 8/02	1.07	0.62	0.45	57.8	42.2
16	9/24/02	1.02	0.49	0.52	48.4	51.6
17	10/21/02	1.05	0.53	0.52	50.5	49.5
18	11/19/02	1.07	0.85	0.22	79.2	20.8
19	12/18/02	1.04	0.73	0.32	69.7	30.3
Average Value		1.07	0.67	0.40	62.7	37.3

Table 14: Mean Slope, Two Components and Ratio for Right Profile

No.	Data	$S \times 10^3$ (Dimensionless)	$a(x_1 + x_2) \times 10^3$ (Dimensionless)	$b \times 10^3$ (Dimensionless)	$a(x_1 + x_2)/S$ (%)	b/S (%)
1	2/23/01	1.44	0.18	1.26	12.7	87.4
2	4/25/01	1.41	0.29	1.13	20.4	79.6
3	6/ 4/01	1.38	0.29	1.09	20.9	79.1
4	7/ 3/01	1.42	0.5	0.92	35.3	64.7
5	9/ 5/01	1.43	0.34	1.09	23.9	76.1
6	10/20/01	1.43	0.25	1.18	17.3	82.7
7	11/ 2/01	1.50	0.37	1.12	25.0	75.0
8	11/30/01	1.55	0.27	1.29	17.0	83.0
9	12/27/01	1.59	0.52	1.08	32.5	67.5
10	1/25/02	1.55	0.44	1.12	28.1	71.9
11	2/26/02	1.52	0.44	1.08	29.0	71.0
12	3/27/02	1.48	0.29	1.20	19.2	80.8
13	4/25/02	1.50	0.52	0.98	34.9	65.1
14	7/11/02	1.44	0.35	1.09	24.5	75.6
15	8/ 8/02	1.37	0.44	0.93	32.3	67.7
16	9/20/02	1.44	0.42	1.03	28.8	71.2
17	10/22/02	1.50	0.31	1.19	20.9	79.1
18	11/18/02	1.45	0.33	1.12	22.7	77.3
19	12/17/02	1.50	0.33	1.17	21.8	78.2
Average Value		1.47	0.36	1.11	24.5	75.5

4.1.4 Vertical displacement parameter

The time series of the cross-shore averaged bed level deviation has been shown in Section 3.1 and Fig. 21 to be correlated with the average tide level varying seasonally. For the parameterized mudflat profile, the vertical displacement, D, is defined as the average deviation of the quadratic profile z given by Eq. (7) about the average profile z_m given by Eq. (11).

$$D \equiv \frac{1}{x_2 - x_1}\int_{x_1}^{x_2}(z - z_m)dz$$
$$= -\frac{(a - a_m)}{3}\left(x_2^2 + x_1 x_2 + x_1^2\right) - \frac{(b - b_m)}{2}(x_2 + x_1) + (c - c_m) \qquad (20)$$

which depends on the parameters a, b, and c for given x_1 and x_2. The parameter D (m) expresses the average vertical accretion (positive) or erosion (negative) depth in the region $x_1 \le x \le x_2$.

4.2 Temporal Variations of Profile Parameters

Tables 15 and 16 list the values of Q, S and D for each of the left and right profiles. The vertical displacement D for the left and right profiles is in the range –7 to 7 cm and much less than the survey distance $(x_2 - x_1)$ = 950 m. Correspondingly, the mean slope S is of the order of 10^{-3} and is approximately 1.5 times larger (steeper) for the right profile. The quadratic convexity Q is of the order of 10 cm and is approximately two times larger (more convex upward) for the left profile. Thus, these three parameters concisely describe the characteristics and differences between the left and right profiles in the region $x_1 \le x \le x_2$.

Table 15: Summary of Left Profile Parameters

No.	Date	Q (cm)	$S \times 10^3$ (Dimensionless)	D (cm)
1	2/22/01	9.41	1.11	-6.68
2	4/23/01	8.65	1.03	-4.71
3	6/ 1/01	9.90	1.08	-1.95
4	7/ 2/01	10.1	1.03	-3.19
5	9/ 4/01	8.27	1.03	3.45
6	10/18/01	8.70	1.07	1.16
7	10/31/01	7.05	1.05	4.26
8	11/28/01	8.58	1.14	-1.19
9	12/26/01	6.74	1.12	-3.50
10	1/24/02	11.0	1.18	-5.00
11	2/25/02	11.7	1.18	-3.96
12	3/29/02	9.62	1.06	0.45
13	4/26/02	7.05	1.06	2.73
14	6/13/02	7.40	1.03	4.62
15	7/ 8/02	8.06	1.07	0.18
16	9/24/02	6.44	1.02	5.62
17	10/21/02	6.96	1.05	1.74
18	11/19/02	11.1	1.07	2.00
19	12/18/02	9.49	1.04	3.96
Average Value		Q_m (cm)	$S_m \times 10^3$ (Dimensionless)	D_m (cm)
		8.75	1.07	0.00

Table 16: Summary of Right Profile Parameters

No.	Date	Q (cm)	$S \times 10^3$ (Dimensionless)	D (cm)
1	2/23/01	2.38	1.44	-3.80
2	4/25/01	3.77	1.41	0.14
3	6/ 4/01	3.77	1.38	-0.84
4	7/ 3/01	6.57	1.42	1.60
5	9/ 5/01	4.46	1.43	2.66
6	10/20/01	3.23	1.43	1.16
7	11/ 2/01	4.89	1.50	1.73
8	11/30/01	3.46	1.55	-1.91
9	12/27/01	6.77	1.59	-6.04
10	1/25/02	5.72	1.55	-5.26
11	2/26/02	5.77	1.52	-0.28
12	3/27/02	3.73	1.48	-1.78
13	4/25/02	6.84	1.50	-1.12
14	7/11/02	4.59	1.44	2.16
15	8/ 8/02	5.80	1.37	7.06
16	9/20/02	5.44	1.44	1.97
17	10/22/02	4.10	1.50	-2.25
18	11/18/02	4.30	1.45	3.91
19	12/17/02	4.29	1.50	0.89
Average Value		Q_m (cm)	$S_m \times 10^3$ (Dimensionless)	D_m (cm)
		4.73	1.47	0.00

The top panel of Fig. 33 shows the time series of the vertical displacement parameter D for the left and right profiles. The two time series are similar and vary periodically with approximately one year period. The profiles accreted during summer and fall and eroded during winter and spring.

The middle panel of Fig. 33 shows the time series of the mean slope parameter S for the left and right profiles. The two time series vary annually in a similar manner, like the vertical displacement parameter. The mean slope became steeper during erosion and gentler during accretion.

The bottom panel of Fig. 33 shows the time series of the quadratic convexity parameter Q for the left and right profiles. The two time series appear to vary semiannually but their temporal patterns are not similar always.

Figs. 34 and 35 present the correlations between these three profile parameters for the left and right profiles. The top panels of these figures show the scatter plot between the mean slope S and the vertical displacement D, which are negatively correlated with the correlation coefficients R = -0.63 and –0.68. The mean slope becomes gentler (steeper) with the increase (decrease) of the vertical displacement.

The middle panels show the scatter plot between the quadratic convexity Q and the mean slope S, which are negatively correlated with R = -0.51 for the left profile but are not correlated for

the right profile.

The bottom panels show the scatter plot between the quadratic convexity Q and the vertical displacement D, which are positively correlated but the correlation coefficients R = 0.51 and 0.29 are relatively small.

To facilitate the evaluation of the dominant causes of the tidal flat profile changes, the quadratic profile approach together with the three parameters for the quadratic convexity, mean slope and vertical displacement is proposed here. The time variations of these three parameters are compared with the available time series of the average tide level, tidal range, wave height, wind speed, and river discharge in Chapter 5.

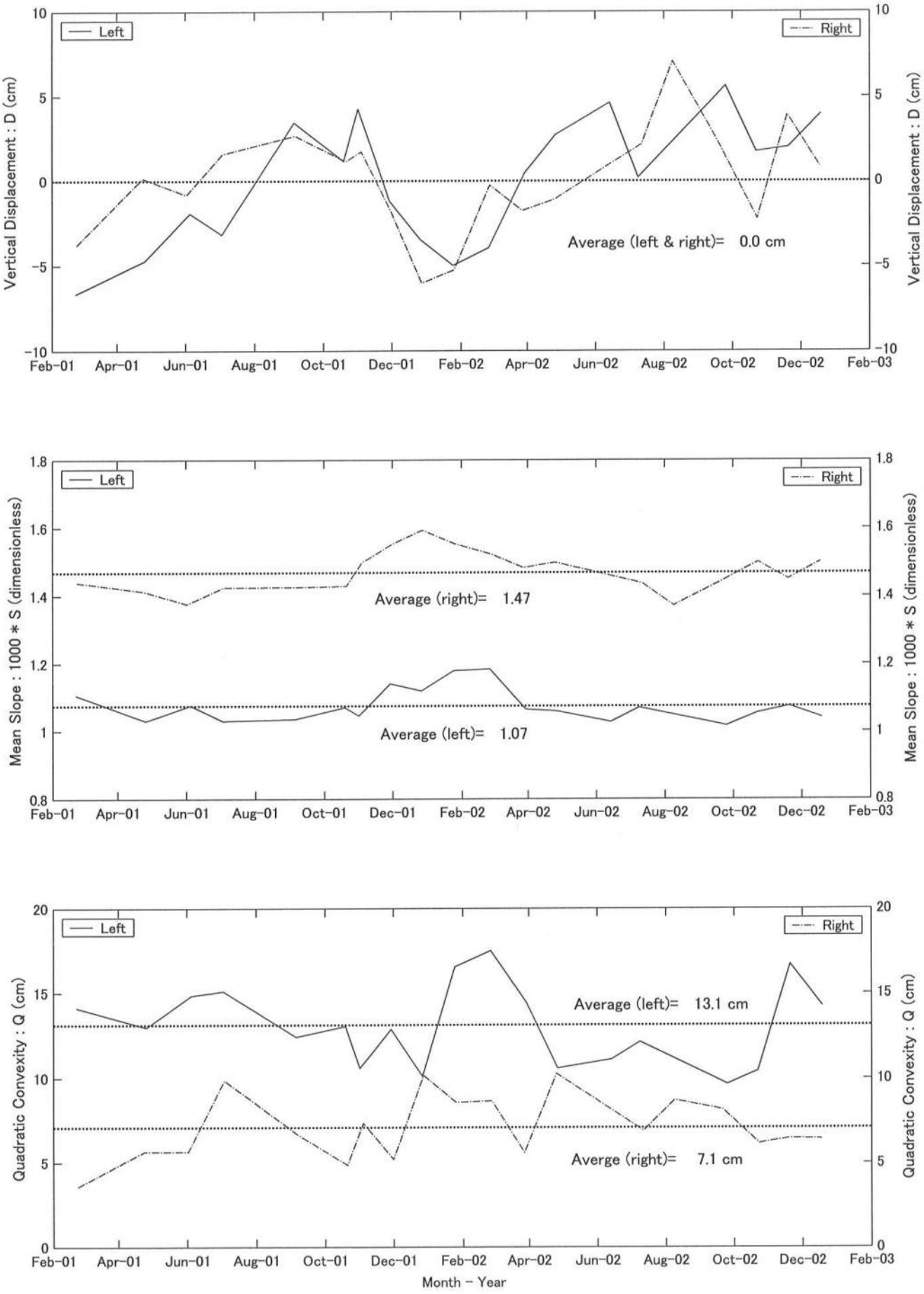

FIG. 33. Temporal Variations of Left and Right Profile Parameters

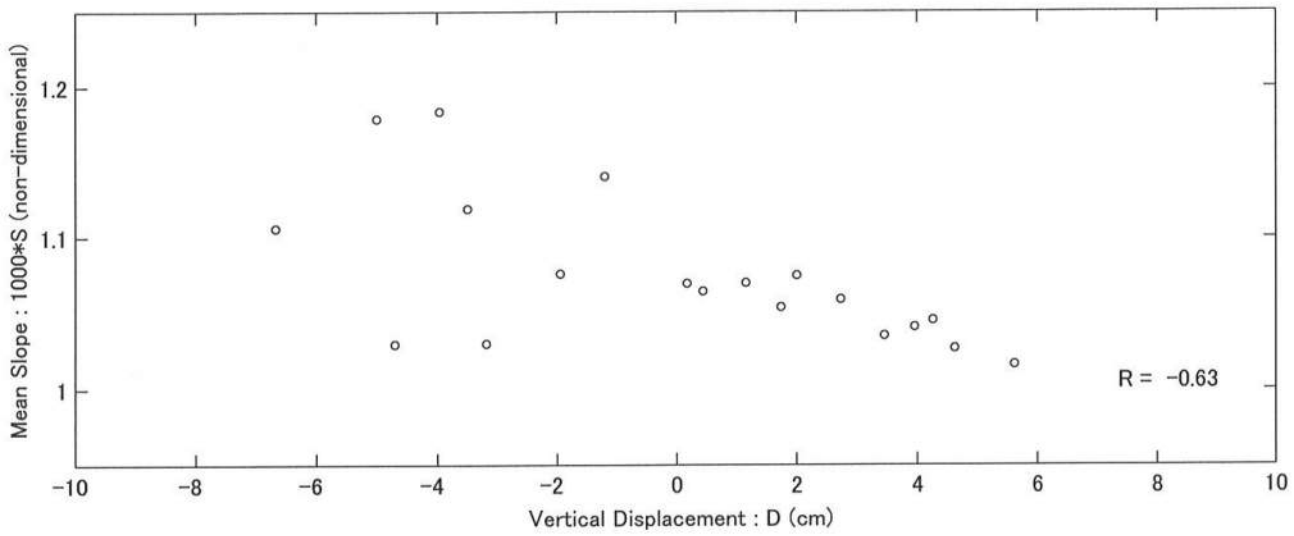

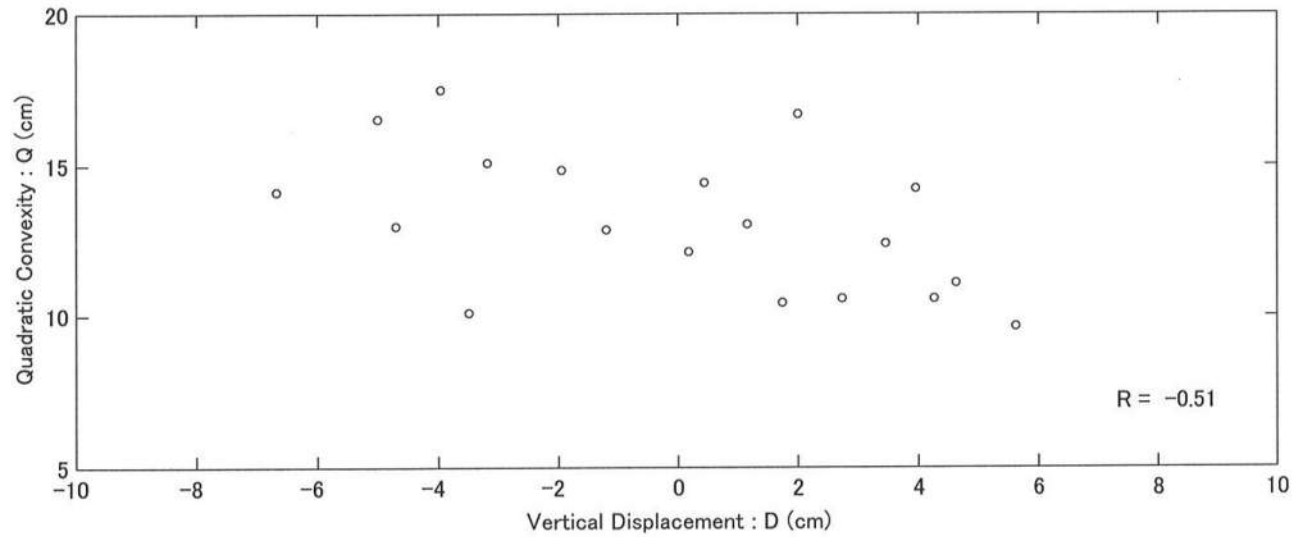

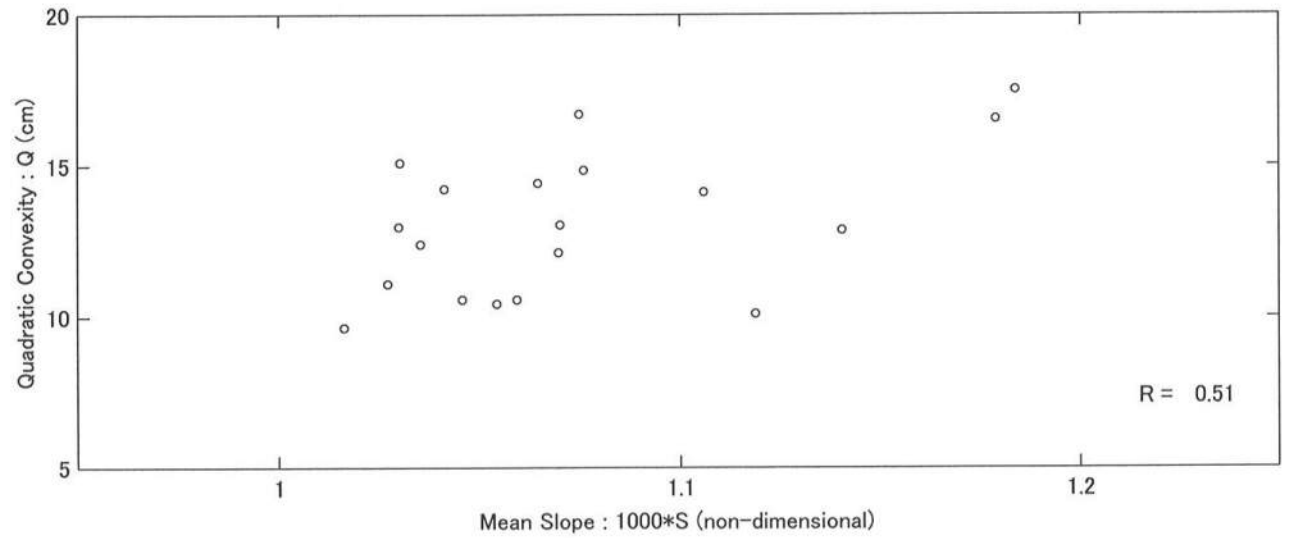

FIG. 34. Correlations between Left Profile Parameters

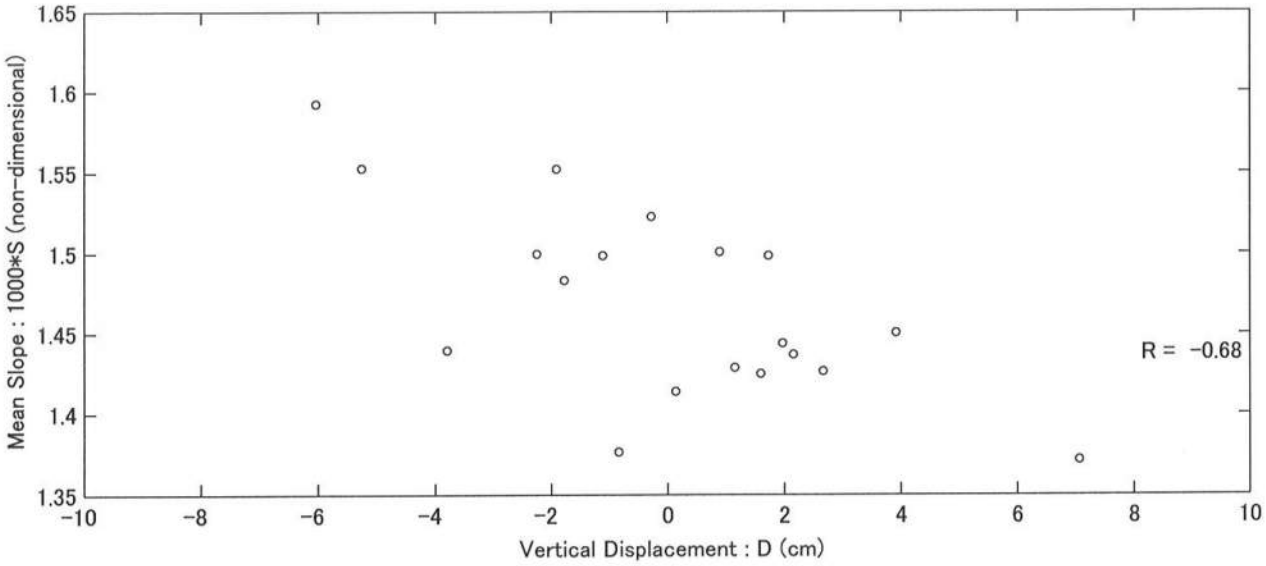

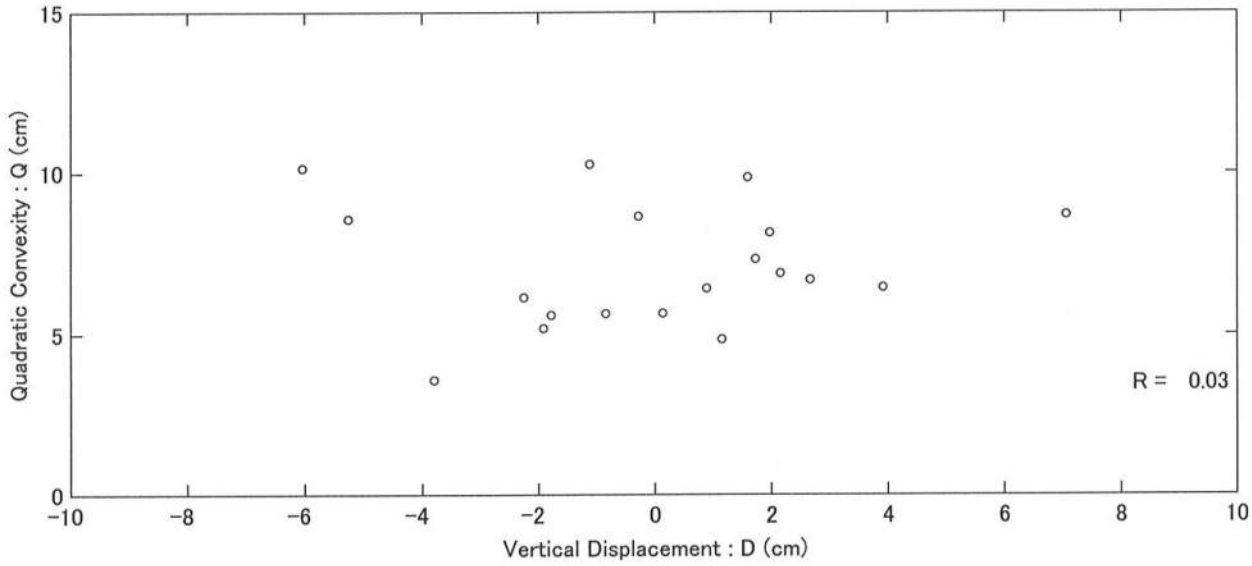

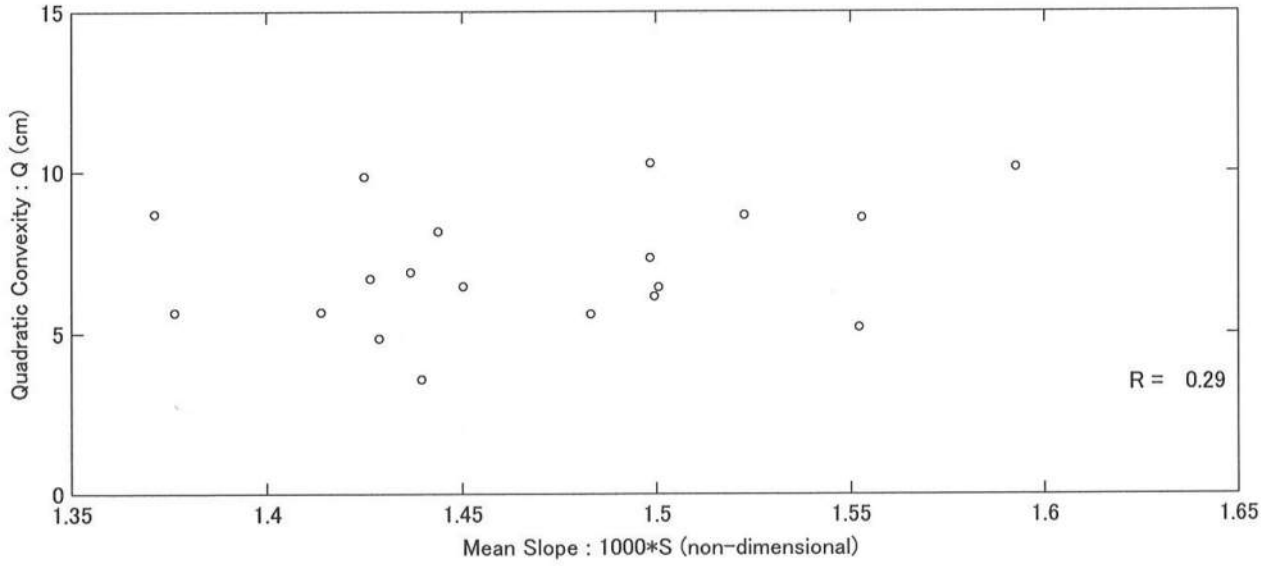

FIG. 35. Correlations between Right Profile Parameters

Chapter 5

CORRELATIONS OF THREE PROFILE PARAMETERS AND DRIVING FORCES

In order to identify the predominant driving forces causing the mudflat cross-shore profile changes in the vicinity of the Shirakwa River mouth, the time series of the vertical displacement, mean slope and quadratic convexity are compared with the time-varying driving forces presented in Section 2.3.

5.1 Vertical Displacement Parameter

Figs. 36 - 41 show the time series of the vertical displacement parameter compared with the driving forces including the 56-day averaged tide level, spring-neap tidal range averaged during 5 spring-neap cycles, significant wave height, squared significant wave height, wind velocity, and rainfall. The top panels of these figures show the results for the left profile during February 2001 to December 2002 and the bottom panels are for the right profile during the same period.

Fig. 36 shows that the time series of the vertical displacement is correlated positively with that of the 56-day averaged tide level. Both time series varied periodically with a one-year period. The mudflat accreted with the average tide level rise, and eroded with the average tide level fall.

Fig. 37 shows that the vertical displacement and the moving averaged spring-neap tidal range were not correlated partly because the vertical displacement varied annually but the moving averaged spring-neap tidal range varied semiannually.

Figs. 38 and 39 show that there was no obvious correlation between the vertical displacement and wind waves partly because the significant wave heights were relatively small. However, the effects of wind waves may be important on a time scale shorter than the monthly profile data used here.

Fig. 40 shows the correlation between the vertical displacement and the wind velocity was very low like the wind waves.

Fig. 41 shows that both time series of the vertical displacement and rainfall varied annually and might be correlated somewhat. However, a time lag of approximately two months was noticeable between the peaks of the two time series. The mudflat accreted during August to October after the heavy rainfall during June to July, which is the rainy season in Japan.

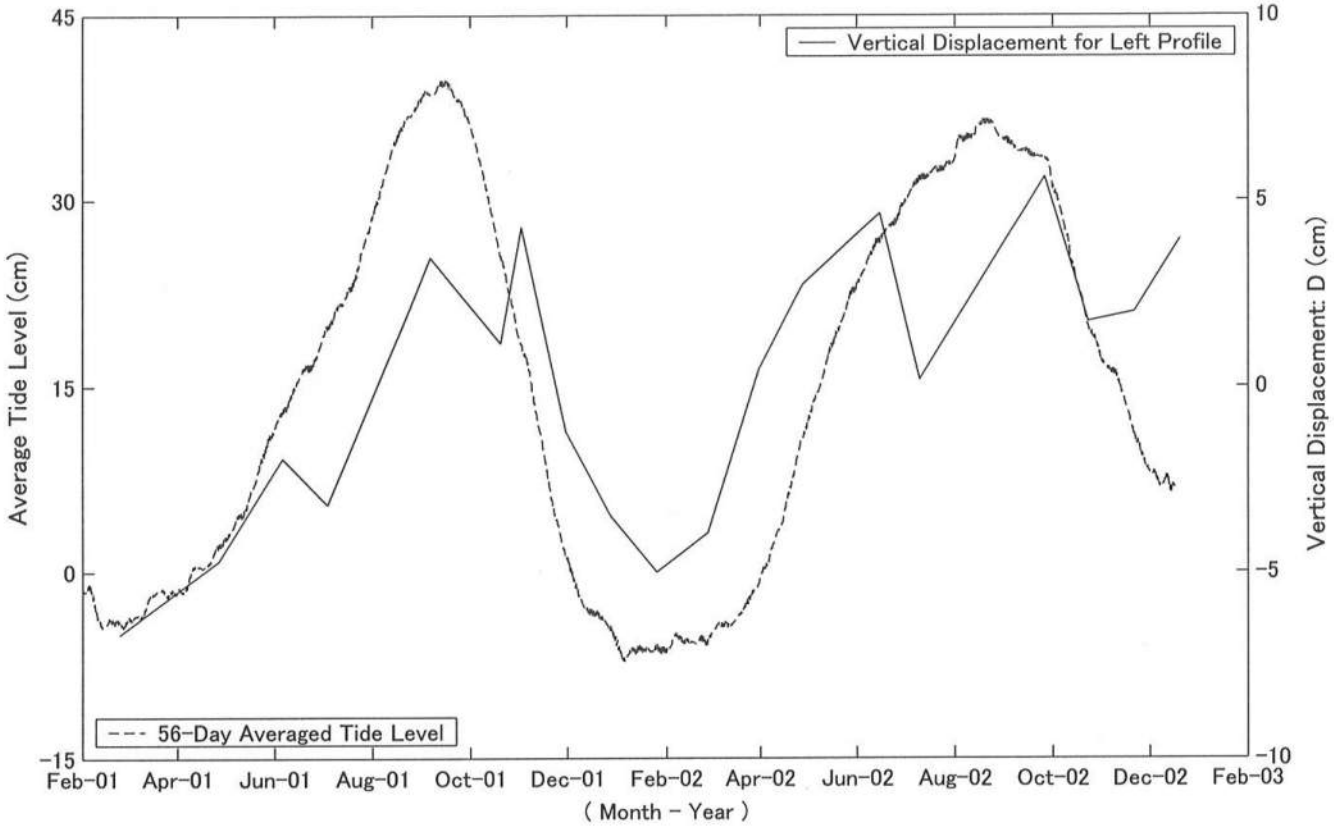

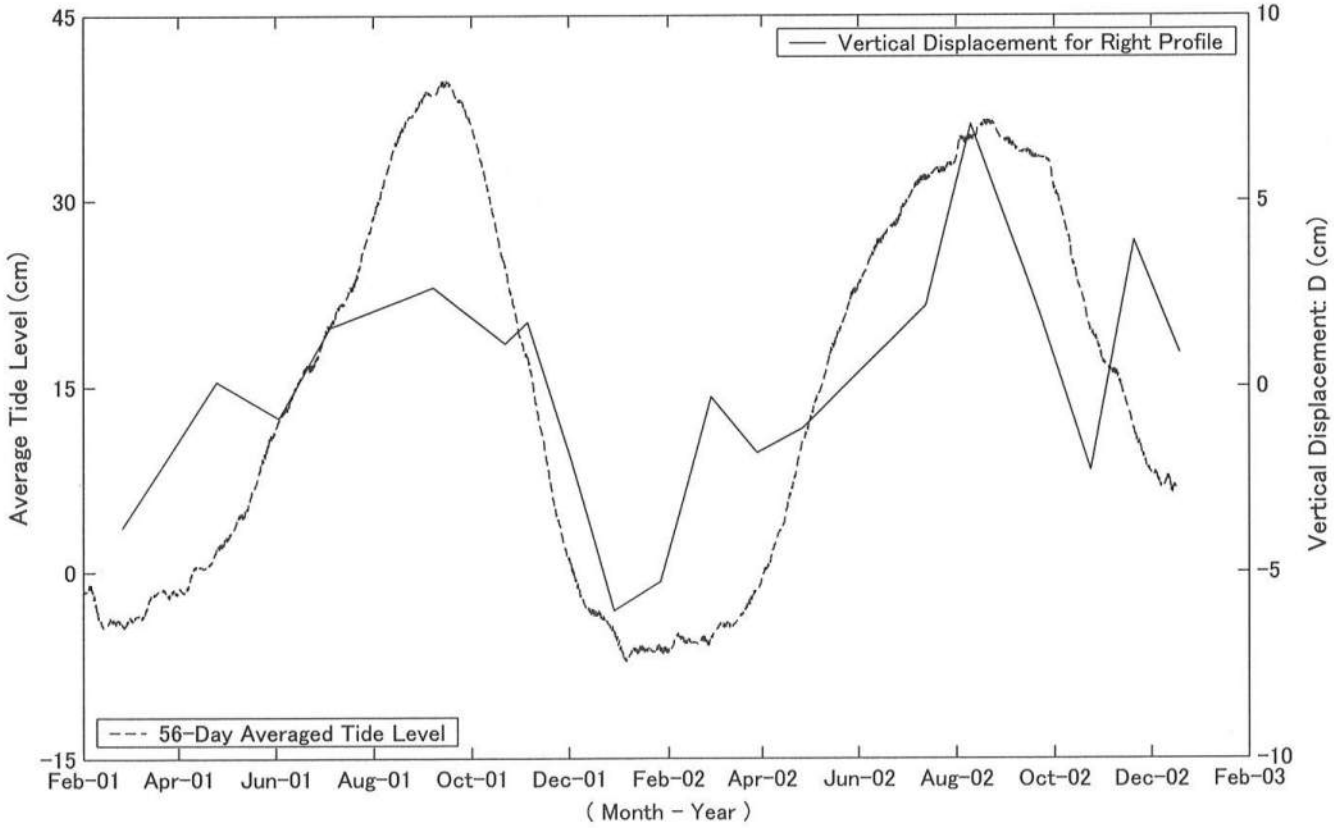

FIG. 36. Time Series of Vertical Displacement and Average Tide Level for Left and Right Profiles

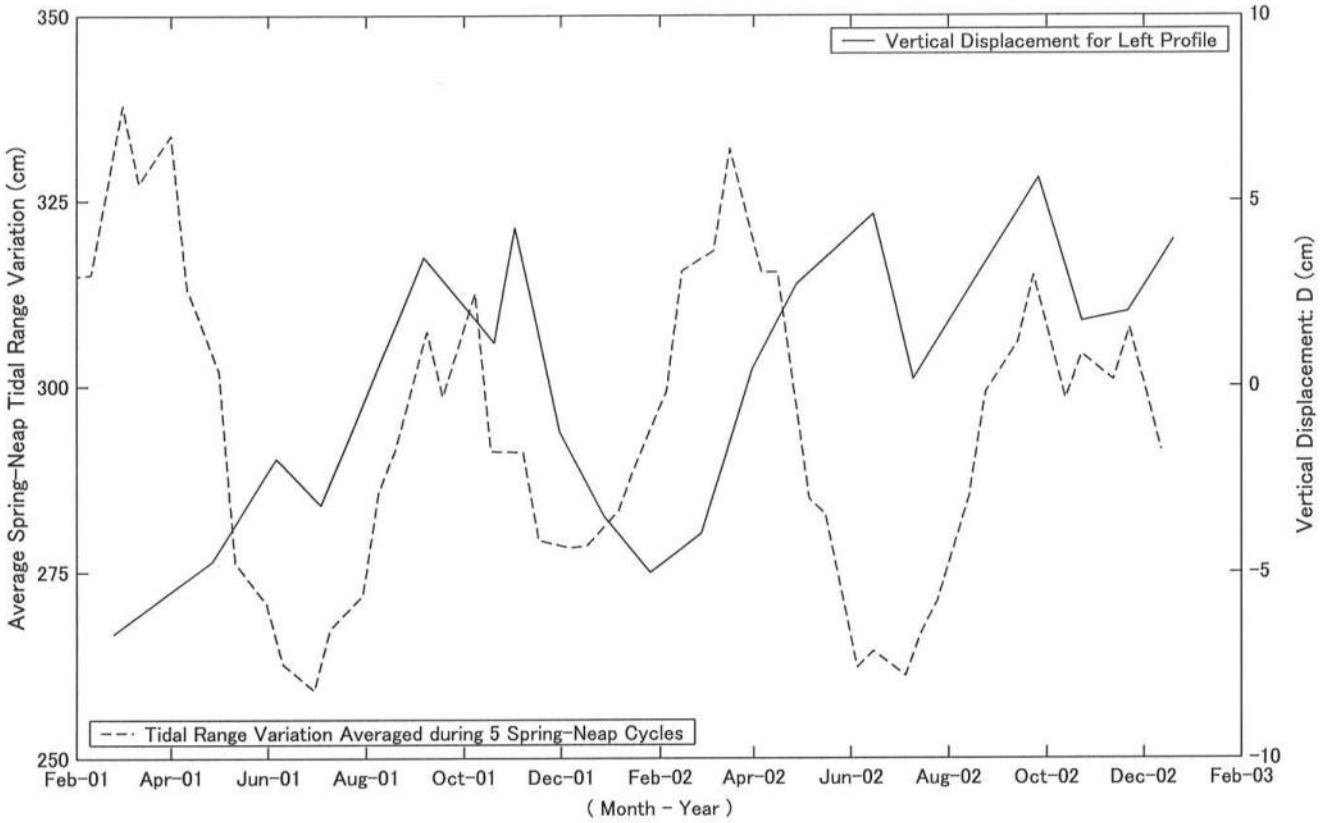

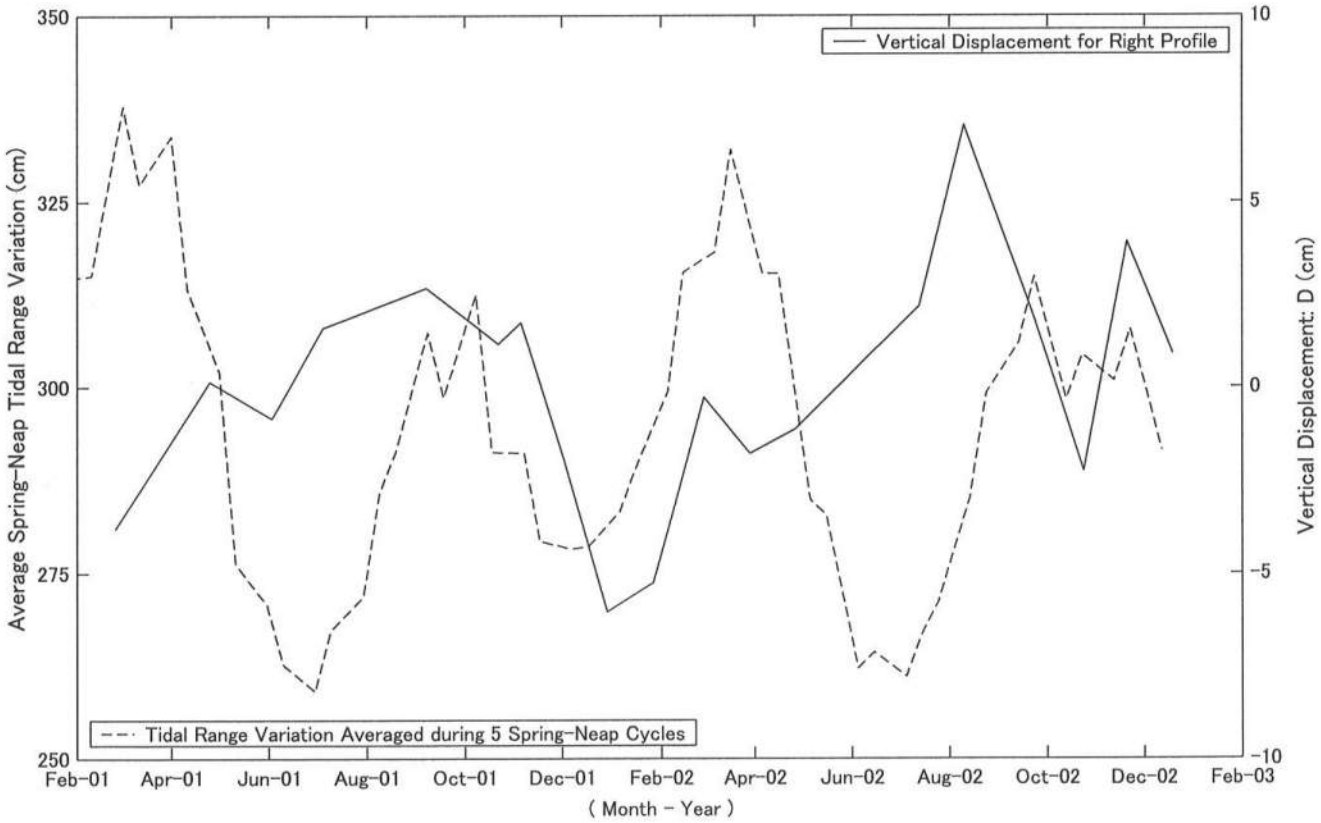

FIG. 37. Time Series of Vertical Displacement and Spring-Neap Tidal Range Variation for Left and Right Profiles

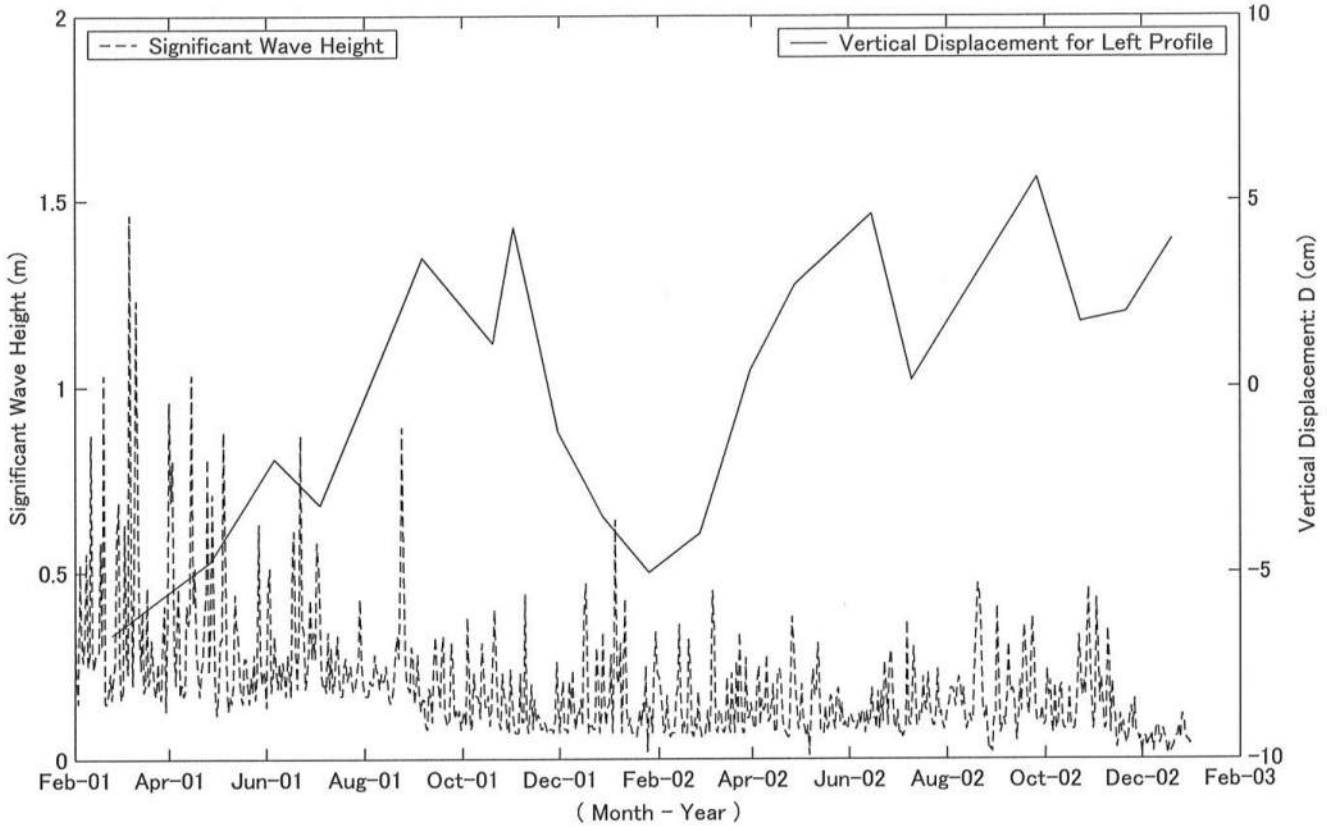

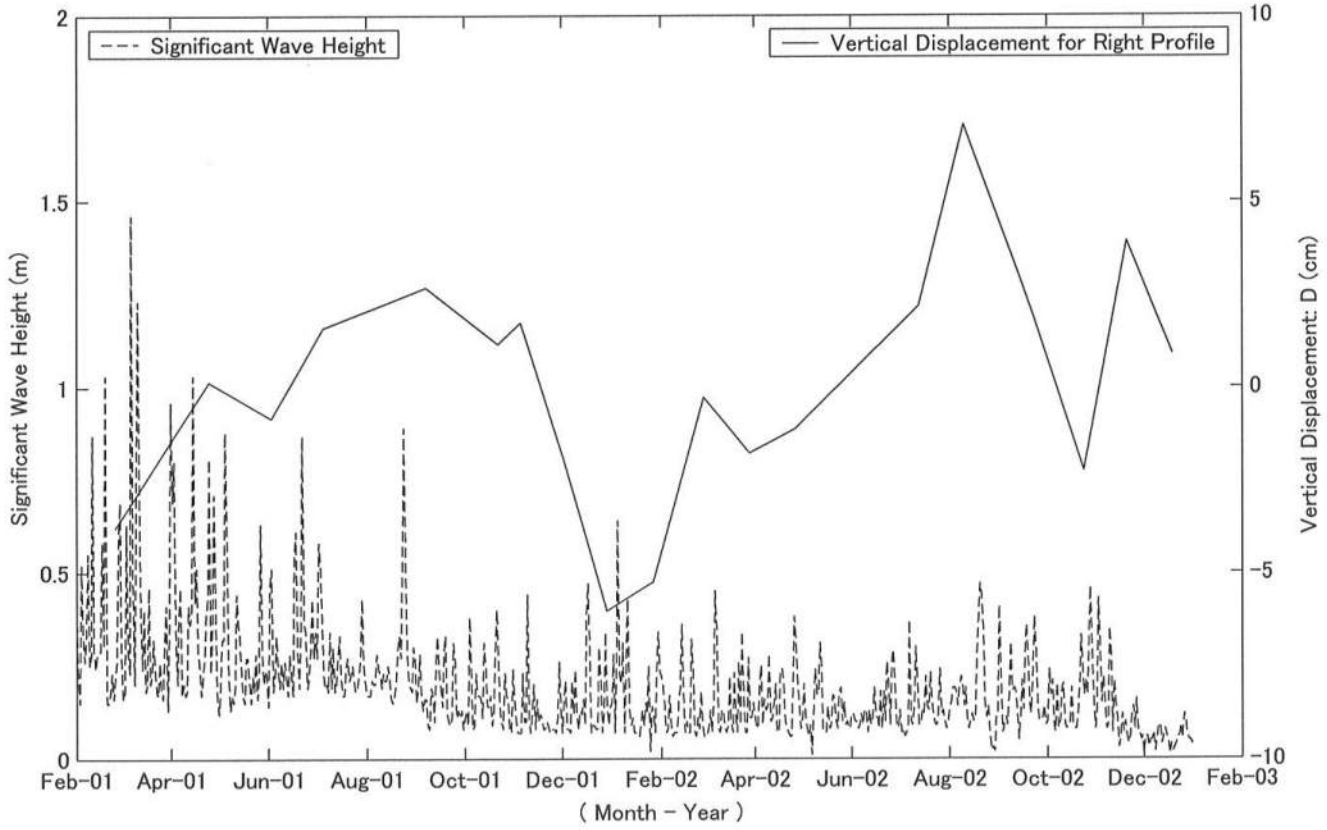

FIG. 38. Time Series of Vertical Displacement and Significant Wave Height for Left and Right Profiles

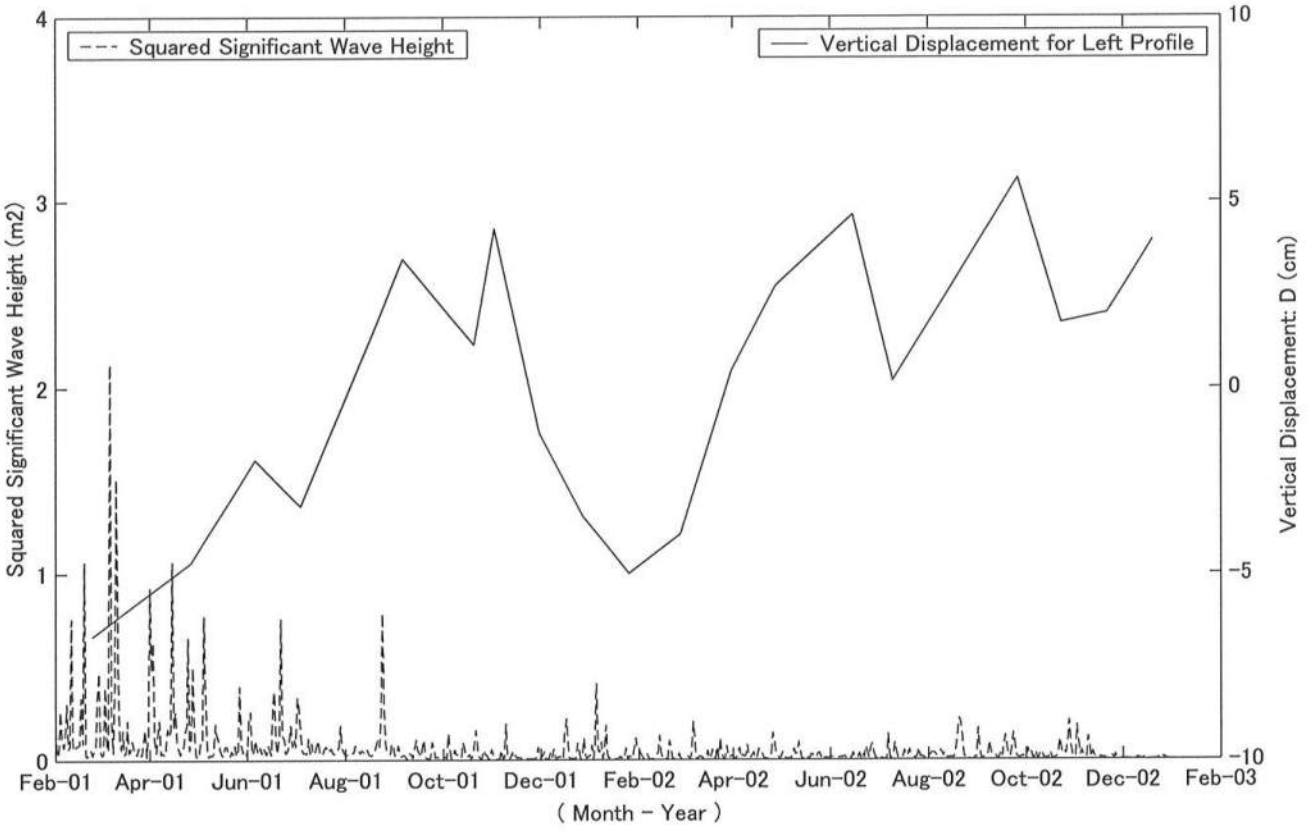

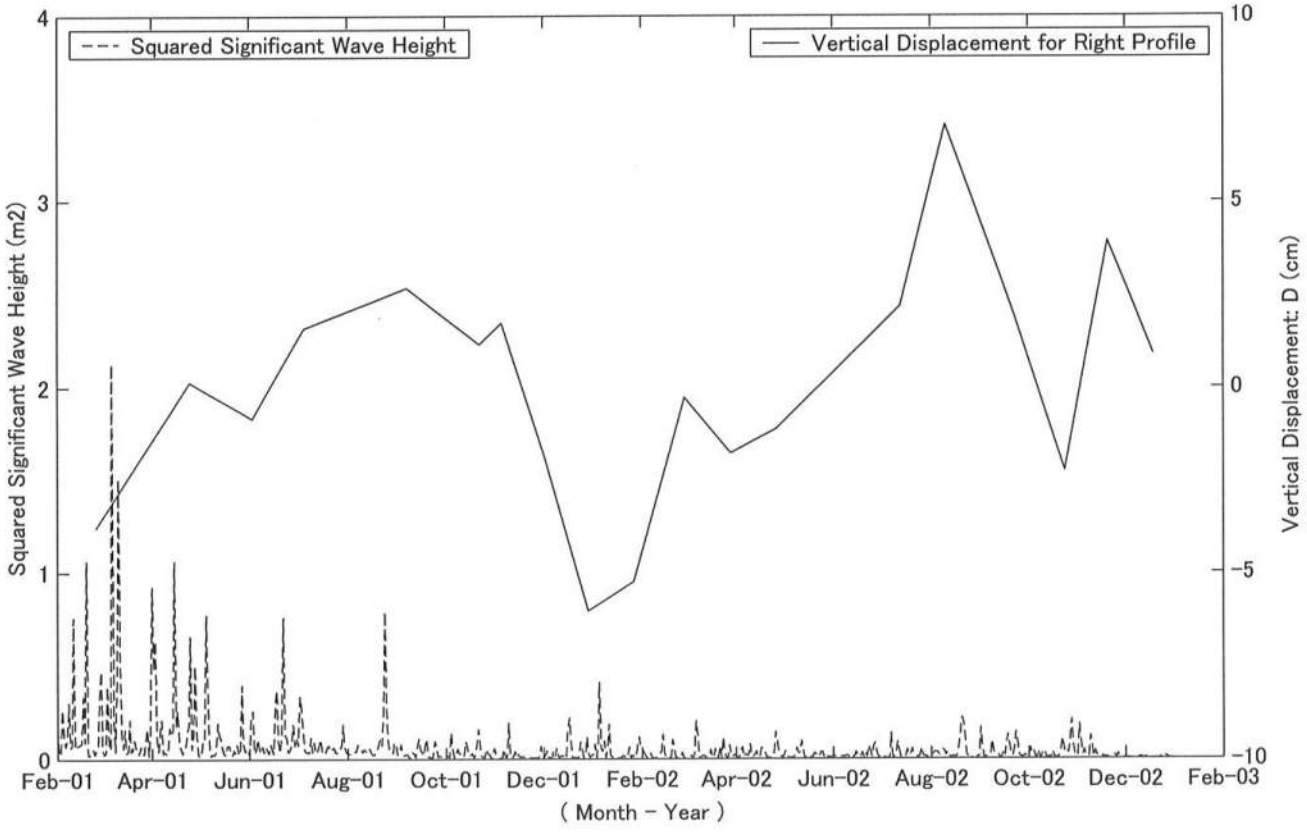

FIG. 39. Time Series of Vertical Displacement and Squared Significant Wave height for Left and Right Profiles

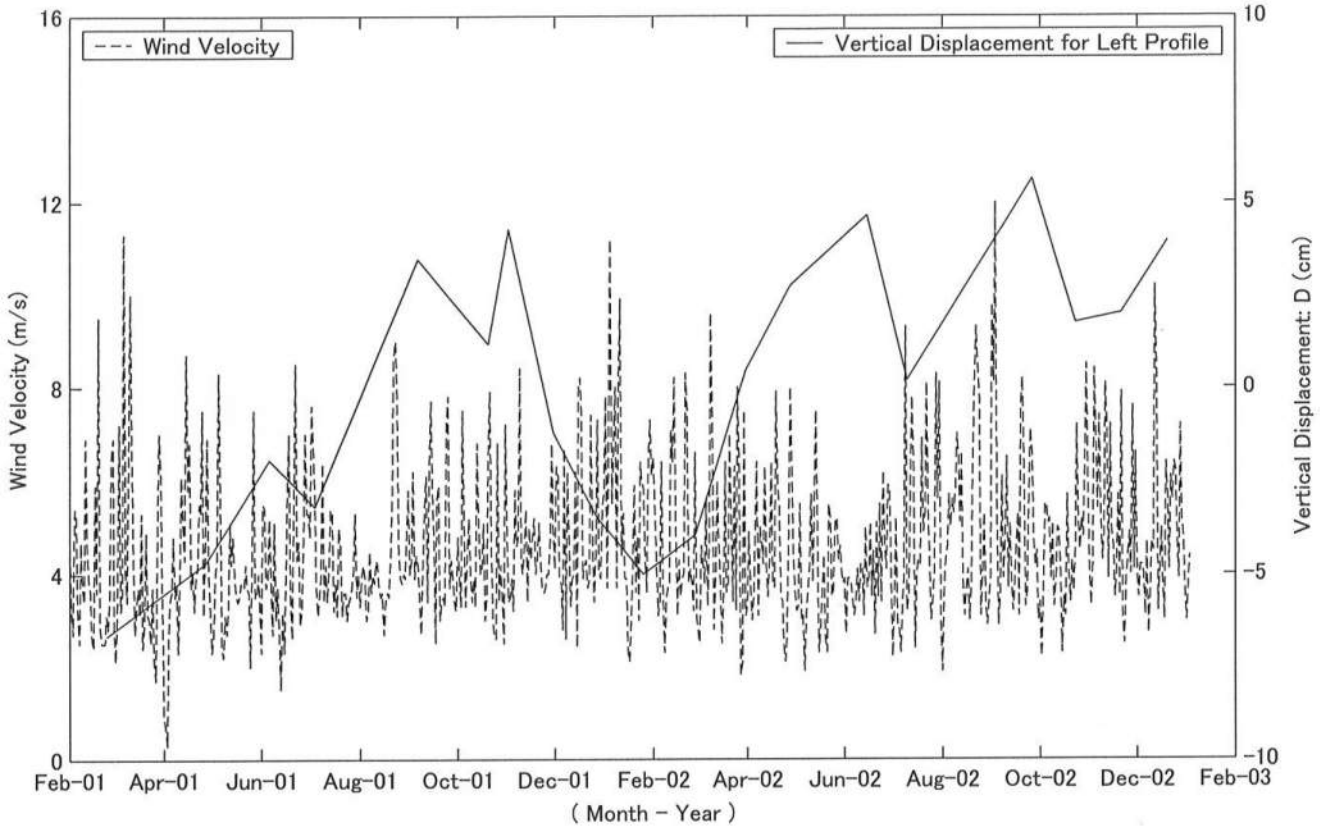

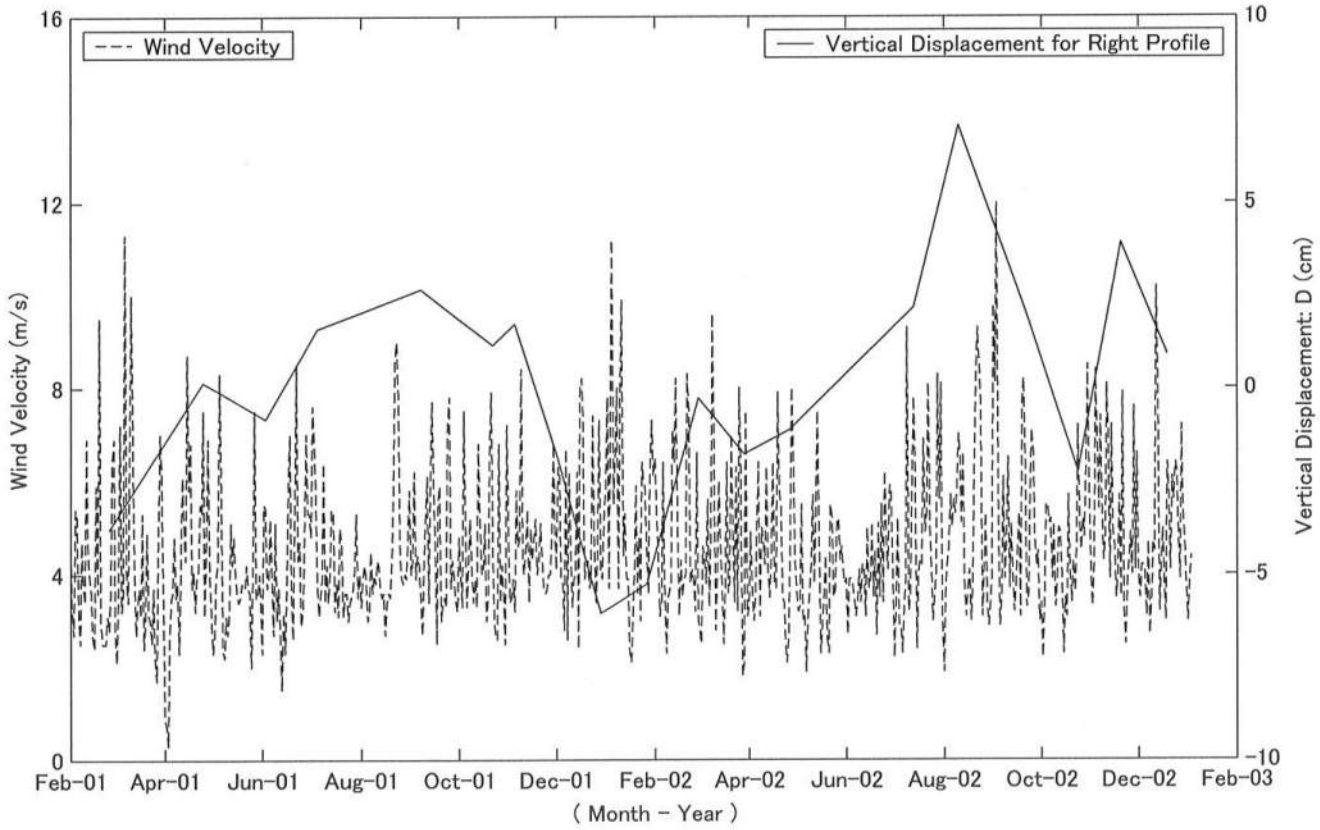

FIG. 40. Time Series of Vertical Displacement and Wind Velocity for Left and Right Profiles

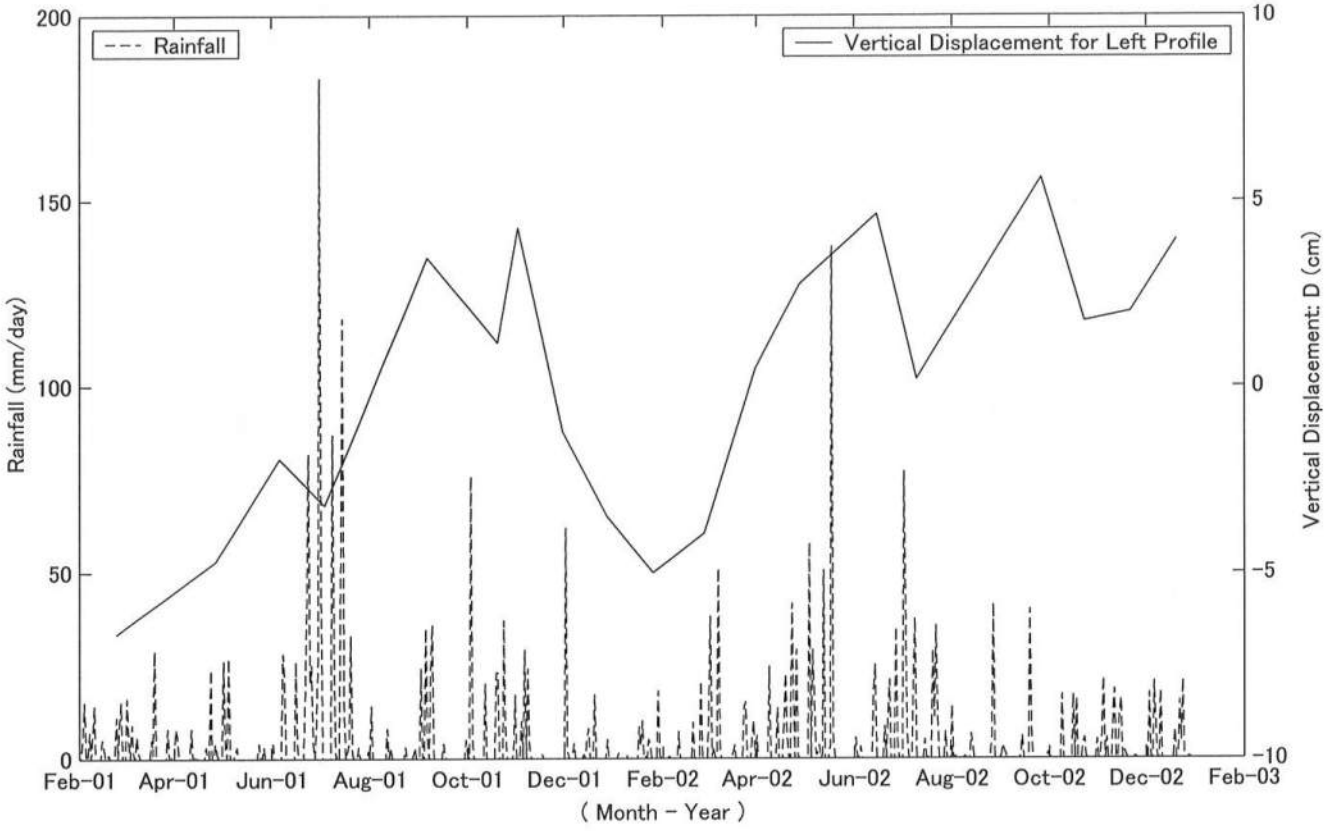

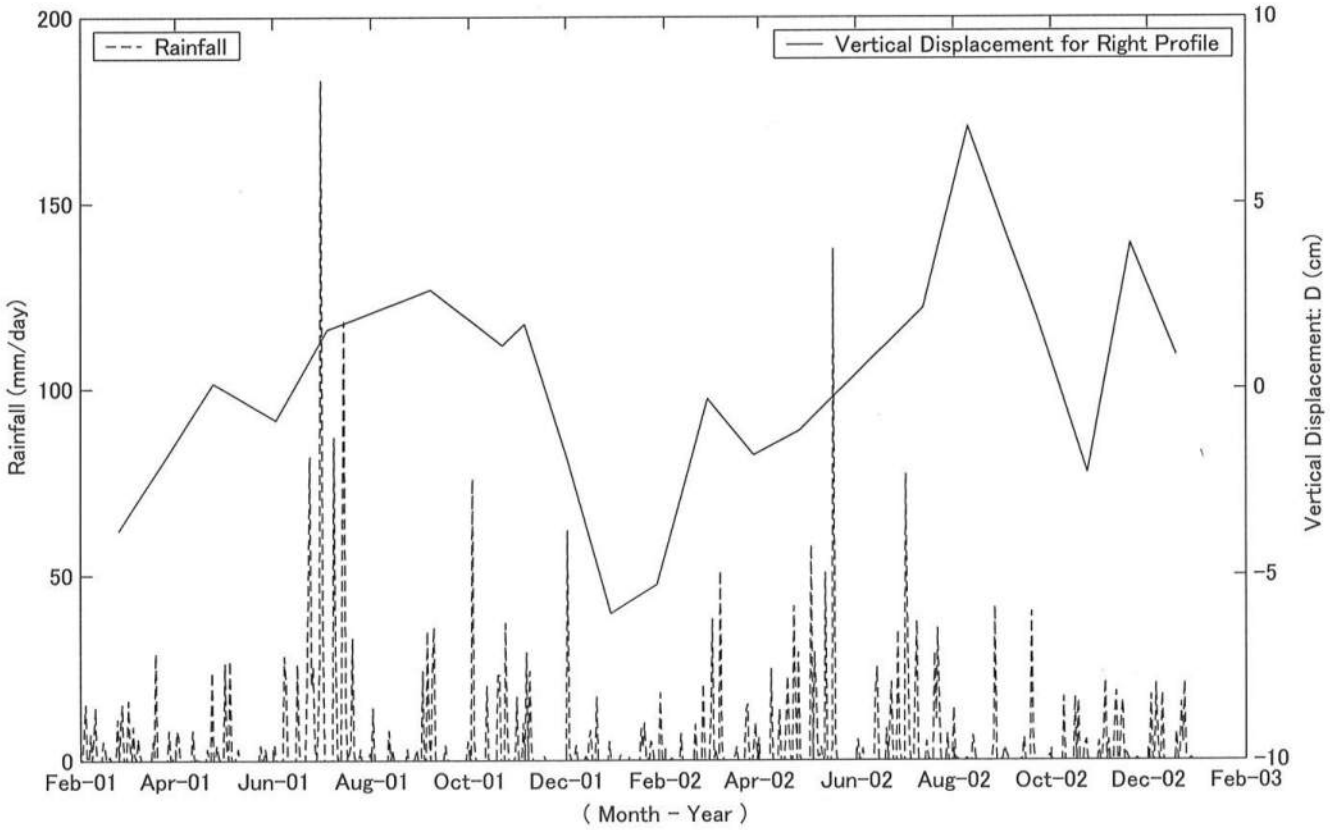

FIG. 41. Time Series of Vertical Displacement and Rainfalll for Left and Right Profiles

Figs. 36 - 41 indicate that a clear correlation exists only between the vertical displacement parameter, $D(t)$, and the 56-day averaged tide level $\eta_{56}(t)$. The linear regression analysis between these time series with no time lag is shown in the top panels of Figs. 42a and 42b for the left and right profiles. The correlation coefficient is 0.701 and 0.753 for the left and right profiles, respectively. The linear relationship is expressed as

$$D(t) = A\left[\eta_{56}(t) - \eta_0\right] \tag{21}$$

where the fitted values of A and η_0 are the listed in Table 17. A is the constant ratio of the vertical bed level increase to the average tide level increase and η_0 is the shift of $\eta_{56}(t)$ such that $D = 0$ at $\eta_{56}(t) = \eta_0$. This shift η_0 turns out to be almost the same as the time averaged value of the 56-day averaged tide level, which was 14.0 cm during the 2-yr survey.

The equilibrium profile concept assumes that the profile adjusts itself to the tide level by the same vertical increment, which requires $A = 1.0$ in Eq. (21). As listed in Table 17, however, the value of A is approximately 0.2 for the left and right profiles. The measured profiles changed much less vertically as the tide level fluctuated, possibly because the rise of the tide level lasted only for several months.

The bottom panels of Figs. 42a and 42b show the measured and predicted vertical displacement parameters where use is made of Eq. (21) with the observed 56-day averaged tide level. The agreement is fairly good in spite of the simplicity of Eq. (21).

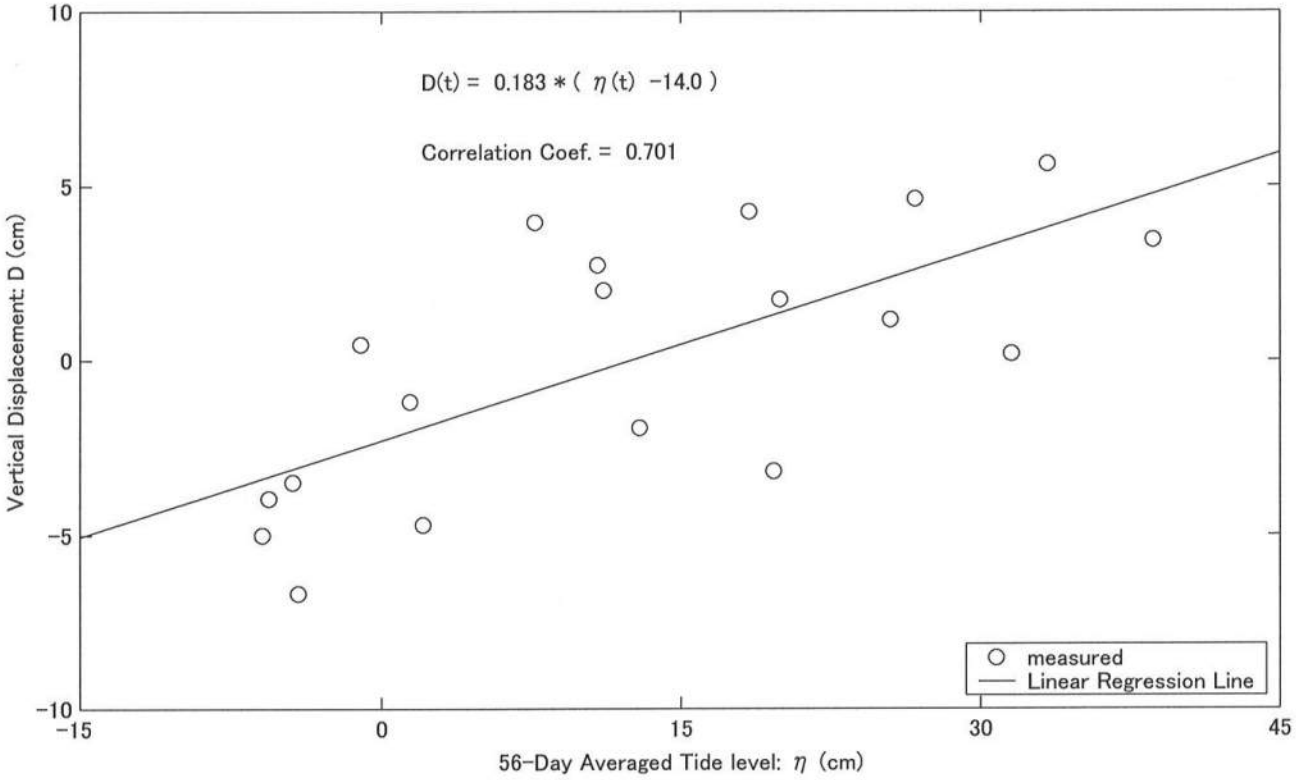

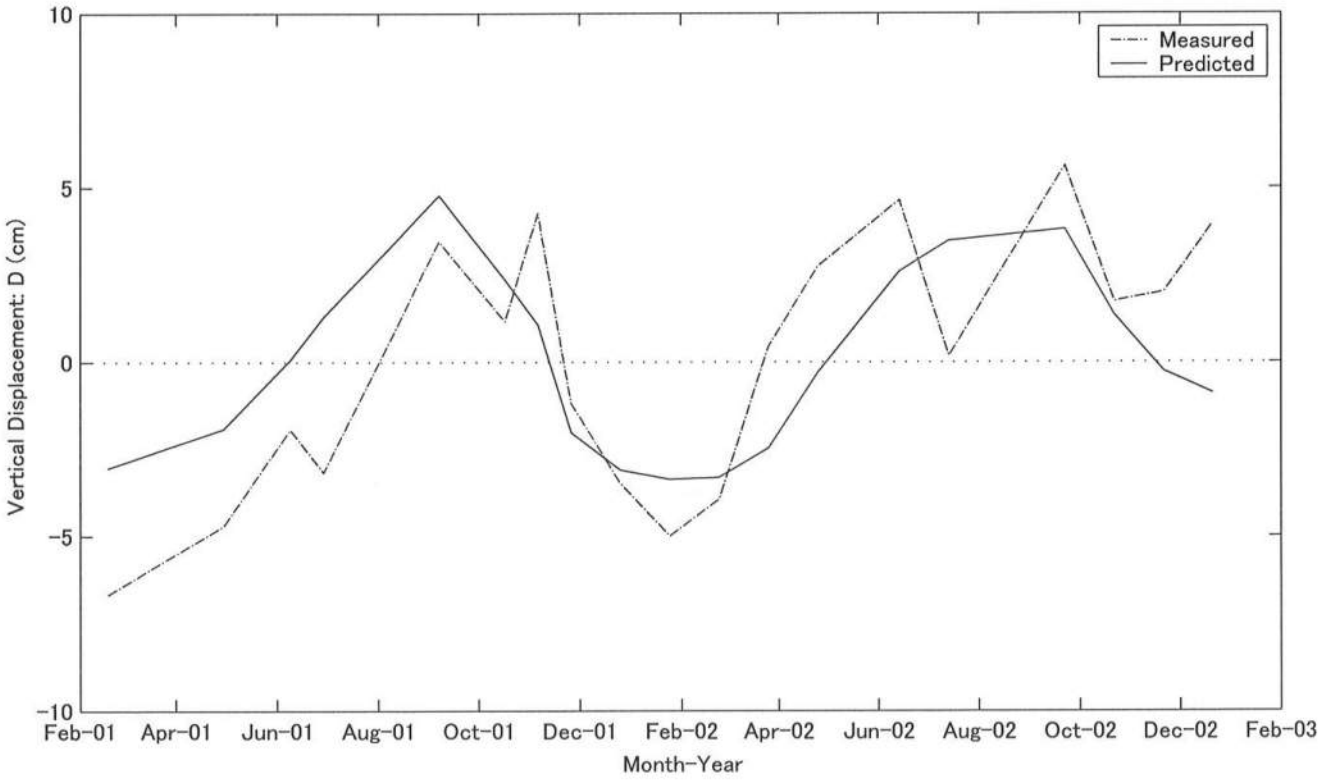

FIG. 42a. Linear Regression Analysis between Vertical Displacement and Average Tide Level for Left Profile

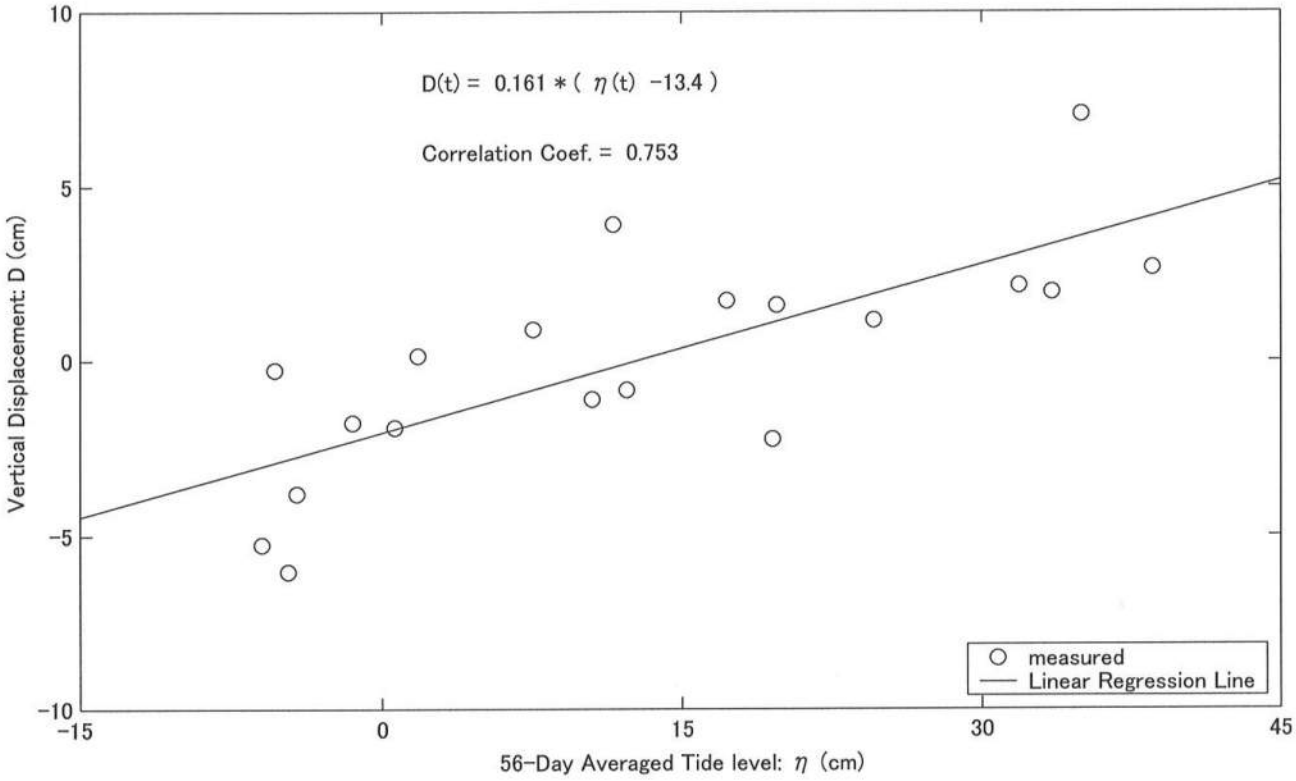

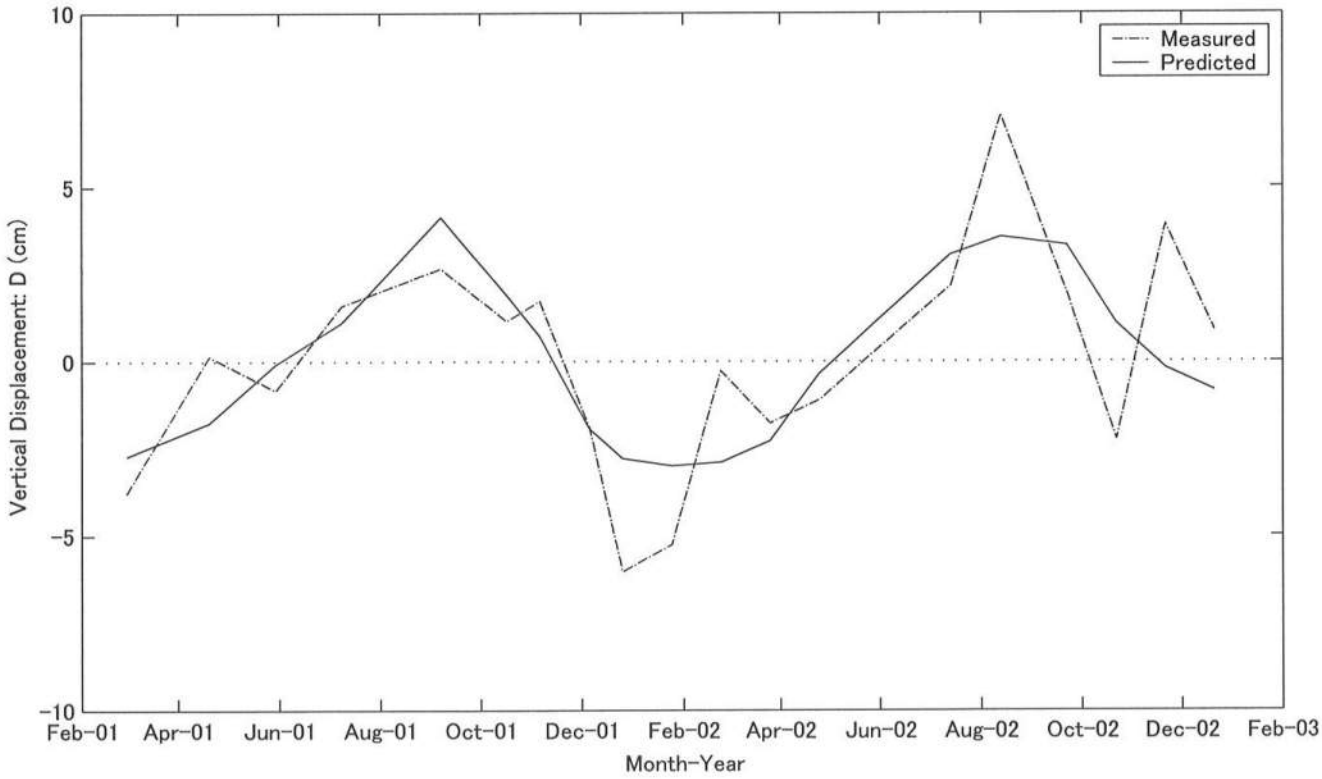

FIG. 42b. Linear Regression Analysis between Vertical Displacement and Average Tide Level for Right Profile

Table 17: Linear Regression Analysis of Time Series between Vertical Displacement $D(t)$ for Left and Right Profiles and 56-Day Averaged Tide Level, $\eta_{56}(t)$, Base on $D(t) = A[\eta_{56}(t) - \eta_0]$ where average value of $\eta_{56}(t)$ is 14.0 cm.

Regression Coefficients	Left Profile	Right Profile
A	0.183	0.161
η_0 (cm)	14.0	13.4
Correlation Coefficient	0.701	0.753

5.2 Mean Slope Parameter

Figs. 43 - 48 show the time series between the mean slope parameter and the driving forces including the 56-day averaged tide level, spring-neap tidal range averaged during 5 spring-neap cycles, significant wave height, squared significant wave height, wind velocity, and rainfall. The top panels of these figures show the results for the left profile during February 2001 to December 2002 and the bottom panels are for the right profile during the same period.

Fig. 43 shows that the time series of the mean slope is correlated negatively with the 56-day averaged tide level. Both time series varied periodically with a one-year period. The mean slope became steeper or gentler as the average tide level rise or fall.

Fig. 44 shows that the correlation between the mean slope and the moving averaged spring-neap tidal range was very low partly because the time series of the mean slope varied annually like the vertical displacement but the averaged spring-neap tidal range varied semiannually.

Figs. 45 and 46 show that there was no obvious correlation between the mean slope and wind waves. The effects of wind waves on the mean slope may be important on a time scale shorter than the monthly profile data used here.

Fig. 47 shows that the correlation between the mean slope and wind velocity was very low like the vertical displacement.

Fig. 48 shows that both time series of the mean slope and the rainfall varied annually and might be correlated somewhat. However, an approximately two-month time lag existed between the peaks of the two time series. The mean slope tends to become gentle during August to October after the heavy rainfall during June to July.

Figs. 43 - 48 indicate that a clear negative correlation exists between the mean slope parameter, $S(t)$, and the 56-day averaged tide level $\eta_{56}(t)$. The linear regression analysis between these time series with no time lag is shown in the top panels of Figs. 49a and 49b for the left and right profiles. The linear relationship is expressed as

$$S(t) = -\frac{\eta_{56}(t)}{L_c} + S_0 \tag{22}$$

where the fitted values of L_c and S_0 are listed in Table 18. The horizontal distance L_c (m) is the representative cross-shore distance for the slope change caused by η_{56} (m), which is approximately twice larger than the cross-shore survey line above the low water level. The slope S_0 (dimensionless) in Eq. (22) is the shift of $S(t)$ such that $S = S_0$ at $\eta_{56} = 0$ and turns out to be almost the same as the average value of the mean slope as shown in Table 18.

The bottom panels of Figs. 49a and 49b show the measured and predicted mean slope parameter where use is made of Eq. (22) with the observed 56-day averaged tide level. The predicted time series is in fairly good agreement with the measured time series.

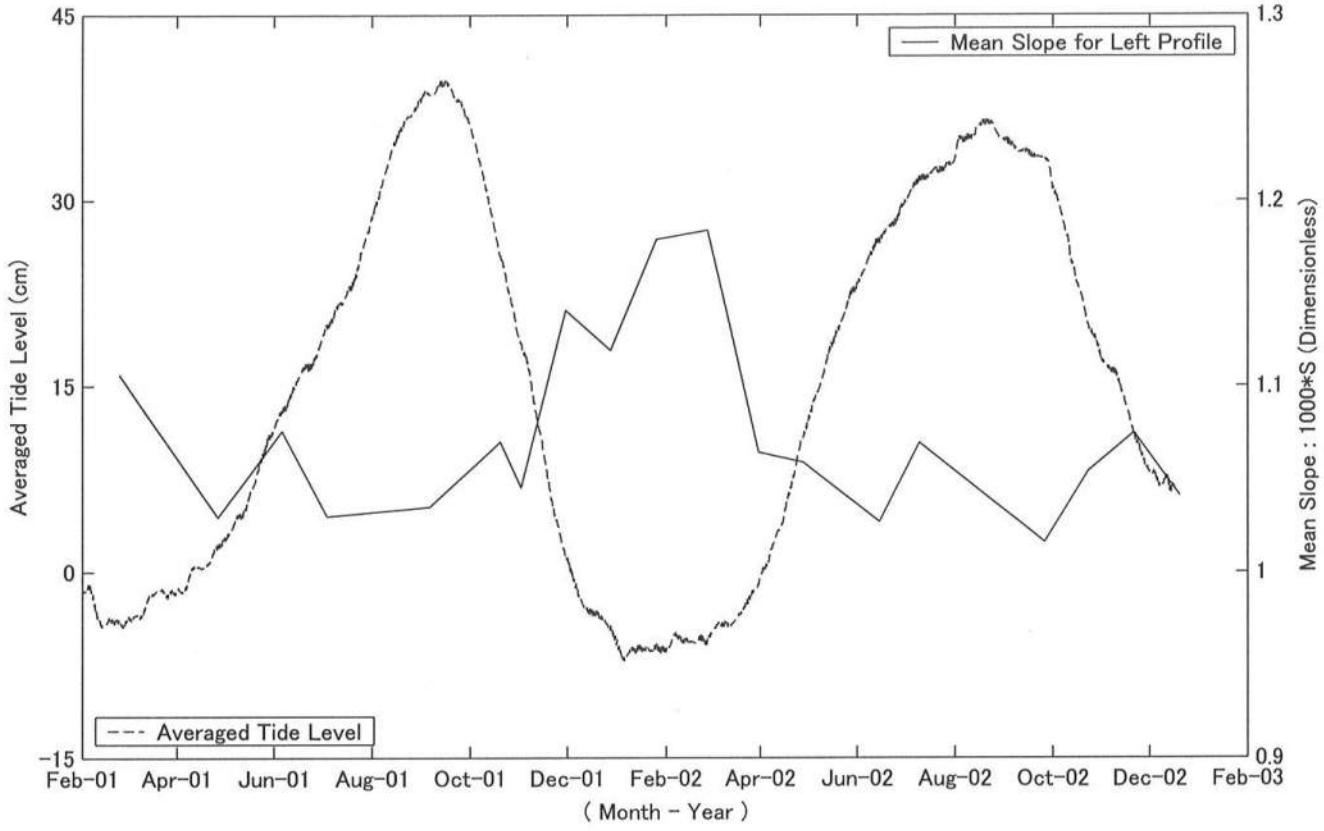

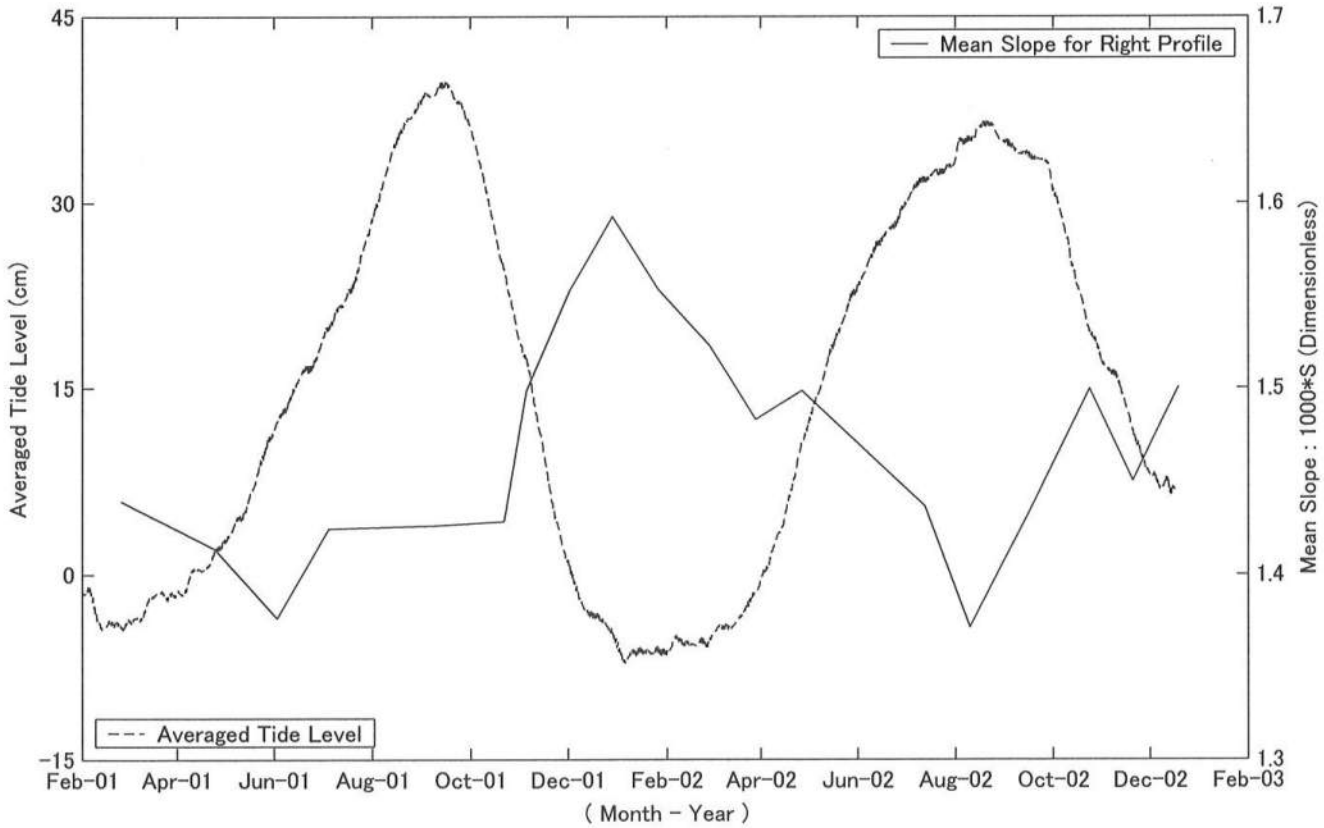

FIG. 43. Time Series of Mean Slope and Average Tide Level for Left and Right Profiles

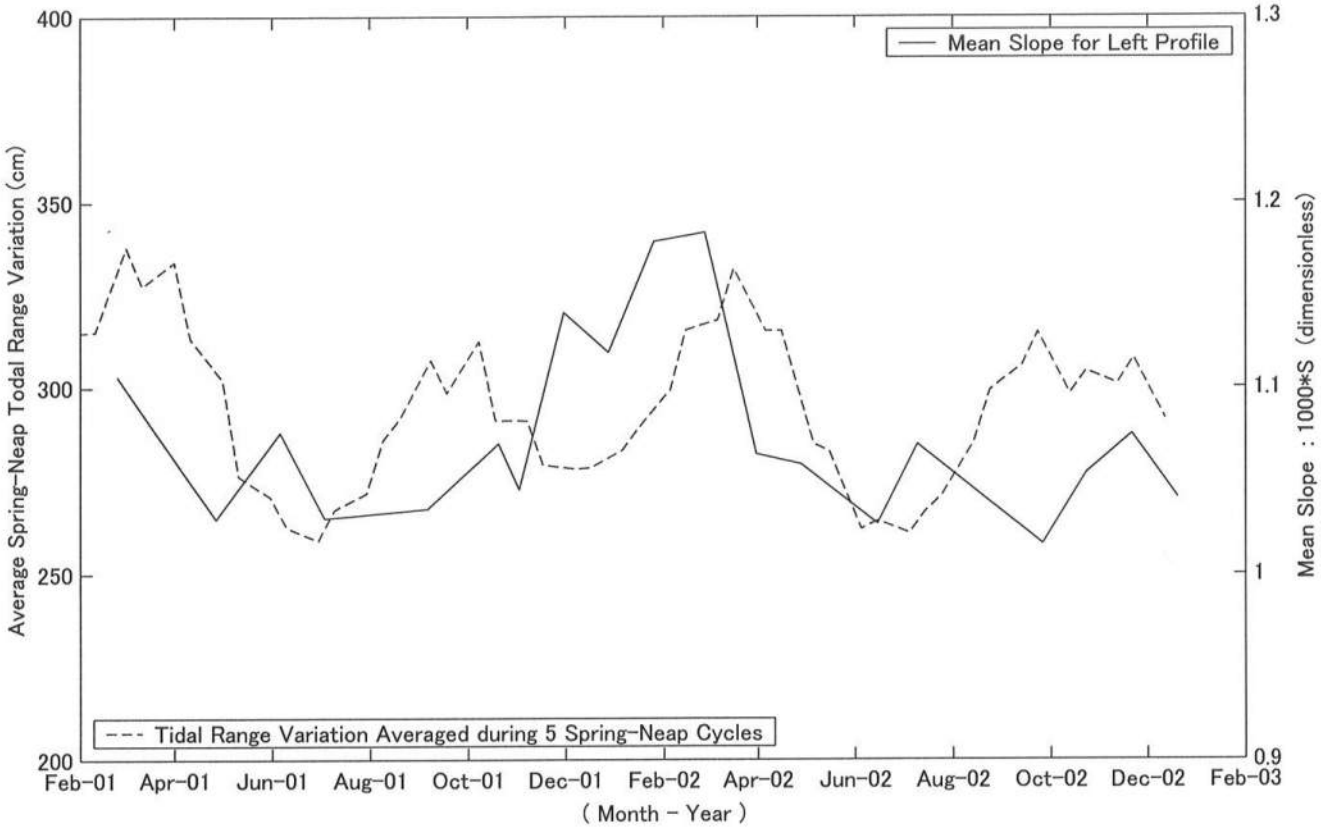

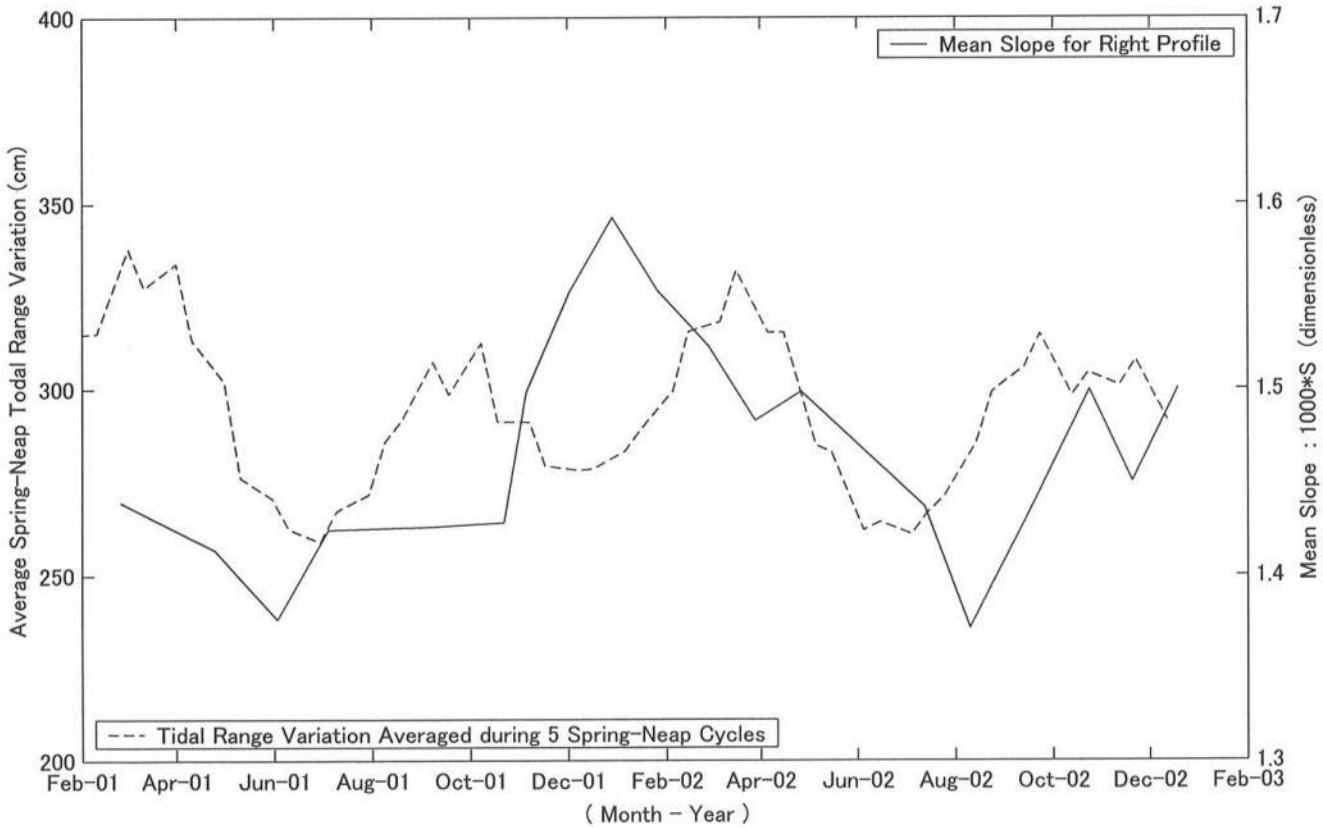

FIG. 44. Time Series of Mean Slope and Spring-Neap Todal Range Variation for Left and Right Profiles

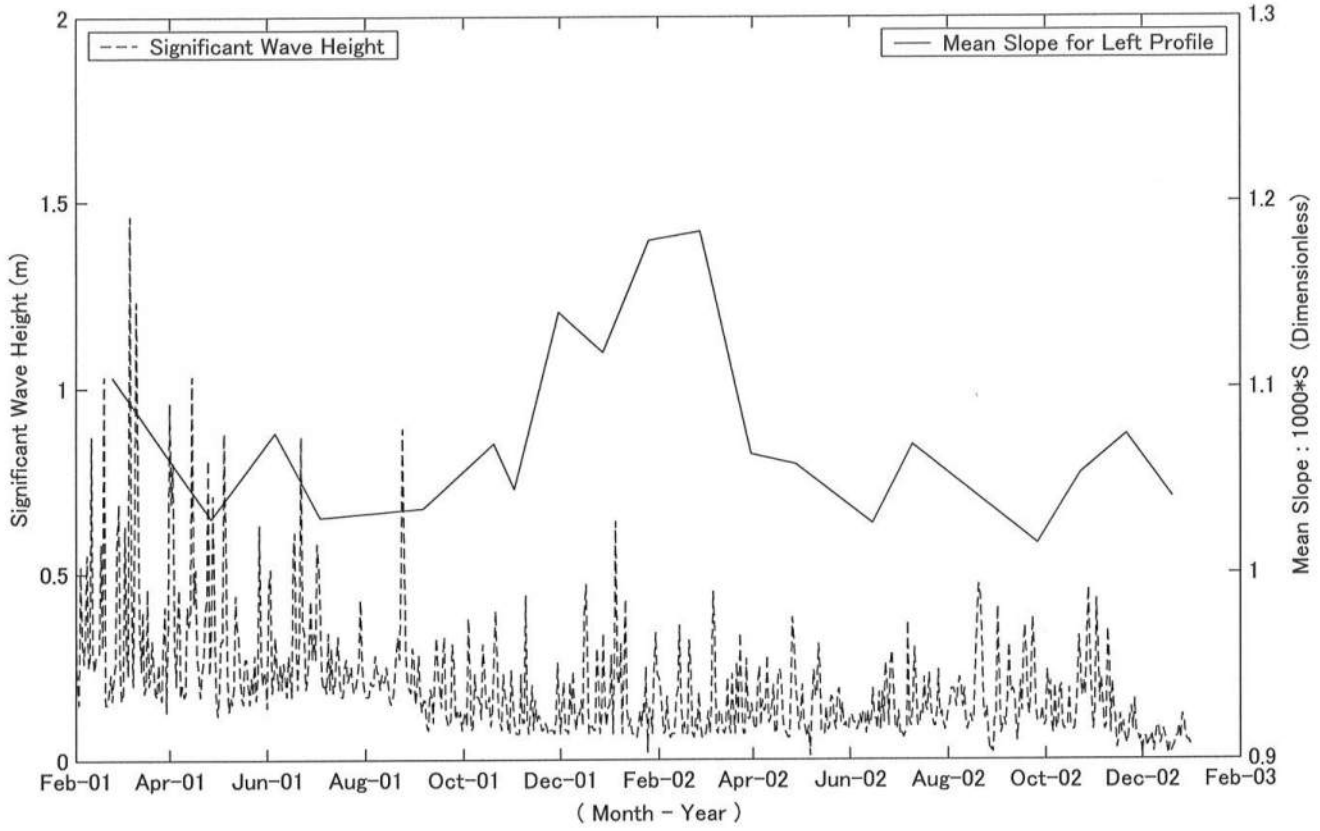

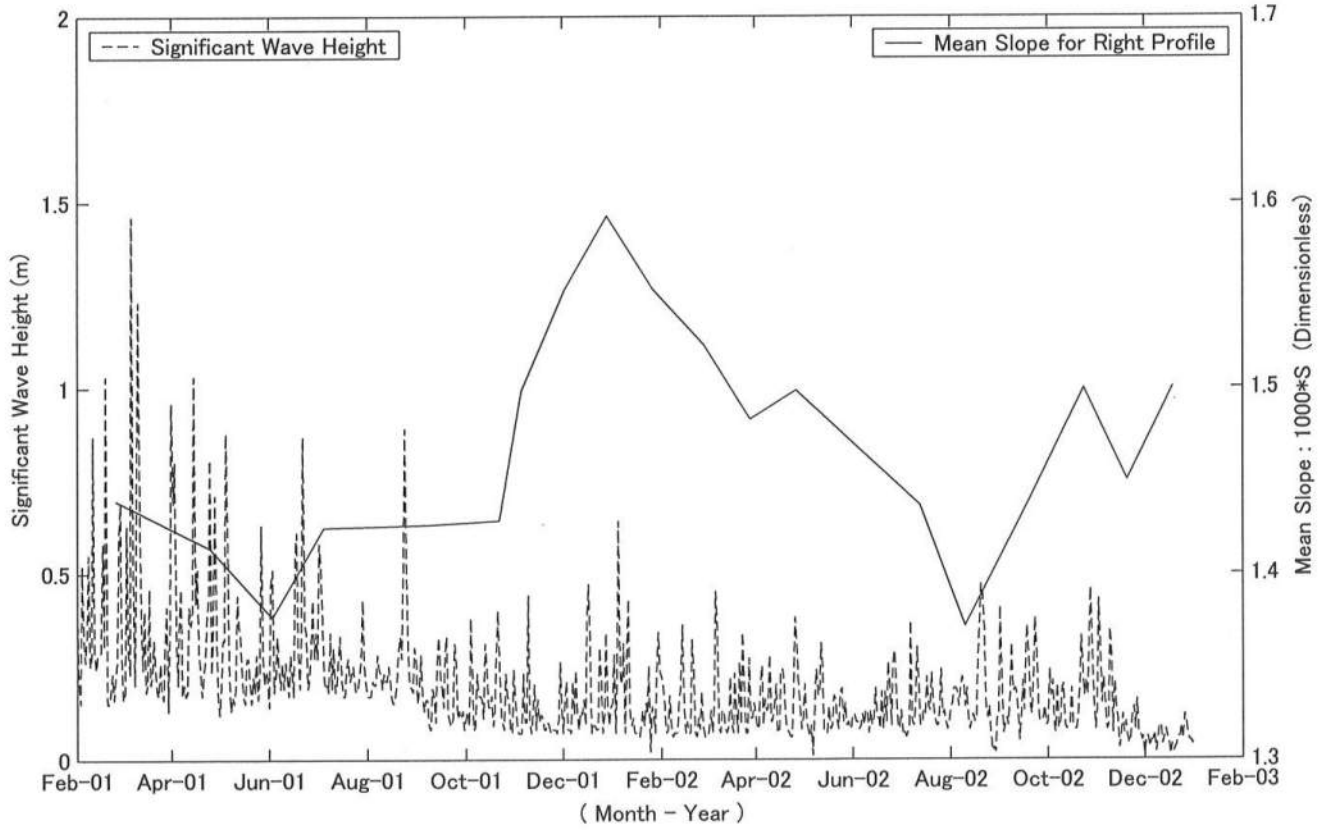

FIG. 45. Time Series of Mean Slope and Significant Wave Height for Left and Right Profiles

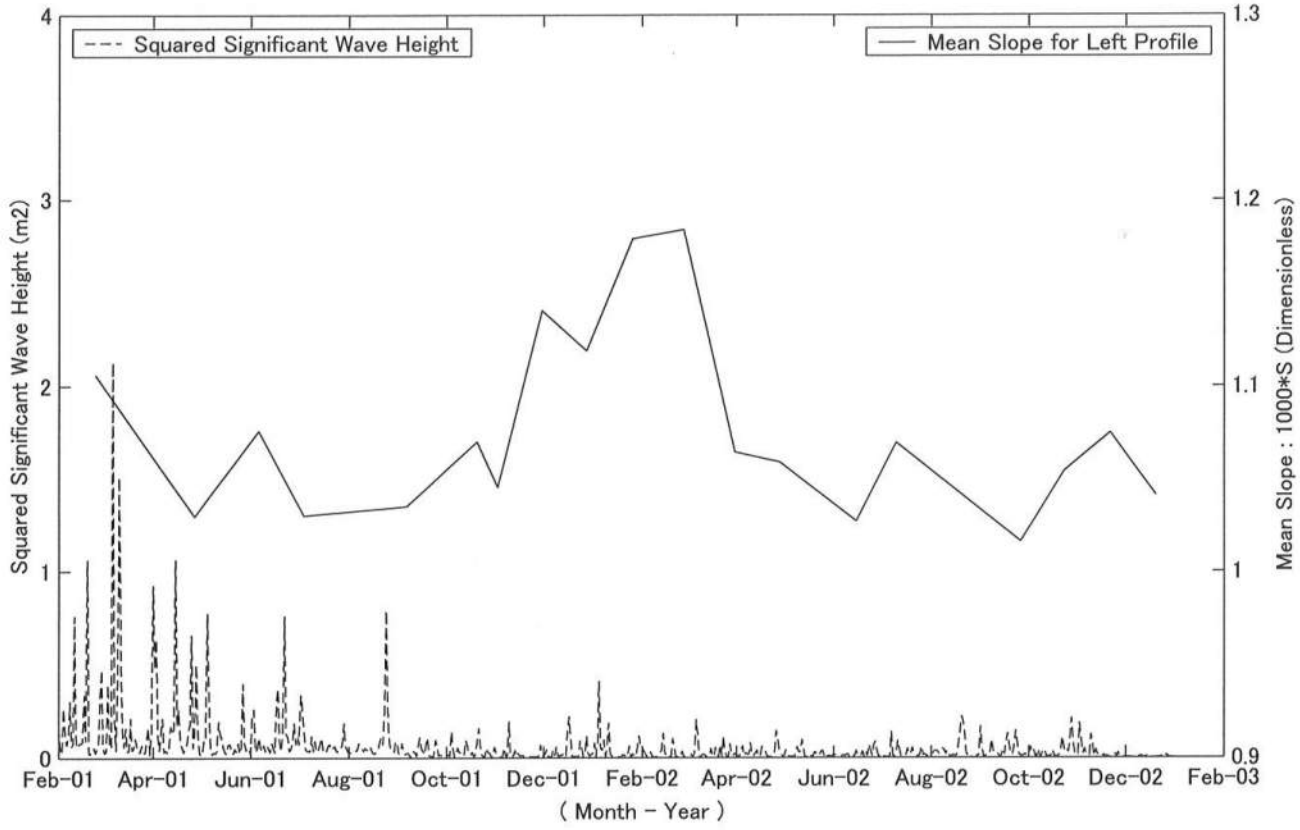

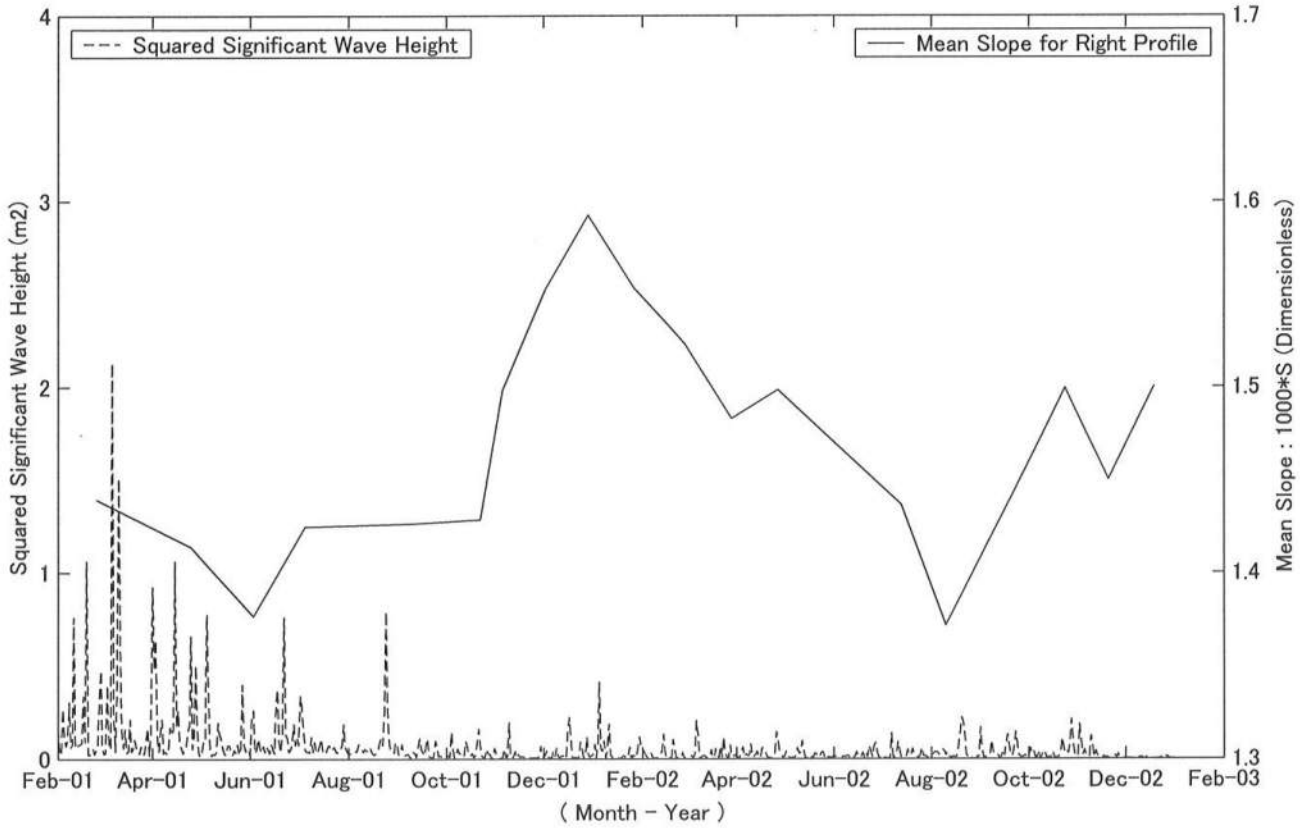

FIG. 46. Time Series of Mean Slope and Squared Significant Wave Height for Left and Right Profiles

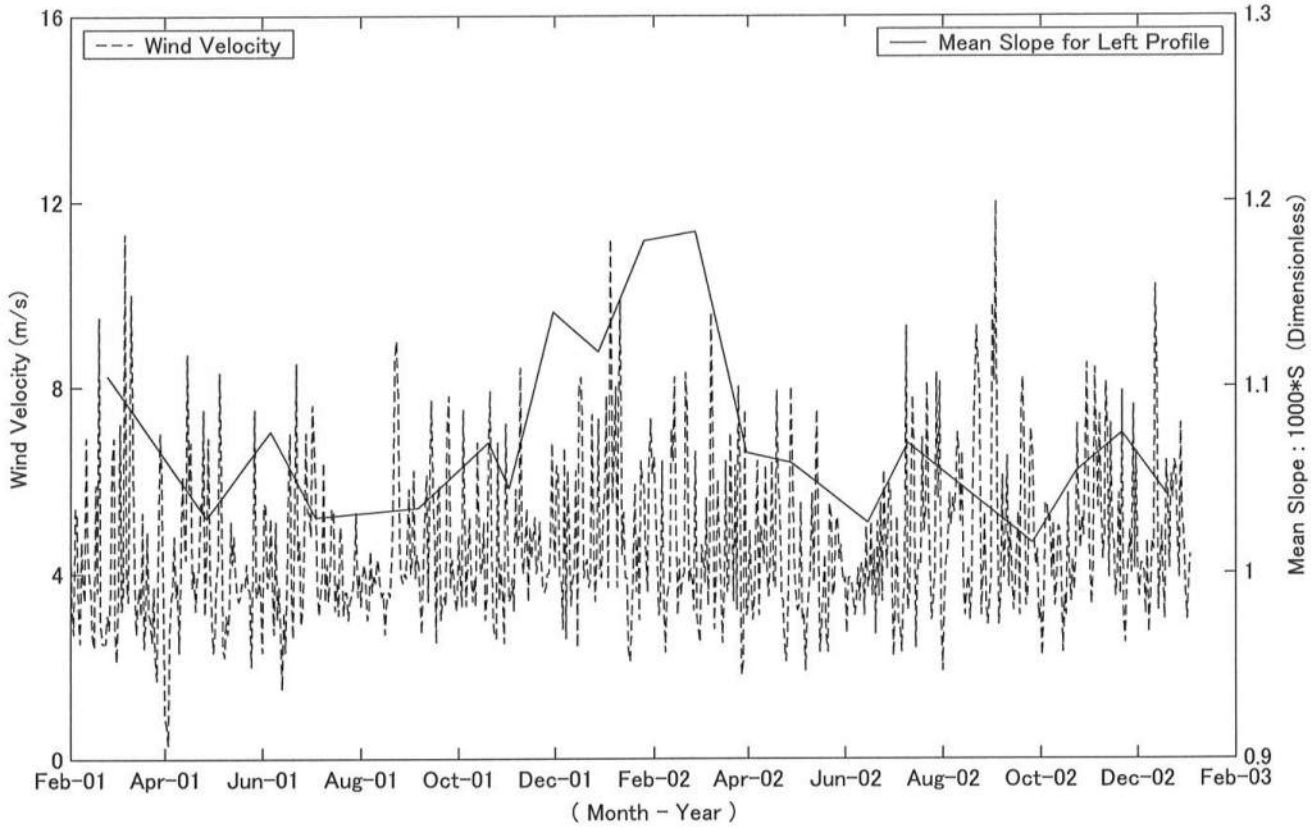

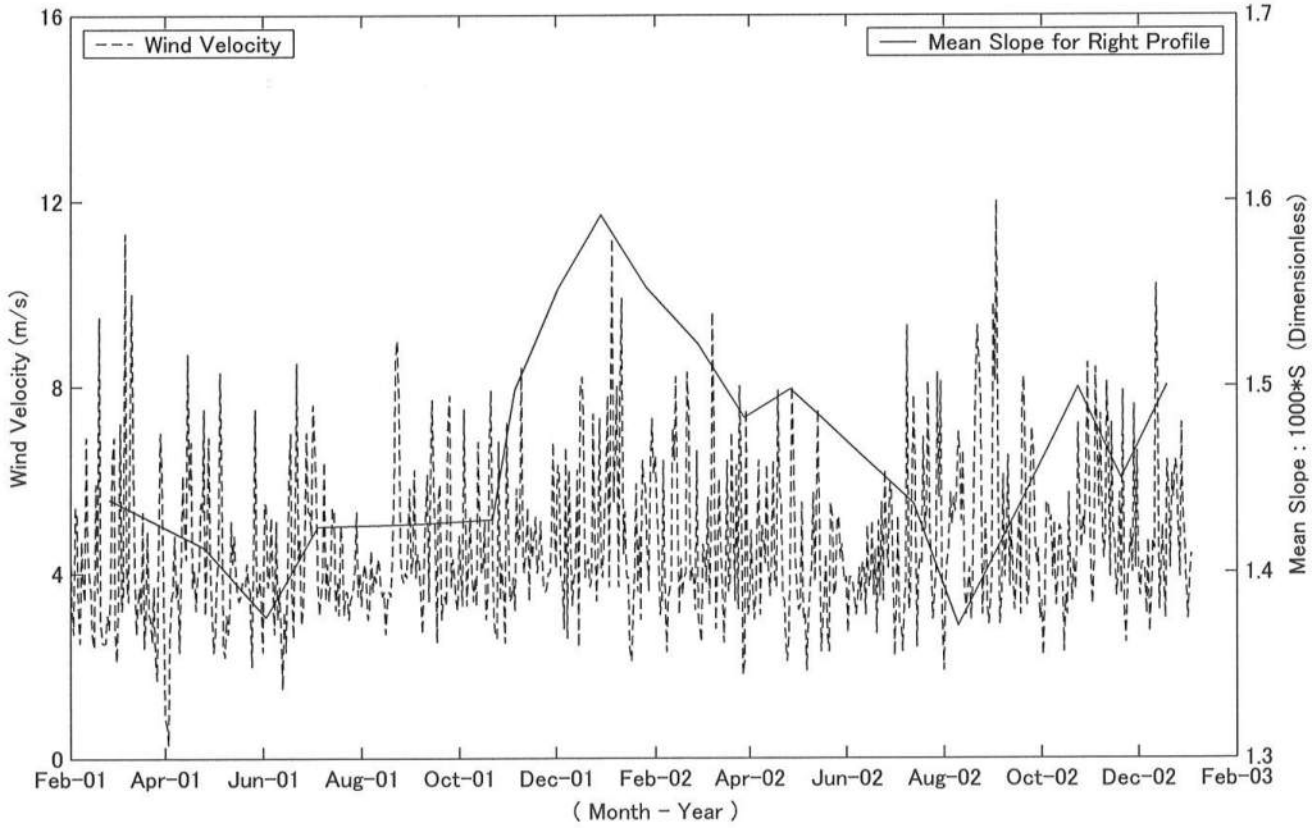

FIG. 47. Time Series of Mean Slope and Wind Velocity for Left and Right Profiles

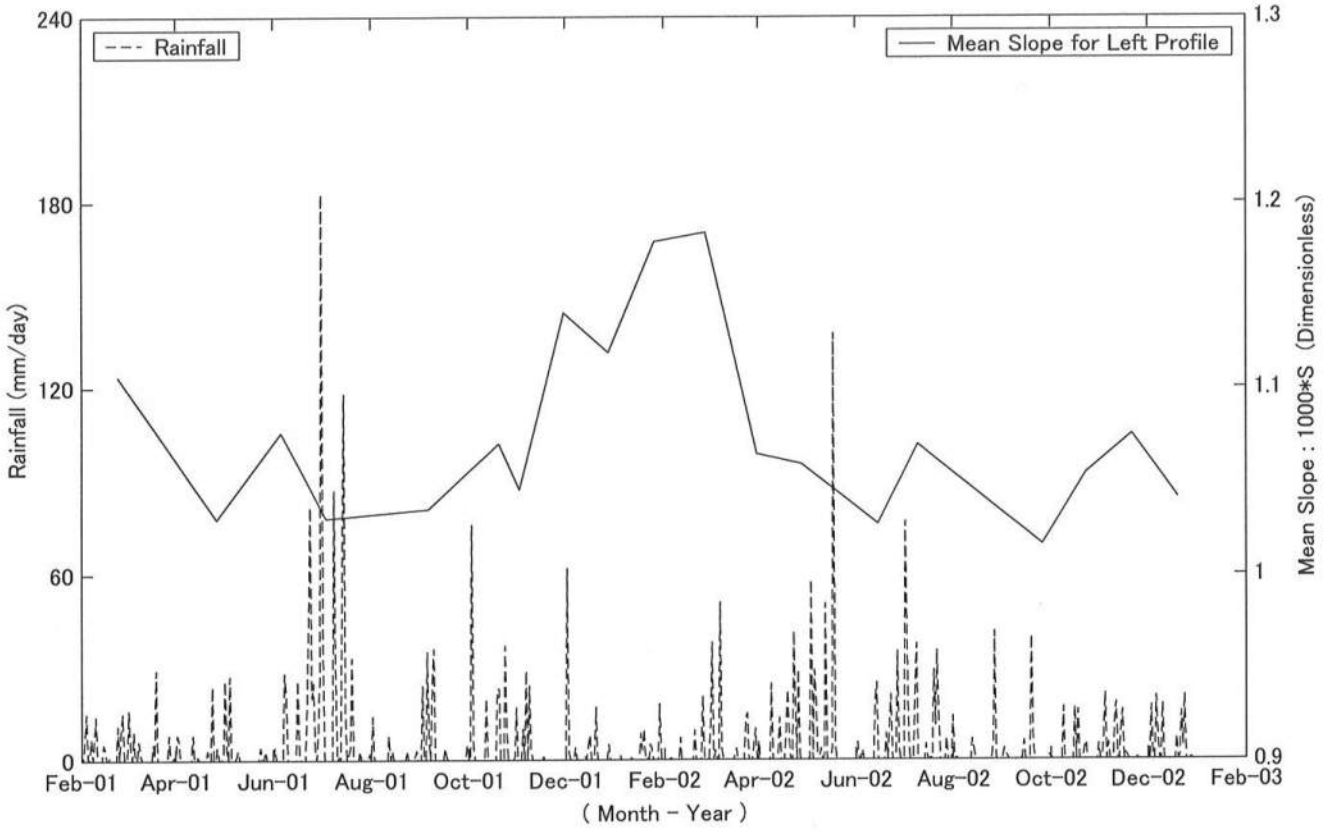

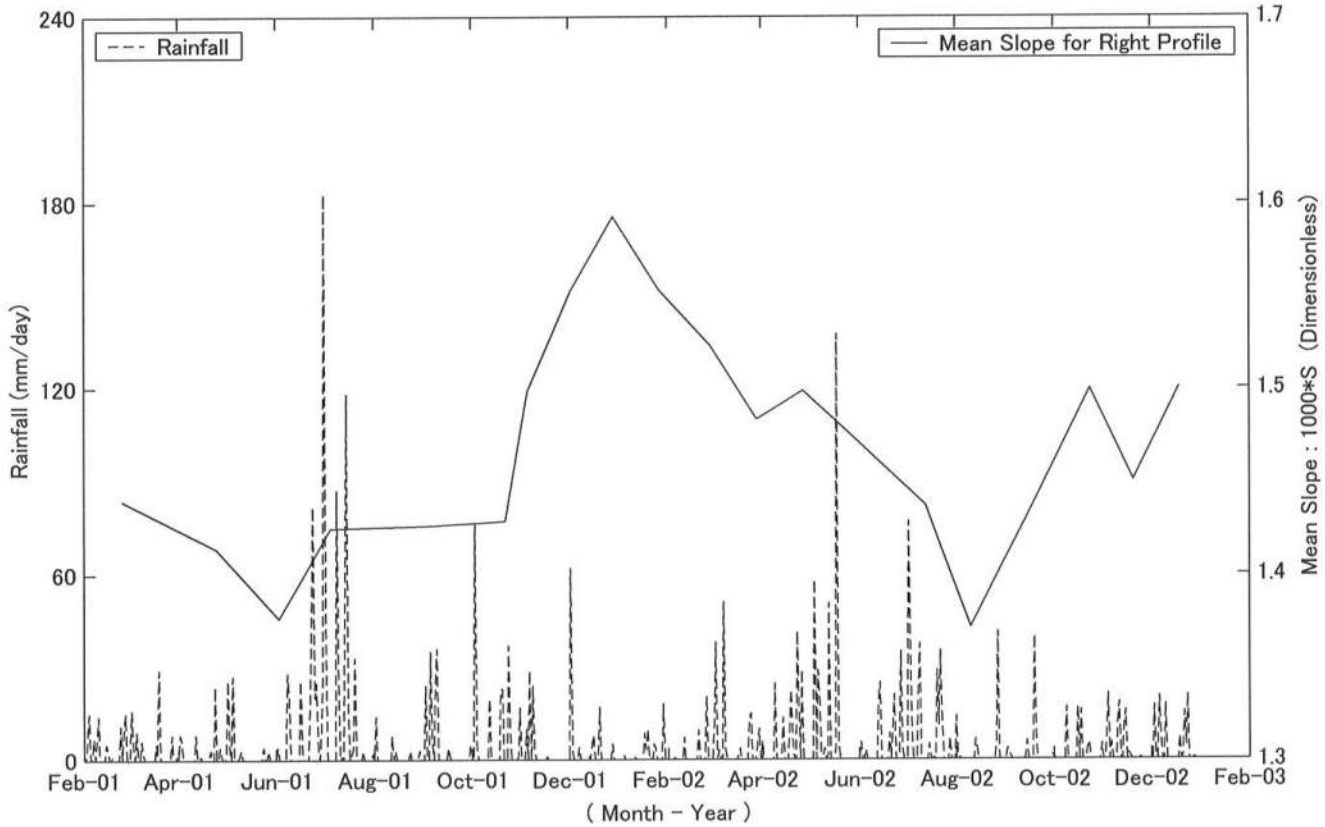

FIG. 48. Time Series of Mean Slope and Rainfall for Left and Right Profiles

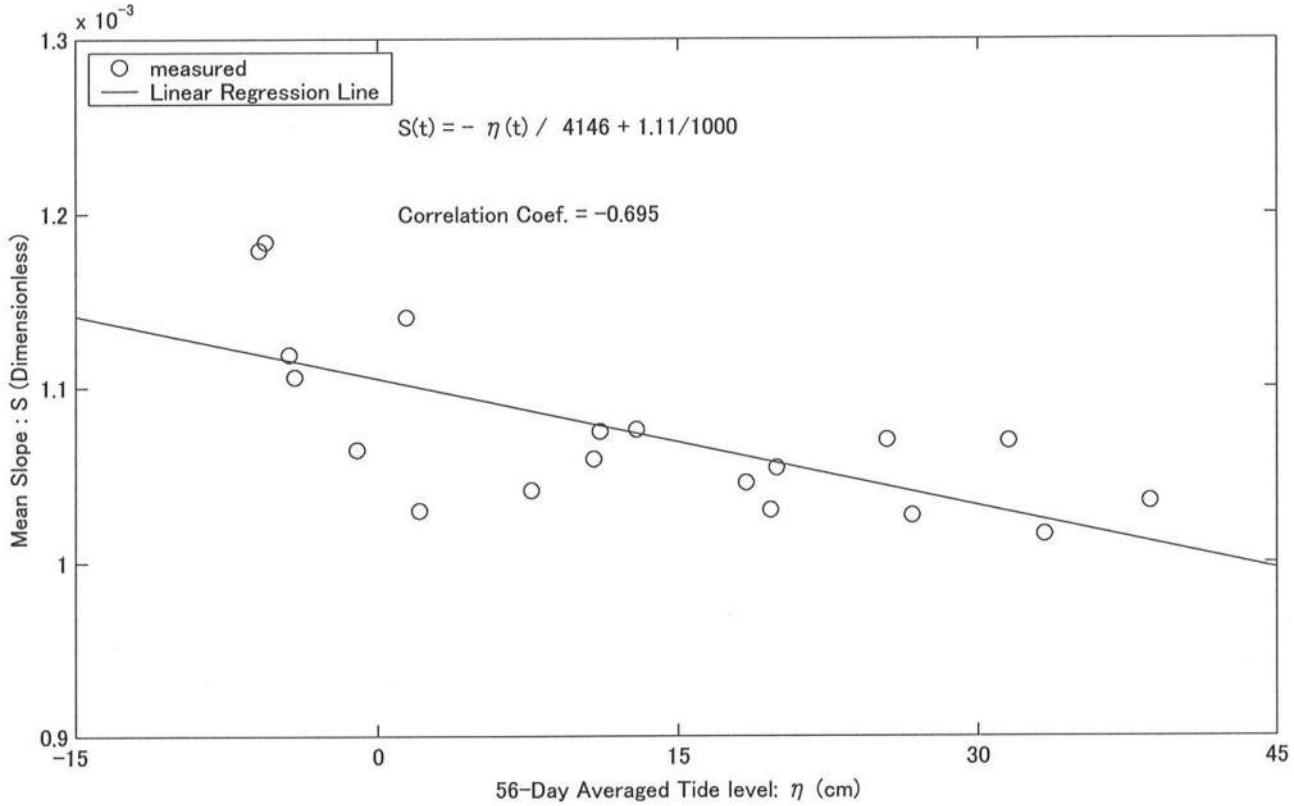

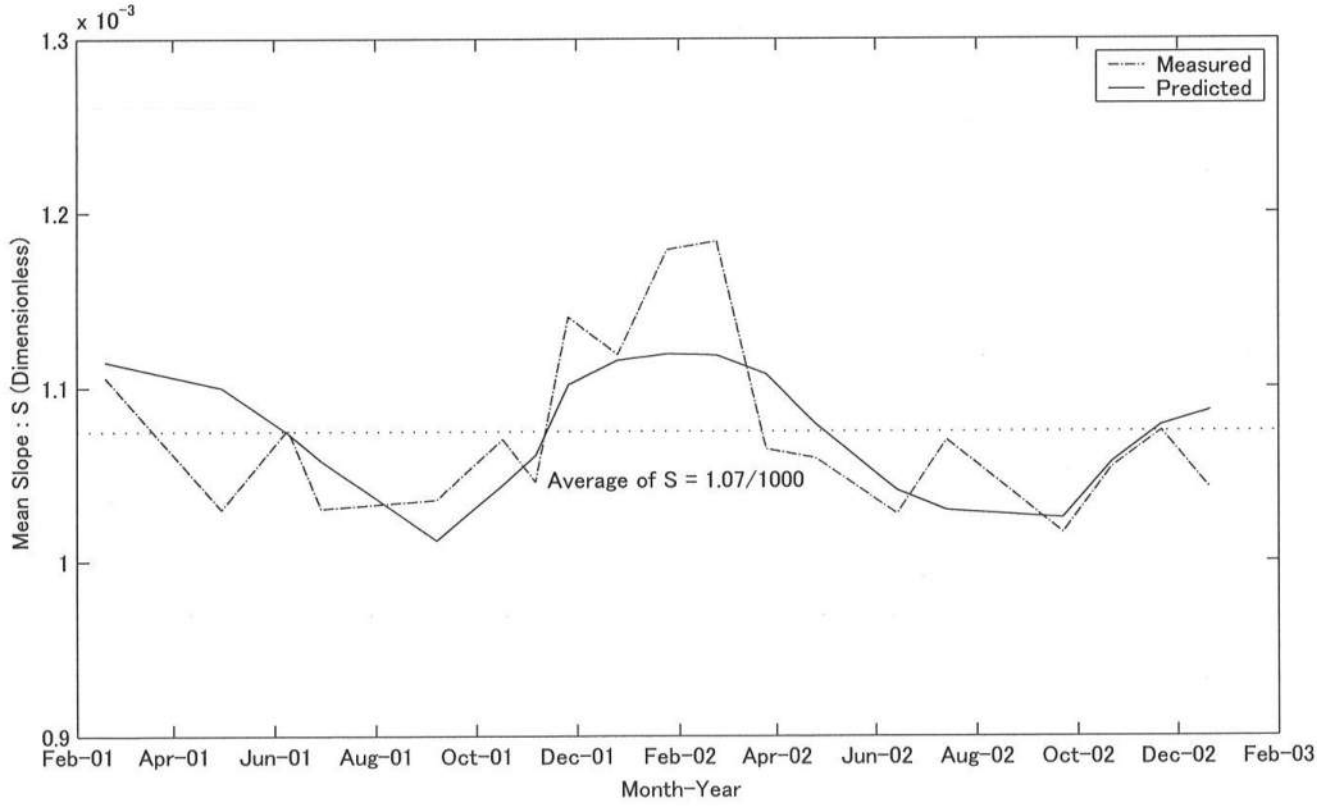

FIG. 49a. Measured and Predicted Mean Slope Parameters for the Left Profile

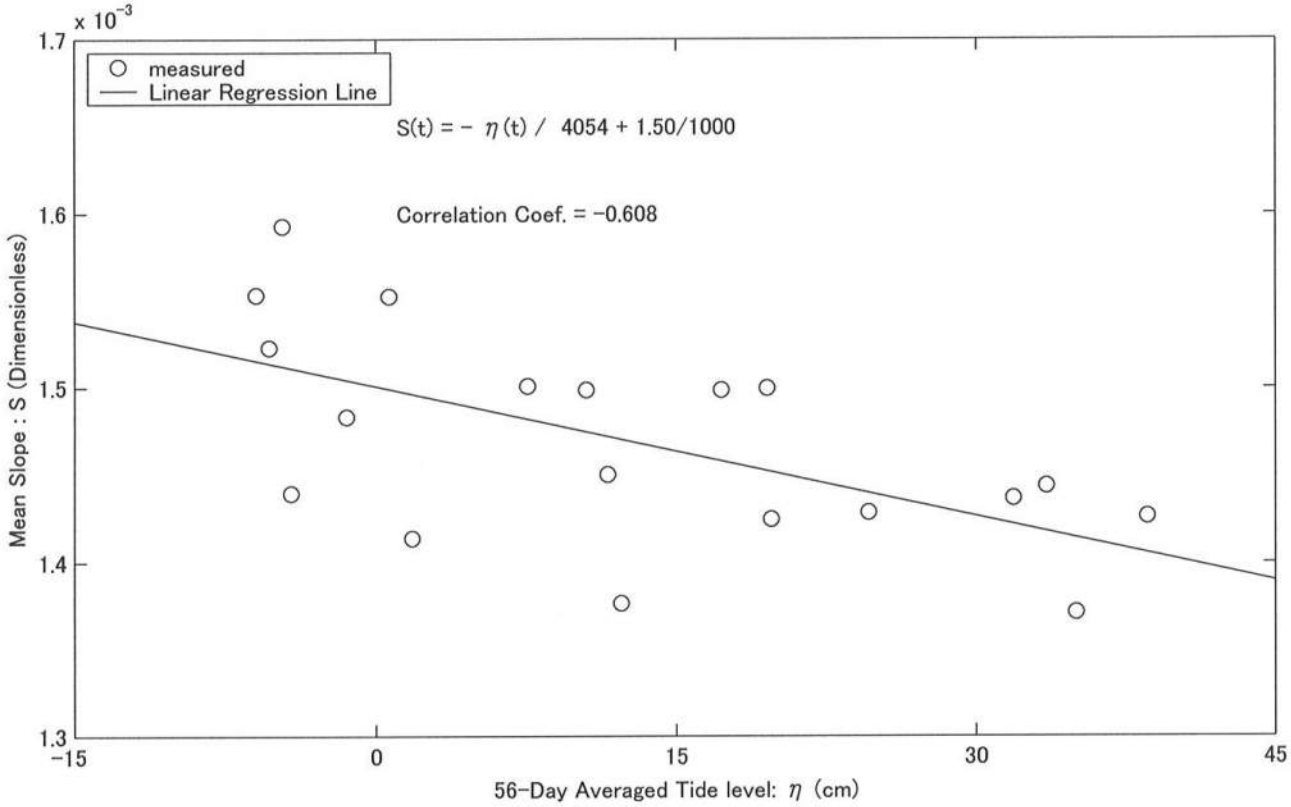

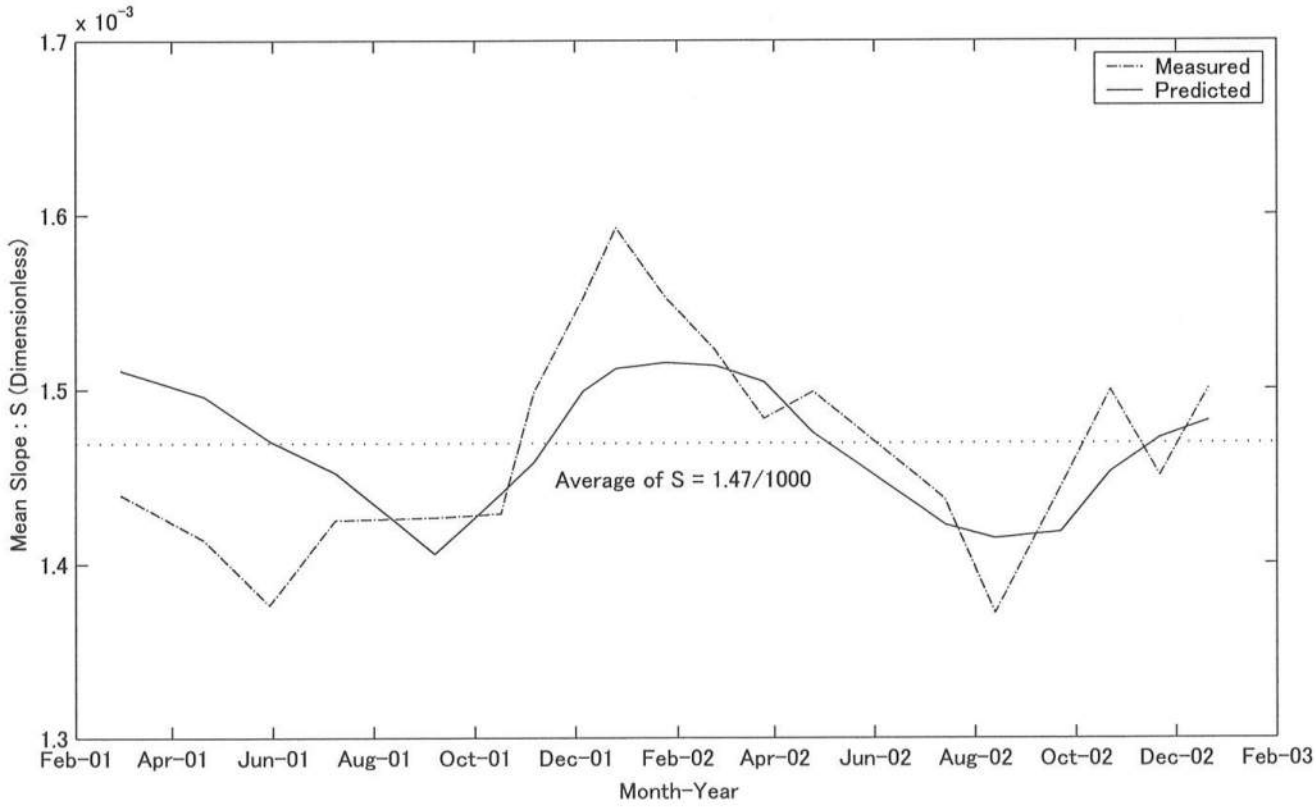

FIG. 49b. Measured and Predicted Mean Slope Parameters for the Right Profile

Table 18: Linear Regression Analysis of Time Series between Mean Slope $S(t)$ for Left and Right Profiles and 56-Day Averaged Tide Level, $\eta_{56}(t)$, Base on $S(t) = -\eta_{56}(t)/L_c + S_0$

Regression Coefficients	Left Profile	Right Profile
L_c (m)	4146	4054
$S_0 \times 10^3$ *(Dimensionless)*	1.11	1.50
Average of $S(t) \times 10^3$ *(Dimensionless)*	1.07	1.47
Correlation Coefficient	-0.695	-0.61

5.3 Quadratic Convexity Parameter

Figs. 50 - 55 show the time series of the quadratic convexity parameter with the driving forces including the 56-day averaged tide level, spring-neap tidal range averaged during 5 spring-neap cycles, significant wave height, squared significant wave height, wind velocity, and rainfall. The top panels of these figures show the results for the left profile during February 2001 to December 2002 and the bottom panels are for the right profile during the same period.

Fig. 50 shows that the time series of the quadratic convexity is not correlated with the 56-day averaged tide level, unlike the vertical displacement and mean slope partly because the quadratic convexity varied semiannually.

Fig. 51 shows that both time series of the quadratic convexity and averaged spring-neap tidal range varied semiannually. The quadratic convexity for the right profile may be correlated slightly with the averaged spring-neap tidal range if the time lag of approximately two months is accounted for.

Figs. 52 and 53 show that there was no obvious correlation between the quadratic convexity and wind waves, like the vertical displacement and mean slope.

Fig. 54 shows that the correlation between the quadratic convexity and wind velocity was very low.

Fig. 55 shows that the correlation between the quadratic convexity and rainfall is not apparent except that the quadratic convexity became larger sometimes during the heavy rainfall during June to July.

In conclusion, the monthly vertical displacement and mean slope varied almost synchronously with the seasonal tide level and can be predicted well by the simple linear regression analysis. However, the predominant driving force for the quadratic convexity is not clear but may be related with the average tide level, averaged spring-neap tidal range, and rainfall in unknown manners. The findings of this chapter will be useful in developing a meso-tidal mudflat morphological model for predicting the three profile parameters as a function of time.

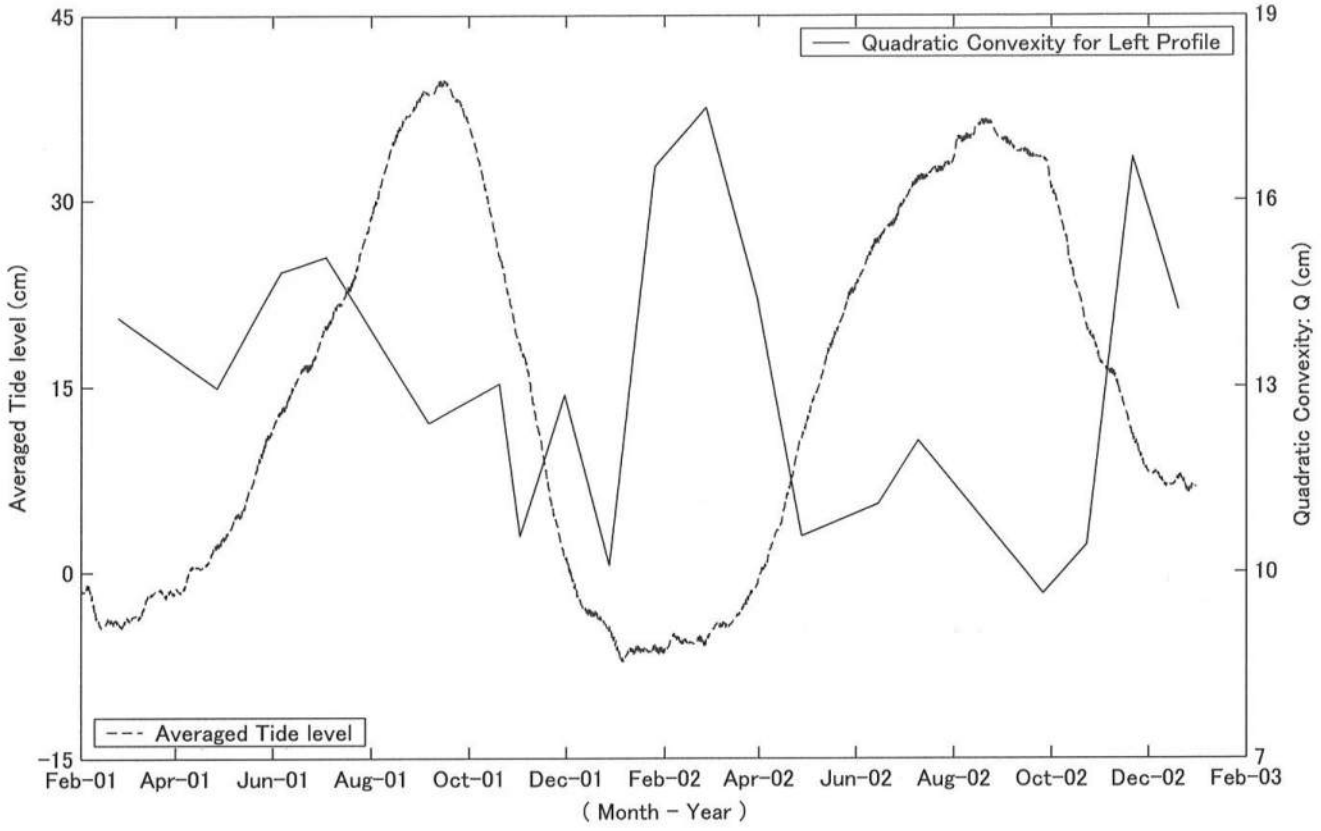

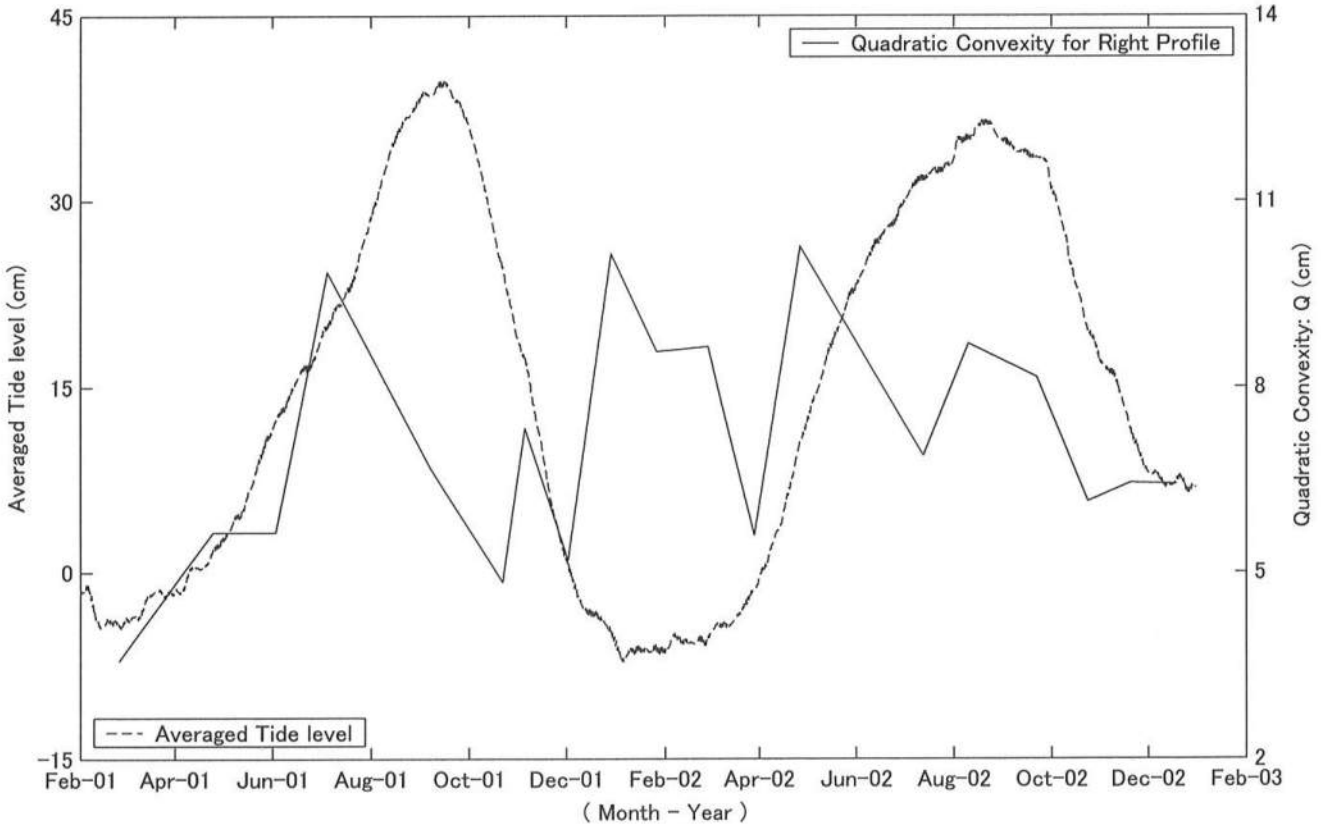

FIG. 50. Time Series of Quadratic Convexity and Average Tide level for Left and Right Profiles

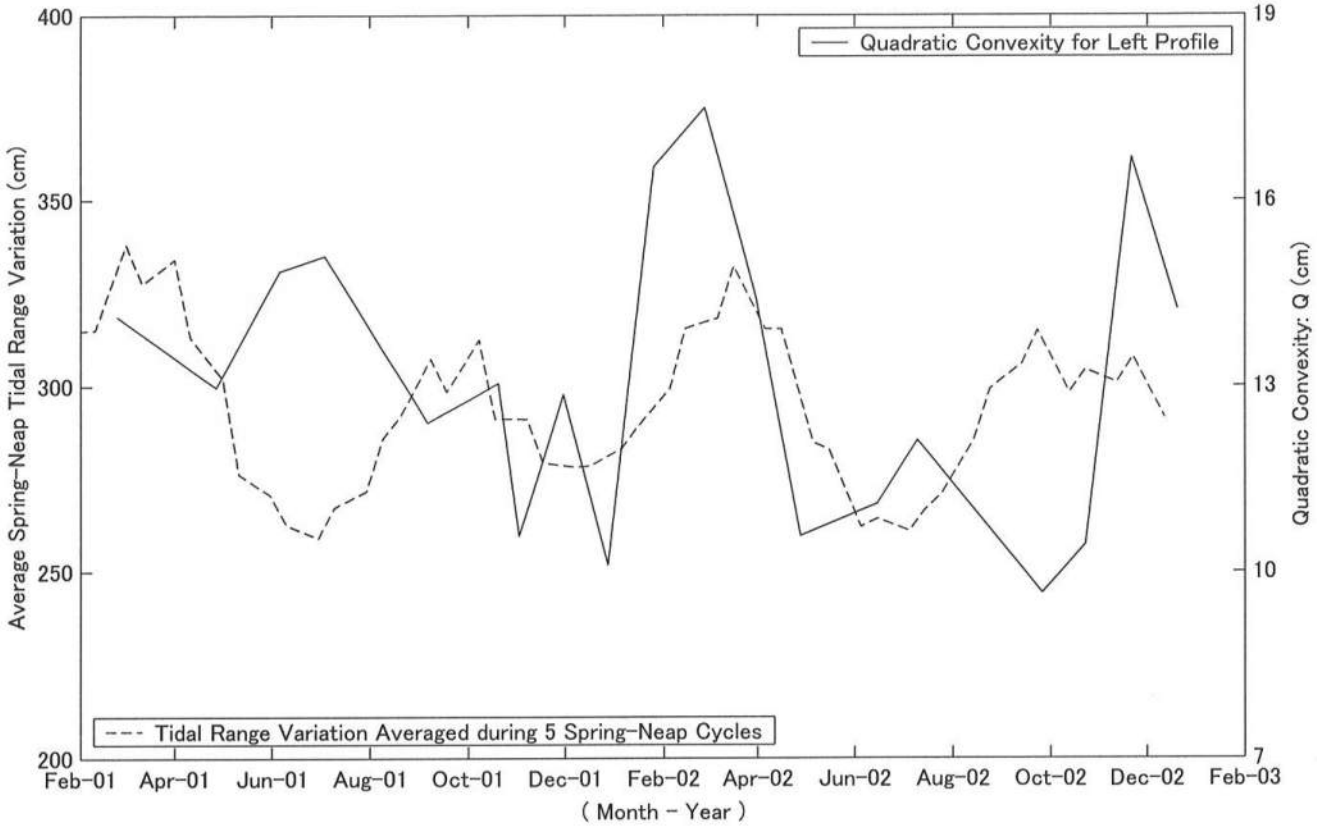

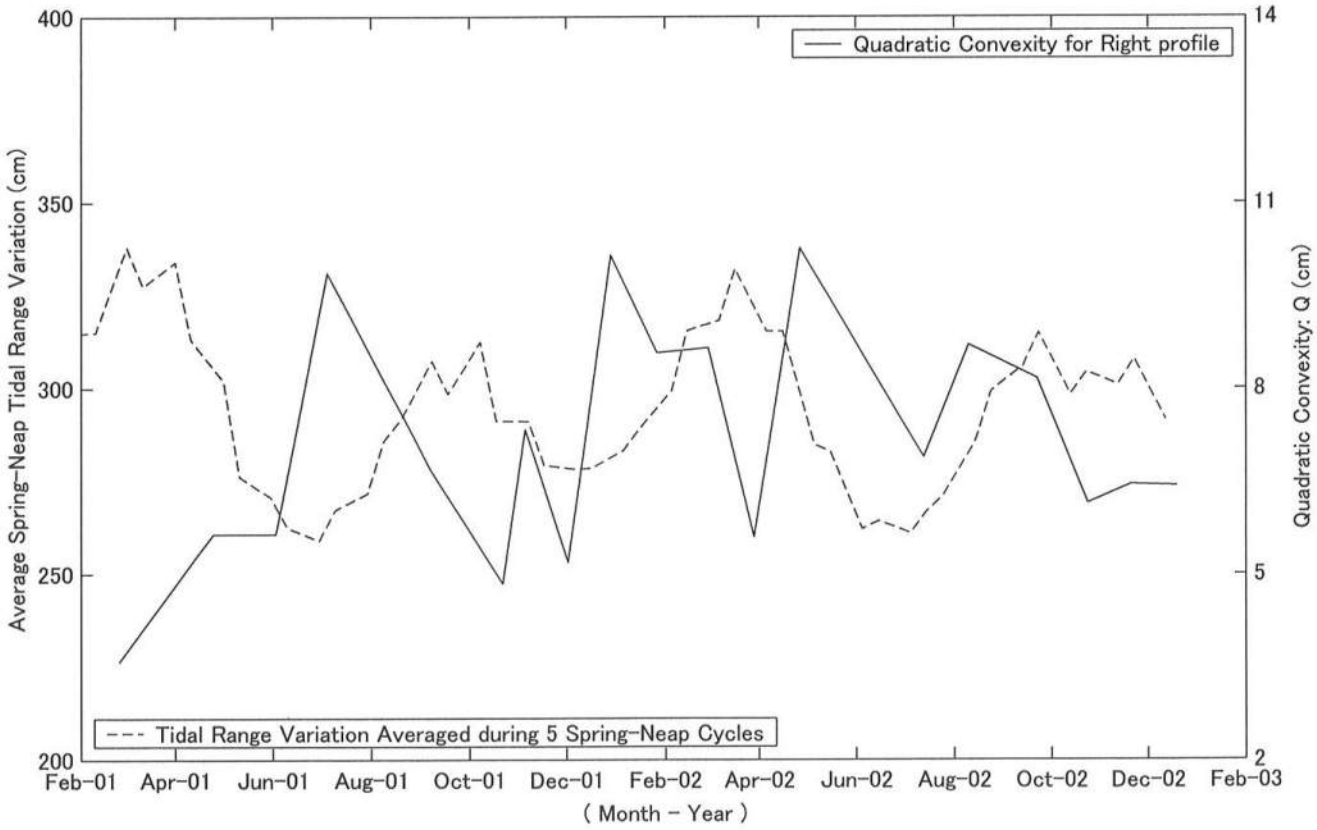

FIG. 51. Time Series of Quadratic Convexity and Spring-Neap Tidal Range Variation for Left and Right Profiles

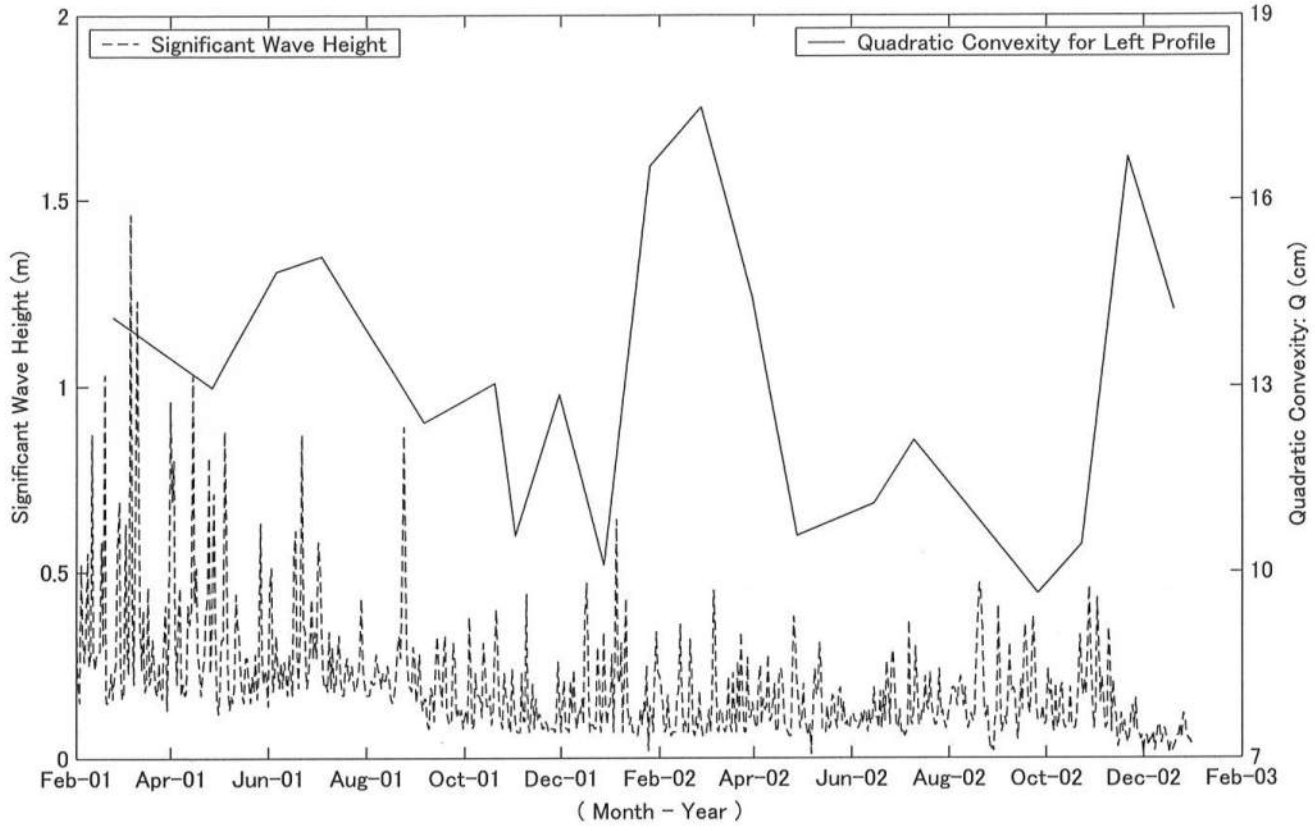

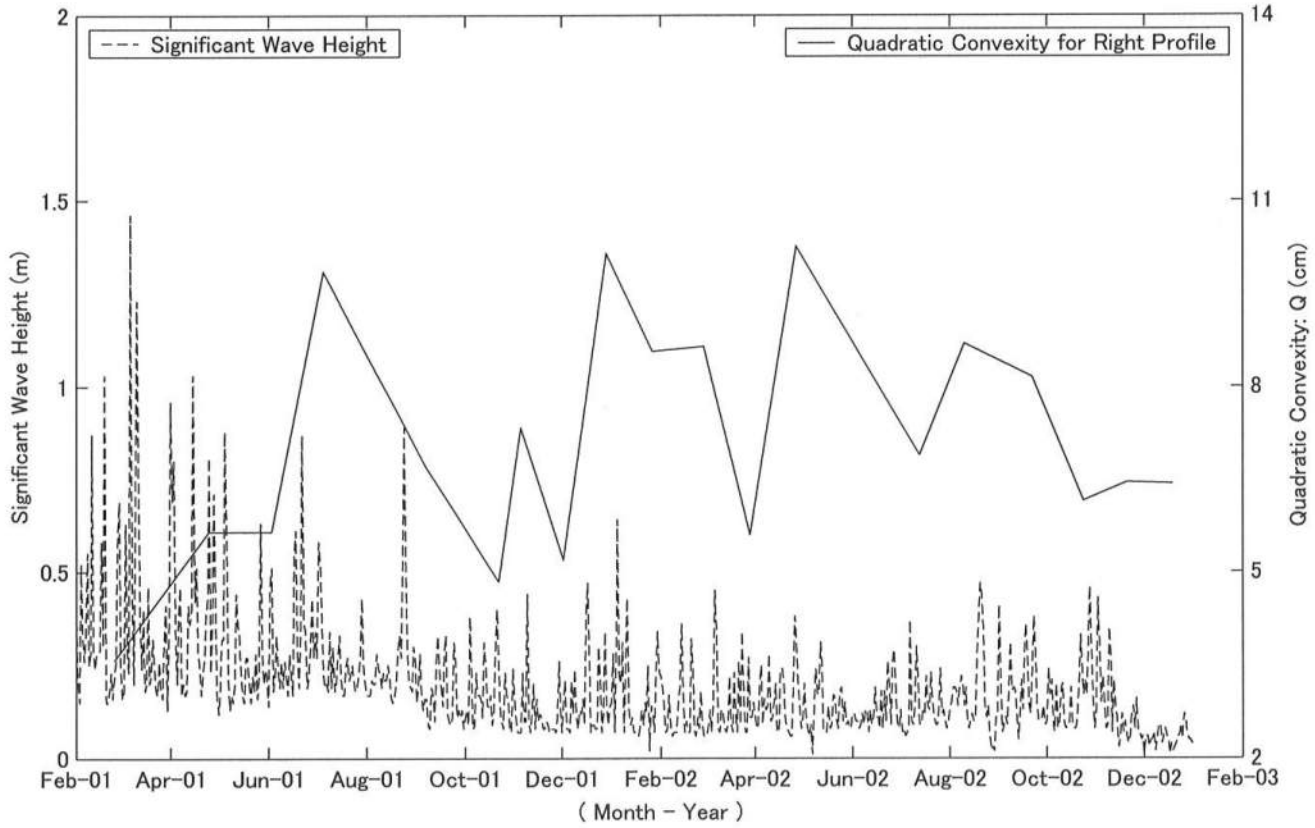

FIG. 52. Time Series of Quadratic Convexity and Significant Wave Height for Left and Right Profiles

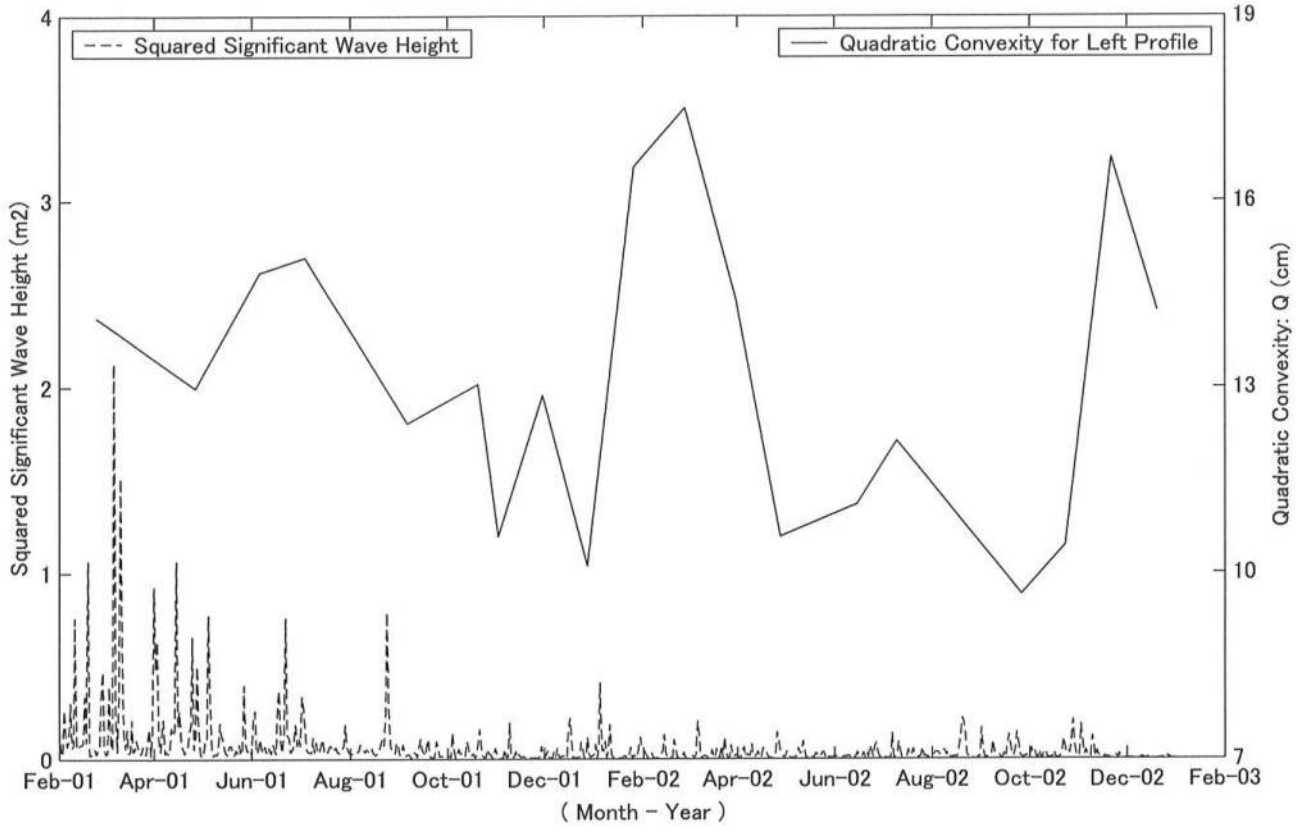

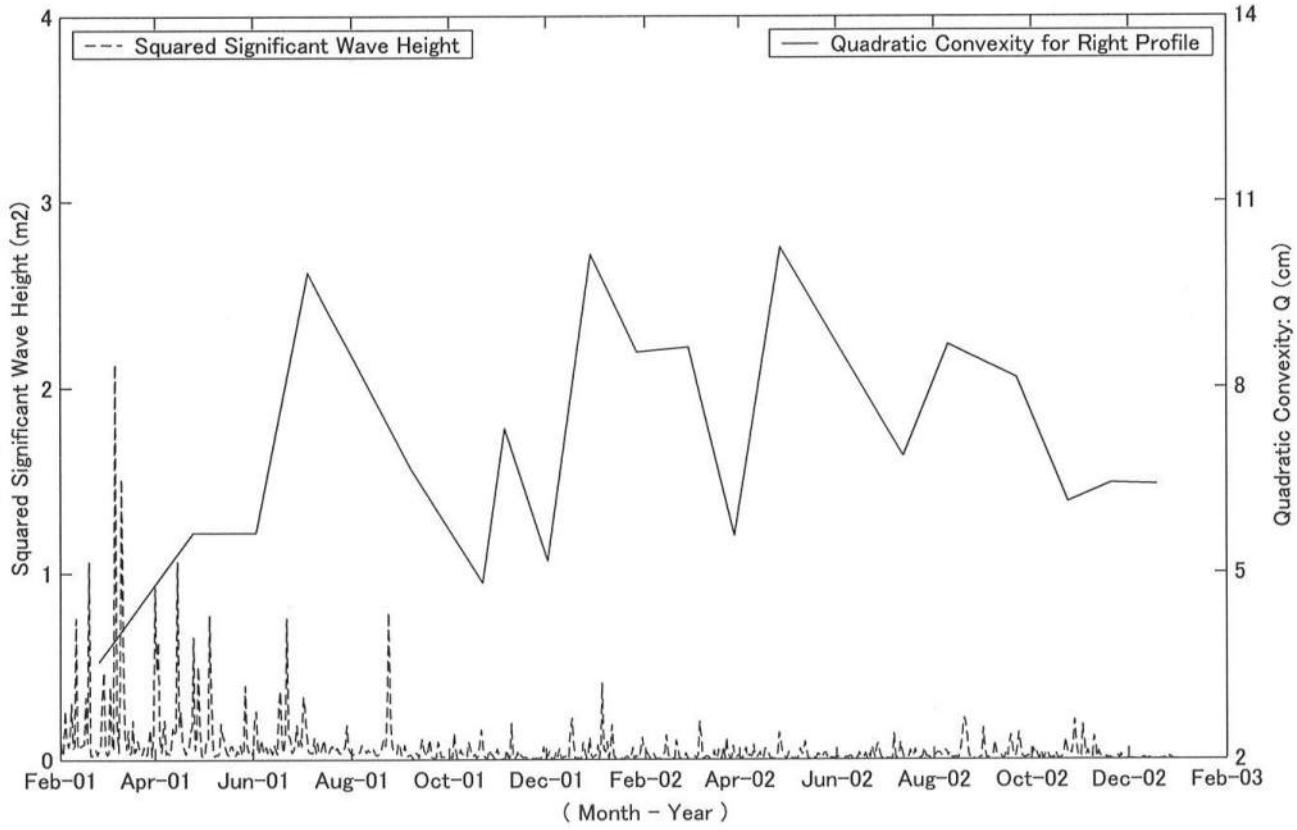

FIG. 53. Time Series of Quadratic Convexity and Squared Significant Wave Height for Left and Right Profiles

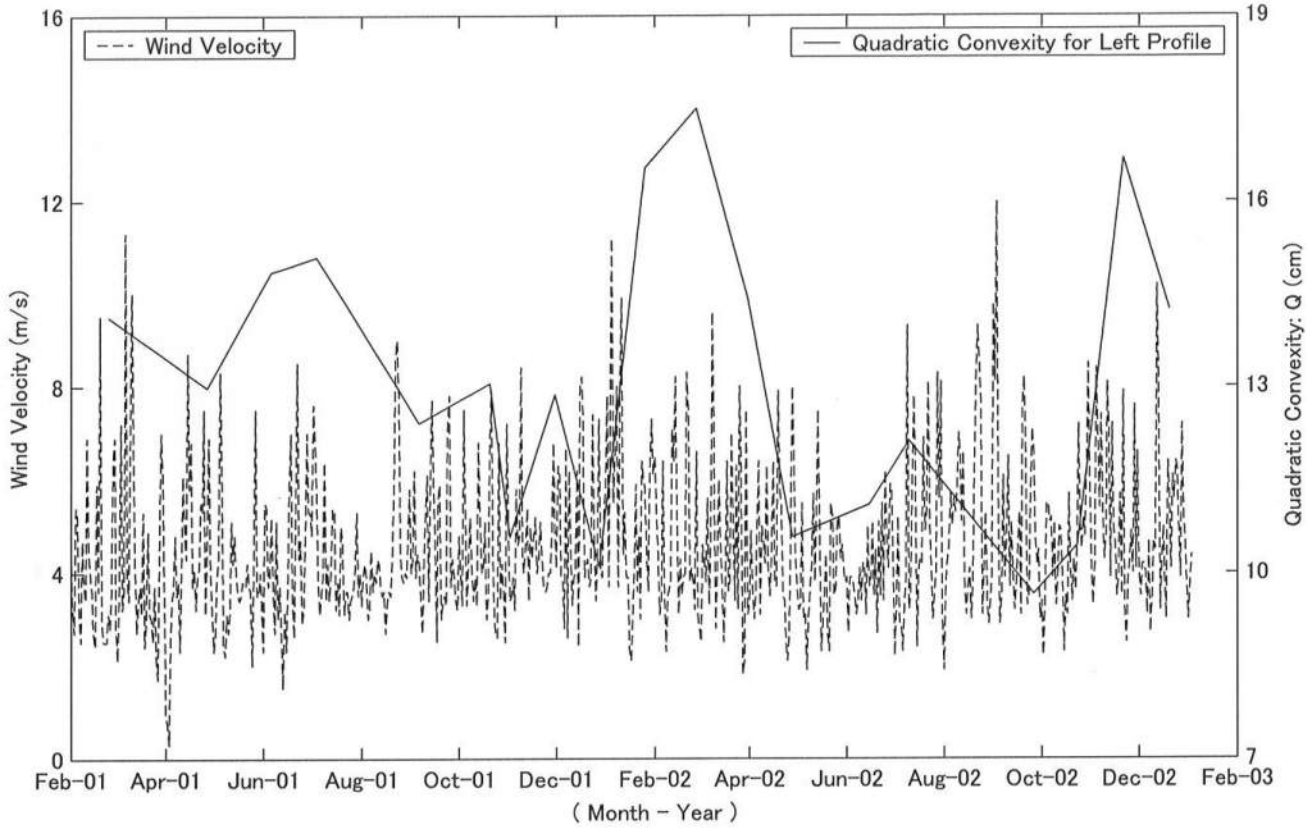

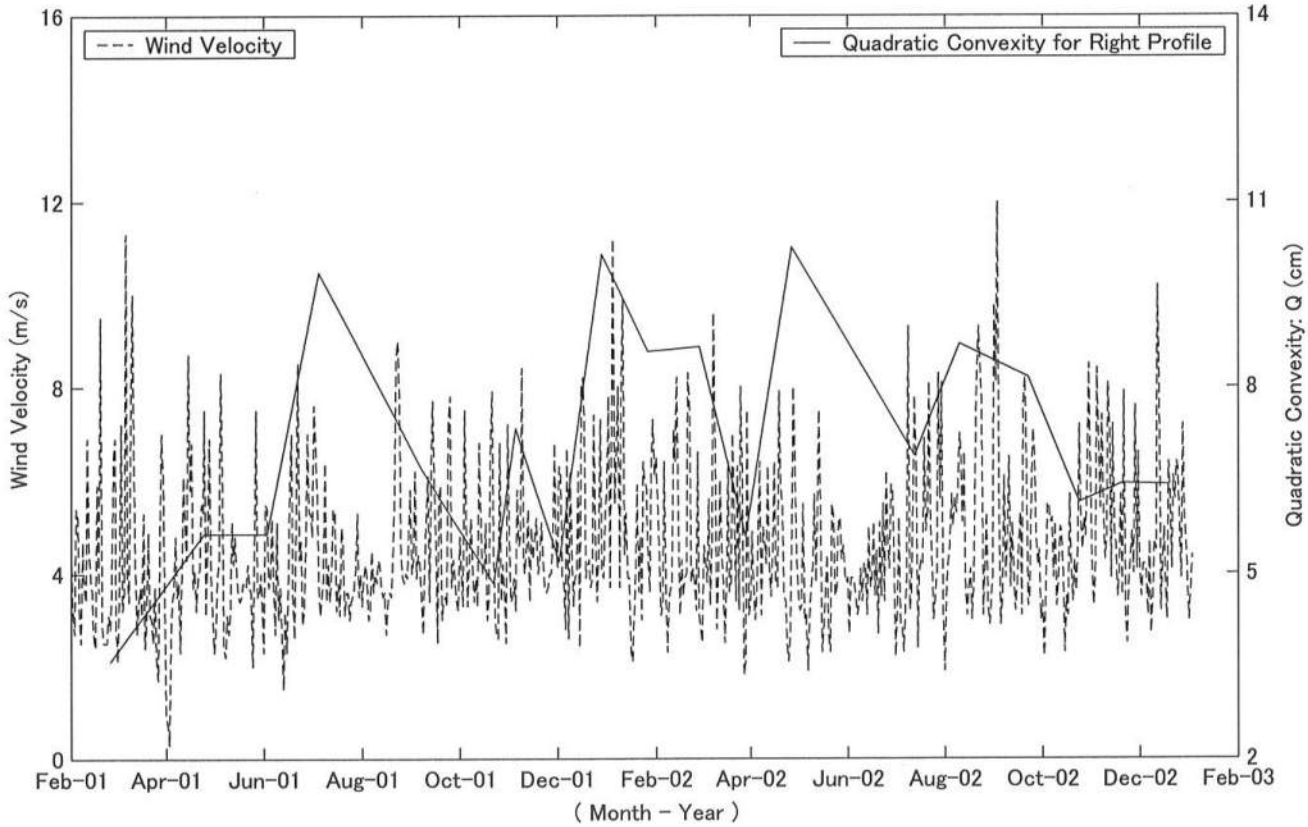

FIG.54. Time Series of Quadratic Convexity and Wind Velocity for Left and Right Profiles

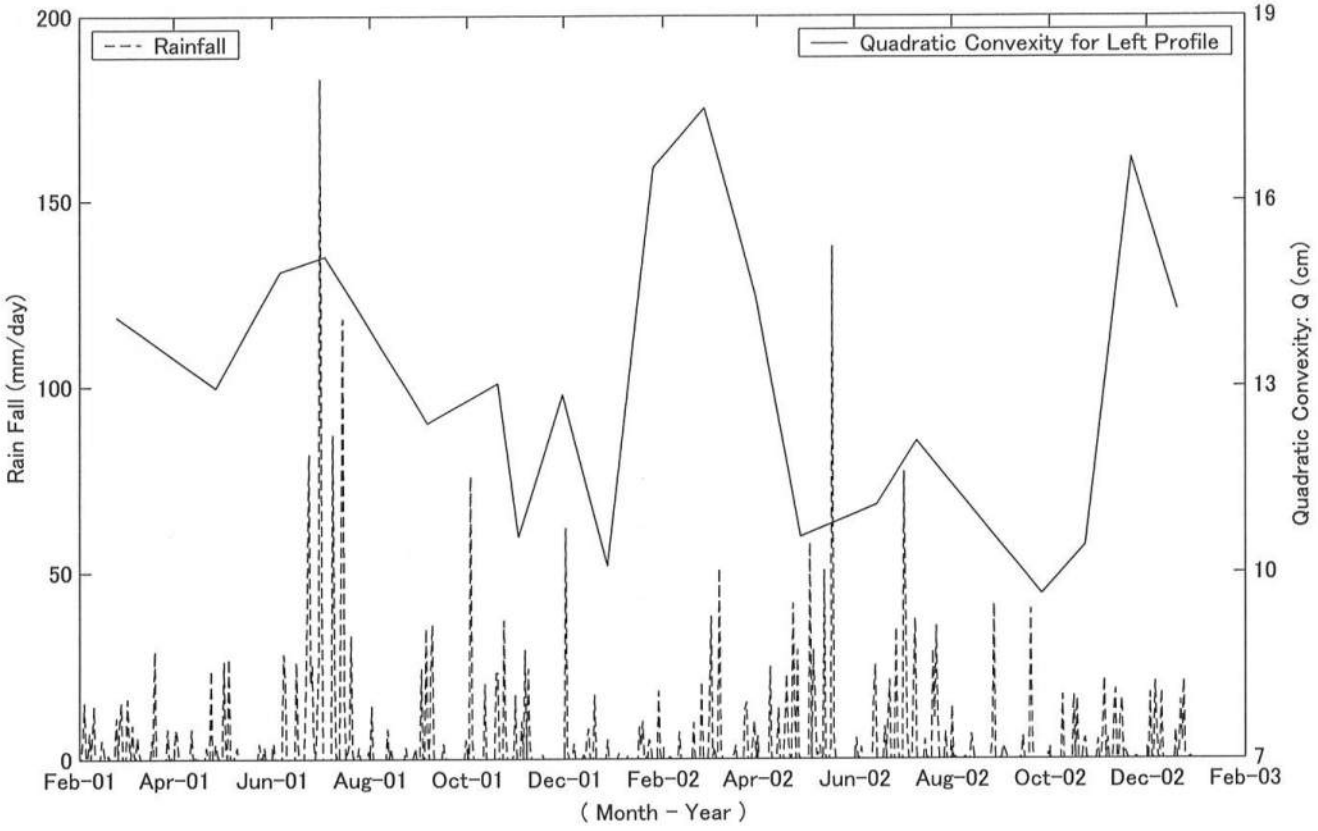

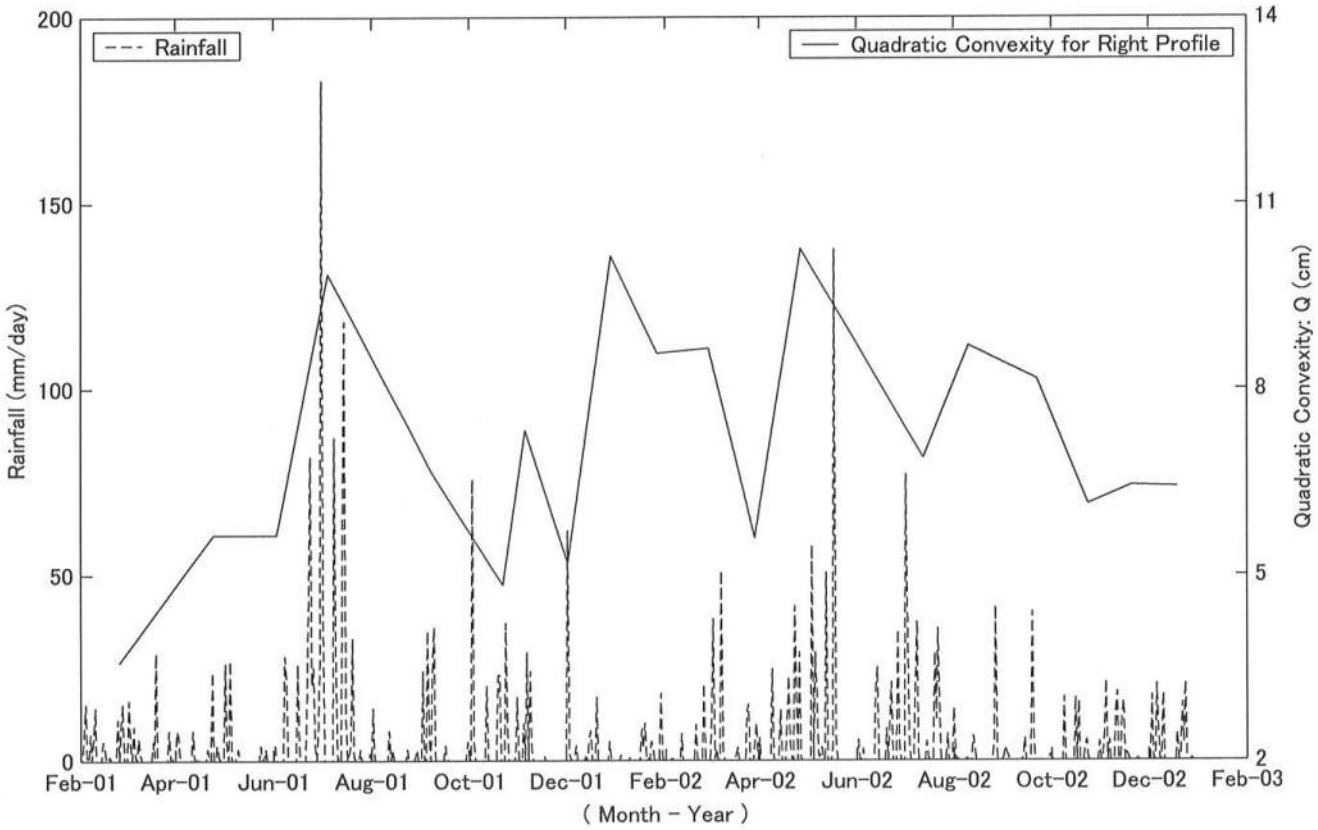

FIG. 55. Time Series of Quadratic Convexity and Rainfall for Left Profile

Chapter 6

RELATIVE IMPORTANCE OF TIDES AND WAVES FOR SEDIMENT TRANSPORT

So far, the temporal variations of the mudflat bed level and the driving forces have been correlated empirically without regard to sediment transport processes in order to identify the dominant causes for the observed morphological evolution. Kirby (2000) pointed out that the cross-shore profile of the mudflat could be classified by the relative contribution of wind waves and tidal currents to the cross-shore sediment transport. In the following, the depth-averaged tidal current velocity and wave orbital velocity are computed numerically using simple models to estimate the relative importance of tides and waves in causing the sediment transport on the meso-tidal mudflat.

6.1 Simple Tidal Current and Wave Models

6.1.1 Depth-averaged tidal current

Assuming the linear long wave theory with a tidal period of 12 hours 25 minutes in water depth of 1.0 m on the mudflat in the vicinity of the Sirakawa River mouth, the tidal

wavelength is 140 km and is 70 times as long as the 2-km wide mudflat as shown in Fig. 2. Consequently, the tide level may be assumed to rise and fall uniformly on the mudflat. This assumption is generally made as a first approximation to estimate the magnitude of depth-averaged tidal currents (e.g., Friedrichs and Aubrey 1996; Robert and Whitehouse 2001).

Fig.56 illustrates the schematic diagram for calculation of the depth-averaged cross-shore tidal current where η= tide level above T.P; h = water depth; U_T = depth-averaged tidal current; x_f = cross-shore location of the moving shoreline defined as $h = 0$ at $x = x_f$ on the mud flat; and $V(t)$ = water volume per unit alongshore width at time t between the shoreline and the specified location x. The bed elevation at $z = (\eta - h)$ is assumed to be stationary for one tidal cycle. Assuming the alongshore and cross-shore uniformity of the tide level $\eta(t)$, the conservation of water volume in the absence of waves is expressed as

$$\frac{\partial h}{\partial t} - \frac{\partial}{\partial x}(h \cdot U_T) = 0 \tag{23}$$

where U_T is taken to be positive landward and the cross-shore coordinate x has been taken to be positive seaward.

Integration of Eq. (23) with respect to x yields.

$$\int_{x_f(t)}^{x} \frac{\partial h}{\partial t} dx - \int_{x_f(t)}^{x} \frac{\partial}{\partial x}(h \cdot U_T) dx = 0 \tag{24}$$

Using the Leibnitz theorem for the differentiation of an integral, Eq. (24) can be simplified as

$$\frac{\partial V}{\partial t} - h \cdot U_T = 0 \tag{25}$$

with $$V = \int_{x_f(t)}^{x} h(t, x')dx' \qquad \text{for } x \geq x_f \tag{26}$$

where $h = 0$ at $x = x_f$. The depth-averaged cross-shore tidal current at the specified distance x from the seawall is given as follows:

$$U_T = \frac{1}{h} \cdot \frac{\partial V}{\partial t} \qquad \text{at given } x \geq x_f(t) \tag{27}$$

where the water depth $h = (\eta - z)$ at given x is known for the specified $\eta(t)$ and the parameterized bottom profile $z(x) = -ax^2 - bx + c$. The shoreline location $x_f(t)$ where $h = 0$ at each time level is determined as the intersection between the mud flat profile including the seawall and the tide level, which is assumed to be horizontal

$$x_f(t) = \frac{-b + \sqrt{b^2 - 4a[\eta(t) - c]}}{2a} \qquad \text{for } \eta(t) < c \tag{28}$$

$$x_f(t) = 0 \qquad \text{for } \eta(t) \geq c \tag{29}$$

where the vertical seawall is located at $x = 0$.

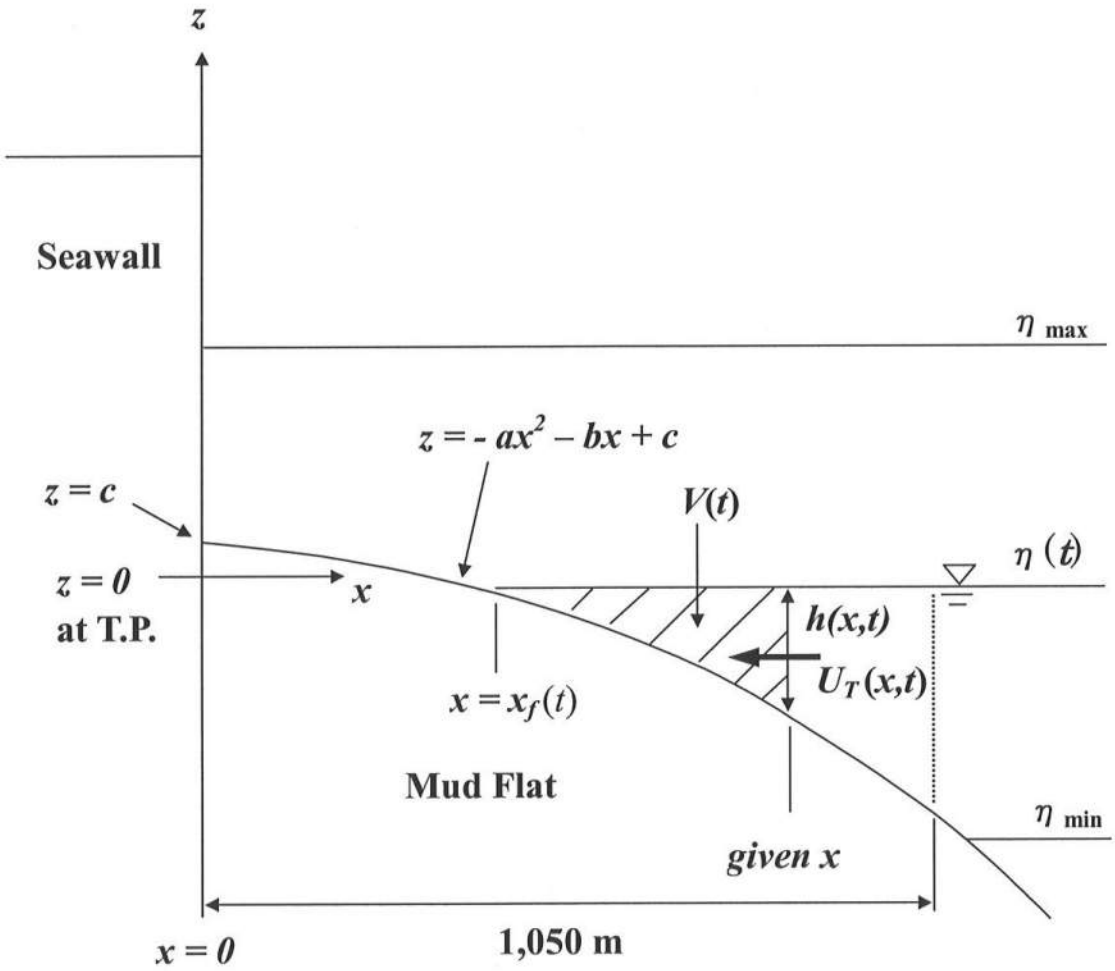

FIG. 56 Schematic Diagram for Calculation of Depth-Averaged Cross-shore Tidal Current

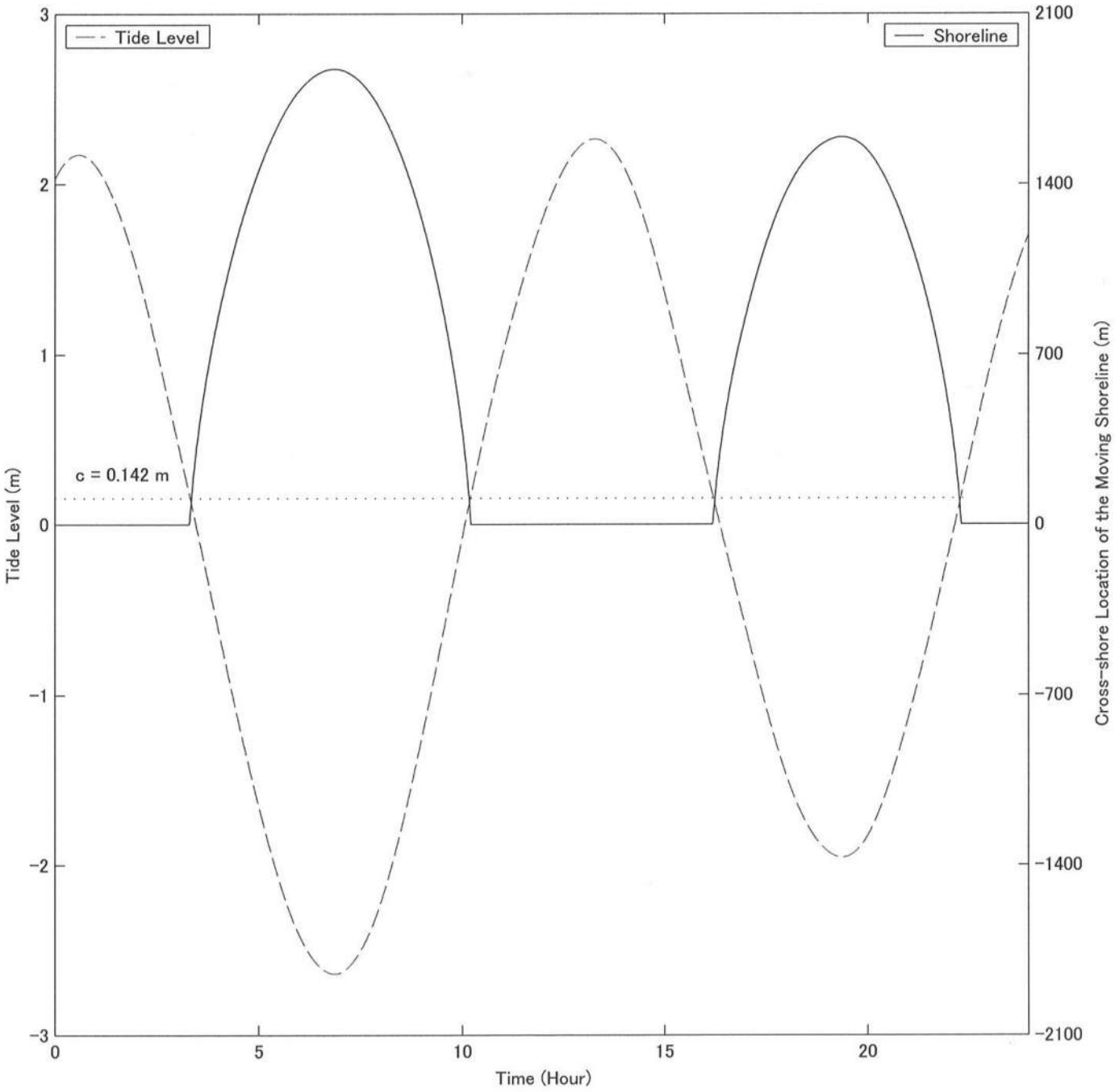

FIG. 57. Temporal Variations of Tidel Level and Moving Shoreline for Eroded Left Profile on Ferbuary 25, 2002

Fig. 57 shows the temporal variations of tide level and moving shoreline for the eroded left profile on February 25, 2002 and $a = 7.76\times10^{-7}$ m^{-1}, $b = 2.92\times10^{-4}$, and $c = 1.42\times10^{-1}$ m for this measured profile as listed in Table 10. The tide is semidiurnal and the tide level varied in the range from 2.2 to –2.6 m about T.P. The shoreline location remains on the seawall surface when the tide level $\eta(t)$ is above c = 0.142 m and moves seaward or landward rapidly when the tide level is slightly below c = 0.142 m. The shoreline reaches the most seaward edge at the low tide and the most seaward shoreline locations are in the range 1500 to 1800 m offshore from the sea wall in Fig. 57.

The cross-shore velocity of the shoreline can be found from Eqs. (28) and (29)

$$\frac{dx_f(t)}{dt} = -\left[b^2 - 4a\left(\eta(t) - c\right)\right]^{-\frac{1}{2}} \cdot \frac{d\eta(t)}{dt} \qquad \text{for } \eta(t) < c \qquad (30)$$

$$\frac{dx_f(t)}{dt} = 0 \qquad \text{for } \eta(t) \geq c \qquad (31)$$

The water volume $V(t)$ in the region landward of given x at each time level is obtained by Eq.(26). The rate of the water volume change, $\frac{\partial V}{\partial t}$, is expressed as

$$\begin{aligned}\frac{\partial V}{\partial t} &= \frac{\partial}{\partial t}\int_{x_{f(t)}}^{x} h(t,x')dx' \\ &= \int_{x_{f(t)}}^{x} \frac{\partial h(t,x')}{\partial t}dx' + \frac{\partial x}{\partial t}(h)_x - \frac{\partial x_f}{\partial t}(h)_{x_f} \\ &= \left[x - x_f(t)\right]\cdot\frac{d\eta(t)}{dt} \qquad \text{for } \eta(t) < c \qquad (32)\end{aligned}$$

and

$$\frac{\partial V}{\partial t} = x \cdot \frac{d\eta(t)}{dt} \qquad \text{for } \eta(t) \geq c \qquad (33)$$

where use is made of the Leibnitz theorem, $h(t,x) = [\eta(t) - z(x)]$, and $x_f(t) = 0$ for $\eta(t) \geq c$.

Substitution of Eqs. (32) and (33) into (27) yields

$$U_T = \frac{1}{h} \cdot \frac{d\eta(t)}{dt} \cdot [x - x_f(t)] \qquad \text{for } \eta(t) < c \qquad (34)$$

$$U_T = \frac{1}{h} \cdot \frac{d\eta(t)}{dt} \cdot x \qquad \text{for } \eta(t) \geq c \qquad (35)$$

Eqs. (34) and (35) are discretized as follows:

$$U_T(x,t^n) = \frac{1}{h(t^n)} \cdot \frac{\eta(t^n) - \eta(t^{n-1})}{\Delta t} \cdot [x - x_f(t^n)] \qquad \text{for } \eta(t) < c \qquad (36)$$

$$U_T(x,t^n) = \frac{1}{h(t^n)} \cdot \frac{\eta(t^n) - \eta(t^{n-1})}{\Delta t} \cdot x \qquad \text{for } \eta(t) \geq c \qquad (37)$$

where t^n = present time level, t^{n-1} = previous time level, and $\Delta t = (t^n - t^{n-1})$ = time step taken as 1 min in the following computation. The time series of the depth-averaged tidal current $U_T(x,t)$ at given x is calculated during one survey day. The location x is then varied from 0 to 1050 m offshore from the seawall with an interval of 10 m. The measured hourly tide level is interpolated using a cubic spline function and the interpolated tide level with Δt = 1 min is used in Eqs. (36) and (37) to obtain the water depth h above the mudflat profile fitted as $z = (-ax^2 - bx + c)$ in the survey domain $0 \leq x \leq 1050$ m.

6.1.2 Wave orbital velocity

The amplitude of wave orbital velocity, $U_b(x,t)$, based on linear wave theory is given by (e.g., Dean and Darlymple 2002):

$$U_b = \frac{1}{2} \cdot \frac{H \cdot \omega}{\sinh(k \cdot h)} \tag{38}$$

where H = local wave height, T = wave period, $\omega = \frac{2\pi}{T}$ = angular wave frequency, L = local wavelength, $k = \frac{2\pi}{L}$ = wave number, and g = gravitational acceleration. The product $k \cdot h$ is calculated by solving the dispersion relationship $\omega^2 = g \cdot k \tanh(k \cdot h)$ iteratively for the specified wave period T and $h(t,x)$. In shallow water, Eq. (38) can be approximated as

$$U_b = \frac{1}{2} \cdot \frac{H \cdot \omega}{k \cdot h} \qquad \text{for } \frac{h}{L} < \frac{1}{20} \tag{39}$$

In the following computation with T = 3 sec, Eq. (38) is used in the region where the water depth is larger than or equal to 0.2 m and Eq. (39) is used in the region where the water depth is less than 0.2 m.

The local wave height H at the offshore distance x from the seawall is estimated assuming normally incident linear monochromatic waves on the mudflat profile of alongshore uniformity and is expressed as

$$H = H_i \cdot K_s \tag{40}$$

with

$$K_s = \frac{1}{\sqrt{\tanh(k \cdot h)\left[1 + \frac{2k \cdot h}{\sinh(2k \cdot h)}\right]}} \tag{41}$$

where H_i = incident wave height in deep water and K_s = shoaling coefficient. In shallow water, Eq. (41) is approximated as

$$K_s = \frac{1}{\sqrt{2k \cdot h}} \qquad \text{for } \frac{h}{L} < \frac{1}{20} \tag{42}$$

The time series of the wave orbital velocity U_b for the known water depth $h = \left[\eta(t) + ax^2 + bx - c\right]$ is calculated every one minute in the region $0 \le x \le 1050$ m with an interval of 10 m. The incident wave height H_i = 0.2 m and the wave period T = 3.0 sec are specified as an example where the average significant wave height and wave period during the last two years at Kumamoto port are approximately 0.2 m and 3 sec, respectively, as shown in Fig. 17. Computation is limited to the region of $\frac{H}{h} \le 0.8$ because Eqs. (38) and (39) do not account for wave breaking.

6.2 Computed Tidal Currents and Waves

Fig. 58 shows the spatial variations of the maximum and minimum depth-averaged tidal currents calculated at the interval of 10 m along both the average and accreted left profiles. The flood current toward the seawall is positive and the ebb current directed offshore is negative. The magnitudes of the maximum and minimum depth-averaged tidal currents are smaller on the accreted profile than on the averaged profile because the water depth on the accreted profile is smaller, resulting in the decrease of the rate of the fluid volume change. The maximum difference on the accreted and average profiles is approximately 0.1 m/sec at 20 m offshore from the seawall and the difference decreases gradually with the offshore distance x. The maximum onshore current for the accreted profile increases rapidly with the offshore distance x from the seawall and decreases gradually in the region $x > 10$ m. The minimum offshore current for the accreted profile decreases rapidly with the offshore distance x up to 10 m before its gradual offshore increase. The depth-averaged tidal current speed at $x = 1050$ m is approximately 30 cm/sec which is consistent with the current speeds measured by Yamada *et al.* (2001).

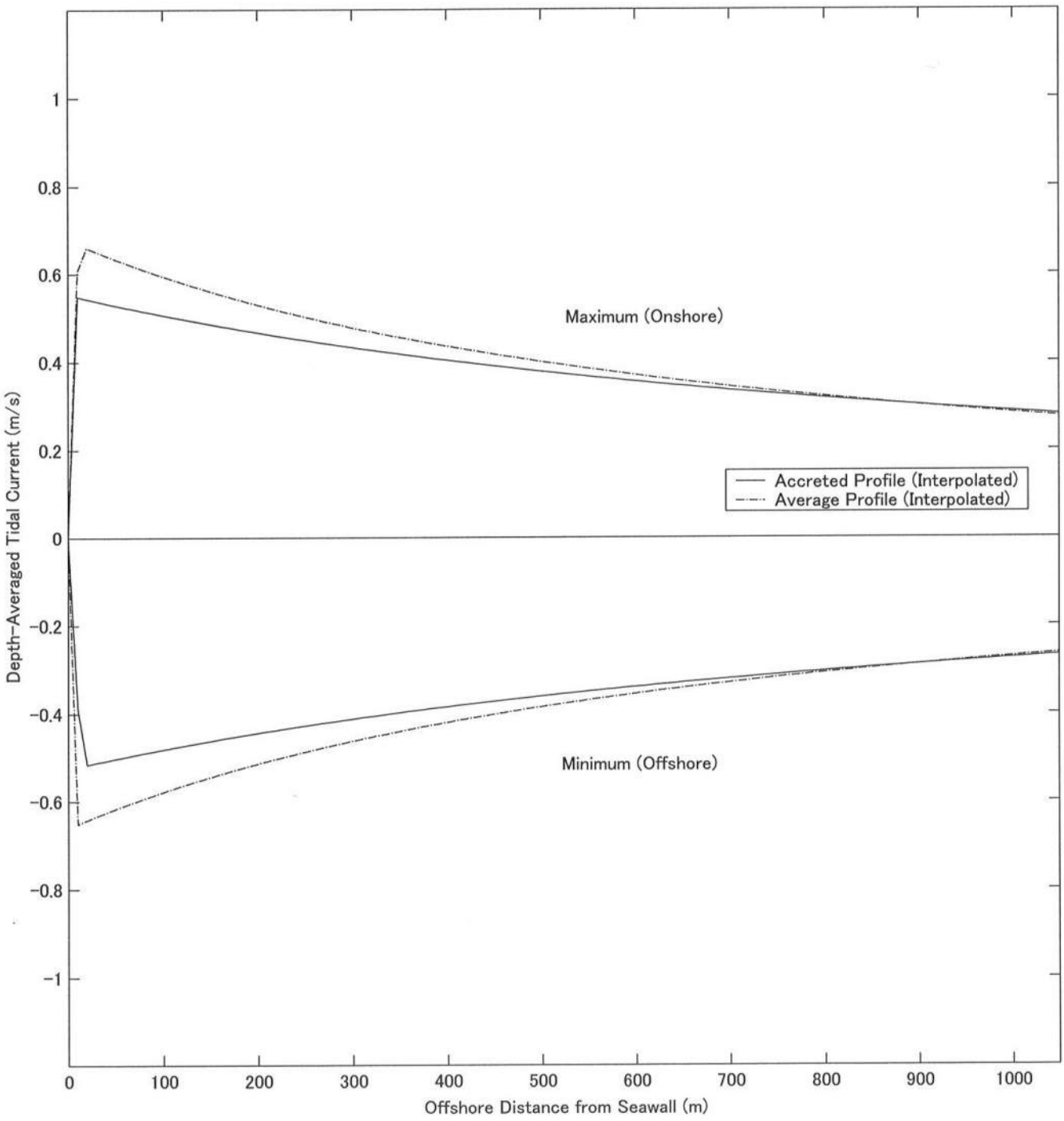

FIG. 58. Spatial Variations of Maximum and Minimum Depth-Averaged Tidal Current for Accreted Left Profile on October 31, 2001

Fig. 59 shows the spatial variations of the maximum and minimum depth-averaged tidal currents calculated every 10 m on the average and eroded left profiles. Unlike the accreted profile, the magnitudes of the maximum and minimum depth-averaged tidal currents on the eroded profile tend to be larger than those on the averaged profile partly because the water depth is larger along the eroded profile, resulting in the increase of the rate of the fluid volume change. The maximum difference of the onshore and offshore current speeds on the eroded and average profile is approximately 0.3 m/sec at the 10 m offshore from the seawall and the difference decreases gradually with the offshore distance x. The maximum onshore current for the eroded profile increases rapidly with the offshore distance up to 10 m and decreases gradually. The minimum offshore current for the eroded profile decreases rapidly with the offshore distance up to 10 m and increases gradually. The depth-averaged tidal current speed at x = 1050 m is approximately 30 cm/sec, which is also in agreement with the measured current speeds by Yamada *et al.* (2001).

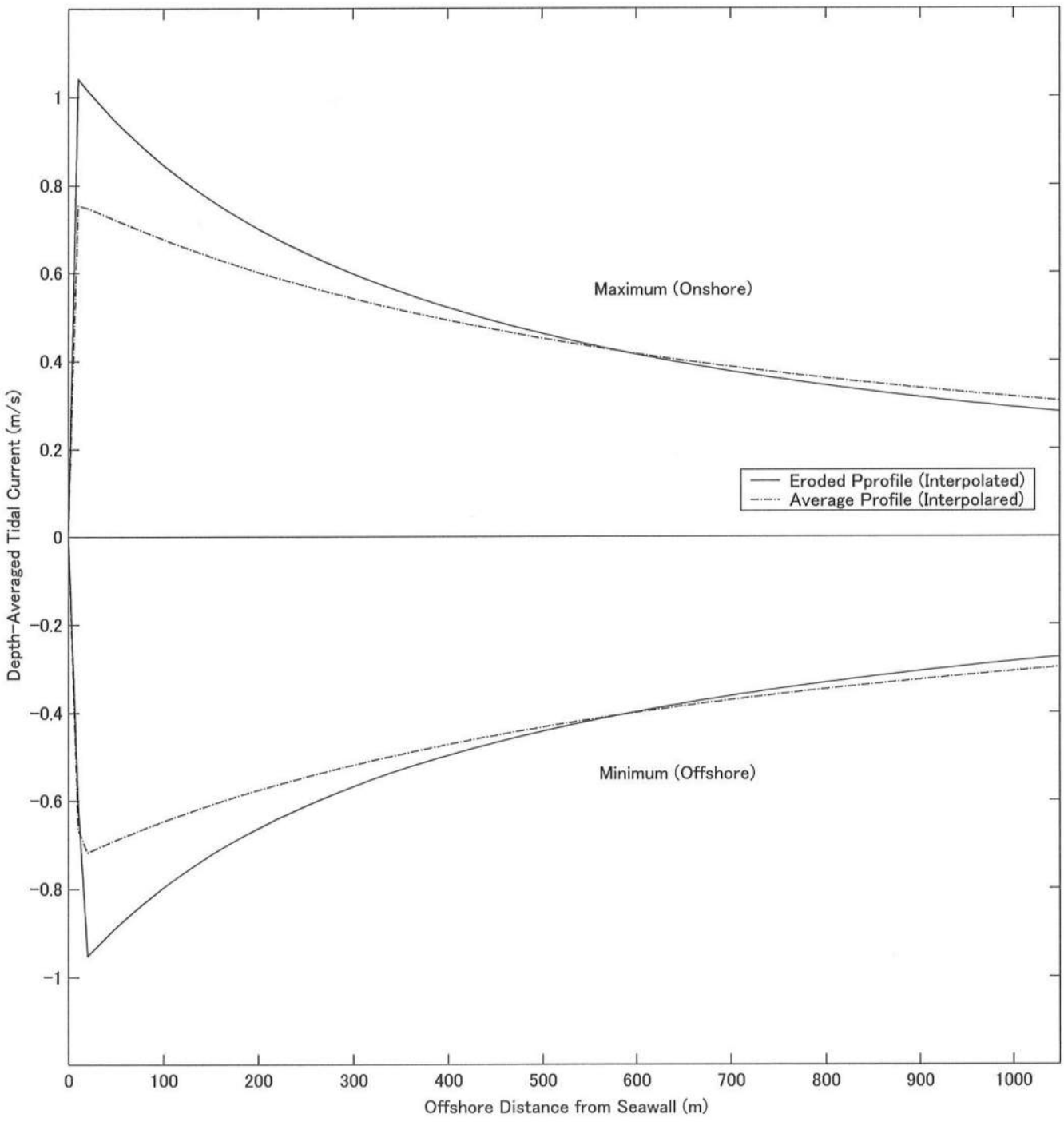

FIG. 59. Spatial Variations of Maximum and Minimum Depth-Averaged Tidal Current for Eroded Left Profile on February 25, 2002

Fig. 60 shows the temporal variations of the water depth and depth-averaged tidal current at x = 100 m offshore on the accreted left profile. The onshore (positive) current increases suddenly with the increase of the water depth and become the maximum when the water depth is approximately 0.1 m. Then, the current decreases exponentially and remains nearly zero when the water depth exceeds approximately 1 m. When the water depth becomes less than 1 m, the offshore (negative) current starts and varies with time in a manner similar to the onshore current apart from the negative sign.

The computed temporal variation of the depth-averaged cross-shore tidal current exhibits symmetry between the flood and ebb tides but Friedrichs et al. (1992) pointed out velocity asymmetry due to the phase lag caused by the fluid momentum on the tidal flat. This simple model may not be adequate for the prediction of cross-shore net sediment transport. The effect of fluid inertia (e.g., Pritchard *et al.* 2002) is neglected in the present simple model based only on the conservation of water volume. Therefore, it may be necessary to use a better numerical hydrodynamic model, such as RBREAK based on the finite-amplitude shallow-water equations, which has been developed and verified extensively by Kobayashi et al. (1989) and Kobayashi and Wurjanto (1992).

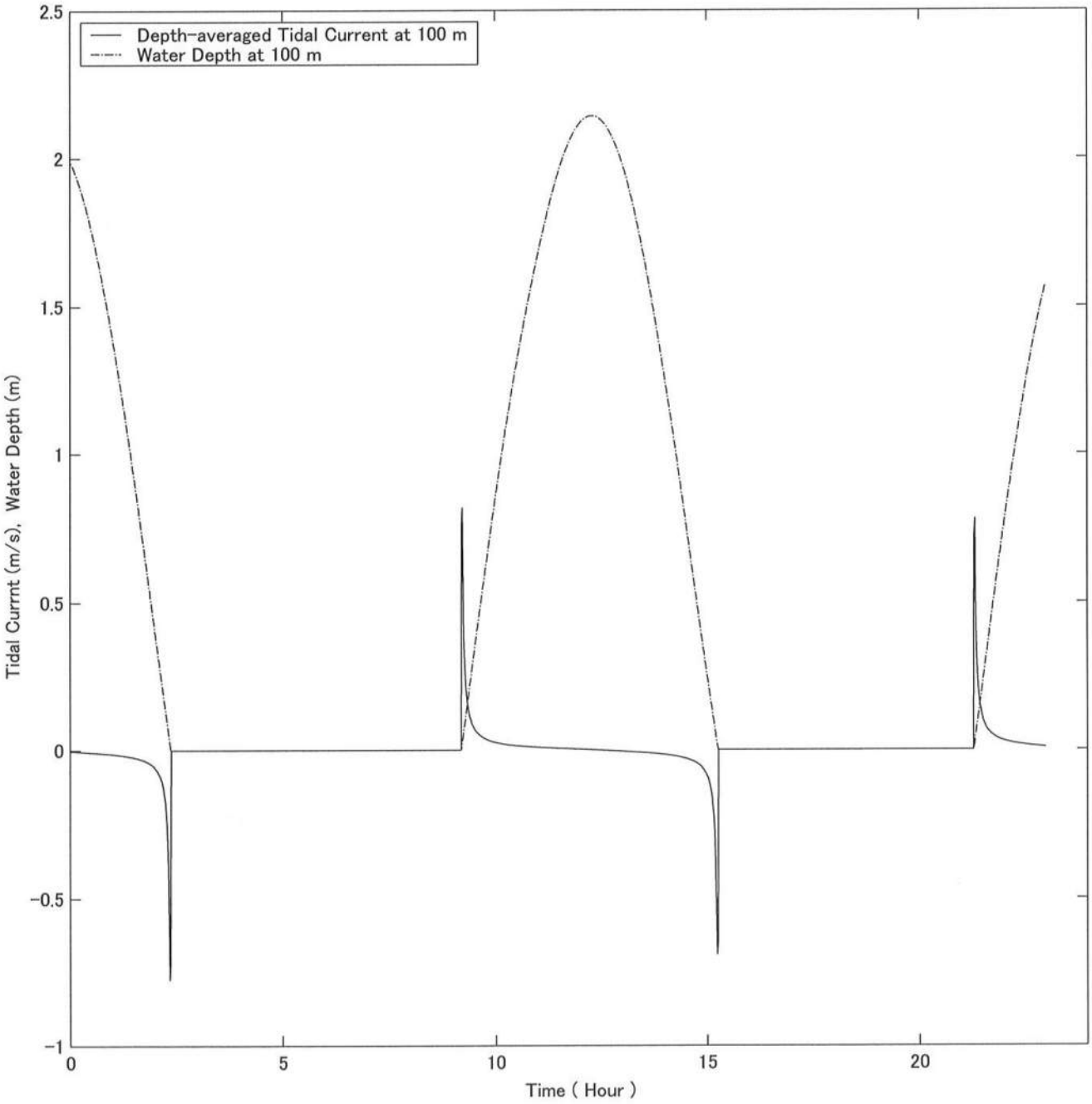

FIG. 60. Temporal Variations of Depth-Averaged Tidal Current and Water Depth at 100 m Offshore for Eroded Left Profile on February 25, 2002

Figs. 61 and 62 show the spatial variation of the computed wave orbital velocity on the eroded left profile at time = 10.2 hr and 10.5 hr during the flood tide shown in Fig. 57. The maximum velocity occurs near or at the moving shoreline within the restriction of $H/h \leq 0.8$. The magnitude of the velocity decreases fairly rapidly with the increase of the offshore distance.

Figs. 63 and 64 show the spatial variations of the maximum wave orbital velocity calculated every 10 m on the accreted and eroded left profiles, respectively. The maximum velocities are practically uniform and approximately 0.65 m/sec, unlike the depth-averaged tidal currents. The maximum wave orbital velocity on the left profile is of the same order as the depth-averaged tidal current.

Figs. 65 shows the temporal variations of the water depth, wave height, and wave orbital velocity at 100 m offshore on the eroded left profile. The wave height increases with the increase of the water depth and becomes the maximum in the water depth of approximately 0.2 m where use is made of H_i = 0.2 m in Eq. (40) and the computation is limited to the non-breaking waves of $H/h \leq 0.8$. The wave orbital velocity begins almost 30 minutes after the depth increases due to the breaking wave criterion and becomes the maximum when the water depth becomes approximately 0.4 m. Then, the wave orbital velocity near the bed decreases when the water depth becomes larger where wave action decreases downward for the short waves with T = 3 sec.

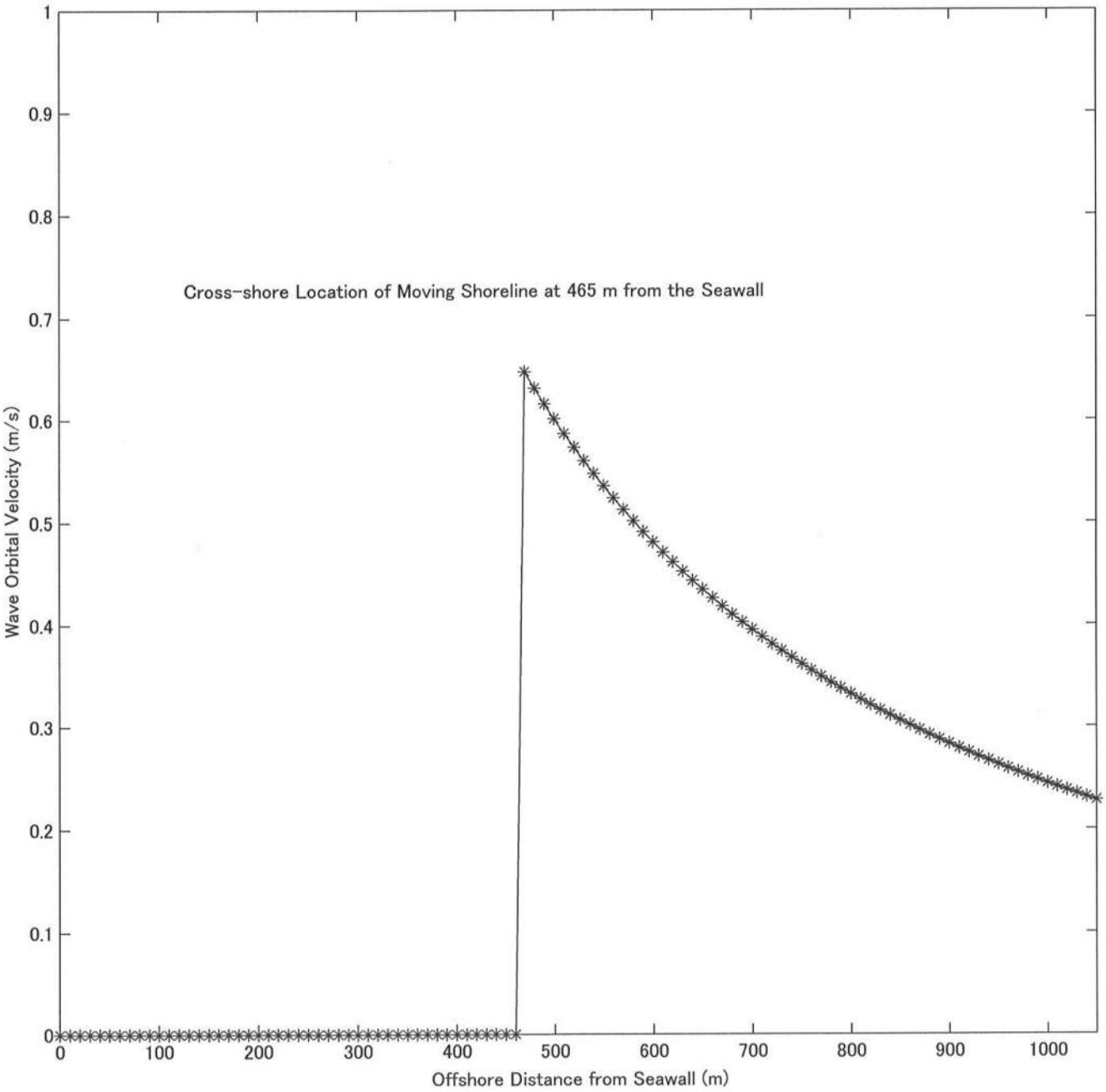

FIG. 61. Spatial Variation of Wave Orbital Velocity at Time = 10.2 hr for Eroded Left Profile on February 25, 2002

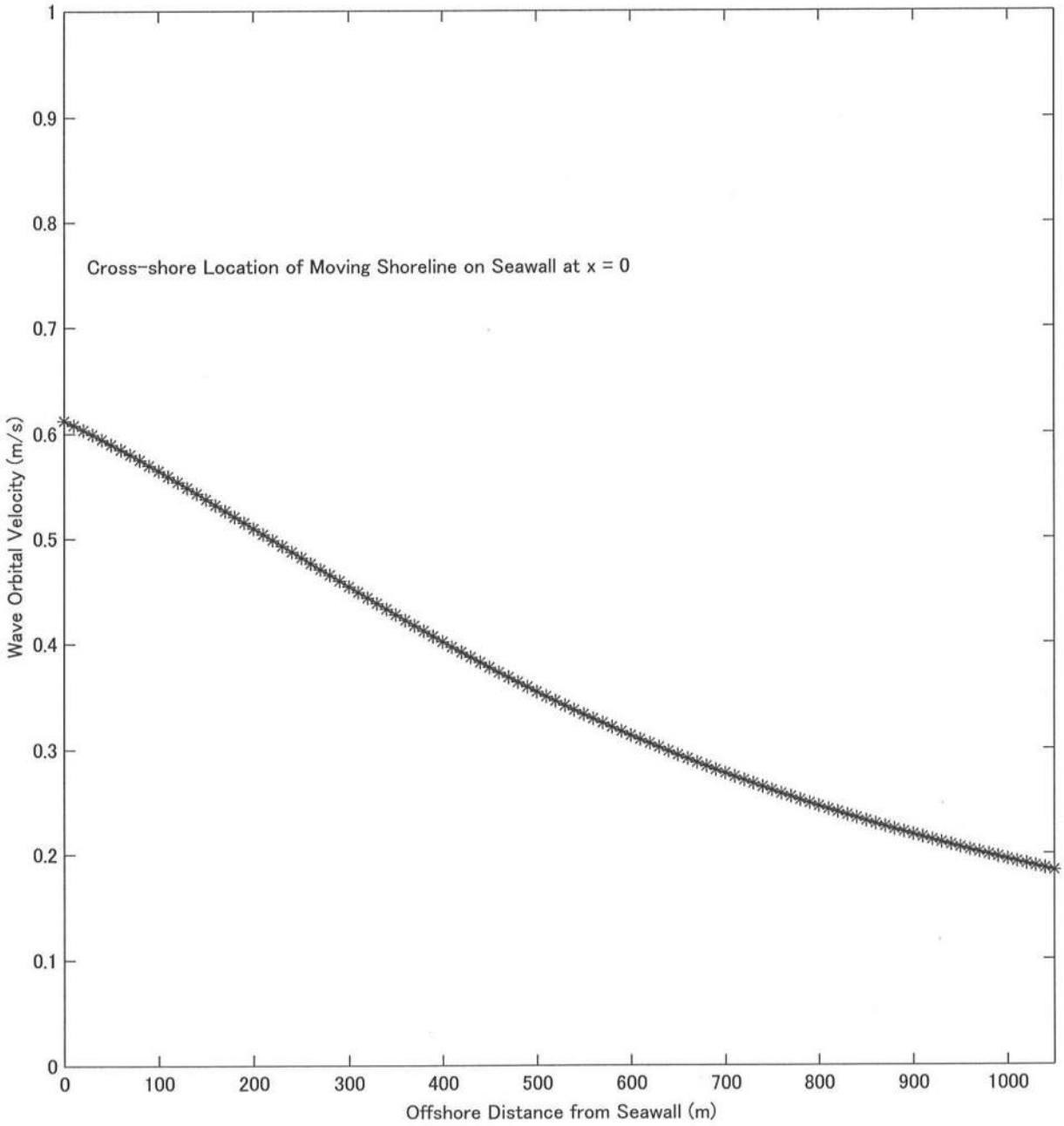

FIG. 62. Spatial Variation of Wave Orbital Velocity at Time = 10.5 hr for Eroded Left Profile on February 25, 2002

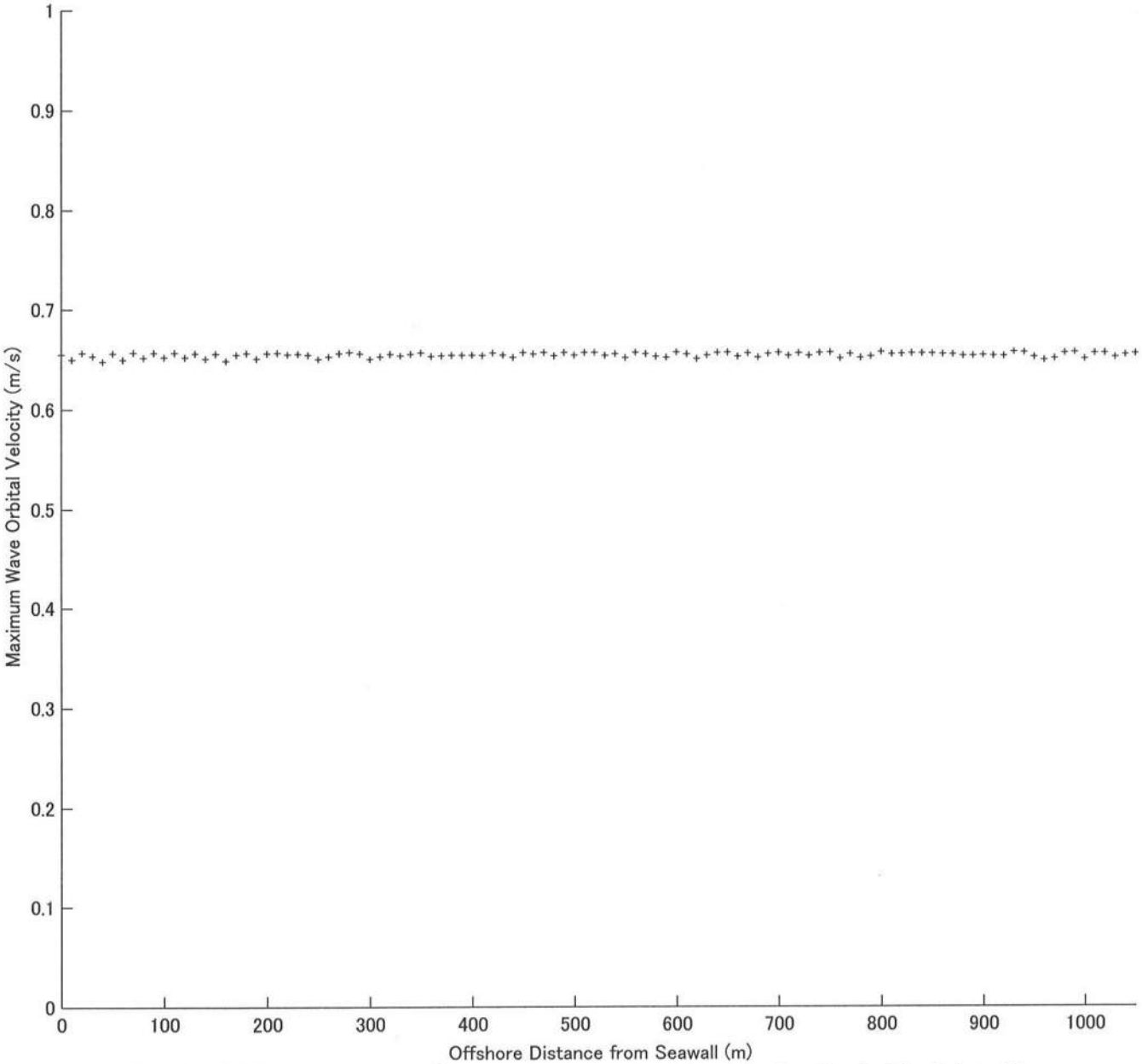

FIG. 63. Spatial Variation of Maximum Wave Orbital Velocity for Eroded Left Profile on February 25, 2002

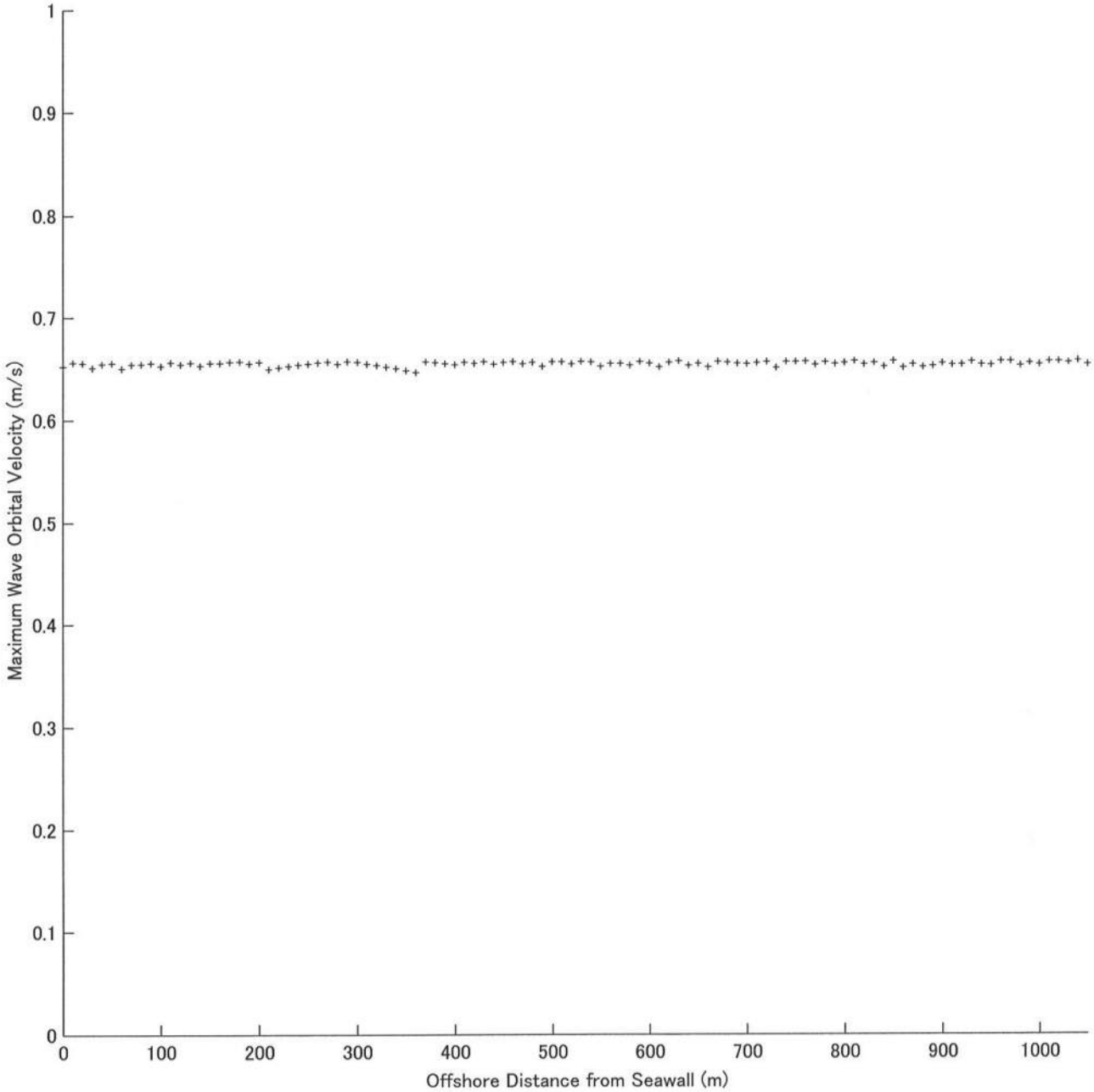

FIG. 64. Spatial Variation of Maximum Wave Orbital Velocity for Accreted Left Profile on October 31, 2001

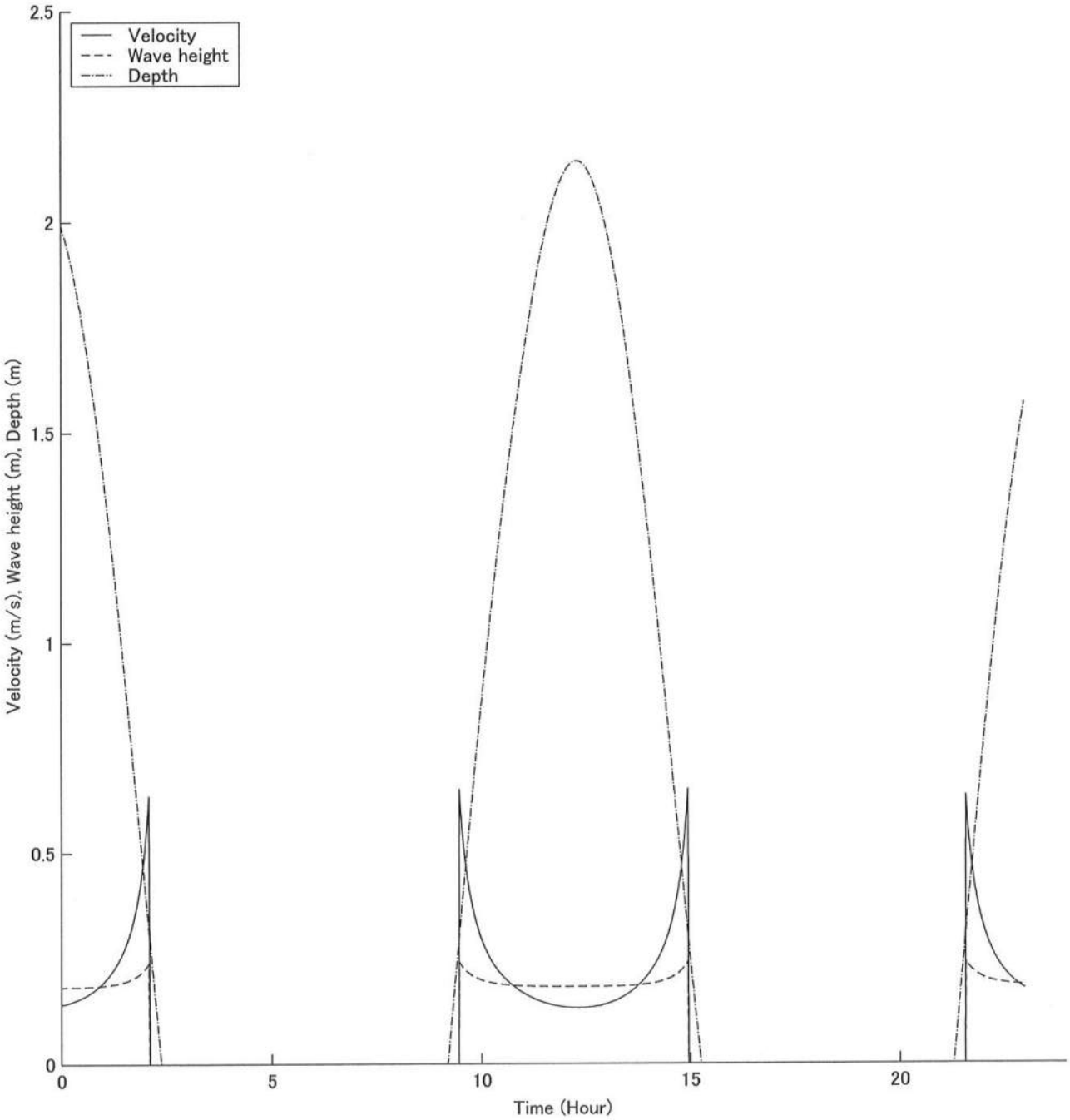

Fig. 65. Temporal Variations of Wave Orbital Velocity, Wave Height, and Water Depth at 100 m Offshore for Eroded Left Profile on February 25, 2002

Figs. 66 shows the time series of the depth-averaged tidal current and wave orbital velocity at 100 m offshore on the eroded left profile. The wave orbital velocity and the depth-averaged tidal currents become large when the water depth is small. These computed results indicate that wind waves may play an important role in mud suspension and transport. Muddy sediments can easily be transported over long distances in suspension and a local equilibrium of sediment may not exist (Lee and Mehta 1997). Thus, the combined effects of tides and wind waves will need to be accounted for to predict the mud transport.

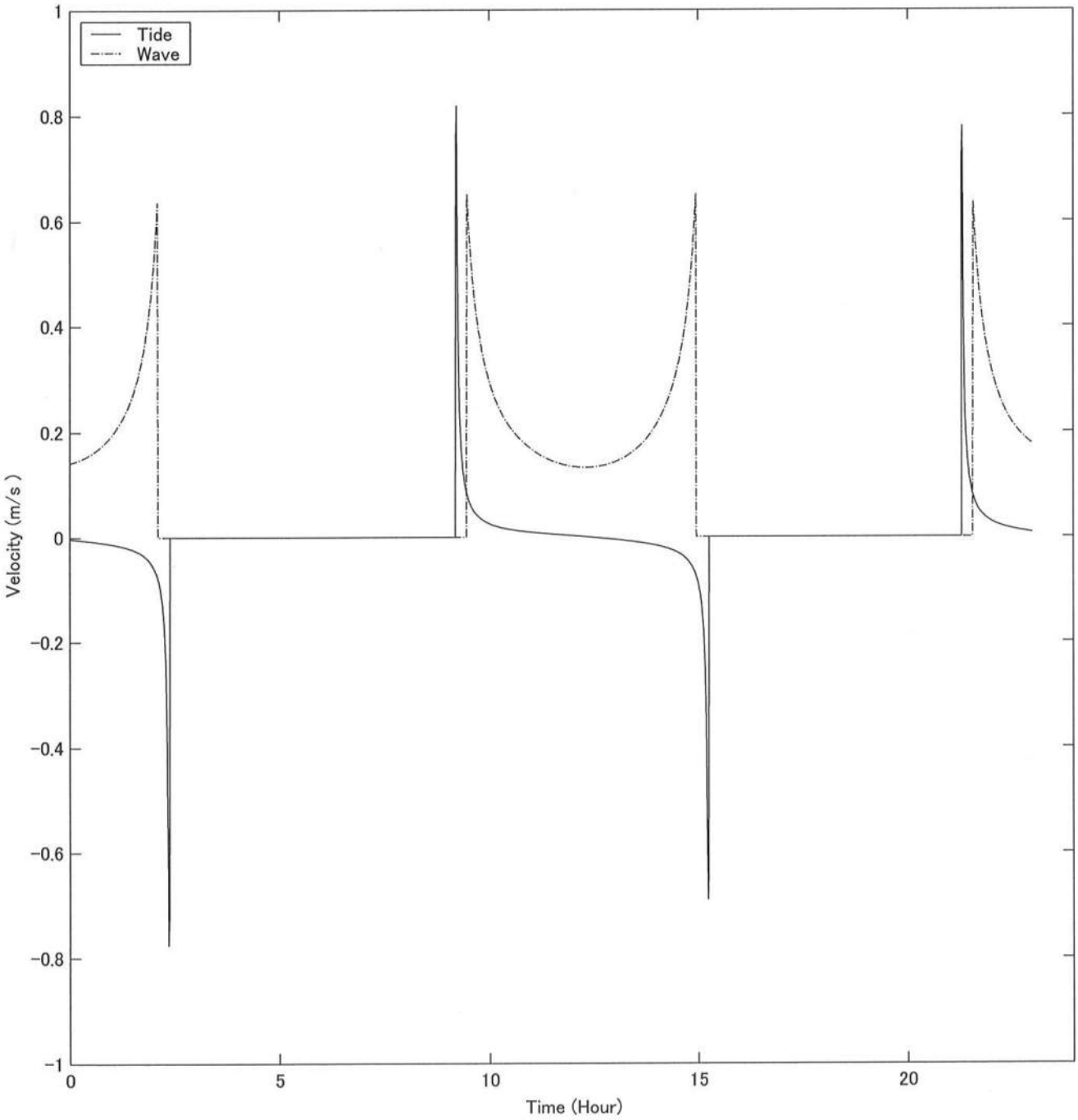

FIG. 66. Time Series of Depth-Averaged Tidal Cirrent and Wave Orbital Velocity at 100 m for Eroded Left Profile on February 25, 2002

Chapter 7

CONCLUSIONS

Knowledge of the morphological changes of mudflats due to long-term sea level rise is essential for the long-term environmental protection and management in estuaries and inner bays. However, no quantitative model exists to predict the temporal variation of the mudflat profile under time-varying driving forces. In order to facilitate the evaluation of the dominant causes of mudflat cross-shore profile changes on meso-tidal mudflats in the vicinity of the Shirakawa River mouth, a parameterized mudflat profile with no nearshore bar is proposed using a quadratic polynomial equation fitted to the measured bed levels where the equilibrium profile approach and Empirical Orthogonal Eigenfunction method (EOF) for sandy beaches are shown to be ineffective for mudflat profiles.

The time series of the three parameters for the vertical displacement, mean slope and quadratic convexity are correlated with those of the tide level, tidal range, wind waves, winds, and rainfall related to river discharge in order to identify the dominant oceanographic factors. The vertical displacement and mean slope parameters are shown to have relatively high correlations without any time lag with the seasonal tide level change of approximately 40 cm. The predominant driving forces for the quadratic convexity parameter are not certain but may be

related with the average tide level, averaged spring-neap tidal range, and rainfall. The findings of this study will be used in future to develop a meso-tidal mudflat morphological model based on the three profile parameters varying with time.

The depth-averaged tidal currents and wave orbital velocities are computed numerically to estimate the relative importance of tides and waves in causing the sediment transport on the meso-tidal mudflats. The computed results indicate that wind waves may play an important role in mud suspension and transport and that the combined effects of tides and wind waves will need to be taken into account for the sediment transport on the mudflats where tidal currents are more important on mudflats than sandy beaches. However, existing cross-shore beach profile models, which usually consist of three modules for hydrodynamics, sediment transport and beach profile evolution, cannot predict the long-term cycle of beach erosion and recovery caused by sequences of storms partly because no sediment advection is accounted for in the existing models (Kobayashi 2002).

More recently, the time dependent cross-shore sand transport model called CBREAK, which includes sand suspension, storage, advection, and settling, was developed and verified by Kobayashi and Johnson (2001) and Kobayashi and Tega (2002). Therefore, CBREAK could be modified for mud sediment suspension, storage, advection, and settling and compared with field measurements of sediment concentrations and velocities in order to examine the detailed sediment dynamics on the mudflat.

REFERRENCES

ASCE Task Committee on Sea Level Rise and Its Effects on Bays and Estuaries. (1992). "Effects of sea-level rise on bays and estuaries." *J. Hydralic. Engrg.*, ASCE, 118 (1), 1-10.

Anderson, F. E., Black, L., Watling, L. E., Mook, W., and Mayer, L. M. (1981). "A temporal and spatial study of mudflat erosion and deposition." *J. of Sed. Petrology*, 51, 729-736.

Aubrey, D. G. (1979). "Seasonal patterns of onshore/offshore sediment movement." *J. Geophys. Res.*, 84(C10), 6347-6354.

Bale, A. J., Morris, A. W., and Howland, R. J. M. (1985). "Seasonal sediment movement in the Tamar estuary." *Oceanol. Acta*, 8, 1-6.

Bassoullet, P., Hir, P. L., Gouleau, D., and Robert, S. (2000). "Sediment transport over an intertidal mudflat: Field investigations and estimation of fluxes within the Baie de Marennes-Oleron (France)" *Cont. Shelf Res.*, 20, 1635-1653.

Bruun, P. (1962). "Sea-level rise as a cause of shore erosion." *J. Wtrwy., Harbors Div.*, ASCE, 88, 117-130.

Bruun, P. (1983). "Review of conditions for uses of the Bruun rule of erosion." *Coast. Engrg.*, 7, 77-89.

Christie, M. C., Dyer, K. R., and Turner, P. (1999). "Sediment flux and bed level measurements from a macro tidal mudflat." *Estuarine, Coastal and Shelf Science*, 49, 667-688.

Christie, M. C., Dyer, K. R., and Turner, P. (2001). "Observations of long and short term variations in the bed elevation of a macro-tidal mudflat." *Coastal and estuarine fine sediment processes,* McAnally W.H., and A.J. Mehta, eds., Elsevier, Amsterdam, 323-342.

Dean, R. G. (1991). "Equilibrium beach profile: Characteristics and applications." *J. Coast. Res.*, 7 (1), 53-84.

Dean, R. G., and Dalrymple, R. A. (2002). *Coastal processes with engineering applications*, Cambridge Univ. Press, Cambridge, U.K.

Dick, J. E., and Dalrymple, R. A. (1984). "Short and long term beach changes at Bethany beach, Delaware." *Proc., 19th Coast. Engrg. Conf.*, ASCE, 1650-1667.

Dieckmann, R., Osterthun, M., and Partenscky, H.-W. (1987). "Influence of water-level elevation and tidal range on the sedimentation in a German tidal flat area." *Progress in Oceanography*, 18, 151-166.

Dyer, K. R. (1998). "The typology of intertidal mudflats." *Sedimentary processes in the intertidal zone*, Black, K. S., Paterson, D. M., and Cramp, A. eds., Geological Society, London, 11-24.

Dyer, K. R., Christie, M. C., and Wright, E. W. (2000). "The classification of intertidal mudflats." *Cont. Shelf Res.*, 20, 1039-1060.

Friedrichs, C. T., Lynch, D. R. and Aubrey, D. G. (1992). "Velocity asymmetries in frictionally-dominated tidal embayment: longitudinal and lateral variability." *Dynamics and exchanges in estuaries and the coastal zone*, D. Prandle, ed., Am. Geophys. Union, Washington, D.C., 277-312.

Friedrichs, C. T., and Aubrey, D. G. (1996). " Uniform bottom shear stress and equilibrium hypsometry of intertidal flats." *Mixing in estuaries and coastal seas*, C. Pattiaratchi, ed., Am. Geophys. Union, Washington, D.C., 405-429.

Frostick, L. E., and McCave, I. N. (1979). "Seasonal shifts of sediment within an estuary mediated by algal growth." *Estuarine and Coastal Marine Science*, 9, 569-576.

Hayes, M. O. (1975). "Morphology of sand accumulation in estuaries: An introduction to the symposium." *Estuarine Rresearch*, L. E. Cronin, ed., Academic Press, New York, 2, 3-22.

Intergovernmental Panel on Climate Change. (2001). "Third assessment report: Climate change 2001: Synthetic report." IPCC, Geneva, Switzerland, (www.ipcc.ch)

Isozaki, I., and Kitahara, E. (1977). "Tides in the Bays of Ariake and Yatsusiro." *Oceanogr. Mag.*, 28 (1-2), 1-32.

Japanese Standard Association. (2000a). ''JIS A 1204: Test method for particle size distribution of Soils."

Japanese Standard Association. (2000b). ''JIS A 1226: Test method for ignition loss of Soils."

Kirby, R. (1992). "Effects of sea-level rise on muddy coastal margins." *Dynamic and exchanges in estuaries and in the coastal zone*, D. Prandle, ed., Am. Geophys. Union, Washington, D.C., 313-334.

Kirby, R., Bleakley, R. J., Weatherup, S. T. C., Raven, P. J., and Donaldson, N. D. (1993). "Effect of episodic events on tidal mud flat stability, Ardmillan Bay, Strangford Lough, Northern Ireland." *Nearshore and estuarine cohesive sediment transport,* Mehta, A. J. ed., Am. Geophys. Union, Washington, D.C., 378-392.

Kirby, R. (2000). "Practical implications of tidal flat shape." *Cont. Shelf Res.*, 20, 1061-1077.

Kobayashi, N., DeSilva, G. S., and Watson, K. D. (1989). "Wave transformation and swash oscillation on gentle and steep slopes." *J. Geophys. Res.*, 94 (C1), 951-966.

Kobayashi, N., and Wurjanto, A. (1992). "Irregular wave setup and run-up on beaches." *J. Wtrwy., Port, Coast., Oc. Engrg.*, ASCE, 118 (4), 368-386.

Kobayashi, N., and Johnson, B. D. (2001). "Sand suspension, storage, advection, and settling in surf and swash zones." *J. Geophys. Res.*, 106 (C5), 9363-9376.

Kobayashi, N., and Tega, Y. (2002). "Sand suspension and transport on equilibrium beach." *J. Wtrwy., Port, Coast., Oc. Engrg.*, ASCE, 128 (6), 238-248.

Kobayashi, N. (2002). "Numerical modeling as a design tool for coastal structures." *Advances in coastal structure design* (in press)

LaFond, E. C. (1938)."Relationship between mean sea level and sand movement." *Science*, 88 (2274), 112-113.

Larson, M., Capobianco, M., and Hanson, H. (2000). "Relationship between beach profiles and waves at Duck, North Carolina, determined by canonical correlation analysis." *Marine Geology*, 163, 275-288.

Larson, M., Hanson, H., Kraus, N. C., and Newe, J. (1999). "Short- and long-term responses of beach fills determined by EOF analysis." *J. Wtrwy., Port, Coast., Oc. Engrg.*, ASCE, 125 (6), 285-293.

Lee, S.-C., and Mehta, A. J. (1997). "Problems in characterizing dynamics of mud shore profiles." *J. Hydraulic. Engrg.*, ,ASCE, 123 (4), 351-361.

Lisitzin, E., and Pattullo, J. G. (1961). "The principal factors influencing the seasonal oscillation of sea level." *J. Geophys. Res.*, 66 (3), 845-852.

Mehta, A. J., Kirby, R., and Lee, S.-C.(1996). "Some observations on mudshore dynamics and stability." *Rept. No. UFL/COEL/MP-96/1*, Univ. of Florida, Gainesville, Fla.

O'Brien, D. J., Whitehouse, R. J. S., and Cramp, A. (2000). "The cyclic development of a macrotidal mudflat on varying time scales." *Cont. Shelf Res.*, 20, 1593-1619.

Paterson, D. M. (1997)."Biological mediation of sediment erodibility: ecology and physical dynamics." *Cohesive sediments,* Burt, N., Parkwe, R., and J. Watts, eds., John Wiley, Chichester, UK, 215-229.

Pattullo, J.G., Munk, W. H., and Revelle, R., and Strong, E. (1955). "The seasonal oscillation in sea level." *J. Marine Res.*, 14 (1), 88-155.

Pritchard, D., Hogg, A. J., and Roberts, W. (2002)."Morphological modeling of intertidal mudflats: the role of cross-shore tidal currents." *Cont. Shelf Res.*, 22, 1887-1895.

Roberts, W., and Whitehouse, R. J. S. (2001). "Predicting the profile of intertidal mudflats formed by cross-shore tidal currents." *Coastal and estuarine fine sediment processes,* McAnally W.H., and A.J. Mehta, eds., Elsevier, Amsterdam, 263-285.

Teisson, C., Ockenden, M., Hir, P. L., Kranenburg, C., and Hamm, L. (1993). "Cohesive sediment transport processes." *Coast. Engrg.*, 21, 129-162.

Tsuruya, H., Murakami, K., and Irie, I. (1990). "Mathematical modeling of mud transport in ports with a multi-layered model: Application to Kumamoto port." *Rept. of the Port and Harbor research Institute*, 29 (1), 3-51.

Unoki, S. (1983). "Annual variation of the mean sea level and its inclination in a bay." *Coast. Engrg. in Japan,* 26, 219-234.

Wijnberg, K. M., and Terwindt, J. H. J. (1995). "Extracting decadal morphological behavior from high-resolution, long-term bathymetric surveys along the Holland coast using eigenfunction analysis." *Marine Geology*, 126, 301-330.

Winant, C. D., Inman, D. L., and Nordstorm, C. E. (1975). "Description of seasonal beach changes using empirical eigenfunctions." *J. Geophys. Res.*, 80 (15), 1979-1986.

Yamada, F., Kakinoki, T., Nishiyama, D., and Tsujimoto, G. (2001). "Tidal currents and environmental characteristics for Ariake Bay." *Proc. Water Pollution Control and Prediction Technology in the Tidal Waters*, Dalian, China, 7-12.

APPENDIX

Figs. A-1 to A-17 : Quadratic Equation Fitted to the Left Profile

Figs. A-18 to A-34: Quadratic Equation Fitted to the Right Profile

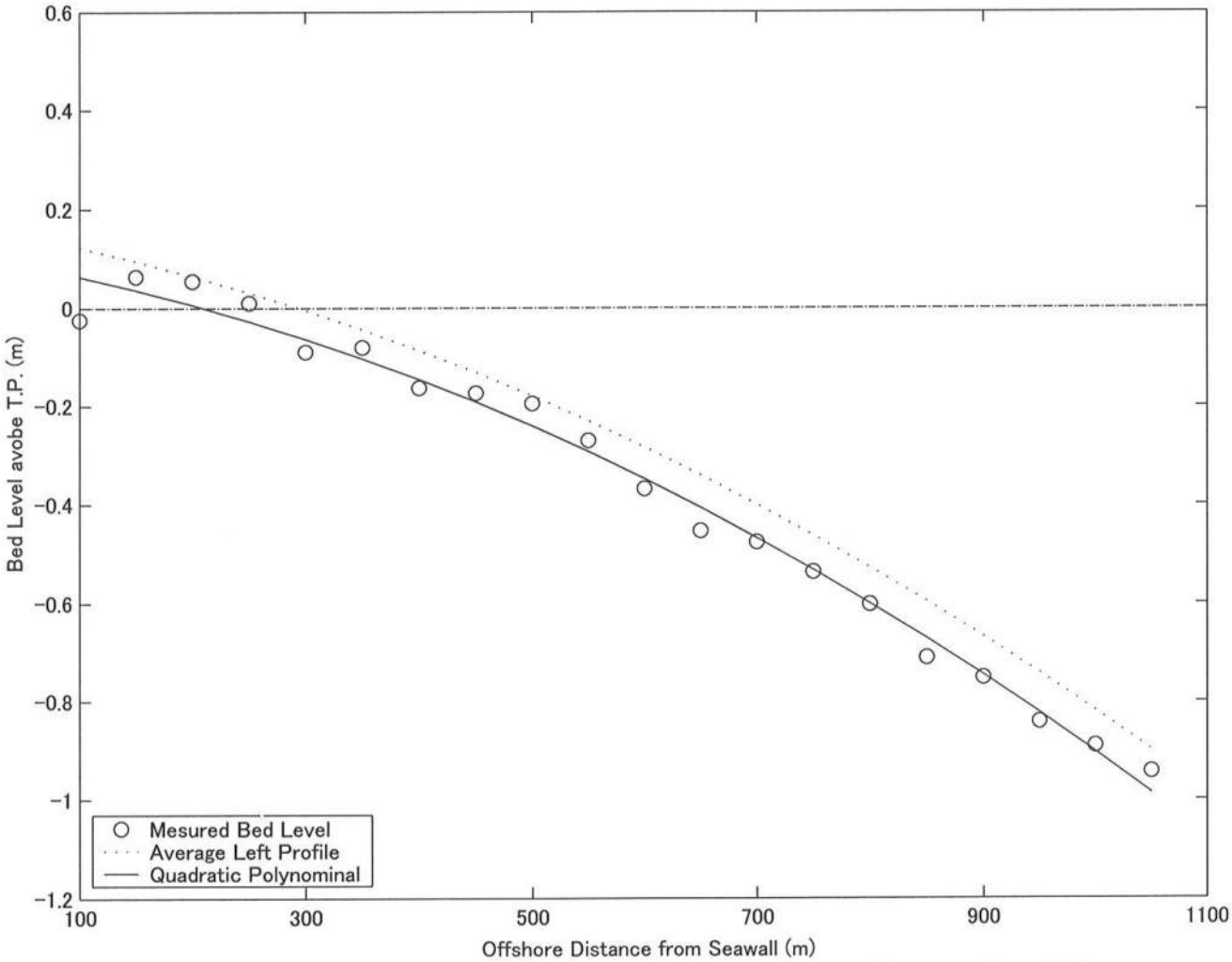

FIG. A-1. Quadratic Equation Fitted to the Left Profile on February 22, 2001

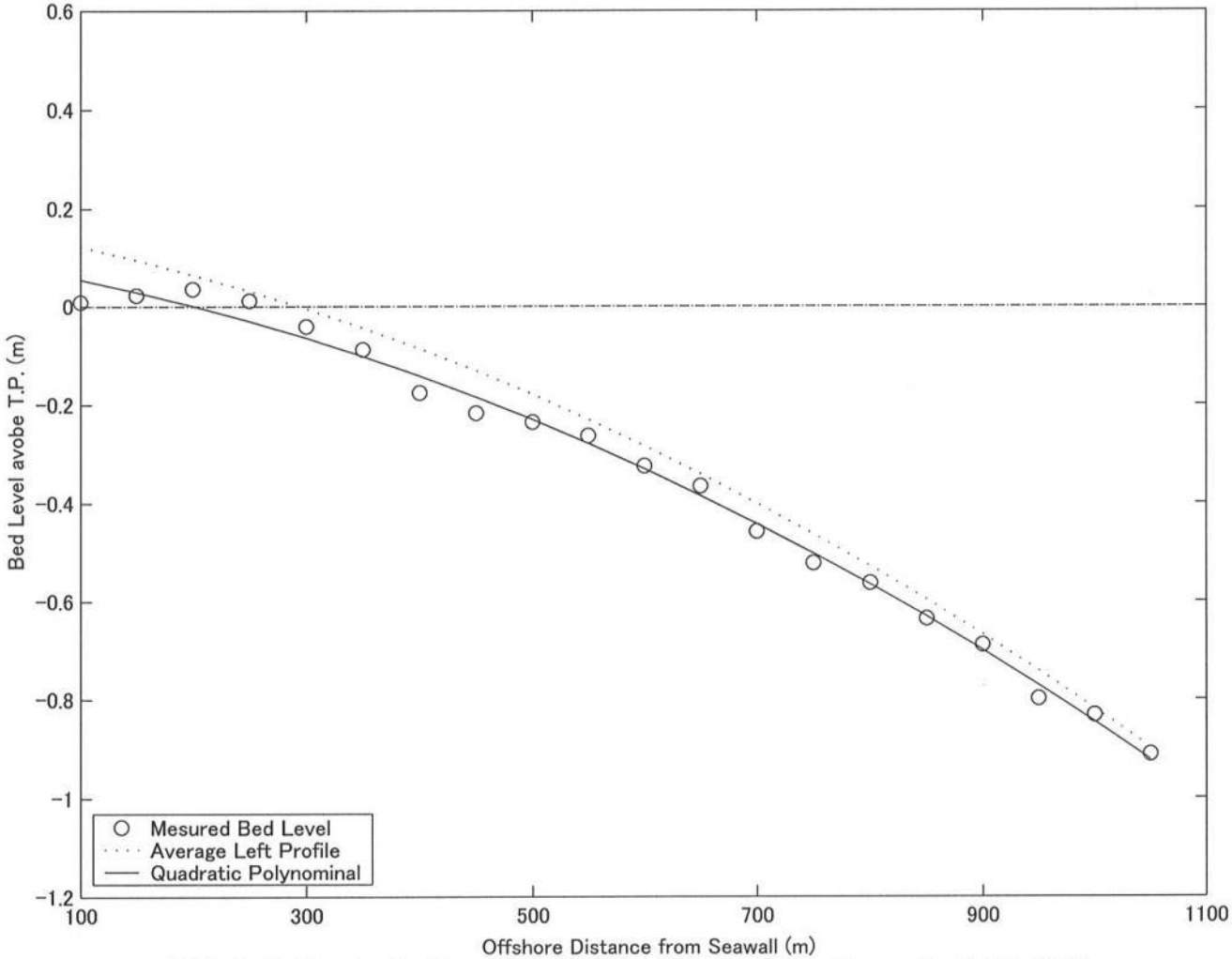

FIG. A-2. Quadratic Equation Fitted to the Left Profile on April 23, 2001

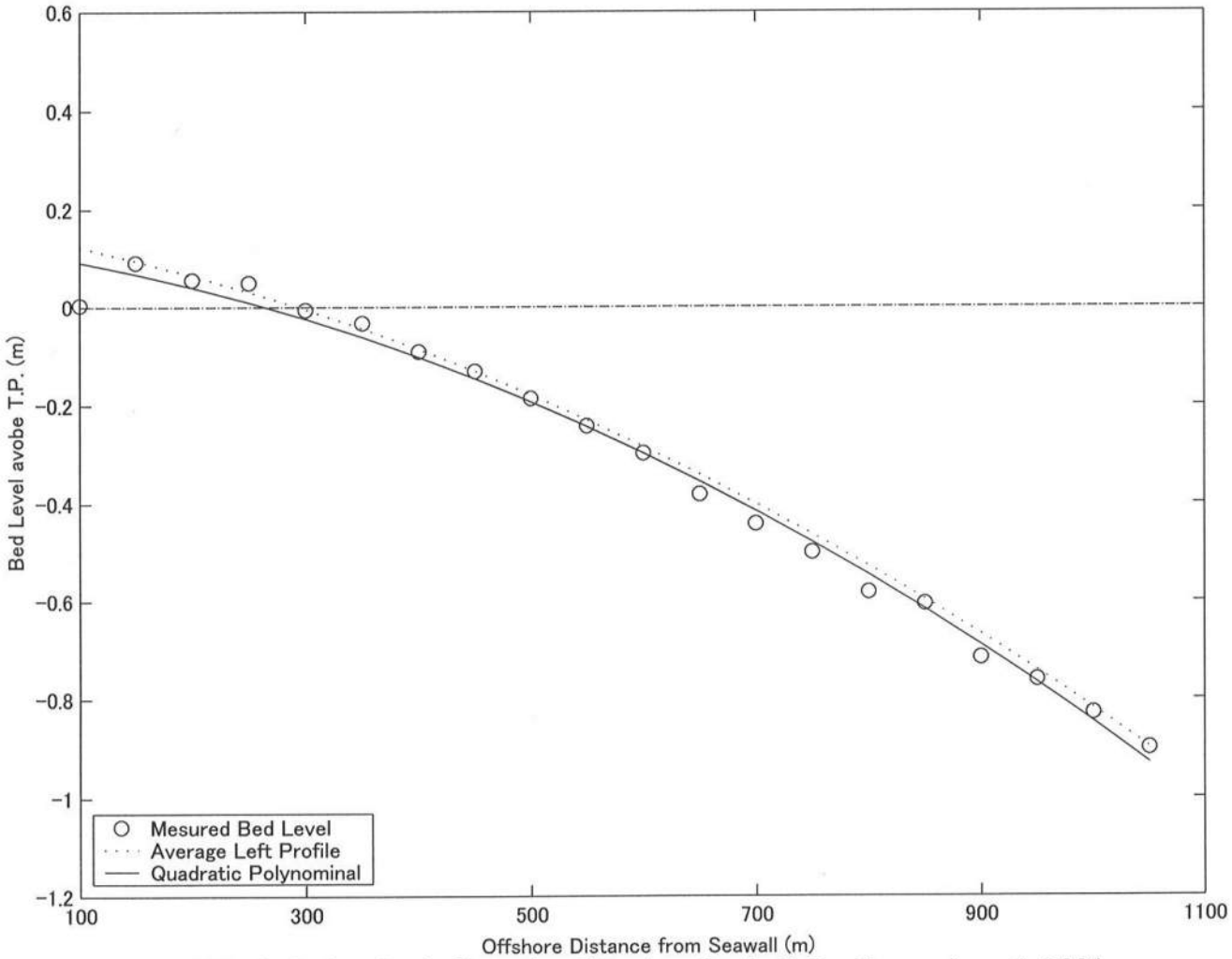

FIG. A-3. Quadratic Equation Fitted to the Left Profile on June 1, 2001

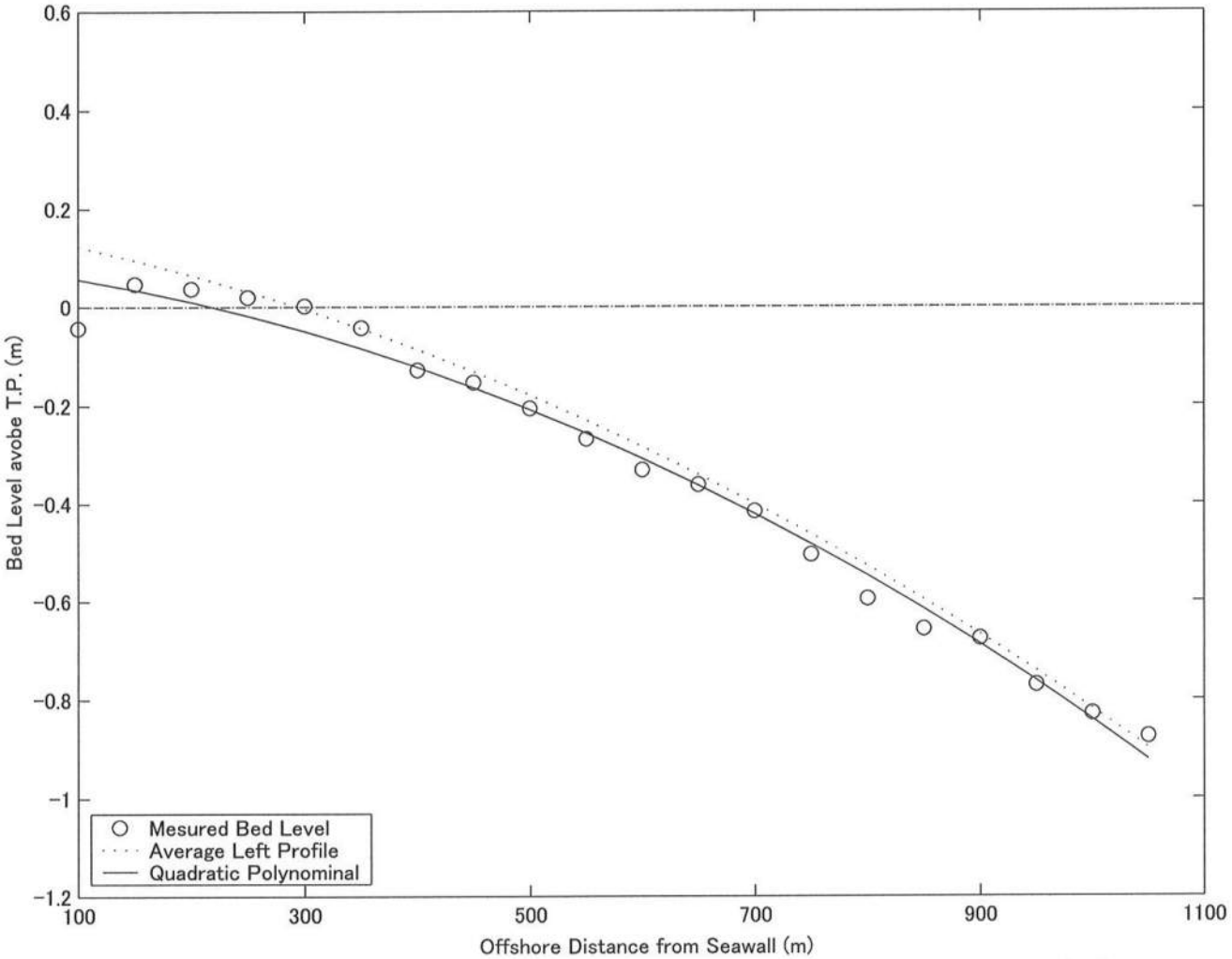

FIG. A-4. Quadratic Equation Fitted to the Left Profile on July 2, 2001

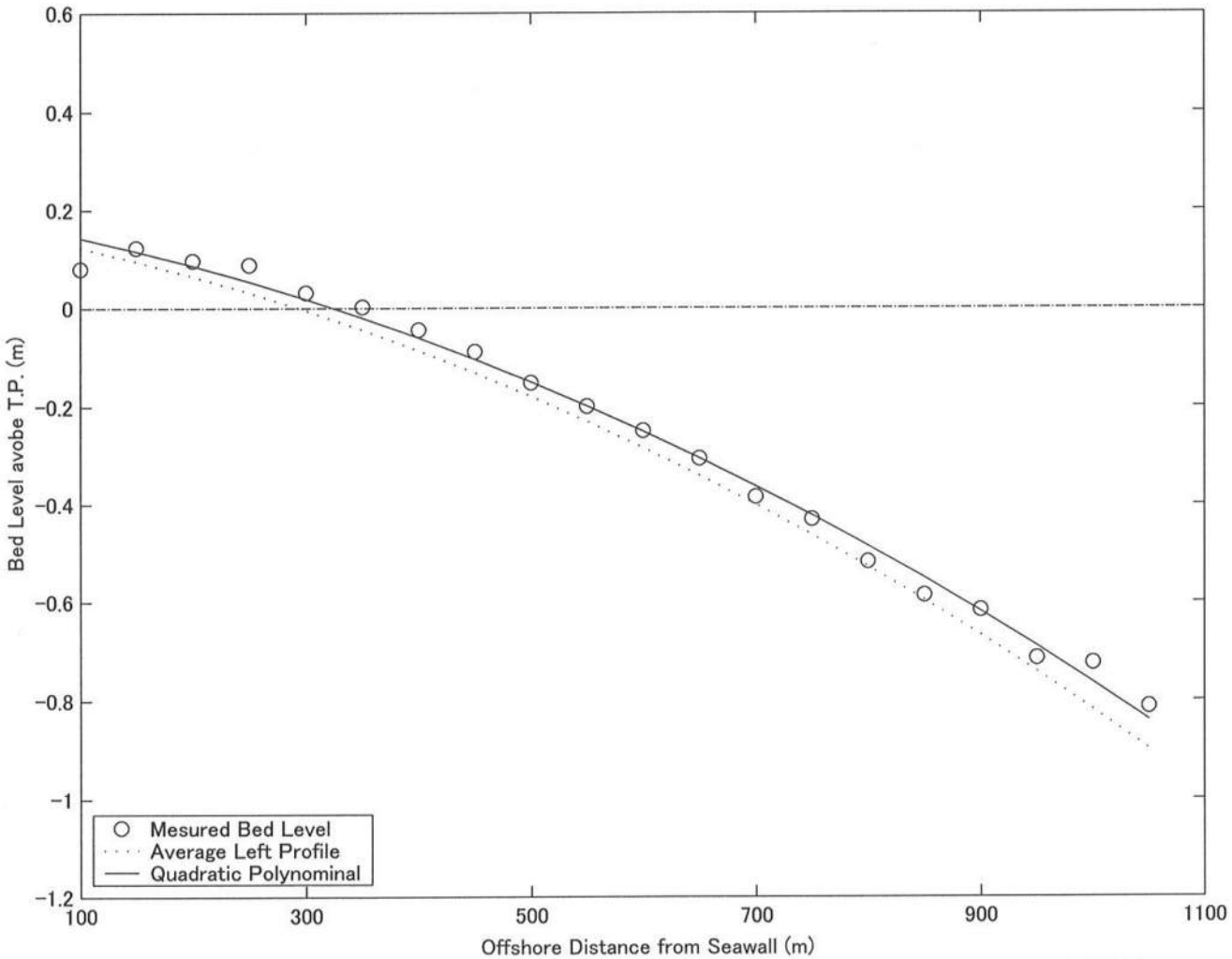

FIG. A-5. Quadratic Equation Fitted to the Left Profile on September 4, 2001

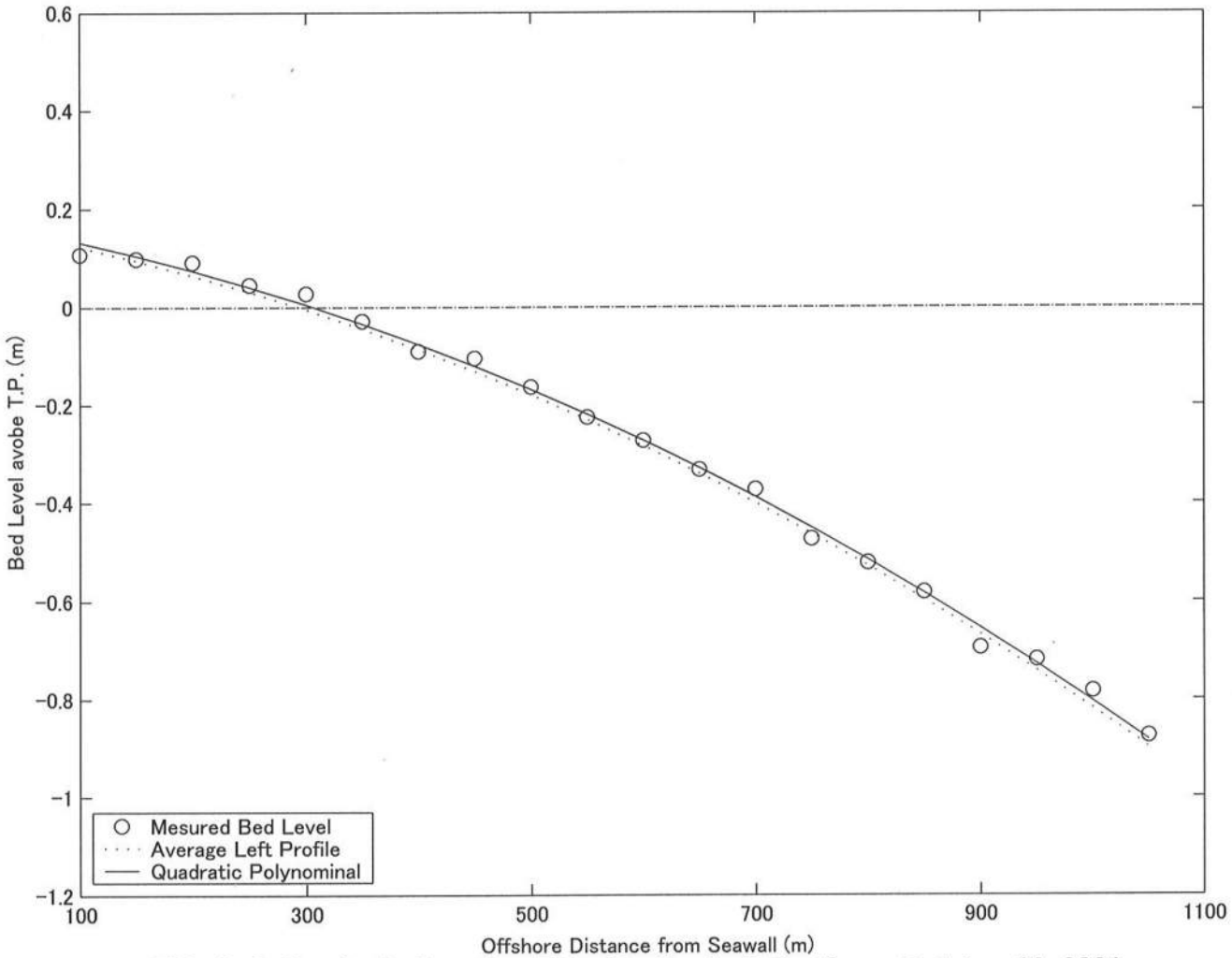

FIG. A-6. Quadratic Equation Fitted to the Left Profile on October 18, 2001

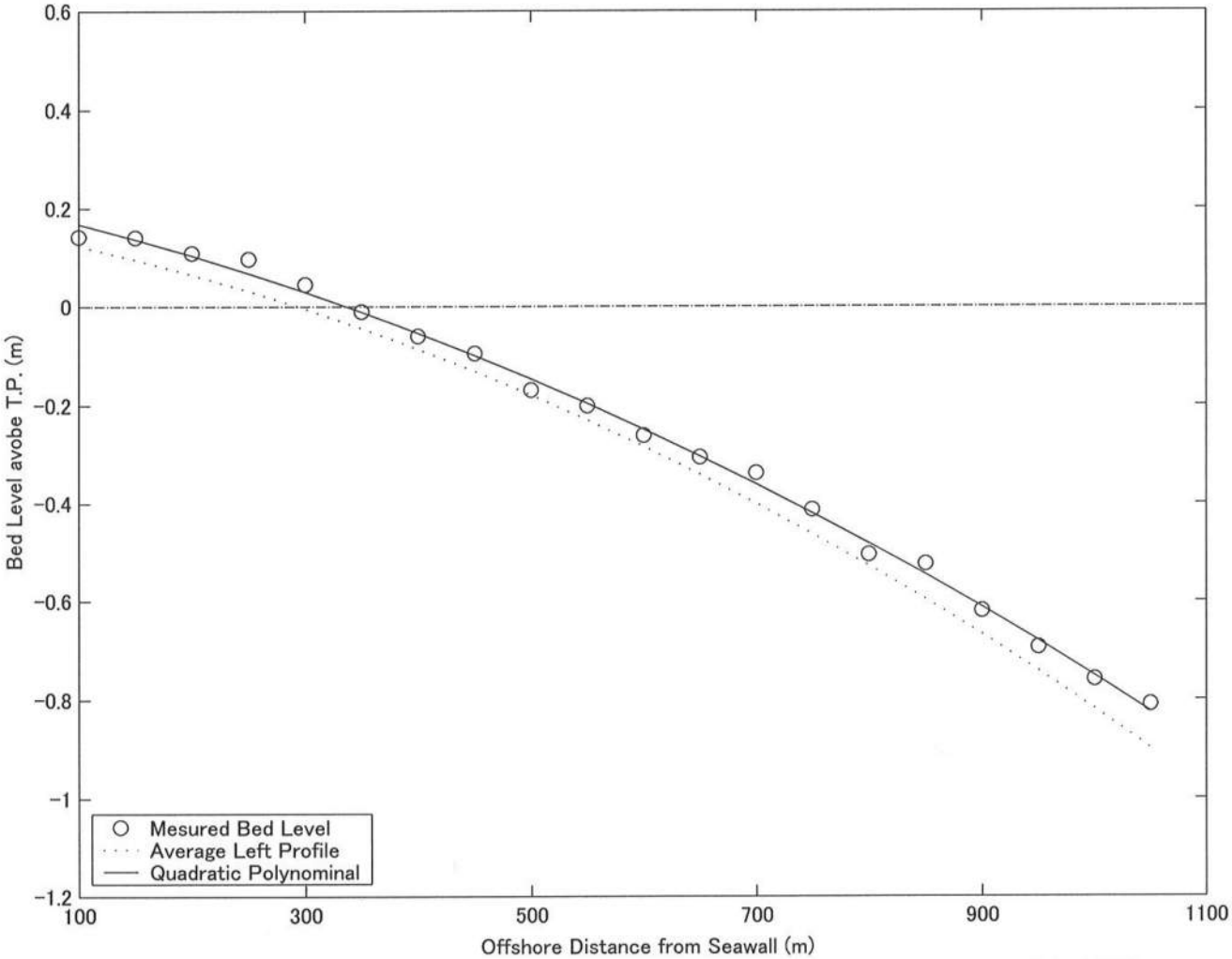

FIG. A-7. Quadratic Equation Fitted to the Left Profile on October 31, 2001

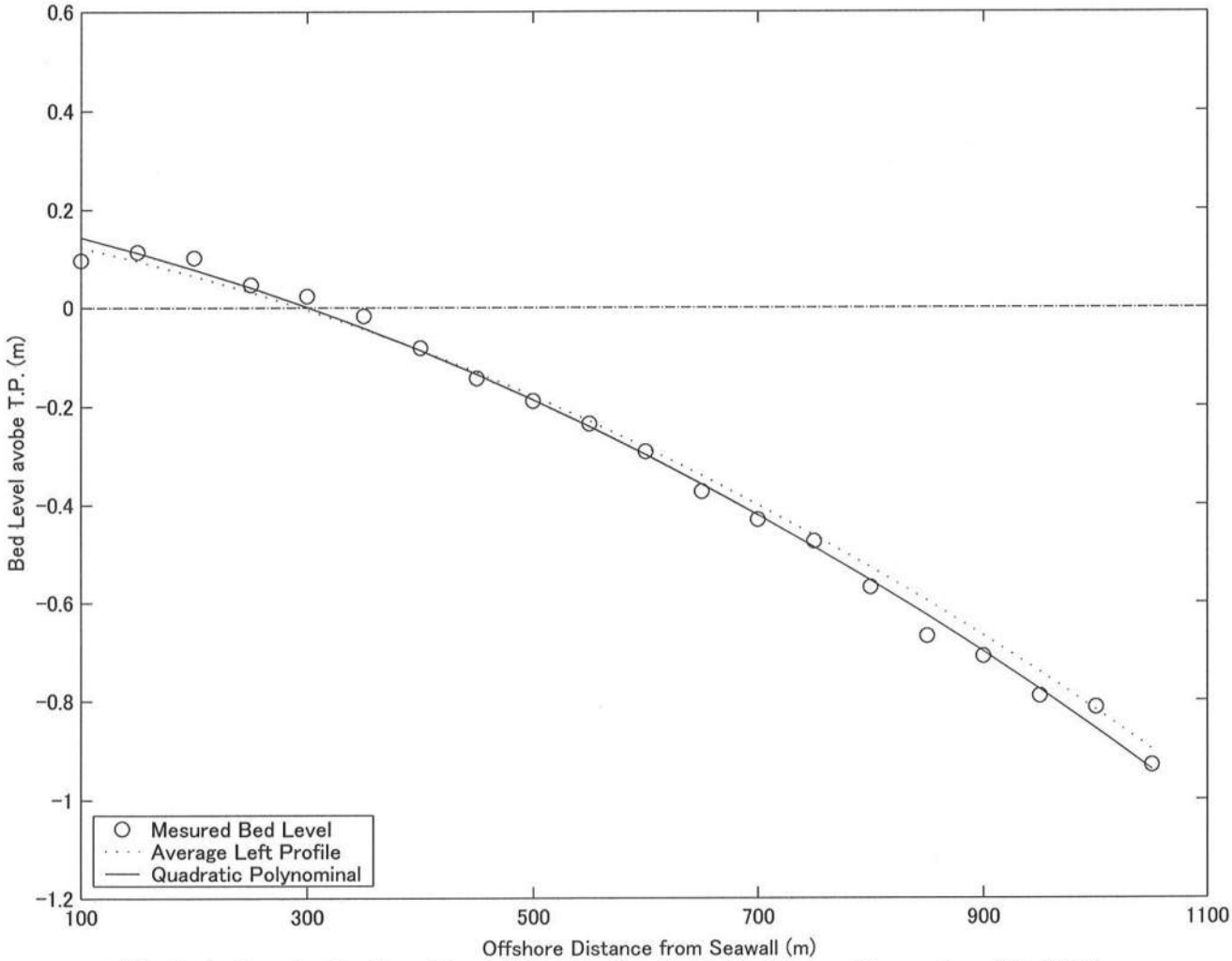

FIG. A-8. Quadratic Equation Fitted to the Left Profile on November 28, 2001

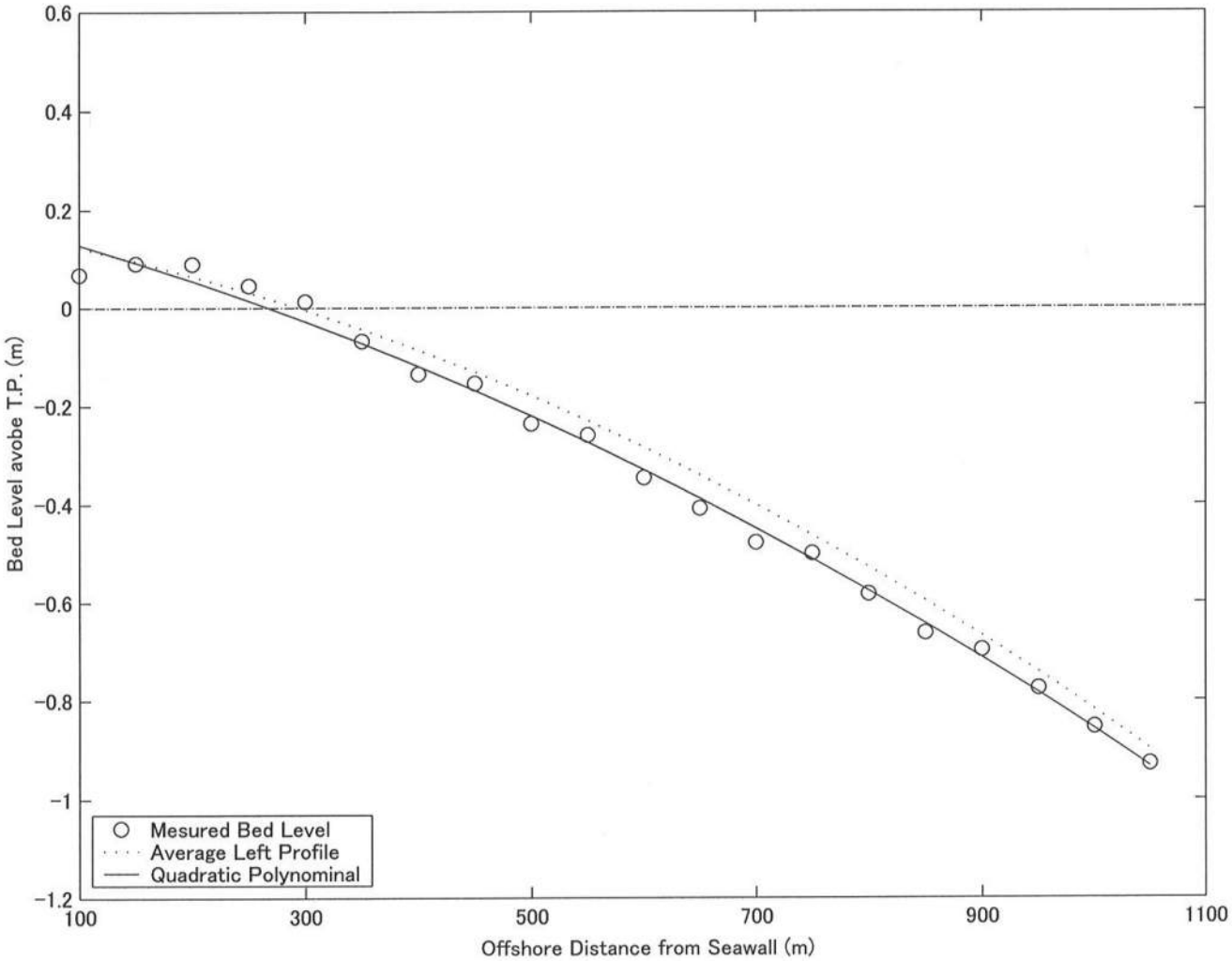

FIG. A-9. Quadratic Equation Fitted to the Left Profile on December 26, 2001

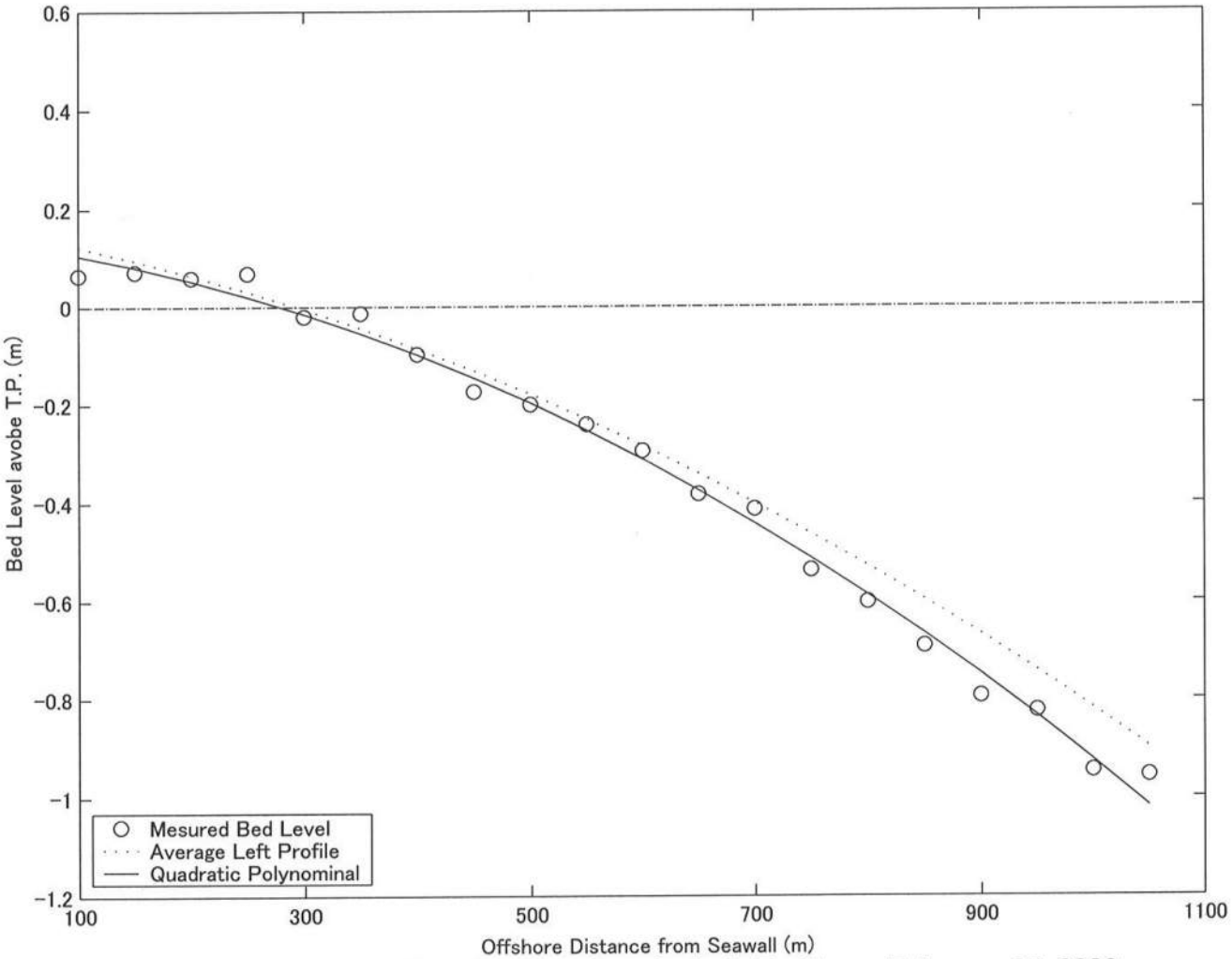

FIG. A-10. Quadratic Equation Fitted to the Left Profile on February 25, 2002

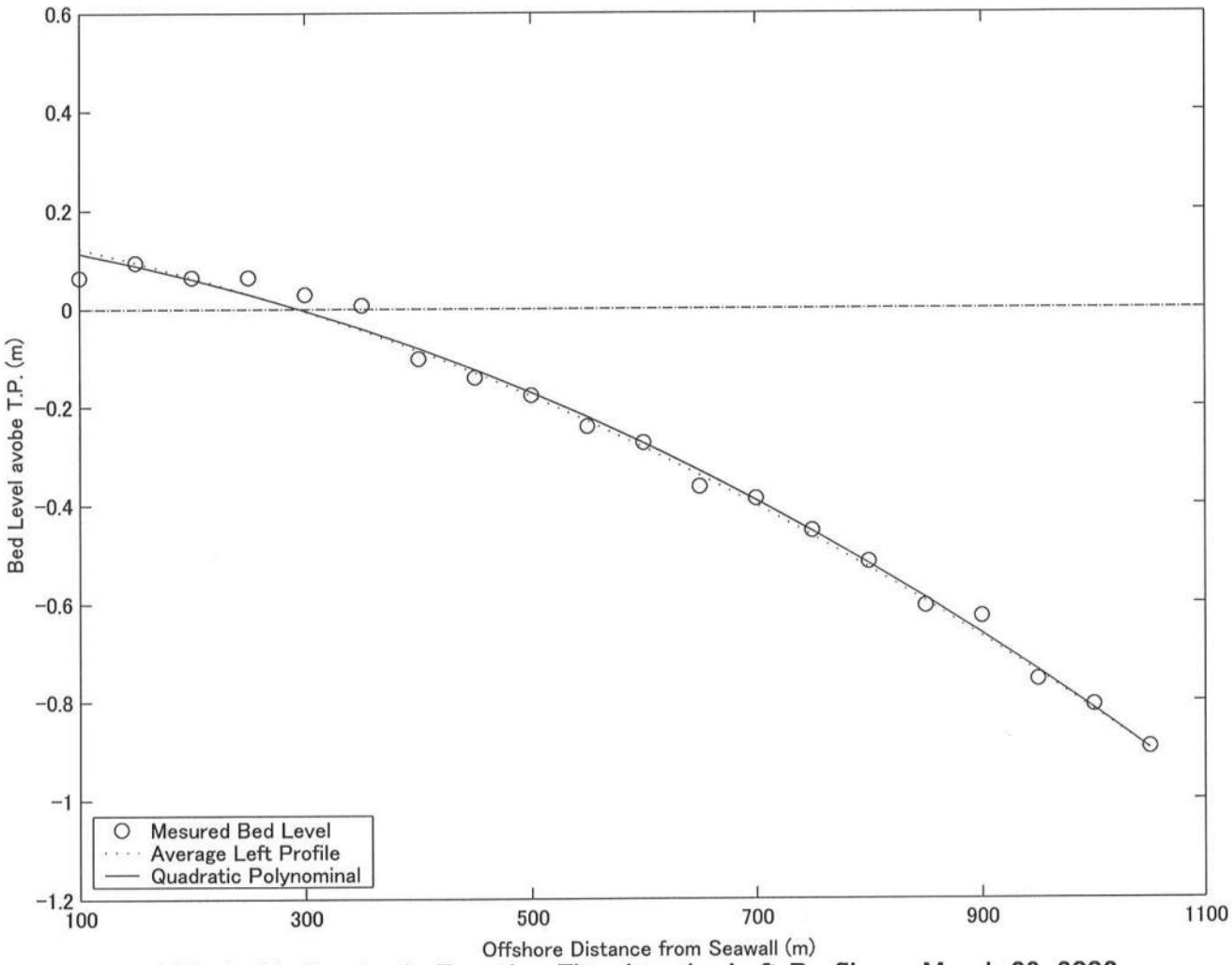

FIG. A-11. Quadratic Equation Fitted to the Left Profile on March 29, 2002

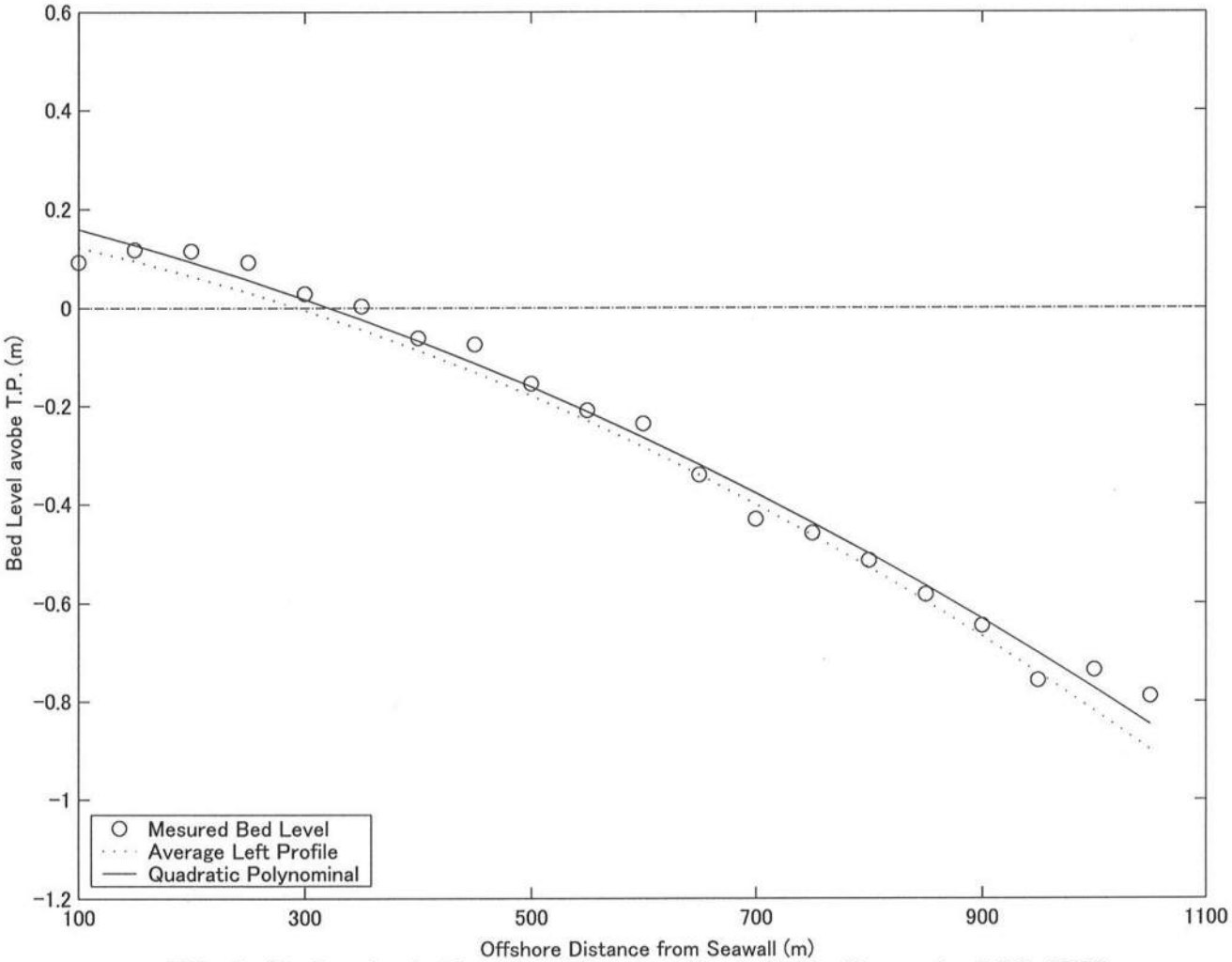

FIG. A-12. Quadratic Equation Fitted to the Left Profile on April 26, 2002

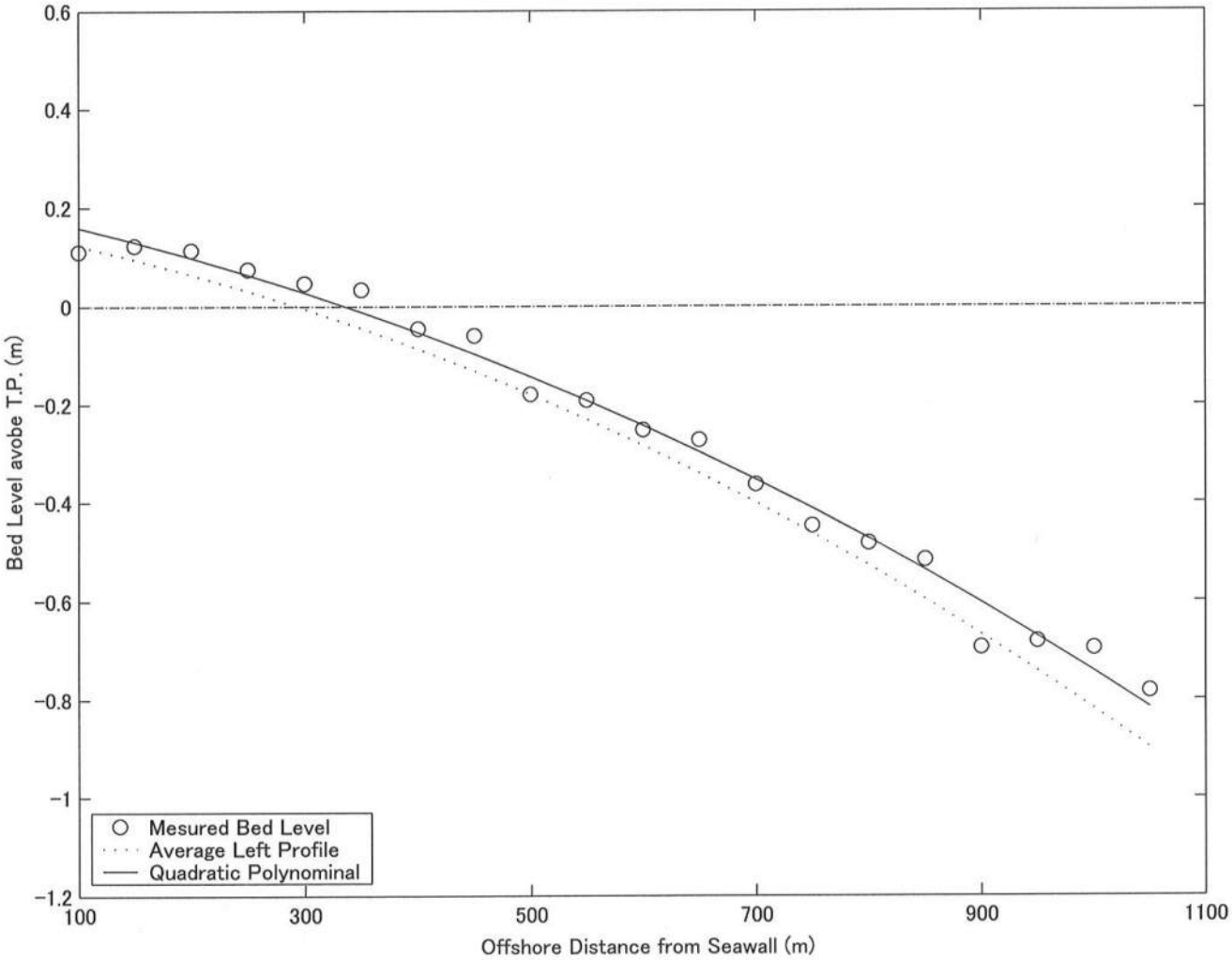

FIG. A-13. Quadratic Equation Fitted to the Left Profile on June 13, 2002

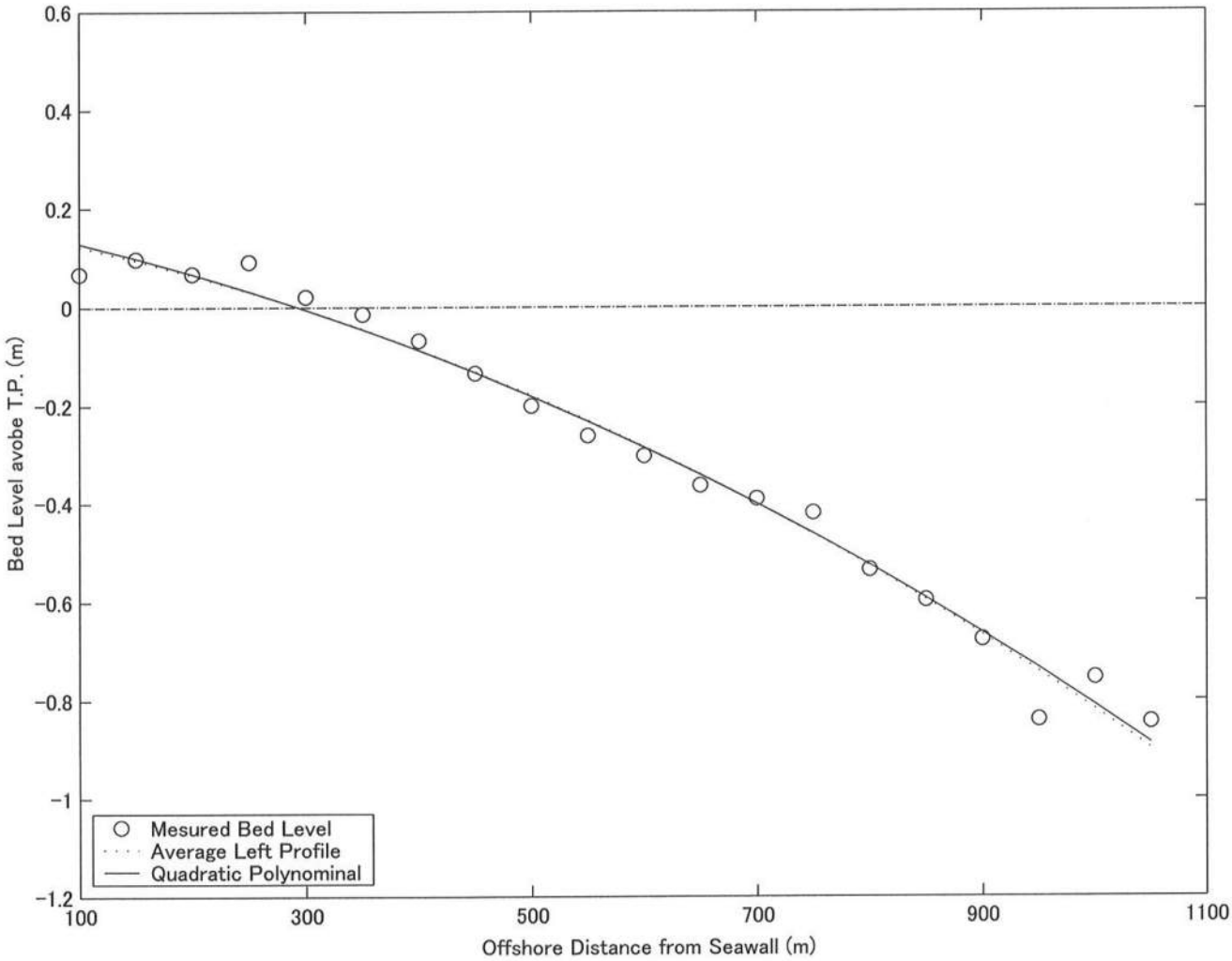

FIG. A-14. Quadratic Equation Fitted to the Left Profile on July 8, 2002

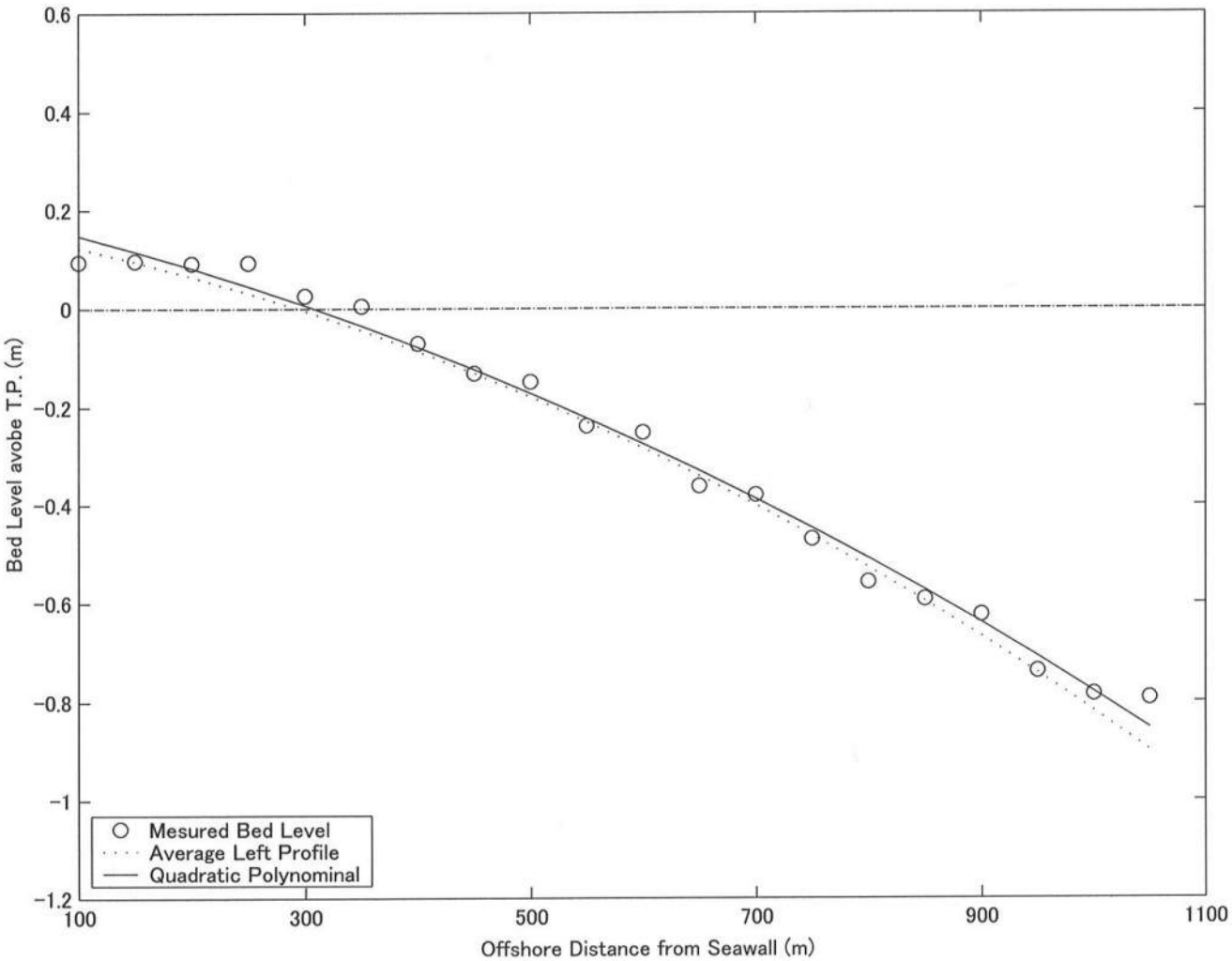

FIG. A-15. Quadratic Equation Fitted to the Left Profile on October 21, 2002

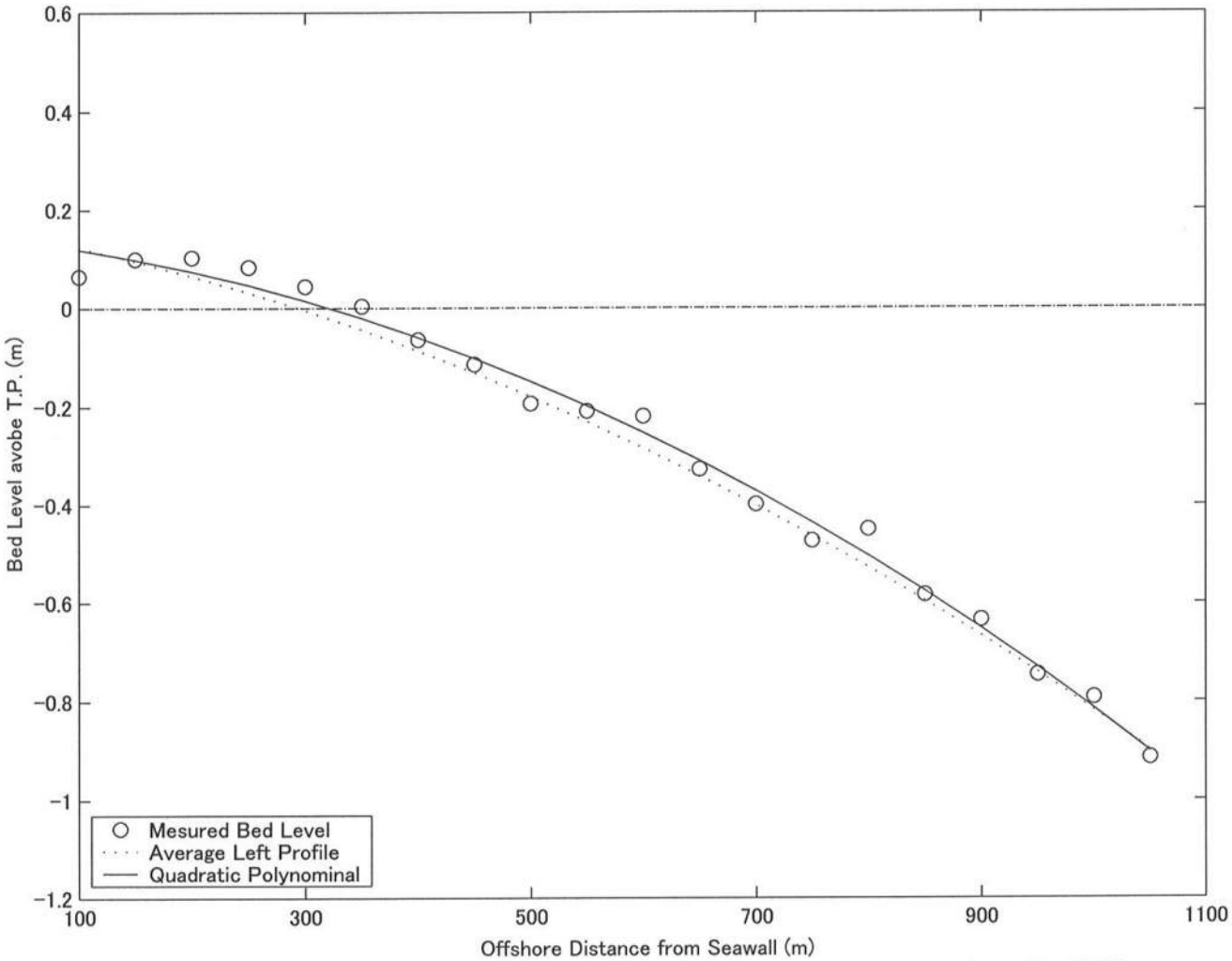

FIG. A-16. Quadratic Equation Fitted to the Left Profile on November 19, 2002

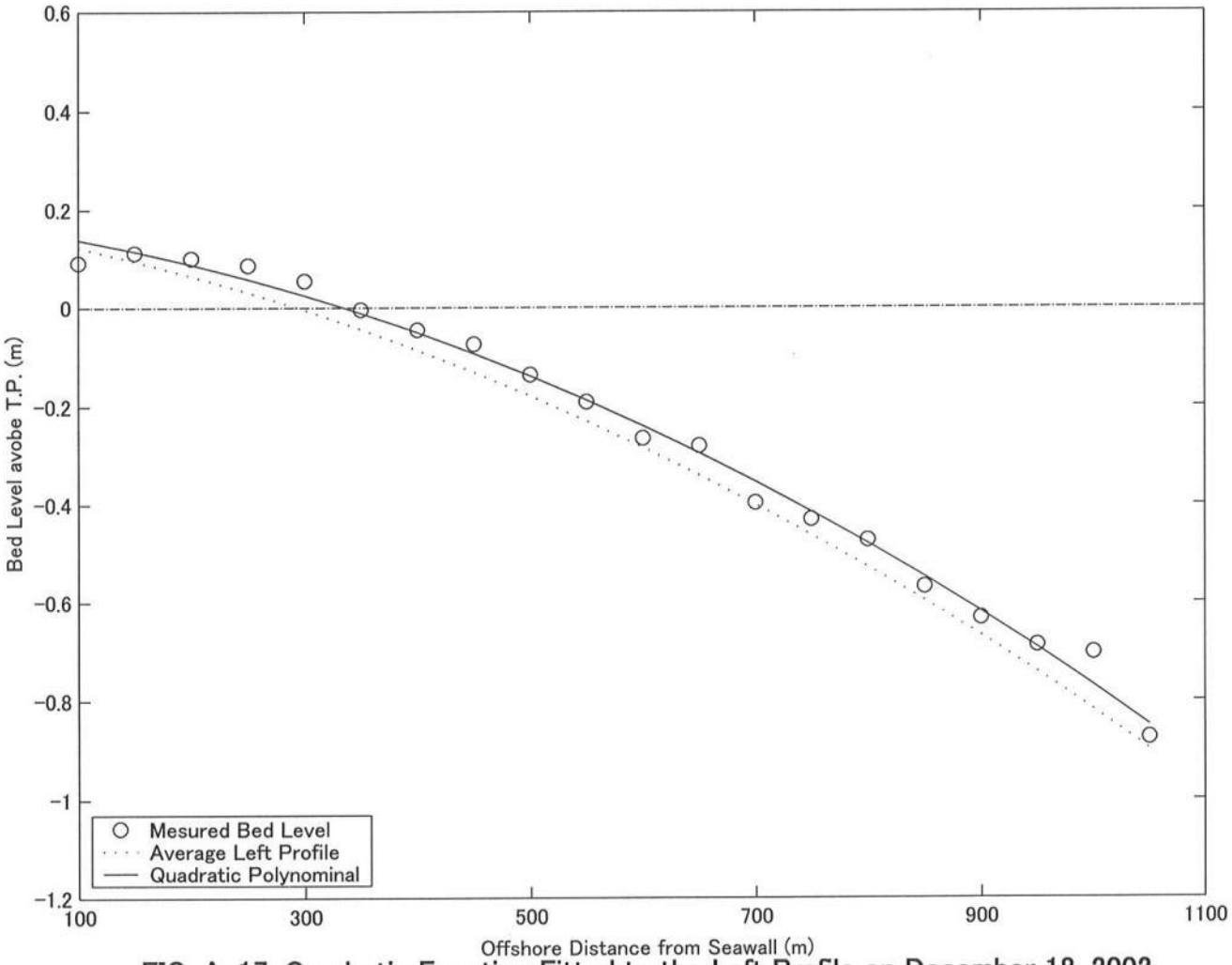

FIG. A-17. Quadratic Equation Fitted to the Left Profile on December 18, 2002

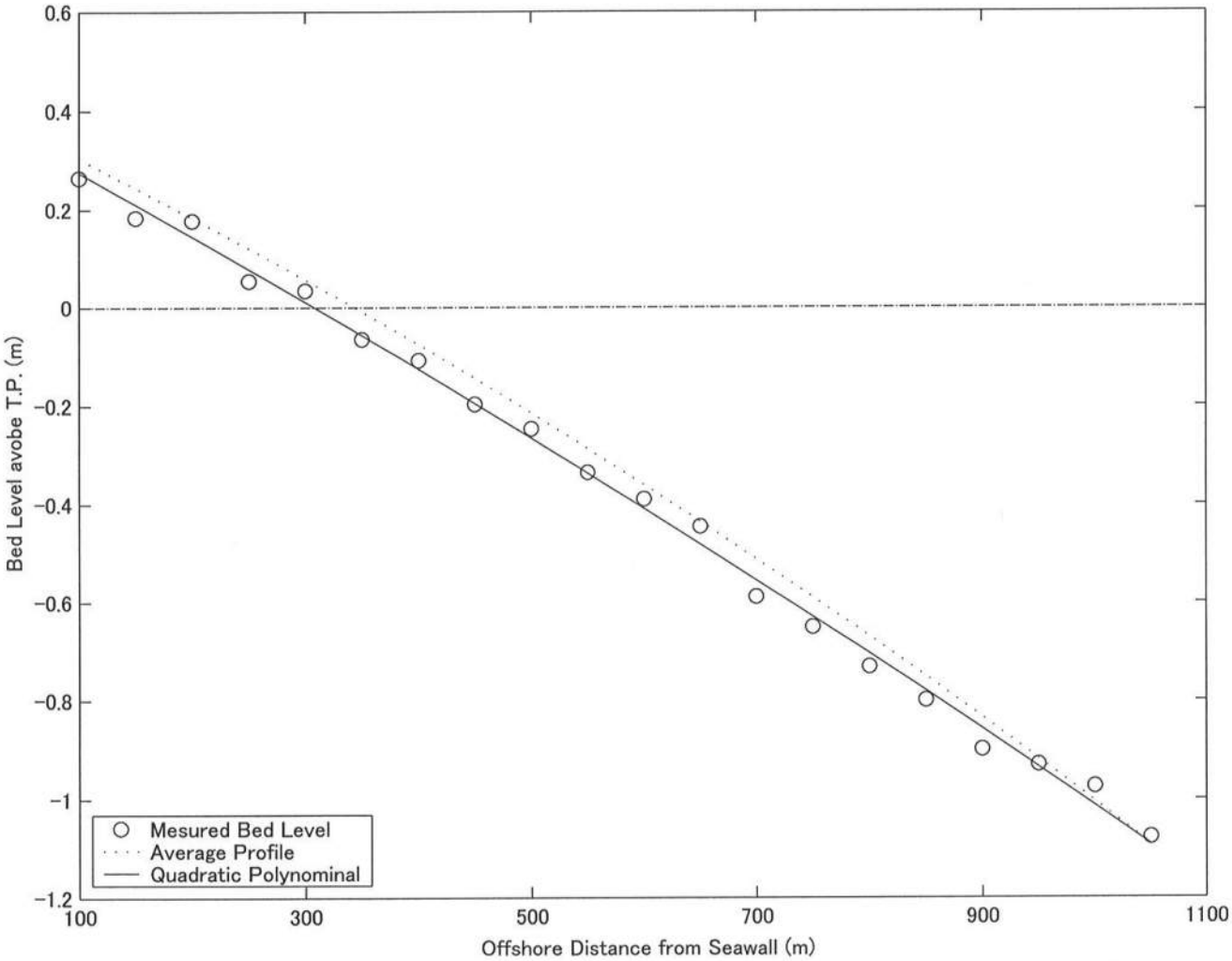

FIG. A-18. Quadratic Equation Fitted to the Right Profile on February 23, 2001

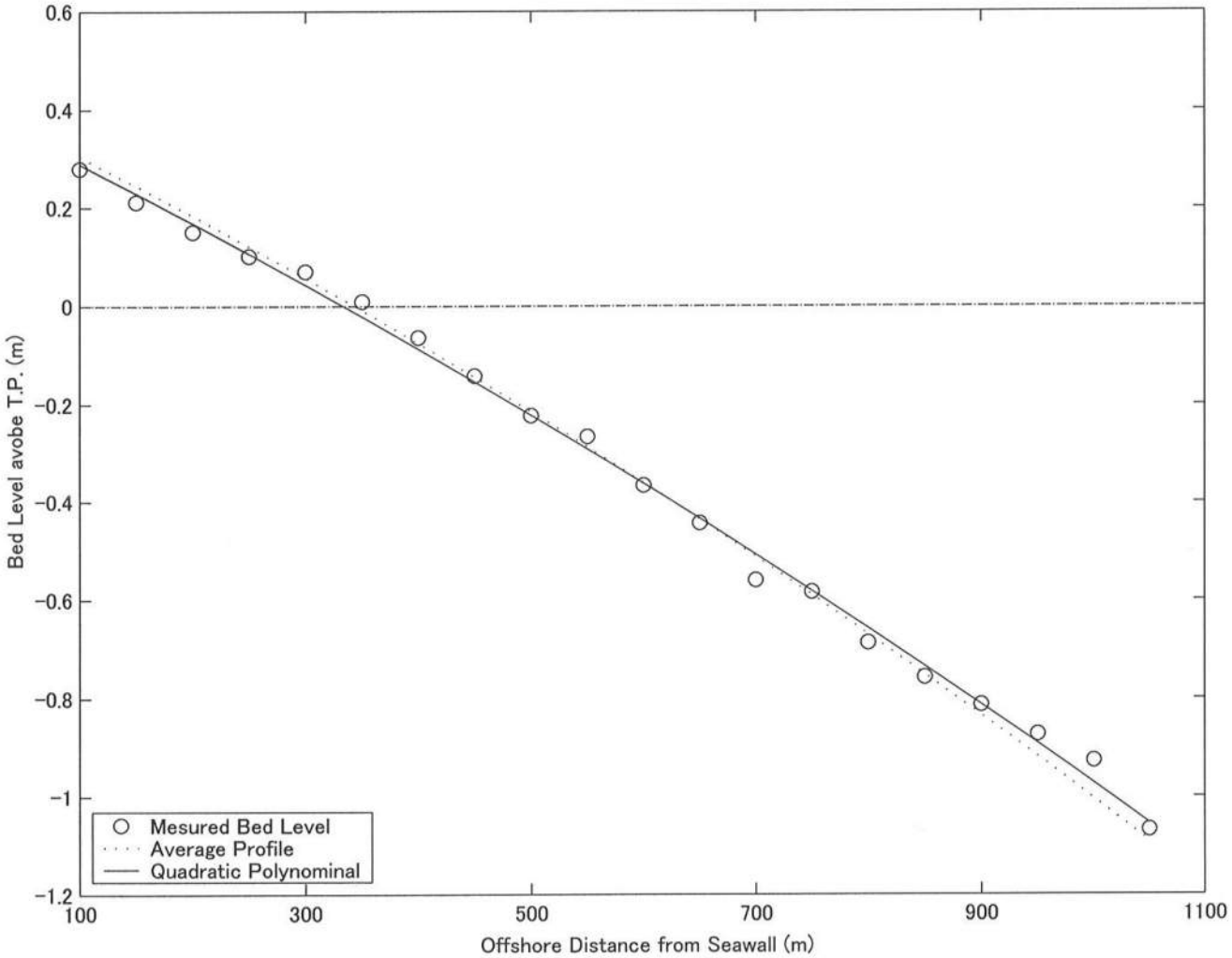

FIG. A-19. Quadratic Equation Fitted to the Right Profile on April 25, 2001

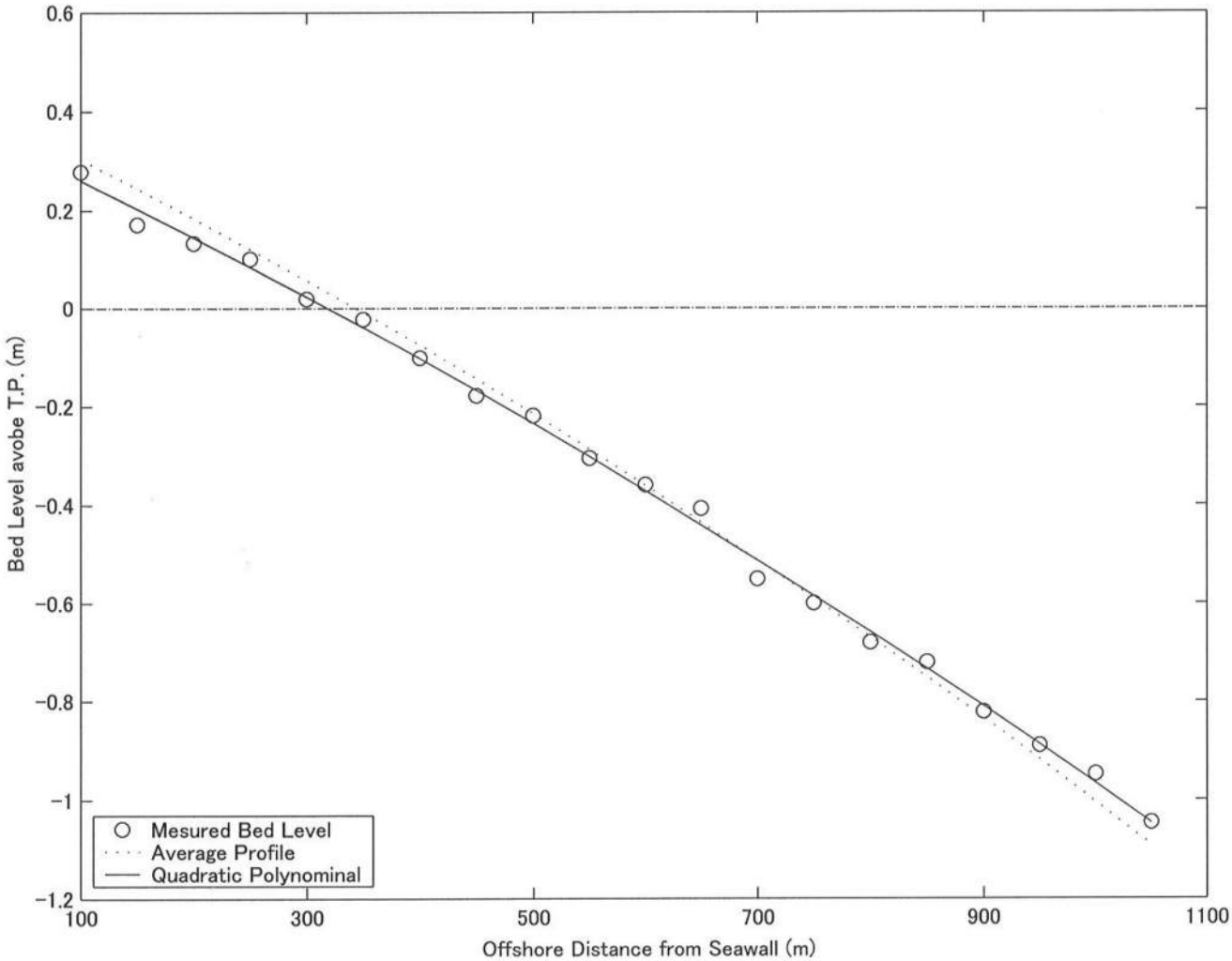

FIG. A-20. Quadratic Equation Fitted to the Right Profile on June 4, 2001

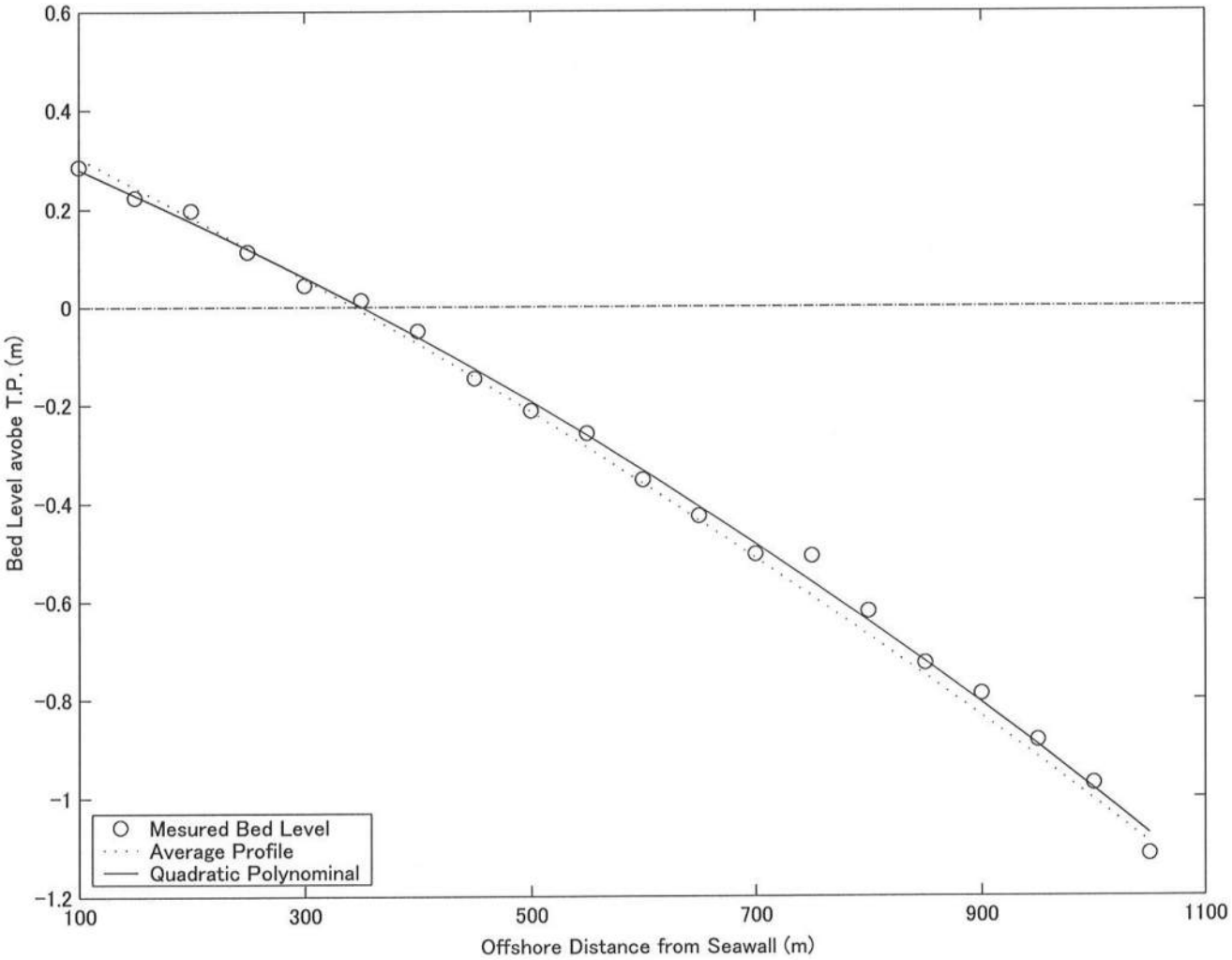

FIG. A-21. Quadratic Equation Fitted to the Right Profile on July 3, 2001

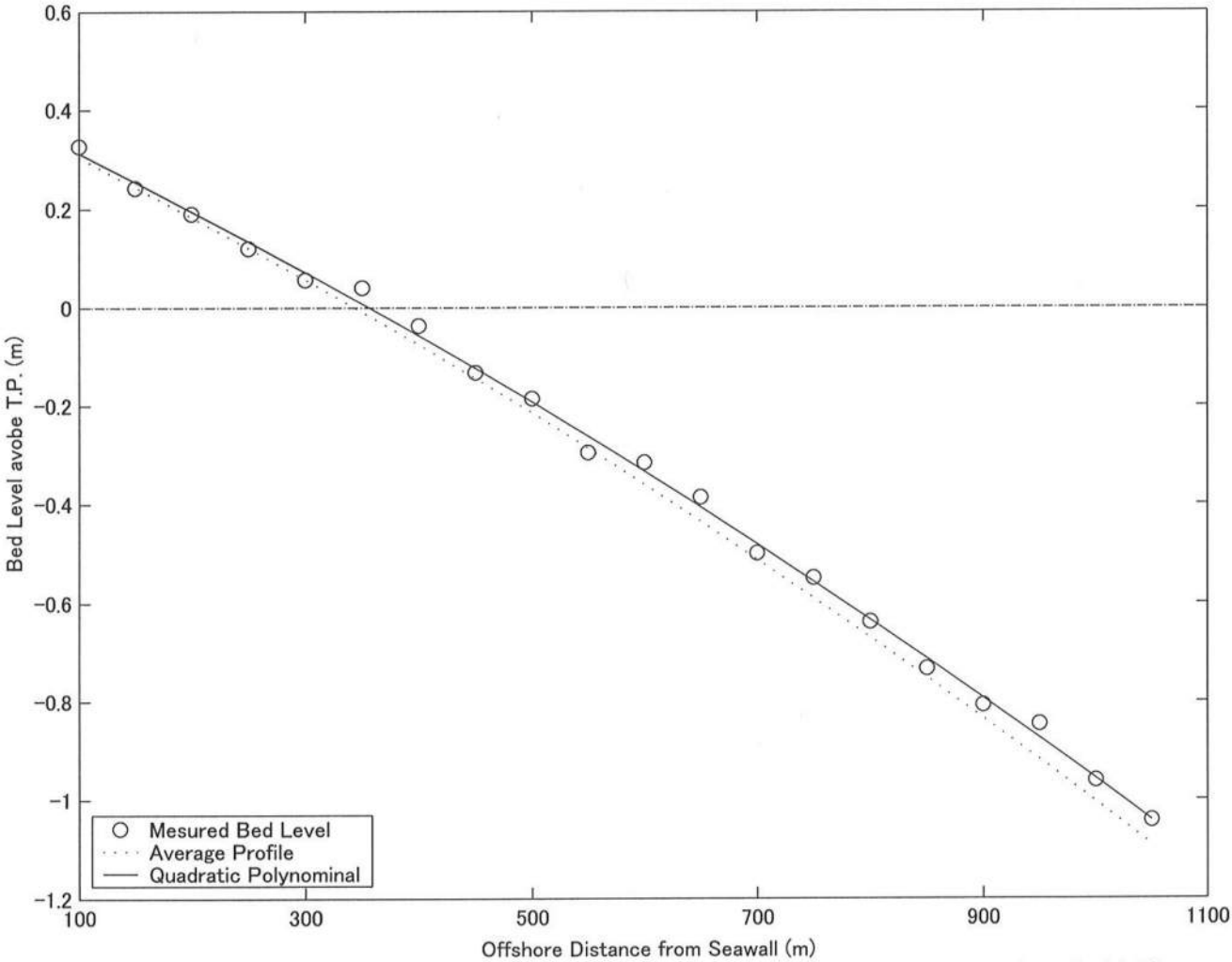

FIG. A-22. Quadratic Equation Fitted to the Right Profile on September 5, 2001

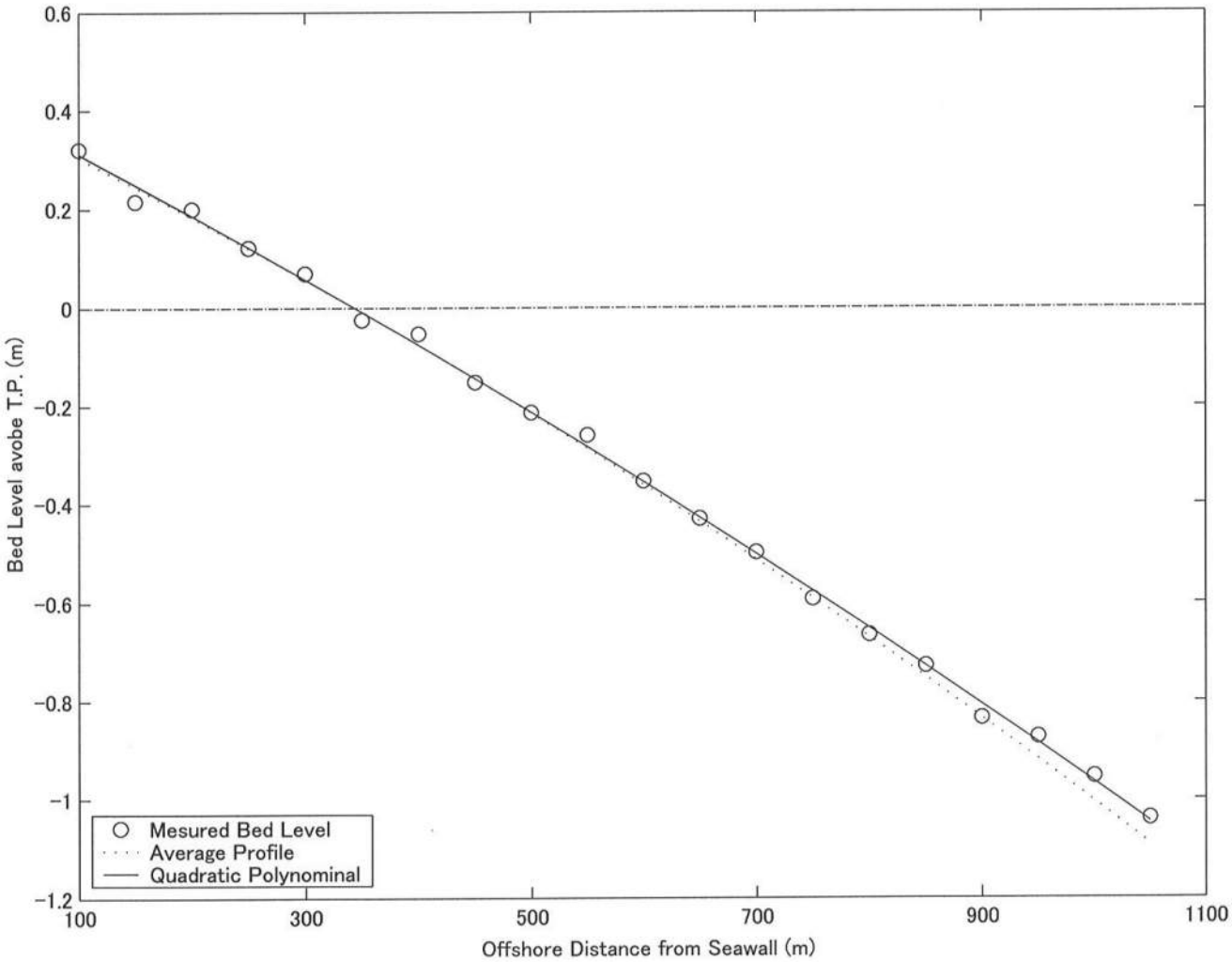

FIG. A-23. Quadratic Equation Fitted to the Right Profile on October 20, 2001

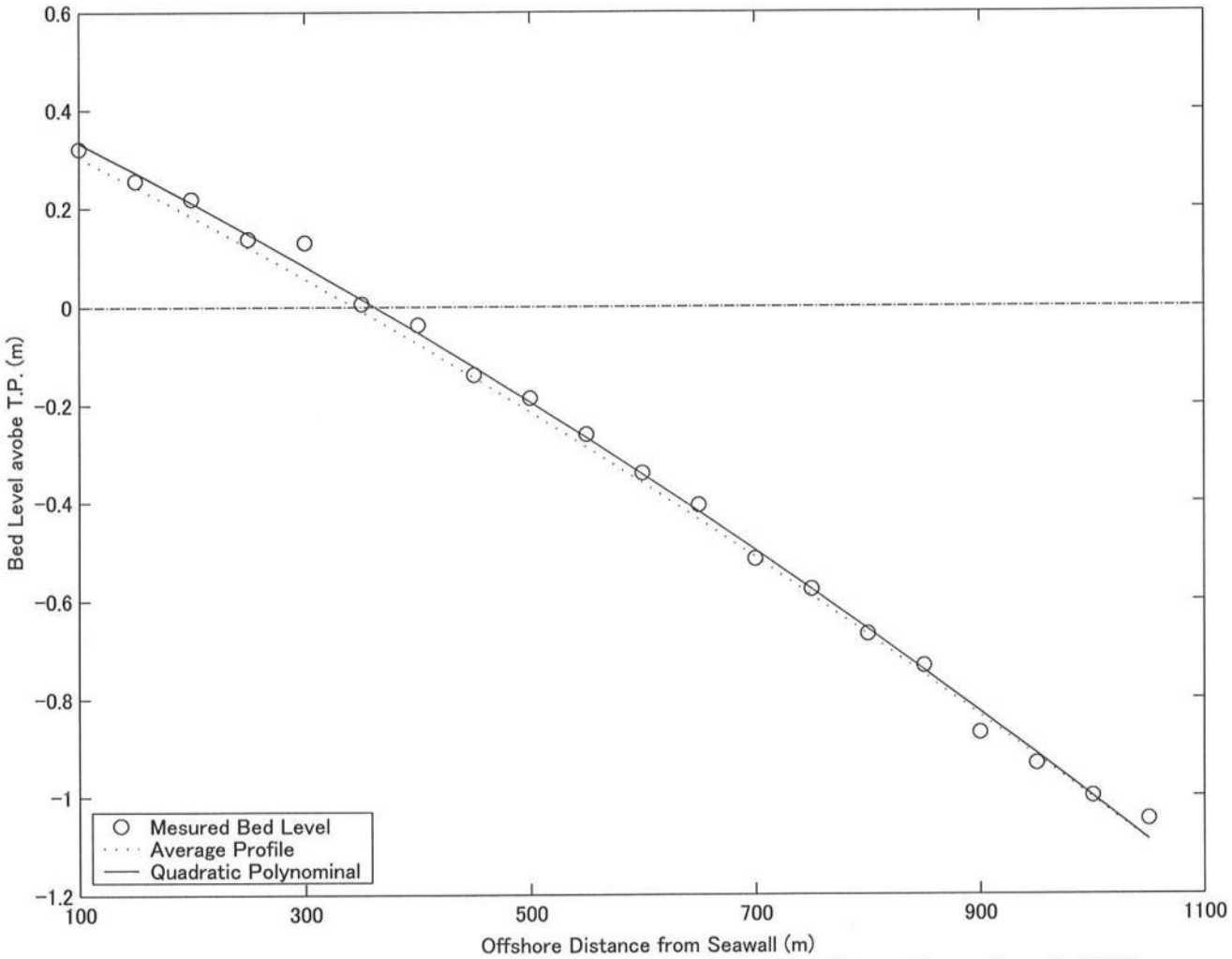

FIG. A-24. Quadratic Equation Fitted to the Right Profile on November 2, 2001

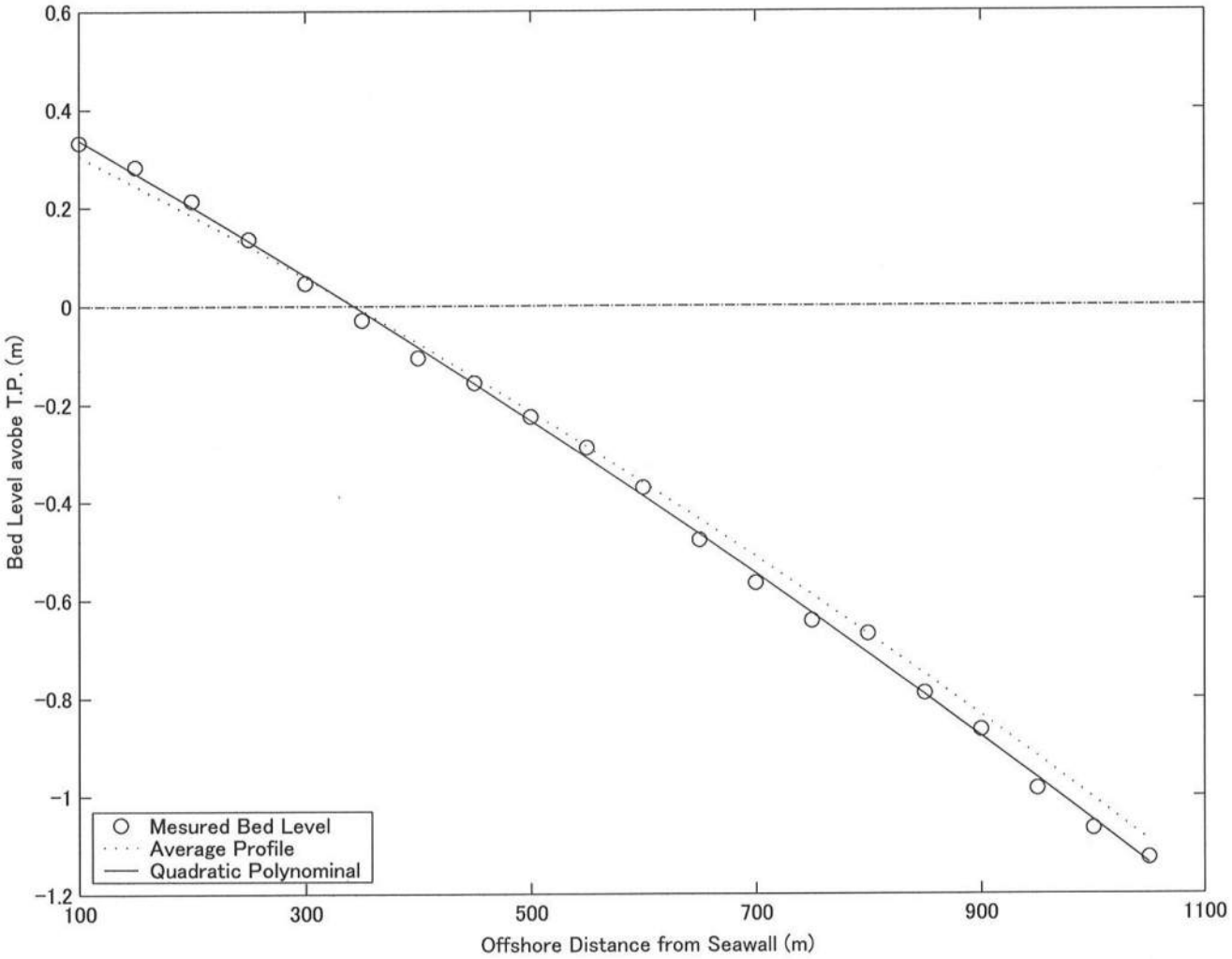

FIG. A-25. Quadratic Equation Fitted to the Right Profile on November 30, 2001

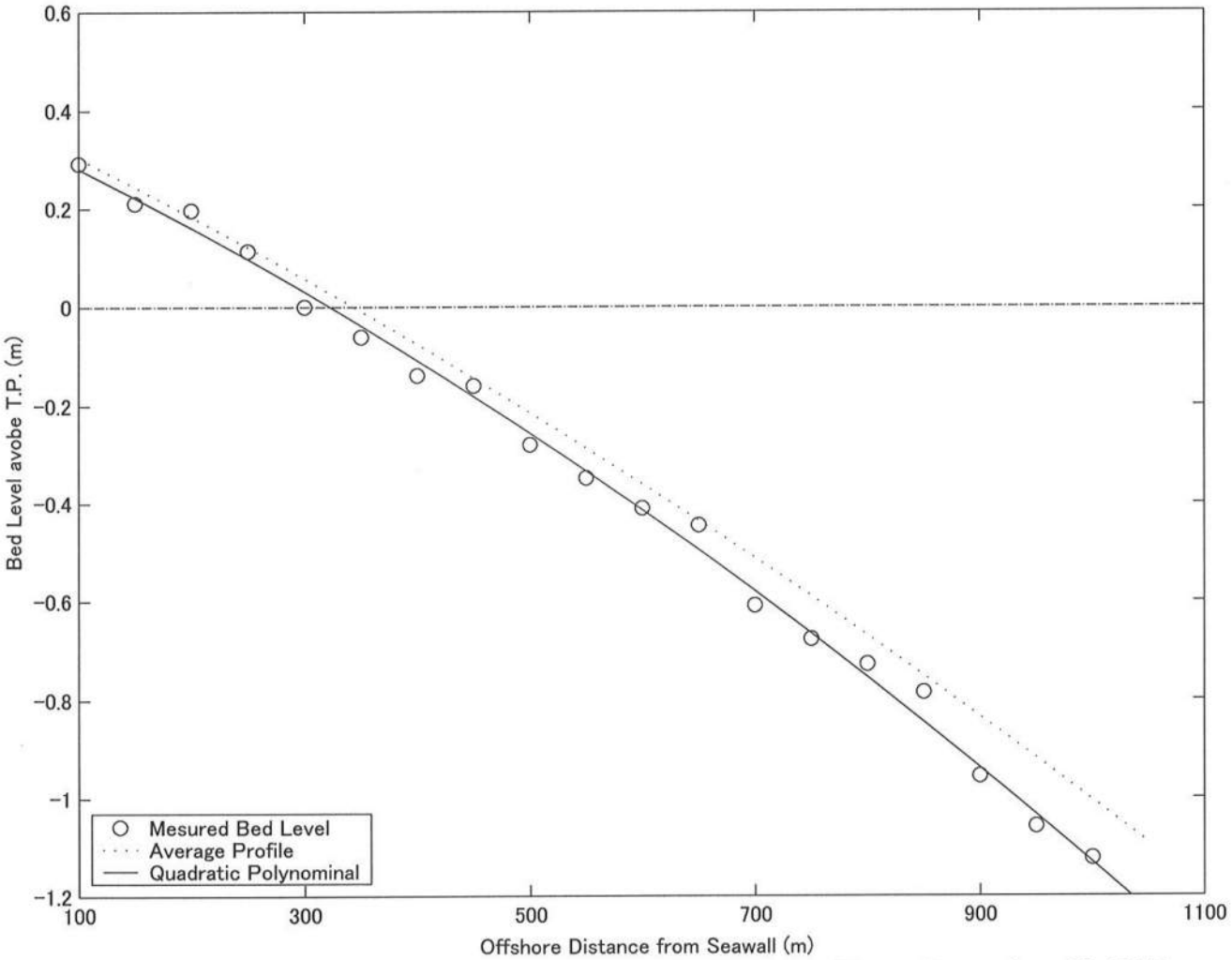

FIG. A-26. Quadratic Equation Fitted to the Right Profile on December 27, 2001

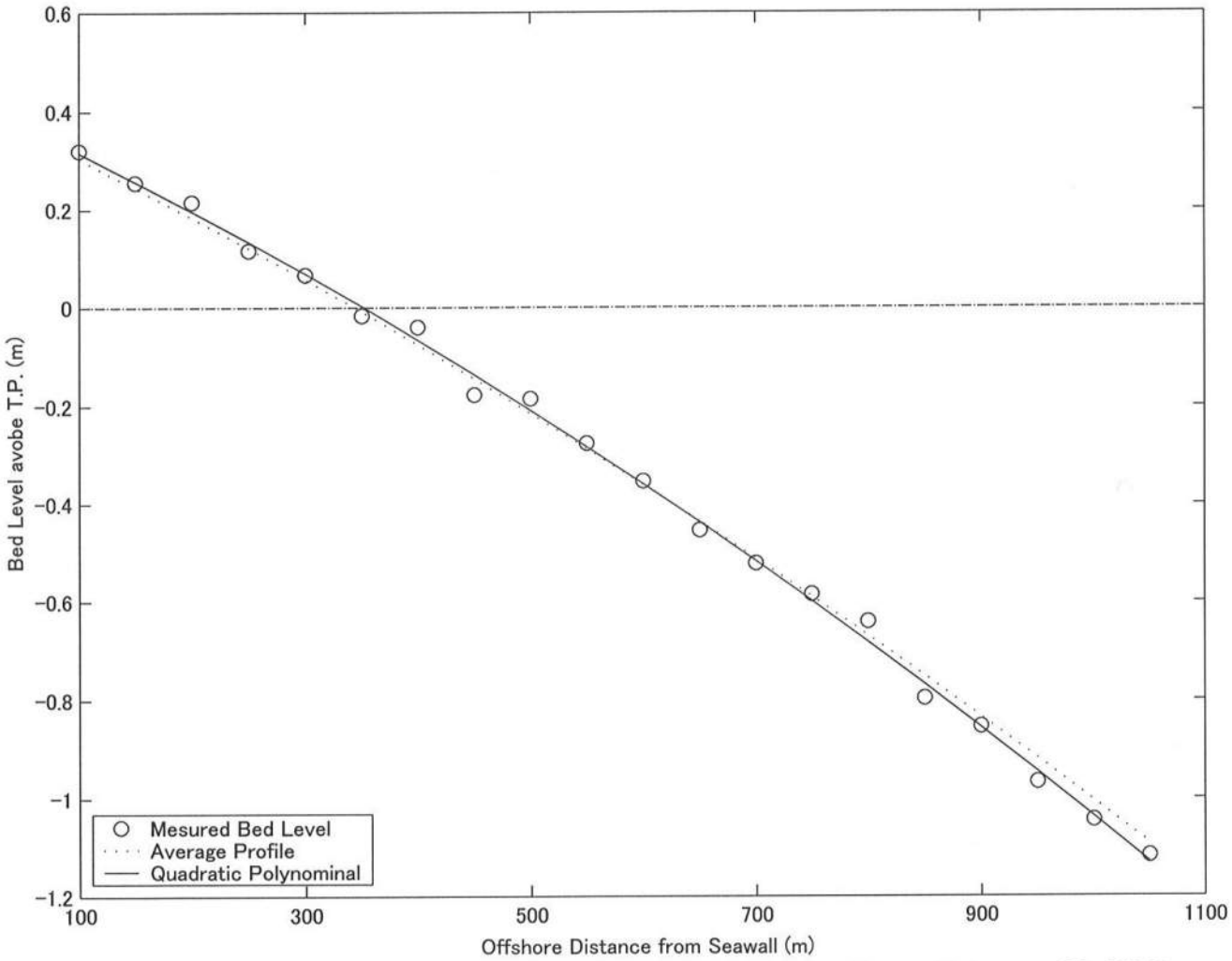

FIG. A-27. Quadratic Equation Fitted to the Right Profile on February 26, 2002

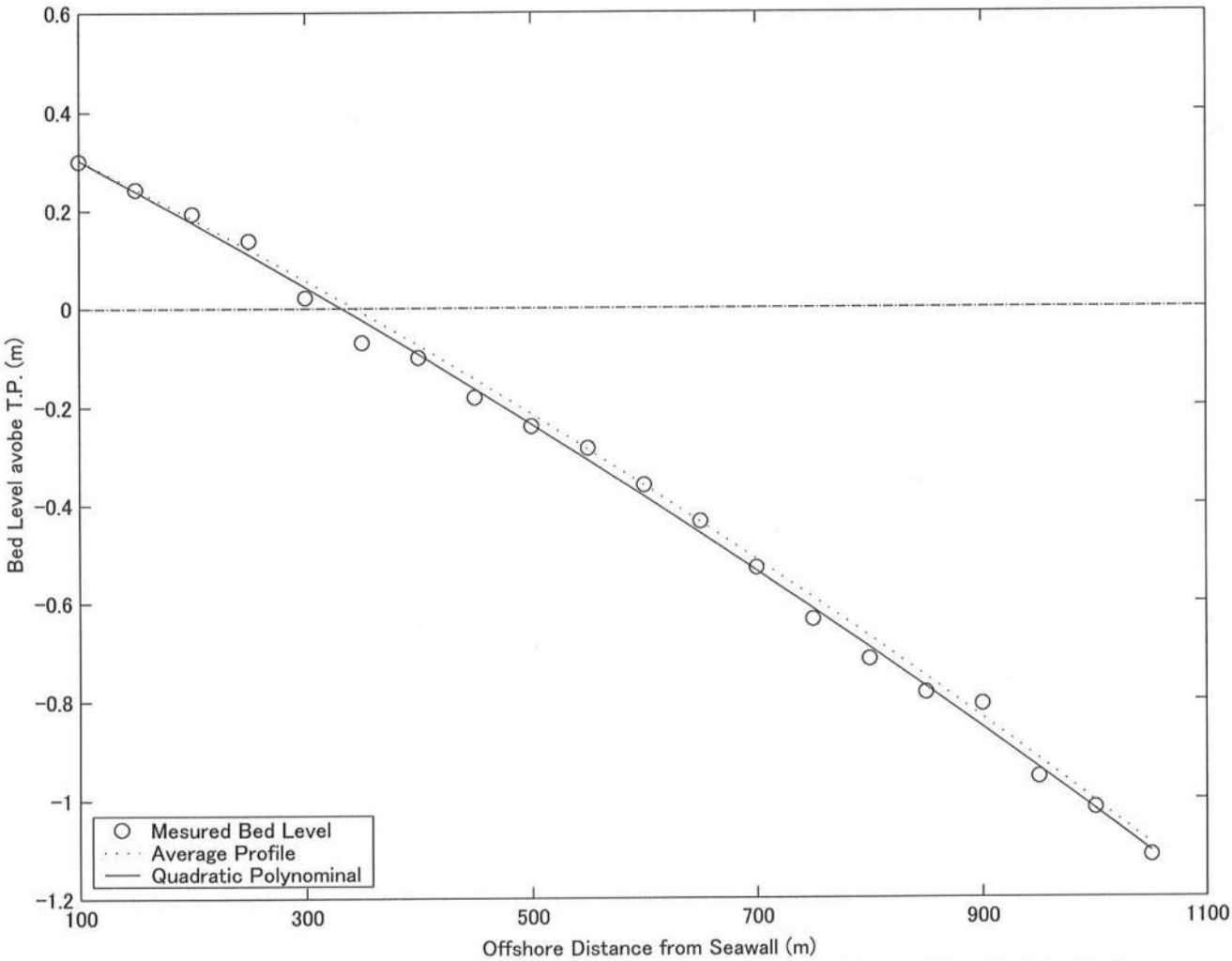

FIG. A-28. Quadratic Equation Fitted to the Right Profile on March 27, 2002

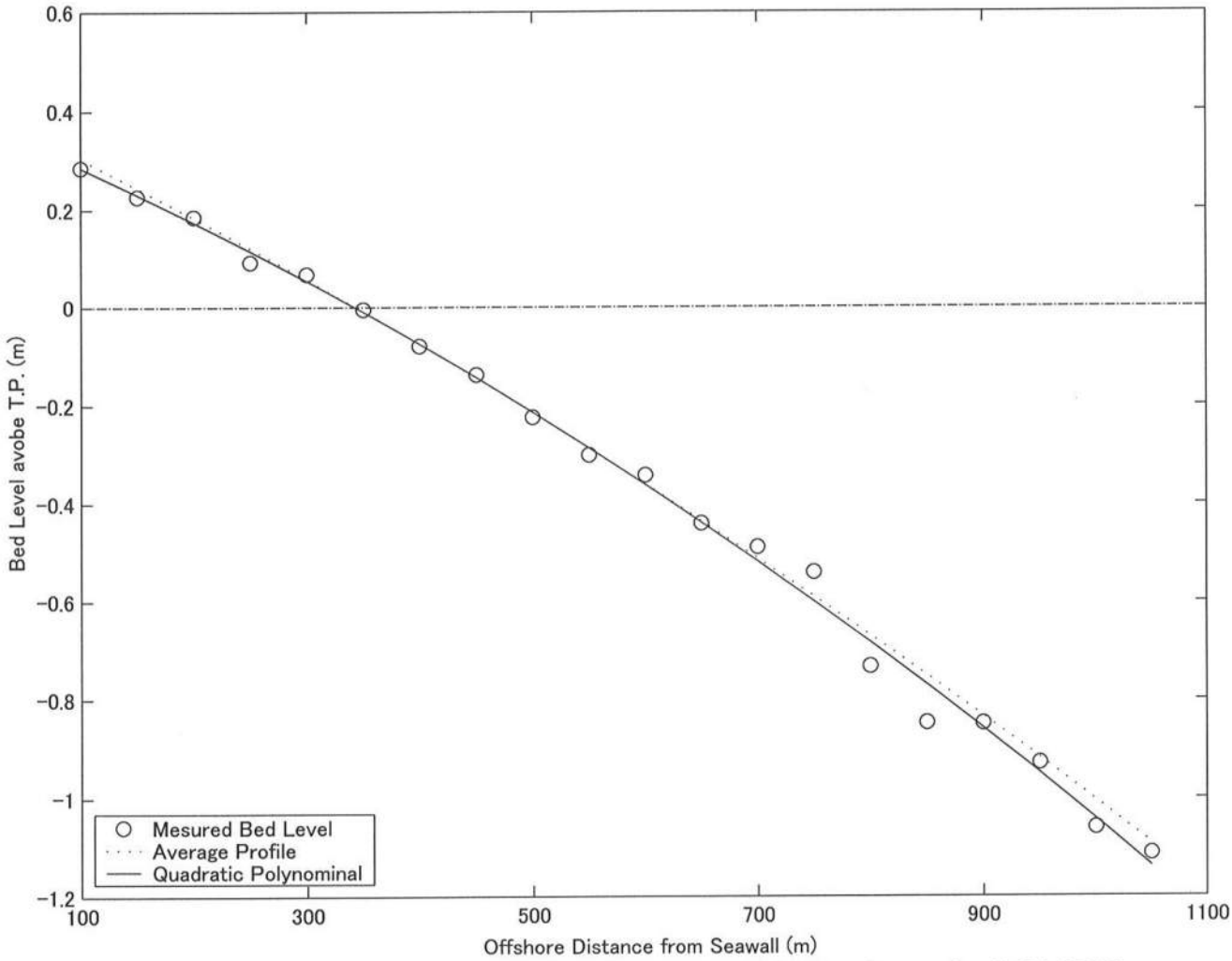

FIG. A-29. Quadratic Equation Fitted to the Right Profile on April 25, 2002

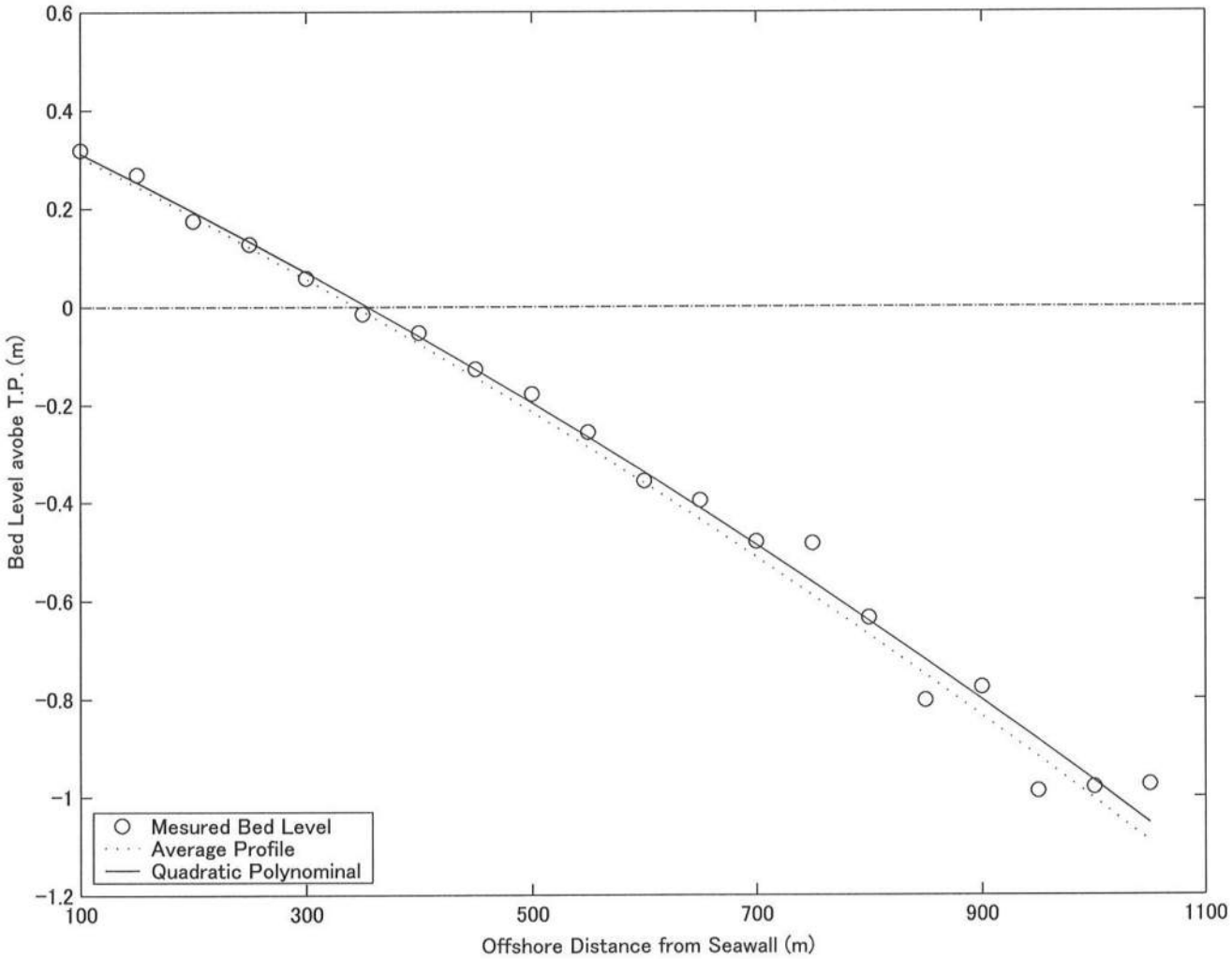

FIG. A-30. Quadratic Equation Fitted to the Right Profile on July 11, 2002

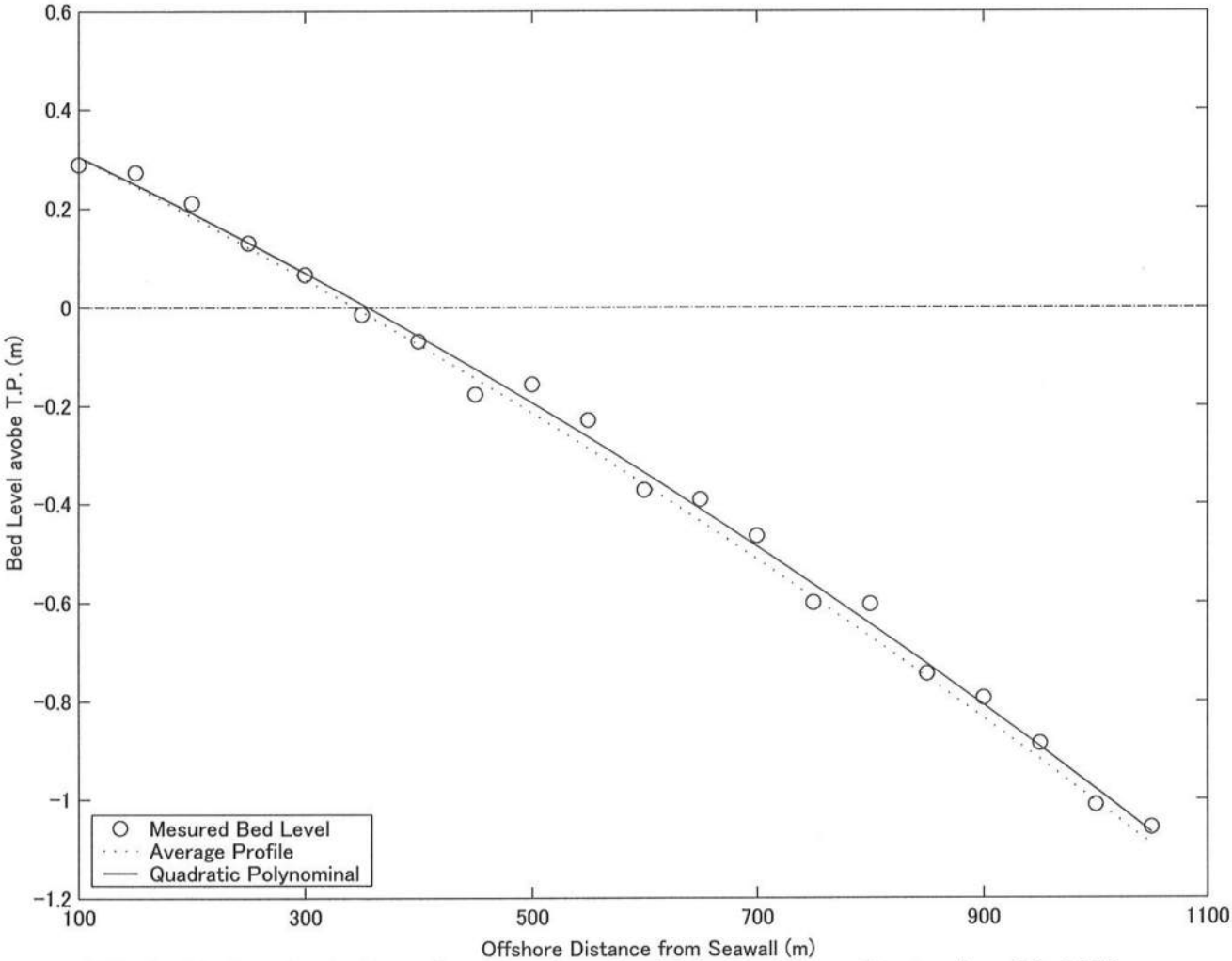

FIG. A-31. Quadratic Equation Fitted to the Right Profile on September 30, 2002

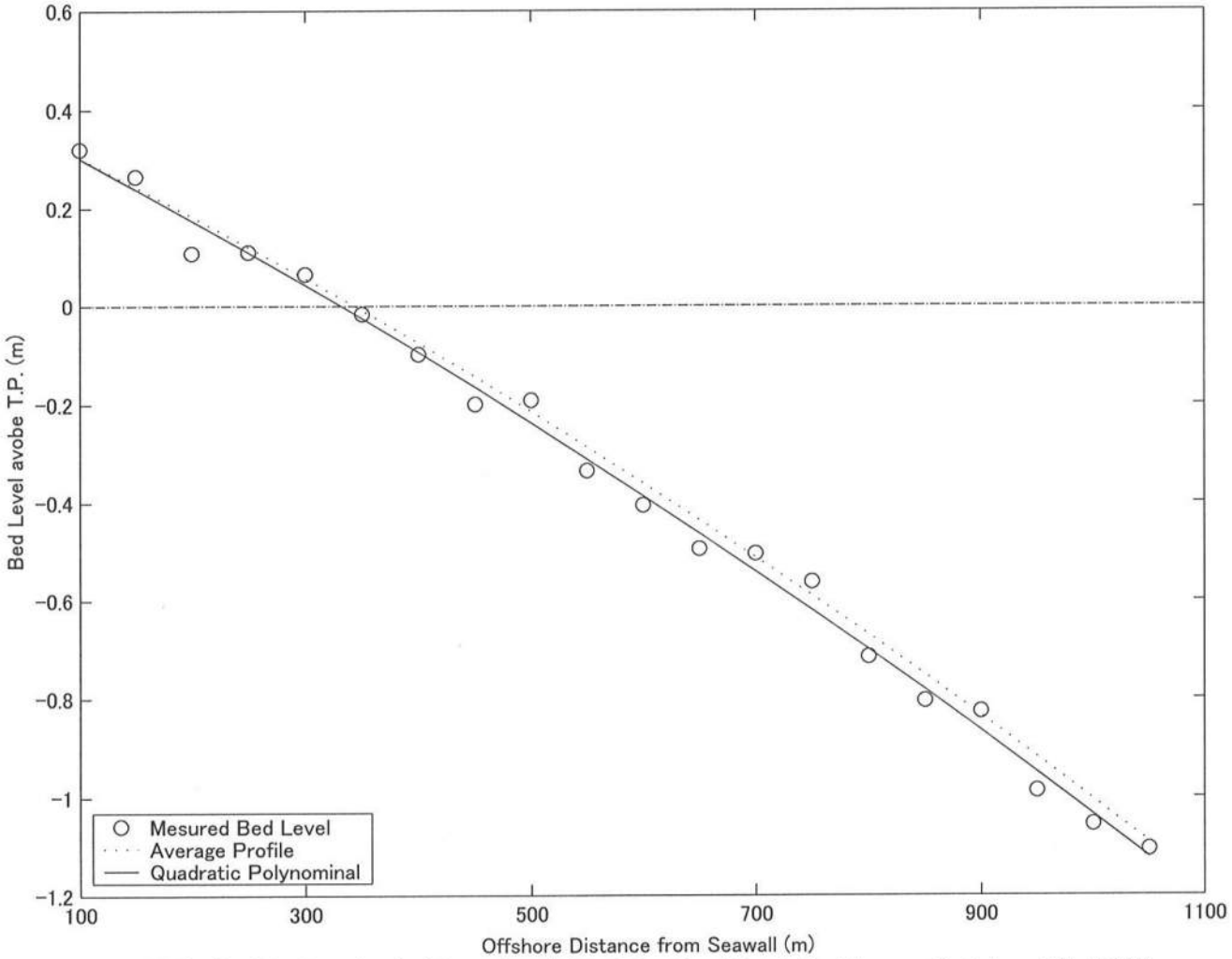

FIG. A-32. Quadratic Equation Fitted to the Right Profile on October 22, 2002

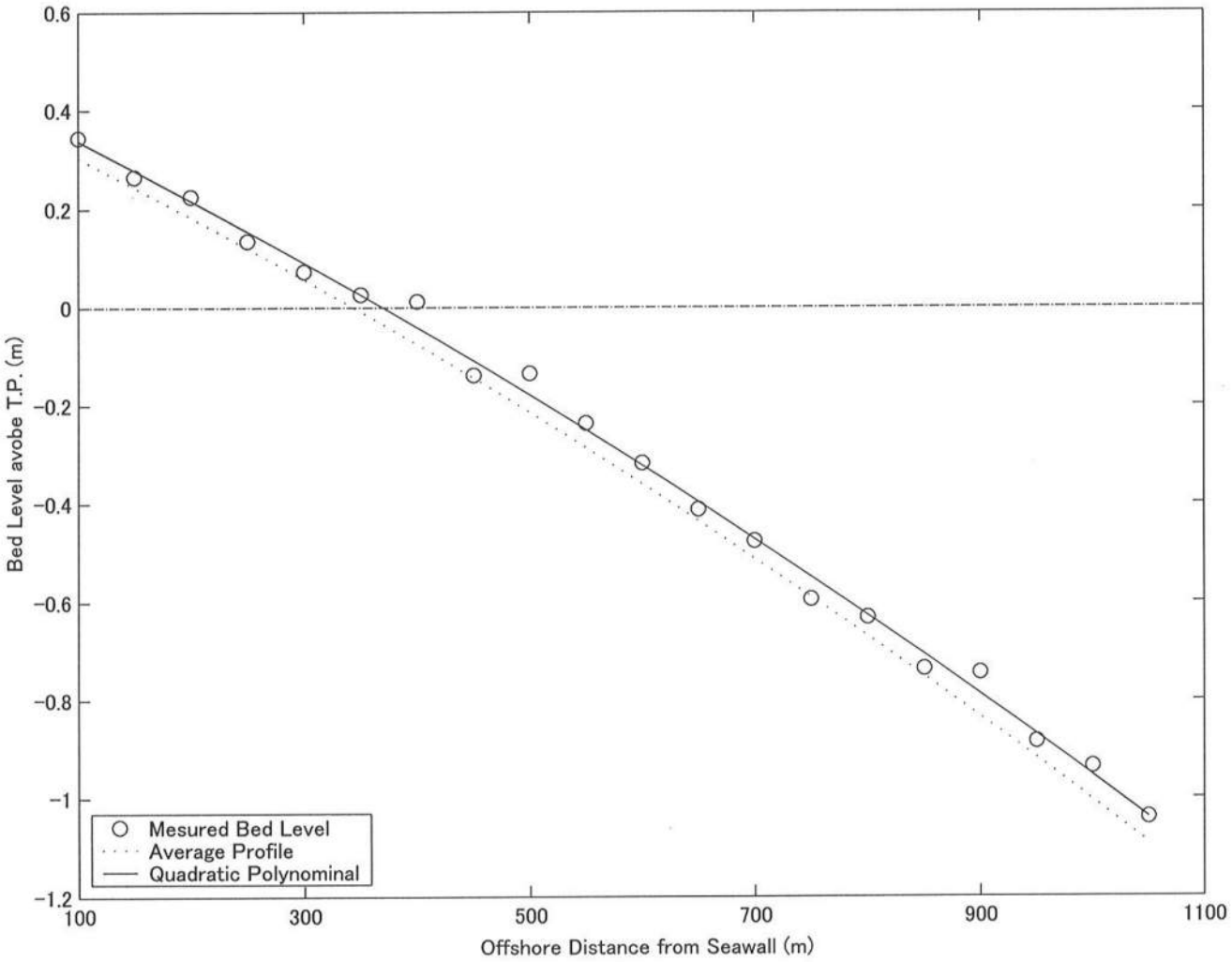

FIG. A-33. Quadratic Equation Fitted to the Right Profile on November 18, 2002

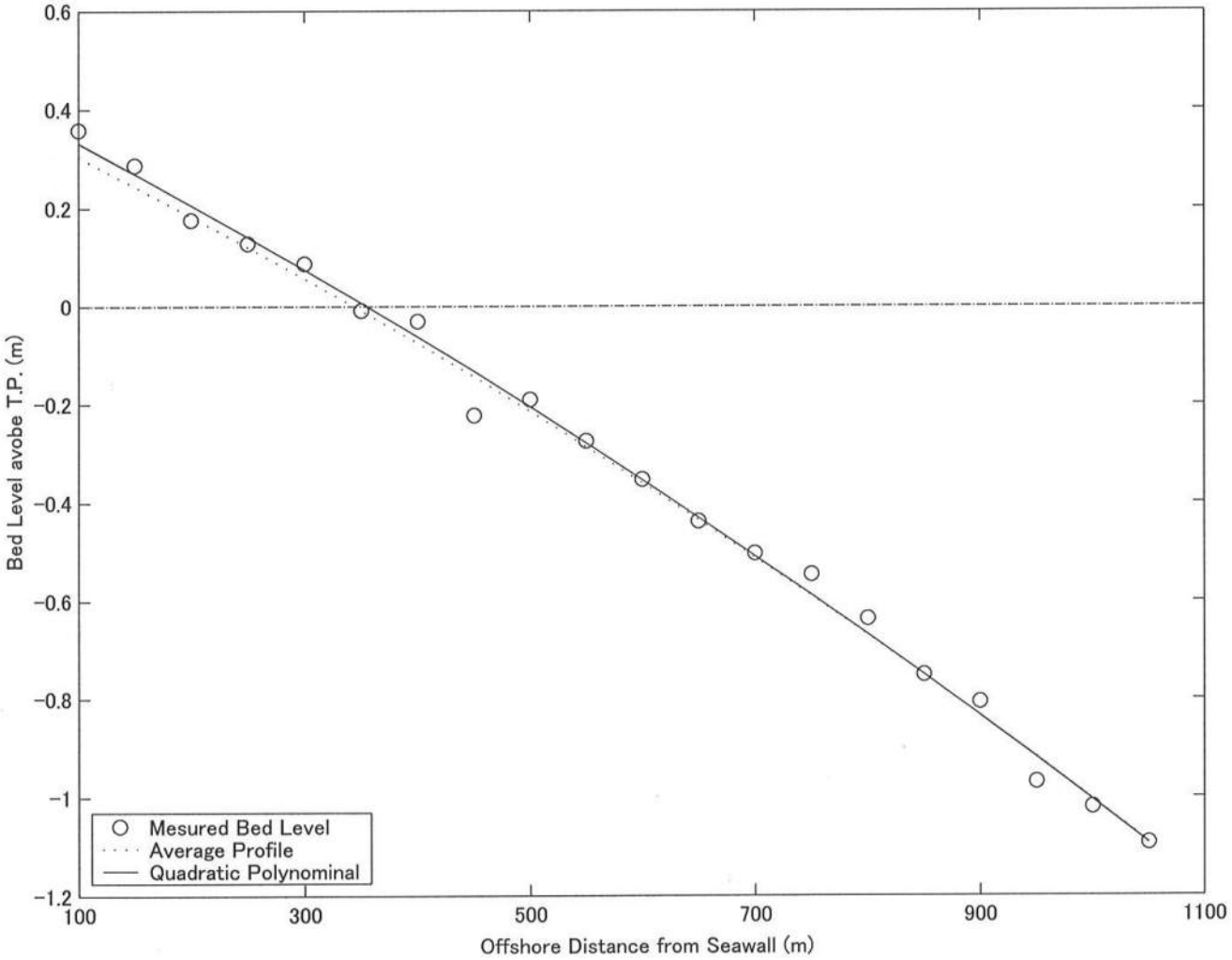

FIG. A-34. Quadratic Equation Fitted to the Right Profile on December 17, 2002